Measuring single spins with single photons

Clément Millet

Clément Millet. Measuring single spins with single photons. Quantum Physics [quant-ph]. Université Paris-Saclay, 2023. English. NNT : 2023UPASP002 . tel-04023581

HAL Id: tel-04023581
https://theses.hal.science/tel-04023581v1

Submitted on 10 Mar 2023

Measuring single spins with single photons

Mesure de spins uniques à l'aide de photons uniques

Thèse de doctorat de l'université Paris-Saclay

École doctorale n°572, Ondes et Matière (EDOM)
Spécialité de doctorat : Physique
Graduate School : Physique
Référent : Faculté des sciences d'Orsay

Thèse préparée dans l'unité de recherche **C2N (Université Paris-Saclay, CNRS)**,
sous la direction de **Pascale SENELLART**, directrice de recherche,
et le co-encadrement de **Loïc LANCO**, maître de conférences HDR

Thèse soutenue à Paris-Saclay, le 1^{er} février 2023, par

Clément MILLET

Composition du jury

Membres du jury avec voix délibérative

Emmanuelle DELEPORTE Professeure, ENS Paris Saclay Laboratoire Lumière, Matière et Interfaces	Présidente
Maria VLADIMIROVA Directrice de recherche, CNRS Laboratoire Charles Coulomb	Rapporteuse & Examinatrice
Henri MARIETTE Directeur de recherche émérite, CNRS Institut Néel	Rapporteur & Examinateur
Alberto BRAMATI Professeur, Sorbonne Université Laboratoire Kastler Brossel	Examinateur

THÈSE DE DOCTORAT

NNT : 2023UPASP002

université PARIS-SACLAY
ÉCOLE DOCTORALE
Ondes et matière
(EDOM)

Titre : Mesure de spins uniques à l'aide de photons uniques

Mots clés : photonique, boîte quantiques semiconductrice, spin, interaction lumière-matière, microcavité

Résumé : L'émergence de technologies quantiques est favorisée par les progrès dans la manipulation et le contrôle de qubits uniques. Ces technologies se construisent autour des principes fondamentaux de la physique quantique, que sont la superposition d'états, l'intrication et la mesure projective. Un réseau quantique reliant des qubits stationnaires via des canaux photoniques pourrait permettre de surpasser les protocoles de communication et de calcul classiques. Une interface entre des qubits matériels stationnaires et des qubits photoniques messagers serait alors indispensable pour faire circuler l'information quantique dans le réseau.

Nous présentons ici le développement d'une interface à l'état solide, où un qubit de spin stationnaire, un électron ou un trou unique piégé dans une boîte quantique semi-conductrice, interagit avec un qubit photonique dans une cavité micropilier. L'interaction spin-photon se produit via la rotation Faraday induite sur la polarisation des photons réfléchis, et dépendante de l'état du spin. Une fois amplifié par la cavité, cet effet peut permettre de transférer la totalité de l'information depuis l'état du spin vers l'état de polarisation des photons, réalisant une interface spin-photon.

Nous commençons par décrire la fabrication des dispositifs. Les propriétés de leur hétérostructure planaire déterminent, d'une part, la structure de bande, et donc la possibilité d'injecter électriquement ou optiquement une charge unique dans la boîte quantique. D'autre part, elles déterminent les spécificités optiques de la cavité, optimisée pour amplifier l'interaction spin-photon tout en extrayant une majeure partie des photons par le canal d'intérêt. Afin d'amplifier l'interaction lumière-matière, la technique de lithographie in-situ développée au C2N permet un couplage spatial et spectral de la cavité à la transition désirée de la boîte quantique.

Les dispositifs ainsi réalisés sont dans un premier temps caractérisés par tomographie de polarisation afin de reconstruire, dans l'état stationnaire, l'état de polarisation complet des photons réfléchis. Les rotations Faraday géantes déduites en font des candidats de choix pour une interface spin-photon. Nous estimons également l'intensité du bruit ainsi que les points de fonctionnement optimaux en termes d'énergie des photons incidents et de polarisations réfléchies associées aux états propres de spin.

Ensuite, nous accédons à la dynamique des photons réfléchis grâce aux corrélations croisées mesurées dans des polarisations complémentaires, ce qui permet de remonter à la dynamique du spin avec lequel ils ont interagi. Les contributions des dynamiques de charge et de spin peuvent être isolées en fonction des polarisations mesurées, et les sources de bruits rapides et lents sont identifiées. L'ensemble de ces résultats expérimentaux est comparé aux prédictions théoriques via une simulation basée sur l'équation maîtresse, permettant de comprendre et caractériser les processus en jeu. Celle-ci reproduit une majorité des observations, et fournit une estimation de l'efficacité de l'interface spin-photon en quantifiant la projection de spin induite par la détection des photons.

Les deux dispositifs étudiés révèlent les différences entre interfaces spin-photons basées sur un électron ou un trou et l'impact de l'hétérostructure qui les entoure. En effet, la faible sensibilité des trous aux fluctuations de spins nucléaires leur confère un temps de vie plus long que celui des électrons. Cependant, le choix d'une injection électrique des électrons dans la boîte quantique induit une meilleure stabilité que l'injection optique (choisie pour les trous) en les protégeant des bruits électriques lents. En parallèle, un régime radiatif transitoire rapide qui suit la projection de spin est susceptible de brouiller les dynamiques les plus rapides. Ceci oriente vers des dispositifs basés sur le spin d'un trou avec une injection électrique pour concrétiser des interfaces spin-photon idéales.

Title: Measuring single spins with single photons

Keywords: photonics, semiconductor quantum dot, spin, light-matter interaction, microcavity

Abstract: The emerging quantum technologies benefit from the increasingly precise manipulation and control of single qubits. These technologies are built upon the core principles of quantum physics that are the superposition of states, entanglement and projective measurement. A quantum network linking stationary qubits with photonic channels could allow outperforming classical communication and computation schemes. To that end, an interface between stationary matter qubits and messenger photonic qubits is required to transfer quantum information through the network. Here, we present a solid-state approach to the development of such an interface, where a stationary spin qubit, trapped in a quantum dot, interacts with a photonic qubit in a micropillar cavity.

In this manuscript, quantum dot-micropillar cavity devices are investigated as spin-photon interfaces. A single electron or hole is trapped in a nanometric semiconductor quantum dot acting as an artificial atom. Its spin constitutes the stationary qubit and interacts with photons in a micropillar cavity through spin-dependent Faraday polarization rotation. As this effect is enhanced by the cavity, photons might be able to extract the full information on the spin state, thus encoded on polarization, achieving a spin-photon interface.

We initially review the fabrication of the devices. Engineering the planar heterostructure sets, on the one hand, the energy band structure, and thus the ability to electrically or optically inject single charges in the quantum dot. On the other hand, it determines the optical properties of the cavity, designed to enhance the spin-photon interaction as well as the extraction of intracavity photons to the output channel. The cavity enhancement of the light-matter interaction requires the spatial and spectral tuning of the appropriate quantum dot transition to the optical mode of the micropillar cavity that we achieve through the in-situ lithography technique developed in the C2N.

The devices thus assembled are first characterized in the steady state through polarization tomography, to measure the full polarization state of the photons reflected from the device. The inferred giant Faraday rotations demonstrate their potential for spin-photon interfaces. We also quantify the intensity of noise, and determine an operating point in terms of energy of the input photons and output polarizations associated to the spin eigenstates.

Then, we measure cross-correlations between complementary polarizations of the reflected photons to access their dynamics, determined by the spin dynamics. The contribution of the charge and spin dynamics can be isolated depending on the measured polarizations, and the fast and slow noise sources are discriminated. The whole set of experimental results is compared to the theoretical predictions via a master equation simulation, in order to understand and characterize the involved processes. This model reproduces most of the experimental observations. It also allows assessing the quality of the spin-photon interface by estimating how efficiently the detection of a photon projects the spin in return.

The two investigated devices reveal the differences between an electron- and a hole-based spin-photon interface and the impact of the surrounding heterostructure. Indeed, the low sensitivity of holes to the nuclear spin fluctuations confers them a much longer spin lifetime than electrons. However, the choice of an electrical injection of electrons in the quantum dot demonstrated a better stability than its optical counterpart (chosen for holes), protecting the electron spin from slow electrical noise. In parallel, a short radiative transitory regime following spin projection blurs out the fastest dynamics. This supports the case for future hole-based devices with electrical charge injection as candidates for ideal spin-photon interfaces.

Remerciements

Les travaux que j'ai menés pendant ma thèse ont été rendus possibles par la confiance que m'ont accordée Loïc Lanco et Pascale Senellart en me donnant une place dans leur équipe. Je leur en suis profondément reconnaissant. Je remercie les membres du jury, pour avoir pris le temps d'examiner ce manuscrit et pour leurs remarques constructives. Je remercie particulièrement Loïc Lanco, avec qui j'ai travaillé au quotidien, sa passion pour la transmission du savoir, sa bienveillance et sa patience ont été et resteront un exemple pour moi. De son côté, Paul Hilaire a été un binôme de thèse brillant et pédagogue, de bonne humeur en toutes circonstances. Ce fut un honneur de prendre sa suite. J'ai eu le plaisir de travailler avec Elham Mehdi pendant la deuxième moitié de ma thèse, après le déménagement du C2N à Palaiseau. Son aide a été inestimable dans la remise en route du projet. Les contributions d'Elham et de Paul aux expériences présentées dans ce manuscrit sont majeures. Je tiens également à remercier Manuel Gundin, qui a rejoint l'équipe à la fin de mes travaux expérimentaux et qui m'a épaulé pour le traitement des données. Je voudrais aussi mentionner les postdoctorants qui ont contribué au projet, Carlos Anton et Juan Loredo, ainsi que Marcio Daldin qui nous a rejoint en tant que chercheur invité. Enfin, merci à nos stagiaires, Maxime Massoudzadegan, Warren Massonneau et Fabrizio Berritta. J'ai été honoré de travailler dans l'équipe que nous avons formée.

Ce travail repose sur les échantillons fabriqués dans la salle blanche du C2N par Aristide Lemaître, Martina Morassi, Isabelle Sagnes, Niccolo Somaschi et Abdelmounaïm Harouri. Il a été mené au sein du groupe d'optique des nanostructures semi-conductrices, dirigé par Pascale Senellart, Loïc Lanco, Olivier Krebs, Daniel Kimura, Jacqueline Bloch, Sylvain Ravets, Nadia Belabas et Anne Talneau. Je remercie particulièrement Olivier Krebs, de nous avoir fait bénéficier de son expertise sur la physique du spin. Enfin, l'activité du laboratoire ne serait possible sans la supervision et le soutien par l'équipe administrative, l'atelier mécanique et le pôle informatique.

J'ai rencontré pendant ma thèse de formidables personnalités que je tiens à remercier chaleureusement. Marie, Hélène, Florian, Ilse, Paul, Elham, Petr, Alexandre, auront marqué cette thèse de moments hauts en couleur, dans le quotidien du laboratoire comme dans nos mémorables sorties. Merci également à tous les doctorants et postdoctorants que j'ai eu la chance de côtoyer au quotidien : Nathan, Sarah, Mathias, Jovana, Lorenzo, Guillaume, Valérian, Anne, Omar, Martin, Fabrice, Priya, Valentin, Philippe, Titta, Nicolas, Marijana.

Merci à mes professeurs de physique-chimie qui ont inspiré le parcours que j'ai suivi, Frédéric Oriol, Nathalie Landraud et Romain Presle.

Enfin, merci du fond du cœur à mes amis et à ma famille pour leur soutien inconditionnel tout au long de ma thèse, ils m'ont donné la force et le courage pour mener ce projet à bien.

Table of Contents

List of symbols

Quantum dot charge states

$\varnothing$	Empty quantum dot
$\mathrm{e}^-,\ \mathrm{h}^+$	Single electron or hole
X, XX, CX	Neutral exciton, biexciton, charged exciton (positive or negative)
$\mathrm{X}^+,\ \mathrm{X}^-$	Positive and negative trions (also called charged excitons)
ω_x	Pulsation associated to the energy of the transition to charge state x

Quantum dot spin states

$\uparrow,\ \downarrow$	Electron spin up and down
$\Uparrow,\ \Downarrow$	Hole spin up and down
$\uparrow\downarrow\Uparrow,\ \downarrow\uparrow\Downarrow$	Negative trion spin up and down
$\Uparrow\Downarrow\uparrow,\ \Downarrow\Uparrow\downarrow$	Positive trion spin up and down
$\lvert e_x\rangle$	Excitonic state along the x direction
$\lvert\uparrow\rangle_x$	Spin state along the x direction (valid for all spin states and directions x, y, z)
$J_e,\ J_h$	Angular momentum of the electron or hole spin
δ_{FSS}	Fine structure splitting of the exciton
δ_Z	Total Zeeman splitting between the two transitions of a trion system
$\omega_d^{(eff)}$	Pulsation associated to the transition of the quantum dot, manually detuned by the diamagnetic shift

Bloch and Poincaré vectors

$\boldsymbol{S}$	Generic Bloch or Poincaré vector
(s_x, s_y, s_z)	Coordinates of a Bloch vector (Bloch components)
(s_{HV}, s_{DA}, s_{RL})	Coordinates of a Poincaré vector (Stokes parameters)

(ϑ, φ)	Angular coordinates of a Bloch vector (colatitude and longitude)
(θ, ϕ)	Angular coordinates of a Poincaré vector (latitude and longitude)
p	Purity (norm) of a Bloch or Poincaré vector

Cavity quantum electrodynamics parameters

$\omega,\ \omega_c,\ \omega_d$	Pulsations associated to the energies of the photons (input laser), the fundamental mode of the cavity and the two-level system (representing the quantum dot)
$\omega_{c,H},\ \omega_{c,V}$	Pulsations associated to the energies of the H and V cavity modes
ω_0	Common value of ω_c and ω_d when they are taken equal
$\Delta\omega$	Laser-quantum dot detuning
g	Light-matter coupling rate
κ	Total rate of the photonic cavity losses (top mirror, bottom mirror, sidewalls)
$\kappa_{top},\ \kappa_{bottom}$	Components of the cavity losses through the top and bottom mirrors
κ_{loss}	Component of the cavity losses through sidewalls
γ	Dephasing rate of the two-level system (quantum dot)
γ^*	Pure dephasing rate
$\gamma_{sp},\ \Gamma_0$	Spontaneous emission rate and Purcell-accelerated emission rate in the cavity mode
Γ	Total emission rate of the two-level system in the cavity (Purcell-enhanced and spontaneous)
C	Cooperativity
η_{top}	Top mirror output coupling
η_{in}	Input coupling
Q	Quality factor of the cavity
$\lvert E_{n,\pm}\rangle, E_{n,\pm}$	Eigenstates and eigenenergies in the Jaynes-Cummings model

Magnetic field parameters

(B_x, B_y, B_z)	Components of the magnetic field in the transverse (x, y) and the longitudinal (z) directions with respect to the growth axis of the micropillar cavity
$(\mathrm{H_B}, \mathrm{V_B})$	Horizontal and vertical polarizations relative to a transverse magnetic field
$Z_e,\ Z_h$	Zeeman splitting of the electron or hole

$Z_{\parallel},\ Z_{\perp}$	Zeeman splitting caused by a magnetic field in the z direction (longitudinal) and or the x and y directions (transverse)
δ_{FSS}	Fine structure splitting of the exciton
$\delta_{dia,\parallel},\ \delta_{dia,\perp}$	Diamagnetic factor in the longitudinal or transverse directions

Other symbols

$\lvert\Psi\rangle$	Generic pure quantum superposition state
$\lvert\Psi_{\Uparrow}\rangle\ ,\ \lvert\Psi_{\Downarrow}\rangle$	Reflected polarization state after interaction with a $\Uparrow$ or $\Downarrow$ spin state
$\boldsymbol{\hat{\rho}}$	Generic density matrix
$T_1,\ T_2,\ T_2^*$	Relaxation, dephasing and pure dephasing time
k_BT	Energy associated to thermal fluctuations
$\boldsymbol{\hat{H}}$	Generic Hamiltonian operator
$\boldsymbol{\hat{S}}^{(e)},\ \boldsymbol{\hat{S}}^{(h)}$	Generic electron or hole spin operator
$\boldsymbol{\hat{I}}$	Generic nuclear spin operator
$A^{(h)},\ A^{(e)}$	Hyperfine coupling constant of the electron or hole
$\mathcal{V}$	Volume of the unit cell in the hyperfine interaction
$\lvert g\rangle\ ,\ \lvert e\rangle$	Ground and excited levels of a generic two-level system
$\boldsymbol{\hat{a}},\ \boldsymbol{\hat{a}}^{\dagger}$	Annihilation and creation operators for photonic Fock states
$\boldsymbol{\hat{\sigma}},\ \boldsymbol{\hat{\sigma}}^{\dagger}$	De-excitation and excitation operators for the two-level system
$r,\ t$	Reflection and transmission coefficients
$R,\ T$	Reflectivity and transmissivity
n	Optical index
$N_t,\ N_b$	Number of top and bottom DBR pairs of the cavity
L_{cav}	Physical cavity length
$\vec{E}$	Generic electric field vector
$\mathbb{N}^*$	Set of non-zero natural numbers

Abbreviations

AFM	Atomic force microscope
BS, PBS, NPBS	Beam splitter, Polarizing beam splitter, Non-polarizing beam splitter
cQED	Cavity quantum electrodynamics

CW	Continuous wave
DBR	Distributed Bragg reflector
DNP	Dynamic nuclear polarization
HBT	Hanbury-Brown - Twiss experiment
HOM	Hong - Ou - Mandel experiment
HWHM	Half width at half maximum
HWP, QWP	Half wave-plate, quarter wave-plate
LA, LO	Longitudinal acoustic, longitudinal optical (phonons)
LP	Linear polarizer
ME	Master equation
MBE	Molecular beam epitaxy
NR, QR	Non-resonant, quasi-resonant (excitation)
PhC	Photonic crystal
PL	Photoluminescence
PLE	Photoluminescence excitation
QD	Quantum dot
QND	Quantum non demolition
RWA	Rotating wave approximation
SK	Stranski-Krastanov
SNS	Spin noise spectroscopy
(SP)APD	(Single photon) avalanche photodiode
SNSPD	Superconducting nanowire single photon detector
SPS	Single photon source
TCSPC	Time-correlated single photon counter
TTL	Transistor-transistor logic

Introduction

In the early 1900s, the problem of the *black body spectrum* – the temperature-dependent spectrum emitted by perfectly absorbing objects – was unresolved by what was to become the *classical* theories of electromagnetism and statistical physics. Only by hypothesizing that light should be quantized was Max Planck able to close the gap between the theoretical predictions and the experimental observations, including for instance the emission spectra of stars and galaxies. This interpretation established the nature of light as a particle without contradicting its existing description as a wave: the *wave-particle duality* gave birth to quantum physics. At the microscopic scale, what was classically envisioned as a wave could behave as a particle and vice versa. Quantum physics reshaped how we viewed the structure of atoms, chemical interactions, light-matter interaction and the behavior of electrons in solids (only to name a few). Numerous everyday devices were developed following this breakthrough: transistors and semiconductor devices, GPS, lasers, MRIs and many others. They inherit what is referred to as the *first quantum revolution*. However, some of the most advanced and also counterintuitive phenomena at the core of quantum mechanics (namely the superposition of states, entanglement and projective measurement), hold the promise of a *second quantum revolution* when technological novelties mature from the four related domains that emerged: quantum simulation [1], quantum sensing [2], quantum communications [3, 4] and quantum computation [5, 6]. Each of these fields seeks to harness the quantum properties of matter to outperform their classical counterparts.

The fundamental building block for quantum applications is the qubit, the quantum analog of a classical bit. While in the classical realm, a bit can only take two values (0 and 1), the quantum superposition of states allows a qubit to take any values $\alpha\left|0\right\rangle + \beta\left|1\right\rangle$ where α and β are two complex numbers such that $|\alpha|^2 + |\beta|^2 = 1$. A qubit can therefore be viewed as a vector on the surface of a three-dimensional sphere. This change of paradigm from a binary state to a continuum of superposition states comes, on the one hand, with potentially tremendous computing capability, but on the other hand, with the vulnerability of the delicate quantum state to environmental noise. Indeed, classical bits in silicon transistors consist in ensembles of tens of thousands of atoms, whereas qubits are commonly made up of a relatively low number of particles (often only a single one) so as to manifest the desired quantum properties. The most common types of qubits are photons, atoms and ions, electrons and other charged particles, and superconducting circuits based on Josephson junctions. Fundamental quantum experiments, such as the entanglement between two matter qubits, were first achieved with trapped atoms and ions [7], owing to sophisticated trapping schemes and extremely pure operating environments. However, the downside is their lack of scalability – a decisive criterion for efficient quantum computation [5]. The interest for qubits trapped by design in solid-state devices thus grew: nowadays, tech giants Google and IBM focus their efforts towards quantum computing with superconducting qubits [8], and the field of artificial atoms is very active as well, investigating for instance colored centers in diamond and semiconductor quantum dots [9]. Photonic qubits, for their part, show an interesting quantum state robustness as they interact very little with their environment. As such, their most common application is to convey quantum information from one stationary qubit to the other, in freespace or through optical fibers [3]. They can also be envisioned as standalone qubits for quantum computation through linear optics [10] (i.e., using only single-photon sources, beam-splitters, phase shifters and photodetectors), however, this paradigm lacks photon-photon gates and has a limited scalability.

An efficient quantum computation scheme relies, on the one hand, on the ability to perform quantum operations on qubits (such as initialization, coherent manipulation, gating operations and measurement), but on the other hand, an equally important feature is to transfer quantum states between stationary qubits over a distance through messenger qubits such as photons [5]. This requirement gives its relevance to the general idea of a *quantum internet* [3], connecting a network of stationary qubit nodes through photons in optical fibers. This opens the path to increasingly elaborate quantum communication [11] and computation schemes [12] through highly entangled light-matter states, even with only a few nodes. The first experimental breakthroughs in this framework are owed to the cold atom field, where cavity quantum electrodynamics (cQED) was pioneered through the extremely efficient coupling between atomic and photonic qubits in optical cavities [13]. Since then, this very active domain has demonstrated advanced experiments towards an atom-photon interface [14, 15] and more recently, towards a quantum network [16]. The efficiency of cold atoms nonetheless comes at the price of cumbersome control apparatus, which led to consider other avenues for large-scale quantum applications. Among them, semiconductor solid-state devices offered a platform of choice, where charged particles can be trapped in quantum dots [17], forming artificial atoms (stationary qubits). Engineering the light-matter interaction in semiconductor microcavities brought cQED to the solid-state domain [18]. The interest towards such devices grew as they could provide efficient and practical single-photon sources for quantum optics applications with an exceptional scalability [19]. The control of a quantum dot charge and spin state in a microcavity [20] later set the stage to conceive a solid-state interface between a stationary spin qubit and photons injected into the device. From then, many quantum optics phenomenon involving spins were demonstrated in the solid-state, from coherent spin control by photons [21] to spin-photon entanglement [22].

The work presented in this manuscript originates from the development of solid-state single-photon sources in the C2N, driven by the team of P. Senellart who demonstrated the deterministic coupling between single quantum dots and micropillar cavities [23]. The assembled devices led to extremely efficient single-photon sources [24], but also to the coherent control of a quantum dot state [25] or the generation of peculiar non-classical states of light [26]. The approach adopted here aims at realizing a spin-photon interface able to coherently transfer the full quantum state from a quantum dot spin to a photon through the spin-dependent Faraday rotation of the photonic polarization, enhanced by the microcavity [27, 28]. Such a device would in turn provide a deterministic entanglement between a stationary spin and an external photon [29], to generate complex entangled states between a single spin and multiple photons [30] or to study the fundamentals of the projective quantum measurement [31, 32].

The manuscript is organized as follows:

Chapter 1 introduces the principle of a quantum dot-based solid-state spin-photon interface, from the confinement and control of a spin qubit in a quantum dot to the cavity-mediated spin-photon interaction, detailing the current state of the art along the way. We initially present the semiconductor quantum dot, the fundamental solid-state unit that is to hold the spin qubit as a single electron or hole. Its nanometric size confers atom-like optical transitions between charge states of spin determined by the photon polarization: there lies the core principle of our solid-state spin-photon interface. The electrical control of the structure coupled to an appropriate optical excitation protocol provides the means of controlling both the charge and spin states of quantum dots. We subsequently examine the direct application to single-photon source. Then, we focus on the spin qubit per se, described in the Bloch sphere, by analyzing how an operator might manipulate or measure its quantum state and how the influence of environmental fluctuations manifests. The spin-noise spectroscopy and spin-photon entanglement with quantum dots give two initial demonstrations of the spin-photon interaction in the solid state, historically limited by the absence of an optical cavity. In the third part of this chapter, we introduce the quantum dot-cavity coupling: its theoretical description in the cQED framework and its experimental implementation through *in-situ* lithography. By describing the quantum state of photons in the Poincaré sphere and detailing the cavity enhancement of the spin-dependent polarization rotation, we show that such a device might transfer an arbitrary quantum state of a spin on the polarization state of a photon.

Chapter 2 initially presents the two devices investigated throughout the manuscript: one couples a single hole spin to a micropillar cavity and the other relies on an electron spin. Their deterministic fabrication assisted by *in-situ* lithography demonstrates the successful enhancement of the desired optical transition by the cavity. We then proceed to review the principle of the main experimental techniques through their preliminary application to the hole-based device, in anticipation of the in-depth characterization to come in the next chapters. First, the polarization tomography reconstructs the complete photonic polarization state in the Poincaré sphere, and its application to measure the cavity birefringence allows to quantify the quality of the optical alignment. Second, the optimization of the device as a spin-based single-photon source focuses on the emission rate, purity and indistinguishability criteria: this provides proper operating conditions to eventually address the device as a spin-photon interface. Finally, photonic cross-correlation measurements reveal the quantum dot charge and spin dynamics imprinted on the photons in specific polarization bases: the former quantifies the occupation probability of the desired charge state while the latter indirectly evidences the spin projection induced by the photonic measurement, a key feature of a spin-photon interface.

Chapter 3 includes the theoretical tools to simulate our devices in the cQED framework through the numerical resolution of the master equation. The model is built progressively until it encompasses most of the physical phenomena of interest, from the spin-photon interaction in a cavity to the effect of fluctuations induced by the solid-state environment. Extracting the possible outcomes of tomography and cross-correlation experiments from the simulation allows to study the influence of the parameters at play and to lay the foundations for the interpretation of real experiments in the next chapters. In particular, focusing first on the steady-state polarization tomography, we show that a wide range of device parameters lead to an ideal spin-photon interface in specific configurations of input laser energy and polarization measurement basis. We then evaluate the spin projection induced by photonic measurement, which is accompanied by three dynamic phenomena on its way back to equilibrium: a radiative rebalancing between excited and ground states, spin flips and charge escape. The interplay between these contributions determines the quality of the spin-photon interface. We finally evaluate the impact of fast and slow electrical noise, both in steady-state and dynamic regimes, so as to distinguish their different contributions in the experiments.

In chapter 4, the hole-based device is experimentally characterized as a spin-photon interface. The polarization tomography assesses a giant spin-dependent polarization rotation as well as a good charge occupation probability, but points out its limitation by noise, bringing it below ideality. We implement cross-correlation experiments to perform spin-noise spectroscopy for the first time with single photon detectors. They show a promising long spin lifetime and unambiguously designate slow electrical fluctuations as the main source of noise. We conclude by simulating a modest overall performance as a spin-photon interface, as quantified by the measurement-induced spin projection. More precisely, slow noise prevents the projective measurement from occuring in a determined spin eigenstate. The performance would, however, significantly be improved by removing the slow fluctuations and would become close to ideal in the complete absence of noise.

In chapter 5, an analogous study is carried out on the electron-based device. From the tomography standpoint, the polarization rotation meets the criterion for ideality with very little noise and a close to ideal charge occupation probability. For their part, the cross-correlation experiments indicate a partial measurement-induced spin projection, obtained for the first time through giant Faraday rotation. That is, the measurement of a photon changes the spin populations. However, this measurement also exposes a complex interplay between fast spin flips and radiative rebalancing, which greatly limits the potential application of this device as a spin-photon interface and steers future development towards an implementation of such a low noise device coupled to a hole spin.

We conclude by presenting perspectives of this work. Immediate improvements of the experimental techniques in a similar paradigm could be followed by prospects towards spin-photon gates with current devices. In the long term, projects based on next-generation devices could include the production of multipartite entangled states involving a spin and a string of consecutive single photons, as well as the fundamental study of quantum measurement.

Chapter 1

Charged quantum dots in microcavities: an overview

The elementary units of quantum computing are logic gates executing operations on one or multiple qubits. A spin-photon interface is a device capable of imprinting the quantum state of a spin on a photon or vice versa: in this regard, it is suited to achieve a wide range of logic operations involving the two types of qubit, starting with the spin-photon entanglement operation. Transferring this technology from the existing cold atoms experiments [15, 16, 33] to the domain of solid-state systems holds tremendous promise and challenges. Promise in terms of scalability and affordability of a device which could become a building block of a complex quantum information system, and challenges inherent to the orders of magnitude of environmental noise separating an atomic qubit in a vacuum chamber and a spin qubit trapped in a solid-state quantum dot, surrounded by millions of fluctuating nuclear spins. Throughout this chapter, we review the technical solutions elaborated over the years to develop cavity quantum electrodynamics (cQED) devices in the solid state. The centerpiece is a quantum dot, acting as an artificial atom and carrying single spins. A microcavity is built around it, enhancing the light-matter interaction. We give the basic theoretical explanations to unravel the physical principle of the spin-photon interface, and present the state-of-the-art experiments in related areas, with a focus on the solid-state applications.

1.1 Confinement of charges in quantum dots

1.1.1 Epitaxial growth

Stranski-Krastanov method

A quantum dot is a semiconductor nanostructure containing approximately 10^5 atoms embedded in a high-bandgap matrix, acting as an artificial atom [17] by confining charges on discrete energy levels like electrons on atomic orbitals. The structures studied in this manuscript are self-assembled InGaAs quantum dots grown by the Stranski-Krastanov (SK) method [34, 35], which proceeds as follows: the deposition of InAs on a bulk GaAs substrate, layer by layer, leads to the formation of nanometric lens-shaped islands, the *quantum dots* (Fig. 1.1a). The stability of the structure is explained by the lattice parameter mismatch between InAs (6.06 Å) and GaAs (5.65 Å), resulting in the build-up of strain when the InAs film grows: after a critical thickness of 1.7 monolayers (called the *wetting layer*), quantum dots form at random positions to relieve strain. The typical quantum dot size is 3 nm in the growth direction and 10-20 nm in the lateral plane (Fig. 1.1b) and this flat asymmetric shape has important implications discussed later in this chapter.

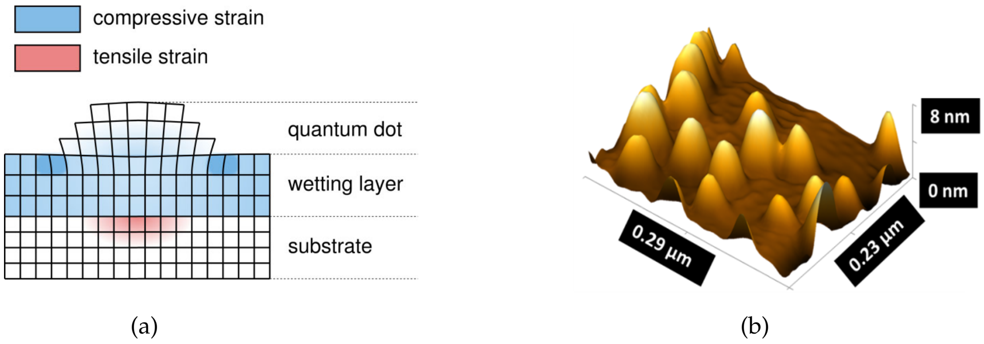

(a) (b)

FIGURE 1.1: **(a)** Illustration of the strain relief by the formation of InAs quantum dots on a GaAs substrate by the SK method. The sketch shows a 3 monolayer thick wetting layer. Figure from [36]. **(b)** Atomic force microscope (AFM) measurement of the quantum dot landscape after SK growth (vertical scale has been enlarged for better visibility). Figure from [37].

A capping layer of GaAs encloses the quantum dots. In addition, they are annealed at high temperature (850-900 °C): the interdiffusion of In and Ga between the quantum dots and the capping layer ensues, making the dots flatter, more symmetrical in the lateral plane and with a more homogeneous shape distribution across the whole sample [38]. After this step, the composition of quantum dots is $\mathrm{In}_{1-x}\mathrm{Ga}_x\mathrm{As}$ but we keep the notation InGaAs for clarity.

While the SK method is widely used in the quantum dot community, other growth protocols are worth mentioning, especially the rapidly expanding *droplet epitaxy* [39], more flexible than SK as far as the shape and composition of quantum dots are concerned. In addition, controlling the location of the growth site motivated the development of techniques such as the epitaxy on a substrate patterned with nanoholes [40, 41].

Energy structure of quantum dots

In the same way that electronic orbitals of an atom are quantized, the charge carriers confined in a quantum dot can only access discrete energy levels due to the nanometric scale of the structure, hence the reference of quantum dots as artificial atoms. An actual quantum dot is shown in Fig. 1.2a as viewed by a transmission electron microscope, evidencing its flatness in the growth direction z. The confined electrons and holes (of respective electric charge $-$e and $+$e) experience the energy band structure represented in Fig. 1.2b, with valence and conduction bands separated by a bandgap evolving along z. At cryogenic temperatures (4 K), the gap energies of the GaAs 3D bulk and InAs 2D wetting layer are respectively 1.5 eV and 1.45 eV. The gap of the quantum dot is diminished by its InAs content to constitute a potential well (the bandgap of pure bulk InAs is 0.42 eV at 4 K).

While the low bandgap of the quantum dot traps electrons in the valence band and holes in the conduction band, its nanometric dimensions cause the quantization of the energy levels. The discrete electronic states of the quantum dot are denoted s, p, d for the conduction band like their counterparts in natural atoms, and the valence band states are labeled *h states* due to their more complex wavefunctions [42]. When the quantum dot and its close surroundings are undoped semiconductors, the Fermi energy E_F lies in the middle of the bandgap, filling the valence band with electrons and leaving the conduction band empty. In this manuscript, a single conduction band electron or a single valence band hole act as solid-state qubits, interacting with photons (messenger qubits) of specific energy and polarization.

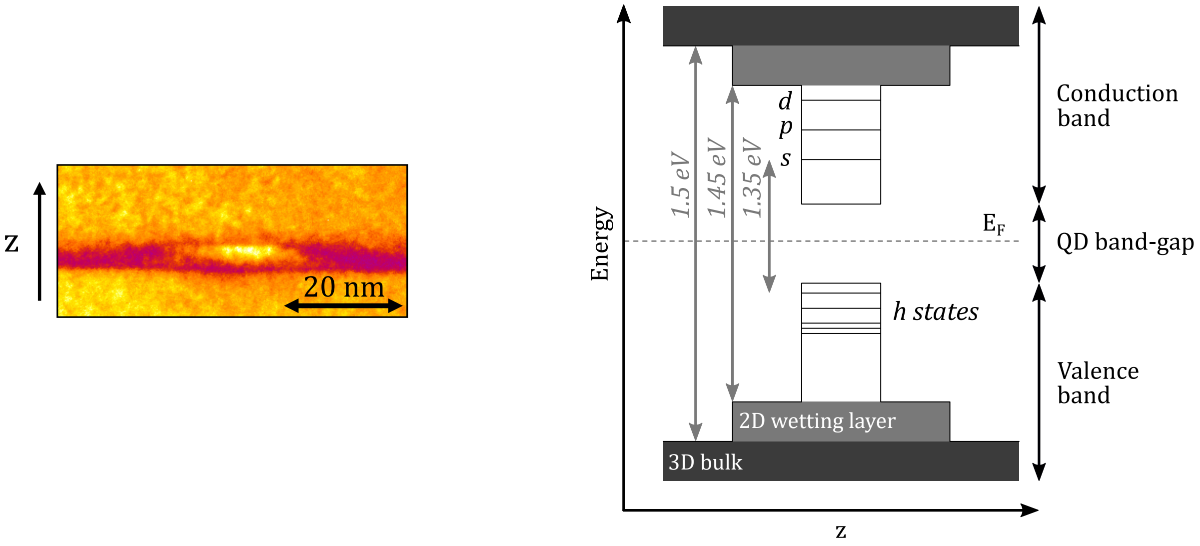

(a) (b)

FIGURE 1.2: **(a)** Transmission electron microscope image of a quantum dot, with the growth direction z in the vertical direction. Picture courtesy of G. Patriarche. **(b)** Energy band structure of the quantum dot and its surroundings, with z as the horizontal axis.

1.1.2 Optical transitions in quantum dots

The absorption of photons in a semiconductor structure leads to the creation of electron-hole pairs. We first describe which combinations of charges a quantum dot can hold, before connecting them with optical transitions and finally detailing how the charge state of a quantum dot can be controlled.

Charge states zoology

An electron from the conduction band might be promoted to the conduction band by absorbing a photon, leaving a hole in the valence band. The energy gained by the electron is equal to the energy of the absorbed photon. The wetting layer and the bulk present a continuum of levels, so absorbing a photon in these regions requires only the photon's energy to be higher than the bandgap. However, in the quantum dot, only photons tuned to the energy difference between a valence and a conduction level can be absorbed, creating an electron-hole pair on the corresponding levels.

Among the variety of possible quantum dot charge states [43], Fig. 1.3 describes the simplest: the empty state $\varnothing$, the single electron e^-, the single hole h^+, the electron-hole (e-h) pair X, commonly referred to as an exciton[1], the positive and negative trions X^+ and X^- and the biexciton XX. In the simple description of Fig. 1.3, we ignore the Coulomb interaction slightly shifting the energy of the quantum dot levels depending on the nature of the confined charge.

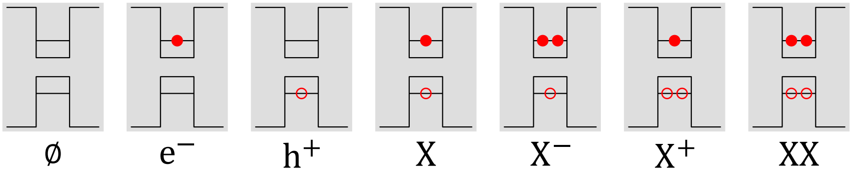

FIGURE 1.3: Elementary charge states of a quantum dot with zero, one or two charges in the valence and conduction bands.

Optical transitions between charge states

Unless stated otherwise, we adopt the unit system $\hbar = 1$*, so that pulsations (usually in rad/s) take the dimension of energies in* μeV*.*

Insofar as the charge of the quantum dot is concerned, optical transitions start from a given charge state and add an electron-hole pair by absorbing a photon of energy tuned to the difference between the given valence and conduction levels where the pair is created. Examples of the transitions between the simple charge states are shown in Fig. 1.4a: the ground states are $\varnothing$, h^+, e^- and X and the corresponding excited states are X, X^+, X^- and XX. The photon energy ω is labeled with the excited state (such as ω_{X^+} for the transition $\mathrm{h}^+ \rightarrow \mathrm{X}^+$) and each of them is distinct due to the specific ground state electrostatically shifting the energy levels in its own way.

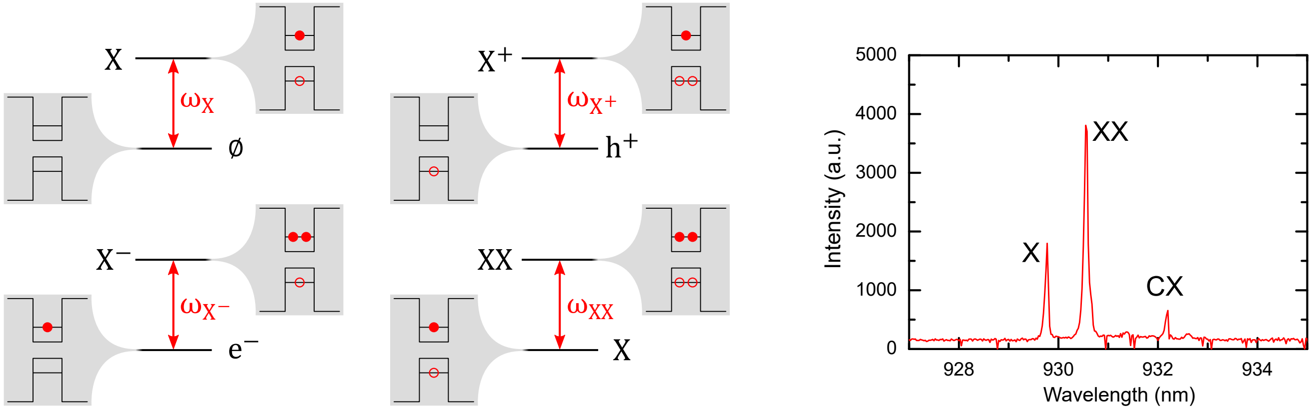

(a) (b)

FIGURE 1.4: **(a)** Photonic transitions between the simplest charge states of a quantum dot. Only the first discrete energy level is represented in the valence and conduction bands. **(b)** Photoluminescence emitted from a quantum dot, adapted from [45].

---

[1] An *exciton* usually defines a Coulomb-bound e-h pair [44] whereas in the present case, it is only bound by the quantum dot confinement.

Experimentally, a photoluminescence (PL) experiment reveals the energy structure of the quantum dot: a high-energy laser creates numerous electrons and holes that recombine by all the allowed canals, each emitting photons at a given energy. Fig. 1.4b represents an example of PL emission lines from a single quantum dot, identified as the radiative recombinations from states X, XX and CX (which stands for charged excitons: X^+ or X^-).

Charge control of quantum dots

Our next aim is to inject a single electron or hole in the quantum dot to interact with photons of energy ω_{X^-} or ω_{X^+}. The charge control of a quantum dot takes two complementary approaches: the electrical and the optical injection. We introduce both techniques here and elaborate them in section 2.1 on the devices studied throughout this manuscript.

The heterostructure surrounding the quantum dots is decisive for their ability to trap and release the electrons and holes flowing in the device. A combination of materials with p-doping or n-doping, electric gates and potential barriers help controlling the charges and selecting only the desired quantum dot state.

On the one hand, the electrical injection relies on a bias applied to the whole structure, that tilts the energy bands to the point where one of the quantum dot levels crosses the Fermi energy E_F, allowing a charge to populate it. Fig. 1.5 shows experimental data from *Gerardot et al. (2008)* [20], who studied the photoluminescence emitted by an electrically controlled device: the voltage is applied between the p-doped side of the sample and the Schottky gate. The emitted light is measured as the voltage is scanned: each stable charge state at a given voltage emits photons by recombination of one e-h pair brought by the non-resonant laser[1]. The difference between ω_X, ω_{X^-} and ω_{X^+} is worth noticing: even if these transitions involve only the lowest energy levels of the valence and conduction bands, the electrostatic interaction with the ground state (respectively empty, single electron and single hole) shifts the energy of the transition.

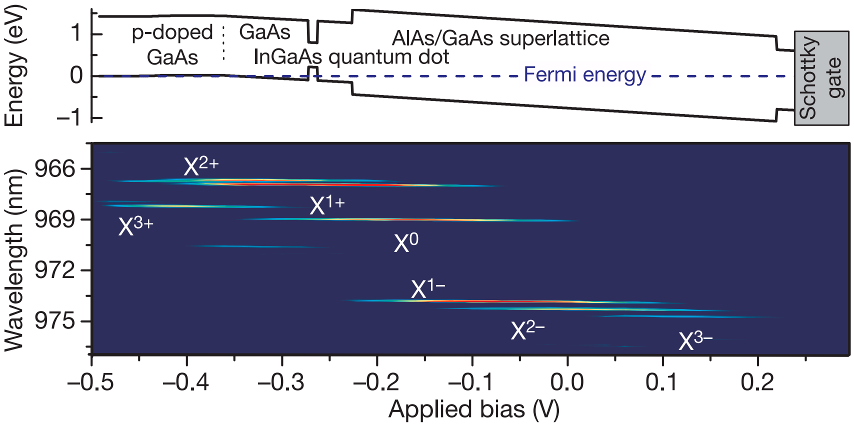

FIGURE 1.5: **(Top)** Band structure of an electrically controlled device. **(Bottom)** PL measurement as the gate voltage is scanned, showing the multiple charge states of the quantum dot. Figure from [20].

---

[1] The non-radiative relaxation of the e-h pair to the lowest energy levels happens on the ps timescale, followed by the radiative recombination observed in the experiment, in the ns timescale. The laser power is kept low for the process to repeat pair after pair.

On the other hand, the optical injection relies on the absorption of photons to create e-h pairs in the structure. Controlling whether the structure favors electrons or holes to be trapped in the quantum dot is achieved by adding a potential barrier made of a high-bandgap material in the vicinity of the quantum dot. *Ardelt et al. (2015)* [46] demonstrated that adding such a barrier on the p-doped side of the structure greatly increased the tunneling time of holes out of the quantum dot, in favor of the single hole charge state. A barrier placed on the opposite side of the quantum dot would trap electrons, but the electrical injection of single electrons is usually implemented without the need for a trapping barrier [47].

In the following, the polarization degree of freedom of the photons is explored, as it constrains the spin difference between the initial and final charge states of the optical transitions.

1.1.3 Spin degree of freedom and fine structure of the transitions

Specifics of electrons and holes in quantum dots

The spin of an electron or hole in their fundamental energy level constitutes our solid-state qubit of interest. The two particles by themselves have different wavefunction properties, but the peculiar environment of a quantum dot also confers them specific energy characteristics from which we can clarify the scope of our study. Fig. 1.6 is a dispersion diagram of electrons and holes confined in a semiconductor like GaAs: it shows the structure of the fundamental energy level of the conduction and valence bands (the s electronic state and higher energy h-state from Fig. 1.2b).

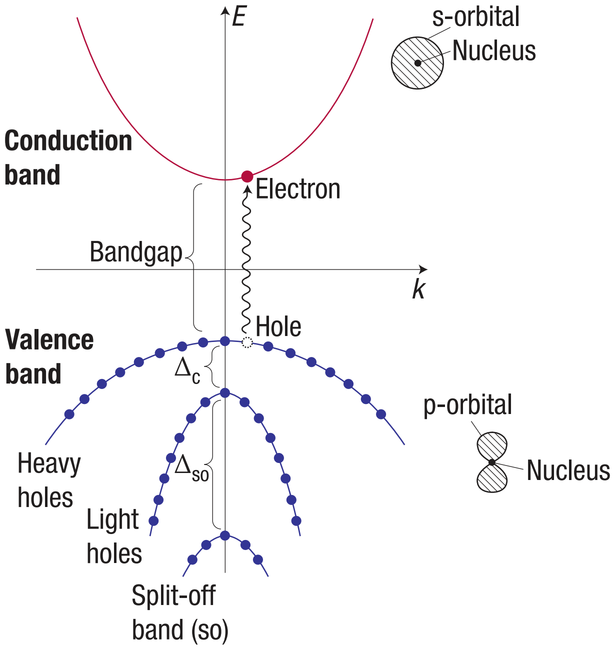

FIGURE 1.6: Dispersion diagram (energy - momentum) in a semiconductor like GaAs: the wavefunctions of the lowest energy states are of s nature for electrons and p for holes. In addition, holes exhibit three sublevels, split by Δ_c in presence of vertical confinement and Δ_{SO} by the spin-orbit coupling. Figure adapted from [48].

Firstly, the wavefunction of each particle has a distinct spatial symmetry around the nuclei of the solid-state matrix: s type for the electron and p for the hole. The immediate consequence is a much stronger coupling of the electron spin with the nuclear spins, called the *hyperfine interaction* (see subsection 1.2.3). Secondly, the substructure of the energy levels are very different: the fundamental conduction band level is just a single level, whereas the holes are split in three sublevels: *heavy holes*, *light holes* and a *split-off band*. In a bulk material, the light and heavy hole states are energy-degenerate, but strong vertical confinement results in the splitting of the light-hole band [49], far enough in energy to be considered inaccessible throughout this manuscript (tens of meV [50])[1]. The split-off band is even further away in energy owing to the spin-orbit coupling (hundreds of meV [50]) and will also be ignored here.

Spin states and optical selection rules

The spin of the charge carriers is expressed by their angular momentum J and its projection about a given quantization axis. In our structures, the optical propagation axis is aligned with the growth axis z, which becomes the natural quantization axis for the light-matter interaction. Electrons and holes are fermions of respective angular momentum $J_e = \frac{1}{2}$ and $J_h = \frac{3}{2}$, hence with possible projections about z of $\pm\frac{1}{2}$ for the electron and $\pm\frac{1}{2}, \pm\frac{3}{2}$ for the hole. The holes with spin $\pm\frac{1}{2}$ are the light holes (ignored in this manuscript) and those with spin $\pm\frac{3}{2}$, heavy holes [50]. The ket notations representing the spin states read:

- $|\uparrow\rangle_z$ for an electron of spin projection $+\frac{1}{2}$ about z, $|\downarrow\rangle_z$ for $-\frac{1}{2}$;
- $|\Uparrow\rangle_z$ for a hole of spin projection $+\frac{3}{2}$ about z, $|\Downarrow\rangle_z$ for $-\frac{3}{2}$.

The Pauli exclusion principle allows at most two charges of opposite spins to occupy the same quantum dot state. What's more, photons also carry a spin, of projection on their propagation axis z equal to $+1$ for the right-handed circular polarization $|R\rangle$ and -1 for the left-handed one, $|L\rangle$. The conservation of momentum in the spin-photon interaction translates as optical selection rules, restricting the optical transitions to photons whose spin projection matches the difference between excited and ground states. The allowed transitions for an electron or a hole in the ground state, that were considered only from the charge standpoint in Fig. 1.4, become the systems shown respectively in Figs. 1.7a and 1.7b when the spin is taken into consideration. The optical selection rules in the case of the hole are elaborated below:

- From the ground state $|\Uparrow\rangle_z$ (spin $+\frac{3}{2}$) to the excited state $|\Uparrow\Downarrow\uparrow\rangle_z$ (spin $+\frac{1}{2}$), the spin difference is -1, so only an L-polarized photon of spin -1 can be absorbed to create an electron-hole pair: $+\frac{3}{2} - 1 = \frac{1}{2}$.
- From the ground state $|\Downarrow\rangle_z$ (spin $-\frac{3}{2}$) to the excited state $|\Downarrow\Uparrow\downarrow\rangle_z$ (spin $-\frac{1}{2}$), the spin difference is $+1$, so only an R-polarized photon of spin $+1$ can be absorbed to create an electron-hole pair: $-\frac{3}{2} + 1 = -\frac{1}{2}$.

---

[1] An asymmetry in the quantum dot lateral confinement might still result in the mixing of the light and heavy-hole bands, but we ignore this effect as the annealing strongly reduces such an asymmetry.

One can also consider a different quantization axis, for example along a transverse direction such as x. This corresponds to a change of basis to $|\Uparrow\rangle_x = \frac{|\Uparrow\rangle_z + |\Downarrow\rangle_z}{\sqrt{2}}$ and $|\Downarrow\rangle_x = \frac{|\Uparrow\rangle_z - |\Downarrow\rangle_z}{\sqrt{2}}$. Since the left- and right-handed circularly polarized photons still only interact respectively with $|\Uparrow\rangle_z$ and $|\Downarrow\rangle_z$, the four-level system now accesses four energy-degenerate transitions presented in Fig. 1.7c, with two in each linear polarization H and V of the photons propagating along z (H and V being themselves superpositions of R and L, associated to the transitions in the z basis –see Eq. 1.24).

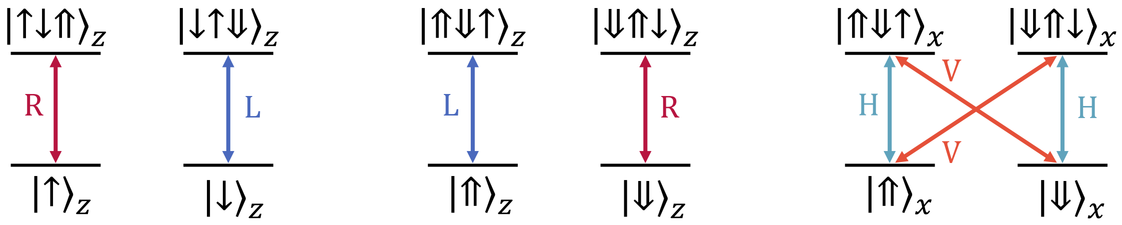

(a) (b) (c)

FIGURE 1.7: Allowed optical transitions by photons traveling along z, for a four-level system constituted by **(a)** an electron spin quantized in the z direction, **(b)** a hole spin quantized in the z direction and **(c)** a hole spin quantized in the x direction.

Effect of a magnetic field on the exciton and trion transitions

A magnetic field initiates the precession of spins about its direction, thereby imposing a spin quantization axis and redefining the optical selection rules. It also shifts the energy of levels with non-zero spin, lifting the spin degeneracy of the transitions by Zeeman splitting. Here we consider two magnetic field configurations: *Faraday* (along z, also called longitudinal or parallel) and *Voigt* (oriented in the (x, y) plane, also called transverse or in-plane). In-depth analyses of the fine structure of quantum dots and how they respond to a magnetic field were conducted by multiple groups [51–53]. Here, we restrict the study to the exciton and the positive trion transitions. Their response to a Faraday or Voigt magnetic fields are described respectively in Fig. 1.8 and Fig. 1.9. The figures represent the optical transitions of the system without any magnetic field (left panel), and with intense Faraday and Voigt magnetic fields[1], respectively B_z (middle panel) and B_x (right panel).

Let us first present the exciton system (Fig. 1.8). Without an external magnetic field, it has two optically active transitions that are linearly polarized in directions X and Y (quantum dot-dependent), as shown in Fig. 1.8a. The corresponding excited eigenstates are respectively labeled $|e_X\rangle$ and $|e_Y\rangle$: they represent specific superpositions of the states $|\Uparrow\downarrow\rangle_z$ and $|\Downarrow\uparrow\rangle_z$. They are separated by a small fine structure splitting δ_{FSS}. Applying a Faraday magnetic field (Fig. 1.8b) mixes the excited states of the system, now labeled $|e_L\rangle$ and $|e_R\rangle$ as the corresponding polarizations of the transitions become circularly polarized at high magnetic fields [51]. Additionally, the separation between the excited levels becomes the Zeeman splitting $Z_{\parallel}$. The case of a Voigt magnetic field (Fig. 1.8c) differs as the polarization of the transitions transforms

---

[1] The value of 9 T is only used here as an indication of the order of magnitude of an *intense* magnetic field.

into $\mathrm{H_B}$ and $\mathrm{V_B}$, linear polarizations depending on the orientation of the magnetic field, and the excited states are accordingly labeled $|e_{H_B}\rangle$ and $|e_{V_B}\rangle$. The separation between the excited levels now becomes the Zeeman splitting $Z_\perp$ [52].

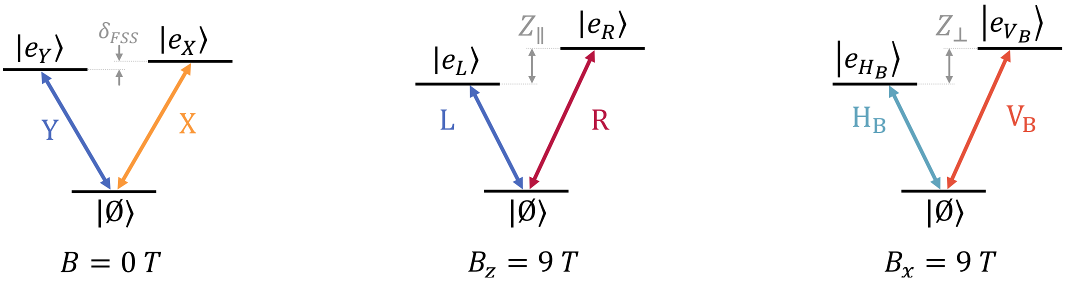

(a) (b) (c)

FIGURE 1.8: Effect of a magnetic field on the exciton transition: **(a)** no magnetic field; **(b)** intense Faraday magnetic field; **(c)** intense Voigt magnetic field.

Regarding the trion system (Fig. 1.9), without an external magnetic field, it has two energy-degenerate circularly polarized transitions with a helicity depending on the optical selection rules, as shown in Fig. 1.9a. A Faraday magnetic field (Fig. 1.9b) introduces Zeeman splittings to the ground and excited states doublets (respectively $Z_{h,\parallel}$ and $Z_{e,\parallel}$ as their magnitudes are determined by the hole for the ground state and the electron for the excited state). It preserves the optical selection rules from the zero magnetic field case as it doesn't change the spin quantization axis z [51]. On the contrary, a Voigt magnetic field (Fig. 1.9c), imposes a new spin quantization axis (such as x in the present case), and the interaction with photons propagating along z allows four linearly polarized transitions in directions $\mathrm{H_B}$ and $\mathrm{V_B}$ (quantum dot and magnetic field-dependent). The Zeeman splittings are then written $Z_{h,\perp}$ and $Z_{e,\perp}$ and the difference between the two results in four distinct transition energies.

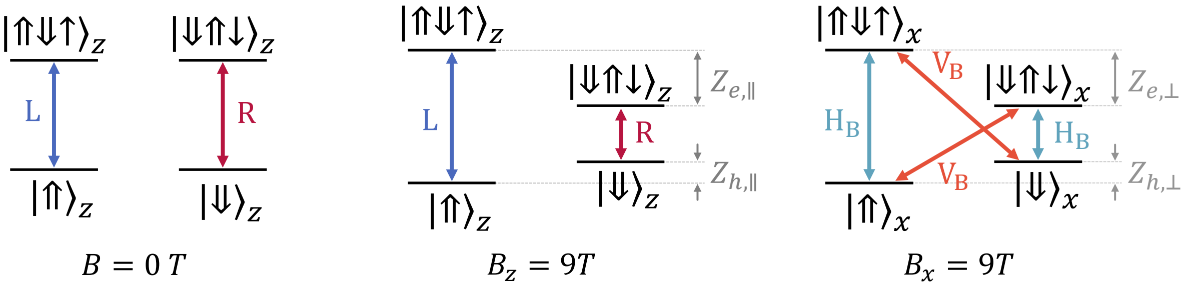

(a) (b) (c)

FIGURE 1.9: Effect of a magnetic field on the positive trion transition: **(a)** no magnetic field; **(b)** intense Faraday magnetic field; **(c)** intense Voigt magnetic field.

A negative trion exhibits an analogous magnetic field dependence, but with splittings Z_e between the ground state and Z_h for the excited states. The distinct responses of the exciton and trion systems to magnetic fields, especially in the Voigt configuration, provide a charge state identification method. In a photoluminescence experiment with an increasing Voigt magnetic field, the exciton splits in two orthogonal linearly polarized lines while the trion splits in four of them, orthogonal two by two. This technique will be applied in particular in chapter 2.

1.1.4 Spin initialization

In order to initialize the spin of an electron or hole in a quantum dot, after such a charge has been injected as previously described, we can take advantage of the polarization and energy selectivity of the positive and negative trion transitions through optical spin pumping schemes. To this effect, the knowledge of the spin flips naturally occurring in quantum dots is required: due to environmental effects described later (namely, the hyperfine interaction), the spin of a hole trapped in an InGaAs quantum dot flips much slower than an electron spin [50, 54, 55]. Two possible optical spin pumping schemes ensue, as shown in Fig. 1.10.

On the left-hand side is the case of a hole spin in the absence of an external magnetic field, as performed for instance in [20]. The fast electron spin-flip time in the excited state, compared to the slow hole spin-flip time in the ground state, offers the opportunity to pump the $|\Uparrow\rangle_z \rightarrow |\Uparrow\Downarrow\uparrow\rangle_z$ transition with a left-handed circularly polarized laser, eventually accumulating the spin in the $|\Downarrow\rangle_z$ state. This scheme is also practical with a longitudinal magnetic field (see subsection 3.4.3 for more details).

The case of the electron spin initialization has inverse constraints as the ground state spin flips much faster than the excited state: the spin initialization is impossible in the absence of an external magnetic field. In Fig. 1.10b, we show how a Voigt magnetic field solves this issue by splitting the energies of $|\uparrow\rangle_x \rightarrow |\uparrow\downarrow\Uparrow\rangle_x$ and $|\downarrow\rangle_x \rightarrow |\downarrow\uparrow\Downarrow\rangle_x$ while also allowing the diagonal decay channels. An excitation laser tuned to $|\uparrow\rangle_x \rightarrow |\uparrow\downarrow\Uparrow\rangle_x$ selectively pumps this transition as it is detuned from the other one: the trion state decays either in $|\uparrow\rangle_x$ and is repumped, or in $|\downarrow\rangle_x$ and is shelved in this state as it cannot be re-excited before a ground spin flip. This protocol incidentally works for both electron and hole spin, and was demonstrated first in [56]. A related scheme allows the electron spin pumping in a longitudinal magnetic field [57].

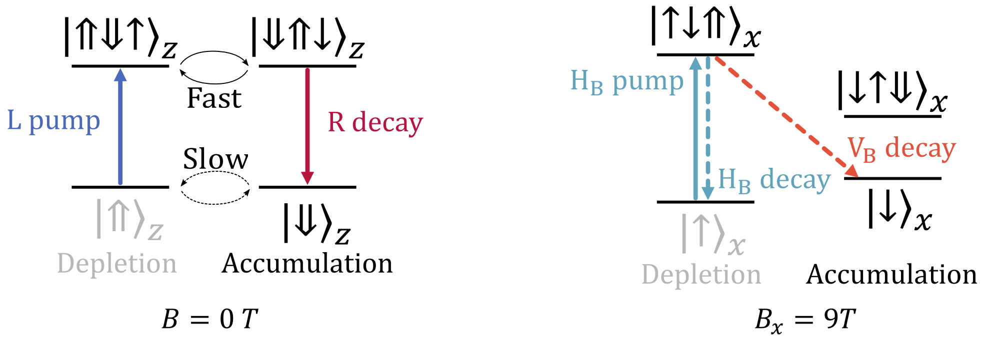

(a) (b)

FIGURE 1.10: Spin initialization protocols: **(a)** hole spin with no external magnetic field; **(b)** electron spin with an external Voigt magnetic field.

1.1.5 Single photon emission and optical excitation schemes

The radiative recombination of charges in quantum dots provides a stream of single photons emitted one by one, realizing a single-photon source with numerous applications in quantum communications [4, 58] and quantum simulation [1]. Let us go through the general principles of single-photon sources before detailing different optical excitation techniques.

Single photon emission

A single-photon source is a device which emits photons one by one. The physical process is either probabilistic or deterministic in nature: probabilistic types emit single photons at random times (they are based on non-linear phenomena such as parametric down-conversion [59]), whereas deterministic sources emit single photons only once they are triggered (it is the case for trapped atoms [60] and artificial atoms like nitrogen-vacancy centers in diamond [61] and quantum dots [24]).

A schematic view of a deterministic single-photon source (SPS) is represented in Fig. 1.11: an optical excitation triggers the device with repeating laser pulses, and each time, the source reflects one single photon superimposed with the remaining of the triggering pulse. A beam splitter directs the reflected beam through a filter which isolates the single photons, either in polarization or in energy. For instance, exciting the trion transition with a horizontally polarized laser produces H and V single photons (see Fig. 1.7c for the optically allowed transitions): they can be isolated in the collection from the H-polarized triggering pulse by selecting only the V component, unfortunately losing the H single photons in the process.

Three figures of merit emerge from the principle of a single-photon source:

- The brightness is the probability that the source emits one photon per triggering pulse.
- The purity is the probability that the source doesn't emit more than one photon per triggering pulse.
- The indistinguishability (also called mean wave-packet overlap) quantifies how identical the emitted photons are to each other, in terms of spatial and temporal profile, energy and polarization.

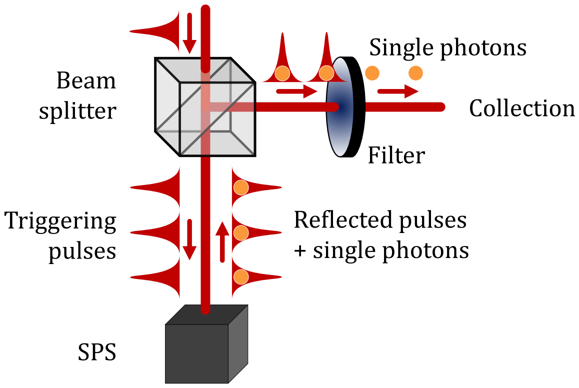

FIGURE 1.11: Principle of an optically excited single-photon source triggered by pulses and reflecting single photons on top of the remaining triggering pulses, filtered out after a beam splitter.

Many optical excitation schemes were developed in the framework of single-photon sources. A comparative study of all these protocols was done by *Reindl et al. (2019)* [62]. Each of them relies on specific photon energies to create an electron-hole pair on given quantum dot levels. In this subsection, we consider a quantum dot initially in the empty charge state and the creation of an e-h pair by photonic excitation of increasing energy, as represented in Fig. 1.12:

- Resonant excitation in the s-shell level (left red arrow) creates an e-h pair on the highest valence and lowest conduction levels. The radiative recombination emits a single photon at the same energy as the excitation, hence the name *resonant*.
- Quasi-resonant excitation, for instance in the p-shell level (middle red arrow), followed by non-radiative relaxation to the s-shell and single photon emission. The detuning with the s-shell transition is typically 13 meV for the p-shell excitation[1]. Any excitation scheme through a combination of quantum dot levels other than resonant excitation belongs to this category.
- Quasi-resonant phonon-assisted excitation in the s-shell (right red arrow): either involving longitudinal acoustic (LA) phonons (detuning $\simeq 1$ meV) or longitudinal optical (LO) phonons (detuning 36 meV). Here, the laser creates a phonon and an e-h pair on the s-shell, before radiative recombination.
- Non-resonant excitation in the wetting layer or in the bulk continuum of levels (respectively orange and yellow arrows), followed by non-radiative relaxation to the s-shell and single photon emission.

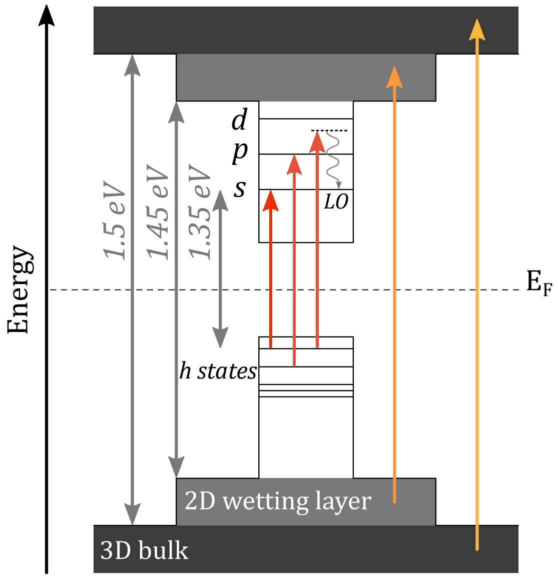

FIGURE 1.12: Electronic structure of the quantum dot and its surroundings and possible optical excitation schemes.

---

[1] This value is from [62]. It can vary from quantum dot to quantum dot, and it strongly depends on the temperature at which the quantum dots are annealed.

Even though we focused on the transitions starting from the empty charge state, these techniques also apply to transitions from any pre-existing charge state, such as the $h^+ \leftrightarrow X^+$ transition. Indeed, the heterostructure design, the electrical and the optical control can be combined to address any charge state, as will be detailed in section 2.1 where we show devices purposefully aiming at selecting the single electron or single hole states in the quantum dot.

Based on the figures of merit of a SPS, we can review the specificities of each optical excitation techniques:

- The resonant s-shell excitation is ideal to minimize the disturbance of the quantum dot's environment by the input laser, but the trade-off is that multiple polarization states can be emitted. In this context, cross-polarized filtering absorbs half of the emitted photons. This scheme is widespread and has led to very high quality single-photon sources [24, 63].
- The quasi-resonant p-shell excitation allows all the photons emitted by the quantum dot to be collected as the input laser is spectrally filtered, but the relaxation to the s-shell before recombination induces a time jitter that can be detrimental to the indistinguishability [64].
- The quasi-resonant phonon-assisted excitation is very efficient as the input laser can be spectrally filtered and the non-radiative relaxation is very fast: therefore both the brightness and the indistinguishability can be high. The LA excitation scheme has been drawing attention recently as the complex physical process is unraveled by theoretical research [65–68] and highly transmissive spectral filters are becoming narrower. Noticeable experimental results were obtained at the C2N in 2021 by *S. Thomas, M. Billard and coworkers* [69, 70] and also by other research groups [71, 72].
- The high energy non-resonant excitation generates an excess of charge carriers, producing a fluctuating electric field that randomly shifts the quantum dot energy (also known as *spectral wandering*). Additionally, the relaxation to the lowest energy level before recombination induces a time jitter that degrades the indistinguishability. It is rarely used on its own, but an interesting feature is that as an auxiliary laser, it can stabilize the charge environment of a quantum dot by filling neighboring traps, which leads to an improved indistinguishability [73].

Other schemes have produced noticeable results, such as the extremely high-purity source based on the two-photon excitation to the biexciton state XX, which radiatively recombines in a two-step cascade to the neutral exciton X^0 and then to the empty state $\varnothing$ [74].

1.2 Single charges confined in quantum dots as solid-state qubits

The optical or electrical injection of a single electron or hole in a quantum dot, followed by its spin initialization, produces a solid-state qubit ready for operation in a variety of protocols. In this section, we first lay out the mathematical framework of the Bloch sphere, describing any spin qubit, and follow by outlining its dynamics: either under the influence of an external operator (spin manipulation and measurement) or of environmental fluctuations inherent to a quantum dot through the hyperfine interaction.

1.2.1 Description of a spin qubit in the Bloch sphere

Coherent superpositions of the basis vectors: pure states

A qubit holds the fundamental property of quantum superposition, whereby it can access any coherent superposition of its eigenstates, which we call $|\uparrow\rangle_z$ and $|\downarrow\rangle_z$ in the case of an electron spin quantized along the z direction (the formalism can be adapted to a hole described as a pseudospin 1/2 with the eigenstates $|\Uparrow\rangle_z$ and $|\Downarrow\rangle_z$ [47]). Let us consider the arbitrary coherent superposition state:

$$|\Psi\rangle = \alpha\,|\uparrow\rangle_z + \beta\,|\downarrow\rangle_z \tag{1.1}$$

where α and β are complex numbers such that $|\alpha|^2 + |\beta|^2 = 1$. Such a coherent quantum superposition is called *pure state*. Without loss of generality, we can assume that α is a positive real number and change the (α, β) set of variables to the angular variables (ϑ, φ) such that:

$$\begin{cases} \alpha = \cos(\vartheta/2) \\ \beta = e^{i\varphi}\sin(\vartheta/2) \end{cases} \tag{1.2}$$

Such a state can be represented by a point on the surface of a sphere, called the Bloch sphere, with the angle ϑ as colatitude and φ as longitude. An example is shown in Fig. 1.13.

In this representation, the axes of the Bloch sphere are labeled x, y, z and the Bloch vector is defined by its Cartesian coordinates $\boldsymbol{S} = (s_x, s_y, s_z)$. The basis vectors shown in the figure are expressed as coherent superpositions of $|\uparrow\rangle_z$ and $|\downarrow\rangle_z$:

$$\begin{pmatrix} |\uparrow\rangle_x \\ |\downarrow\rangle_x \end{pmatrix} = \frac{1}{\sqrt{2}}\begin{pmatrix} 1 & 1 \\ 1 & -1 \end{pmatrix}\begin{pmatrix} |\uparrow\rangle_z \\ |\downarrow\rangle_z \end{pmatrix} \qquad \begin{pmatrix} |\uparrow\rangle_y \\ |\downarrow\rangle_y \end{pmatrix} = \frac{1}{\sqrt{2}}\begin{pmatrix} 1 & i \\ 1 & -i \end{pmatrix}\begin{pmatrix} |\uparrow\rangle_z \\ |\downarrow\rangle_z \end{pmatrix} \tag{1.3}$$

The spin components of a pure spin state in the Bloch sphere are linked with the two sets of variables by the following equalities:

$$\begin{aligned} s_x &= 2\,\mathrm{Re}\{\alpha\beta^*\} = \cos(\varphi)\sin(\vartheta) \\ s_y &= 2\,\mathrm{Im}\{\beta\alpha^*\} = \sin(\varphi)\sin(\vartheta) \\ s_z &= \alpha\alpha^* - \beta\beta^* = \cos(\vartheta) \end{aligned} \tag{1.4}$$

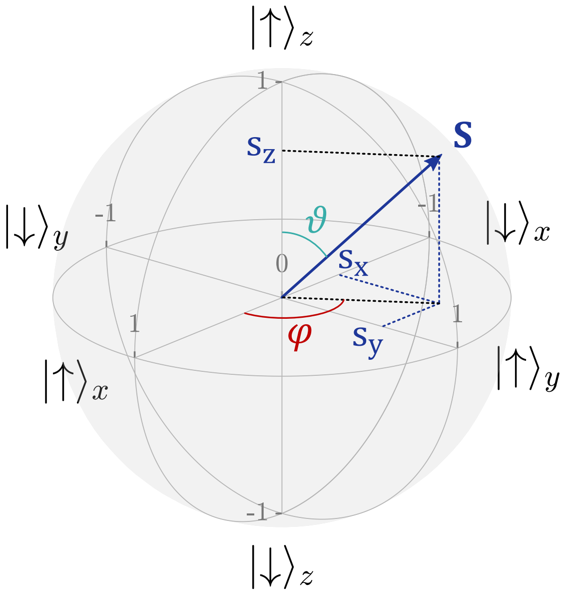

FIGURE 1.13: Bloch sphere representing the quantum state of the spin qubit as a vector $\boldsymbol{S}$ of Cartesian coordinates $s_x = -0.35, s_y = 0.61, s_z = 0.71$, and of colatitude and longitude angles ($\vartheta = 45°, \varphi = 120°$).

A fundamental aspect of the Bloch sphere is its ability to represent coherent superpositions of the spin components along its quantization axis, $|\uparrow\rangle_z$ and $|\downarrow\rangle_z$. We highlight the fact that, despite its representation as a 3D vector, the Bloch vector is not a real space vector.

Incoherent superpositions of the basis vectors: mixed states

The Bloch sphere can also model any incoherent superpositions of pure states, also called *mixed states*. In quantum mechanical terms, an incoherent superposition is a probabilistic combination of pure states. In the Bloch sphere, this translates as a total state vector equal to a weighted sum of multiple pure state vectors. Notice that the information on the incoherently summed vectors cannot be accessed a priori, only the resulting sum.

Mixed states bring the length of the Bloch vector (also called the spin state *purity*) below unity. This phenomenon is known as spin depolarization, and a completely depolarized spin state has a purity of zero. The density matrix is the common approach to describe coherent and incoherent superposition states; it carries the same information as the Bloch vector, in a different form. For the pure state from Eq. 1.1, the density matrix in the $(|\uparrow\rangle_z, |\downarrow\rangle_z)$ basis reads:

$$\hat{\boldsymbol{\rho}} = |\Psi\rangle\langle\Psi| = \begin{pmatrix} \rho_{\uparrow\uparrow} & \rho_{\uparrow\downarrow} \\ \rho_{\downarrow\uparrow} & \rho_{\downarrow\downarrow} \end{pmatrix} = \begin{pmatrix} \alpha\alpha^* & \alpha\beta^* \\ \beta\alpha^* & \beta\beta^* \end{pmatrix} \tag{1.5}$$

For the incoherent superposition of multiple pure states $|\Psi_i\rangle$ with the respective probabilities p_i, the density matrix reads:

$$\hat{\boldsymbol{\rho}} = \sum_i p_i |\Psi_i\rangle\langle\Psi_i| = \begin{pmatrix} \rho_{\uparrow\uparrow} & \rho_{\uparrow\downarrow} \\ \rho_{\downarrow\uparrow} & \rho_{\downarrow\downarrow} \end{pmatrix} \tag{1.6}$$

As far as the Bloch components of a mixed state are concerned, they are expressed either through the density matrix components, or through the (ϑ, φ) variables. In the latter case, the below unity length of the vector is included as the purity $p = \sqrt{s_x^2 + s_y^2 + s_z^2}$ and the Bloch vector components read:

$$\begin{aligned} s_x &= 2\,\mathrm{Re}\{\rho_{\uparrow\downarrow}\} &&= p \cdot \cos(\varphi)\sin(\vartheta) \\ s_y &= 2\,\mathrm{Im}\{\rho_{\downarrow\uparrow}\} &&= p \cdot \sin(\varphi)\sin(\vartheta) \\ s_z &= \rho_{\uparrow\uparrow} - \rho_{\downarrow\downarrow} &&= p \cdot \cos(\vartheta) \end{aligned} \tag{1.7}$$

It is useful to define the scalar product between two Bloch vectors $\boldsymbol{S}^{(1)}$ and $\boldsymbol{S}^{(2)}$ with the following formula:

$$\boxed{\left|\left\langle \boldsymbol{S}^{(1)} \middle| \boldsymbol{S}^{(2)} \right\rangle\right|^2 = \frac{1 + s_x^{(1)} s_x^{(2)} + s_y^{(1)} s_y^{(2)} + s_z^{(1)} s_z^{(2)}}{2}} \tag{1.8}$$

The result ranges from 0 for two opposite vectors to 1 for two identical vectors. This quantity is also named the *fidelity* when comparing a measured spin state to a reference state.

Relaxation and dephasing

The state of a spin qubit evolves over time, either by an external operation described next (optical rotation pulse or external magnetic field), or under the influence of environmental fluctuations. The latter case defines the free evolution of the qubit, determined by two phenomena:

- The relaxation, by which the spin qubit flips from $\left|\uparrow\right\rangle_z$ to $\left|\downarrow\right\rangle_z$ or vice versa in a characteristic time T_1 (or at a rate $\Gamma = 1/T_1$). The relaxation causes a depolarization of the qubit towards the center of the sphere[1].
- The pure dephasing, by which the phase of a pure state is lost in a characteristic time T_2^* (or at a rate $\gamma^* = 1/T_2^*$). That is, for a given pure state such as $\left|\uparrow\right\rangle_z + e^{i\varphi}\left|\downarrow\right\rangle_z$, the time during which the phase term φ stays well defined. The phase blurring results in the depolarization of the qubit towards the z-axis, without modifying s_z.

In general, the qubit is subject to the two mechanisms and we usually define an empiric coherence time T_2 associated to a rate $\gamma = 1/T_2$ to take them both into account:

$$\boxed{\frac{1}{T_2} = \frac{1}{T_1} + \frac{1}{T_2^*} \iff \gamma = \Gamma + \gamma^*} \tag{1.9}$$

Notice that the empiric definitions of T_1 and T_2^* are dependent on the chosen basis. In the presence of an external magnetic field, different eigenstates could be obtained, and we would define T_1 and T_2^* accordingly.

---

[1] As long as the spin flips $\left|\uparrow\right\rangle_z \to \left|\downarrow\right\rangle_z$ and $\left|\downarrow\right\rangle_z \to \left|\uparrow\right\rangle_z$ are equally probable, i.e. for a sufficiently low Zeeman splitting compared to $k_B T$.

1.2.2 Spin manipulation and measurement

Rotating the qubit in the Bloch sphere and measuring its Bloch components are the first steps towards more elaborated quantum computation schemes.

Spin manipulation

The spin manipulation by optical means, called *coherent control*, allows to rotate the quantum state of the spin in the Bloch sphere without loss of purity. In order to implement any possible rotation, only two complementary rotations are required, for instance one about the x-axis, and another one about z. The most advanced technique was theoretically proposed by *Economou et al. (2006)* [75] and demonstrated in multiple teams consecutively [76–79]. They combined the two following phenomena:

- A Voigt magnetic field B_x inducing the spin rotation about the x-axis, as seen in Fig. 1.14a.
- A stimulated Raman transition between the spin states $|\uparrow\rangle_x$ and $|\downarrow\rangle_x$ described in detail in Fig. 1.15 for a hole spin in the presence of a transverse magnetic field, effectively acting as a rotation about the z-axis (see Fig. 1.14b).

An arbitrary spin rotation takes about 20 ps, which is far below the typical dephasing time of electrons and holes in InGaAs quantum dots (0.5 ns for the electron and 10 ns for the hole without an external magnetic field [50, 54, 55]), leaving more than enough time to perform multiple quantum operations on the same qubit during its dephasing time.

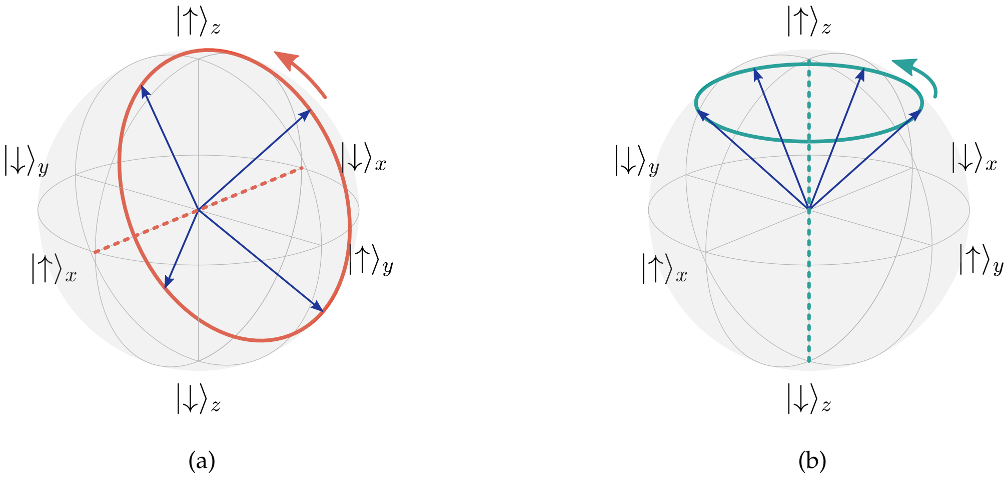

FIGURE 1.14: Examples of qubit rotations, starting from the spin state from the example above (see Fig. 1.13), and rotating **(a)** about the x-axis by a B_x magnetic field and **(b)** about the z-axis by a stimulated Raman transition. The rotation axes are drawn in dashed lines.

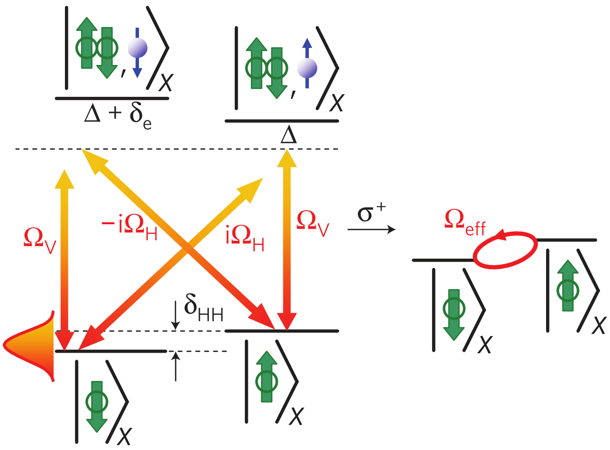

FIGURE 1.15: Coherent rotation of a hole spin about the z-axis induced by a circularly polarized pulsed laser (in red-orange on the four-level system) in the presence of a transverse magnetic field, equivalent to precession between $|\Uparrow\rangle_x$ and $|\Downarrow\rangle_x$, as shown on the right side. The power of the pulse determines the magnitude of the rotation. This technique is also relevant with electron spin qubits. Figure adapted from [76].

Spin measurement

Reading out the quantum state of the spin requires to probe the Bloch components (s_x,s_y,s_z) to reconstruct its Bloch vector: this method is referred to as *tomography*. The ability to readout a single Bloch component combined to coherent spin rotations is enough to achieve a full tomography, as demonstrated in the group of Y. Yamamoto [80]. A common spin readout technique takes advantage of the Zeeman splitting in a transverse magnetic field [21, 76], as shown in Fig. 1.16 in the case of a hole. To measure $|\Uparrow\rangle_x$ (left panel), a laser tuned to the $|\Uparrow\rangle_x \rightarrow |\Uparrow\Downarrow\uparrow\rangle_x$ transition selectively excites the single hole if its spin state is $|\Uparrow\rangle_x$, the consecutive detection of a V$_B$ photon lets the operator know that the spin was in state $|\Uparrow\rangle_x$ before the readout, while an absence of detection in V$_B$ gives no information. The complementary process is applied to measure $|\Downarrow\rangle_x$ (right panel) and gives the rest of the necessary information to compute s_x. The energy of the excitation laser is tuned to differentiate the two situations.

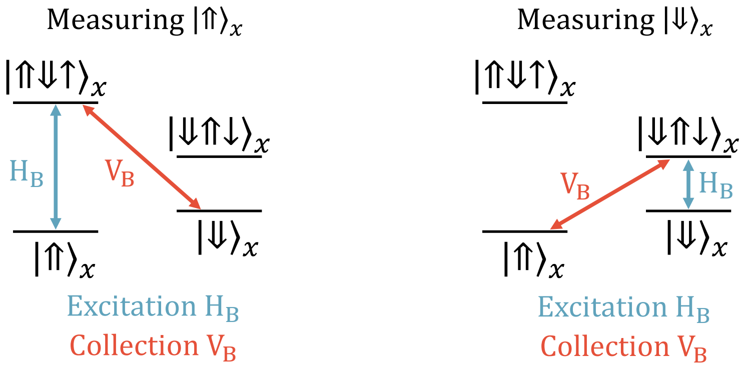

FIGURE 1.16: Readout protocol to compute the Bloch coordinate s_x of a hole spin in a Voigt magnetic field. The collection of a V$_B$ polarized photon after excitation in H$_B$ ensures that the spin was in either $|\Uparrow\rangle_x$ **(left panel)** or $|\Downarrow\rangle_x$ **(right panel)** before the measurement, depending on the excitation energy.

This spin readout technique can be combined with coherent spin rotations, bringing the s_y and s_z components to the x-axis to get a full tomography of the spin state. However, a precise timing of the rotation pulses with the magnetic field is crucial as B_x continuously rotates the spin about x.

Starting from an initial measurement, one can perform two common sequential experiments described below, the results of which are shown in Fig. 1.17, with insets presenting each sequence (green squares for measurement of s_x and red-orange pulses for coherent rotation about z).

- Left panel: applying a rotation pulse of varying power P_{rot} and measuring the state of the qubit after the rotation. This type of evolution is referred to as *Rabi oscillation* in which a π rotation translates as a full population inversion.
- Right panel: applying a $\pi/2$ pulse, aligning the qubit to the z-axis and letting it precess about the transverse magnetic field B_x for a time τ before bringing it back to the x-axis with a second $\pi/2$ pulse and finally measuring the qubit state to quantify the loss of coherence caused by the interactions with the environment. This is known as *Ramsey interferometry* and the decay time of the fringes gives T_2.

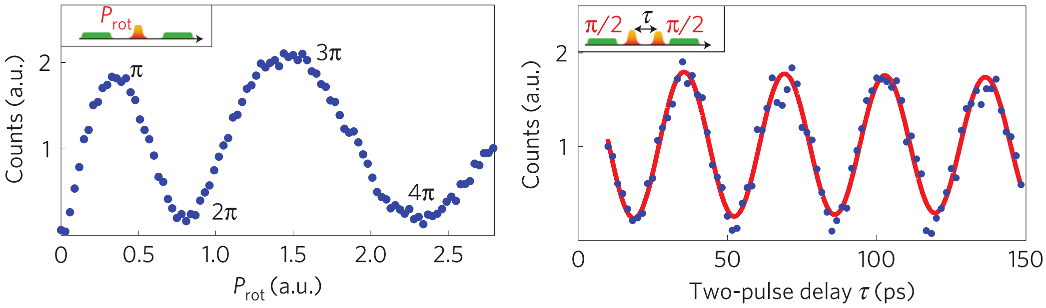

FIGURE 1.17: **(Left panel)** Rabi oscillations measurement. **(Right panel)** Ramsey interferometry. Figure adapted from [76].

Measuring T_1 only requires to initialize the spin in $|\uparrow\rangle$ and to measure its population in $|\downarrow\rangle$ after different delays.

Different types of measurement

A quantum measurement influences in return the state of the measured system [81], and two concepts clarify how the system is left afterwards.

Some measurement methods destroy the measured system, such as the detection of a photon by a photodetector which absorbs it and converts it into an electrical current. On the other hand, some techniques preserve the measured system: they are known as *quantum non-demolition* measurements (QND), a concept introduced by *Grangier et al. (1998)* [31]. By definition, right after a QND, the system can be measured again with the same outcome. The indirect spin measurement in an ideal spin-photon interface, elaborated later in subsection 1.3.4, can be categorized as QND; it is based on the spin-dependent Faraday rotation [57, 82] which imprints the spin state on the photonic polarization. On the contrary, the spin readout method presented in Fig. 1.16 can't be considered a QND as the measurement implies a spin-flip.

The second concept is the wave-packet reduction induced by the projective measurement of a quantum system. In a *strong measurement*, the complete information about the spin state is extracted and it is therefore projected on a given eigenstate, thereby losing any coherent superposition and restarting its natural evolution from the state is was detected in. Successive strong measurements close enough to each other could even freeze the evolution of the system, in what is known as the quantum Zeno effect [32, 83]. By contrast, a *weak measurement* only extracts partial information about the spin state, preserving the majority of its coherence [84]. Both weak and strong measurements can be envisioned in the QND definition, as long as the spin qubit is not destroyed by the measurement and can be measured multiple times with a constant result. An ideal spin-photon interface based on Faraday rotation would be able to display the transition between these different measurement regimes.

1.2.3 Interaction between a single quantum dot spin and its environment

The environmental fluctuations limit the coherence of a spin qubit in a quantum dot through the interaction with the neighboring nuclear spins. The direct environment of a single *central spin*, i.e., confined in a quantum dot (Fig. 1.18a), is composed of 10^5 atoms of In, Ga and As, whose nuclei carry spins of 9/2 for In and 3/2 for Ga and As.

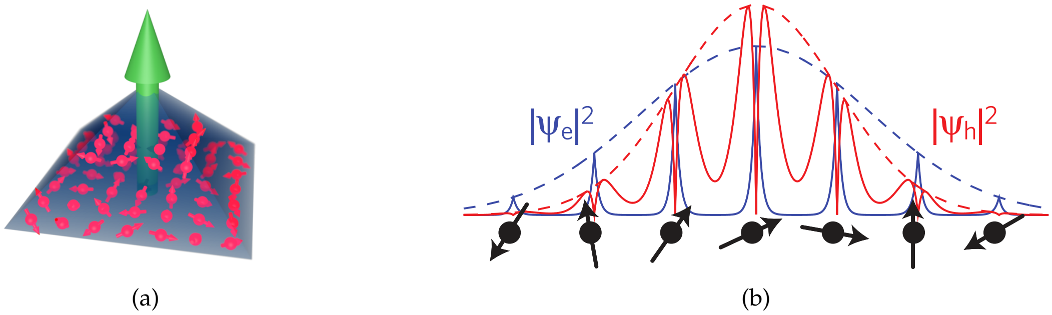

FIGURE 1.18: **(a)** Central spin qubit (in green) in a quantum dot comprising a multitude of nuclear spins (in red). Figure courtesy of M. Glazov and D. Smirnov [85]. **(b)** Wavefunction of the central electron spin (in blue) or hole spin (in red) at the location of the nuclei (black spins with random orientations). The wavefunctions are shown as solid lines and their envelope functions $\left|\Psi_{e/h}\right|^2$ as dashed lines. Figure adapted from [47].

The interaction between the spin qubit and its environment is generally referred to as the *hyperfine interaction* that comprises two specific contributions explained below [47, 50], depending on whether the wavefunction of the central spin overlaps the nuclei or not (see Fig. 1.18b). In the case of an electron spin carrier, with a s-type wavefunction overlapping nuclei, the dominant contribution is the *Fermi contact interaction*, whereas a hole spin carrier, with a p-type wavefunction experiences the *dipole-dipole interaction*.

The electron spin qubit experiences the Fermi contact interaction

The *Fermi contact interaction* takes an Ising form, with the carrier electron labeled (e) and the collection of nuclear spins indexed as (j) [47, 50]:

$$\begin{aligned}\hat{\boldsymbol{H}}_{hf}^{(e)} =&\mathcal{V}\sum_{j} A_{j}^{(e)}\left|\Psi^{(e)}\left(\vec{r_j}\right)\right|^{2}\hat{\boldsymbol{I}}^{(j)}\cdot\hat{\boldsymbol{S}}^{(e)}\\ =&\mathcal{V}\sum_{j} A_{j}^{(e)}\left|\Psi^{(e)}\left(\vec{r_j}\right)\right|^{2}\left(\hat{\boldsymbol{I}}_{z}^{(j)}\hat{\boldsymbol{S}}_{z}^{(e)}+\hat{\boldsymbol{I}}_{x}^{(j)}\hat{\boldsymbol{S}}_{x}^{(e)}+\hat{\boldsymbol{I}}_{y}^{(j)}\hat{\boldsymbol{S}}_{y}^{(e)}\right)\end{aligned} \tag{1.10}$$

where $\mathcal{V}$ is the volume of the crystal unit cell, $A_j^{(e)}$ is the coupling constant between the electron of spin $\hat{\boldsymbol{S}}^{(e)}$ and the nucleus j of spin $\hat{\boldsymbol{I}}^{(j)}$. The envelope of the electronic wavefunction at the location of the nuclei j is denoted $\left|\Psi^{(e)}\left(\vec{r_j}\right)\right|^{2}$ and is represented by the dashed line in Fig. 1.18b. This interaction is isotropic and the x and y components of the scalar product can lead to spin flip-flops between the electron and the nuclear spins.

The hole spin qubit experiences the dipole-dipole interaction

The *dipole-dipole interaction* influences the dynamics of the hole pseudospin $\hat{\boldsymbol{S}}^{(h)}$ and can be accounted for by an anisotropic Ising interaction [47, 50]:

$$\hat{\boldsymbol{H}}_{hf}^{(h)} = \mathcal{V}\sum_{j}\left|\Psi^{(h)}\left(\vec{r_j}\right)\right|^{2}\left(A_{j,z}^{(h)}\hat{\boldsymbol{I}}_{z}^{(j)}\hat{\boldsymbol{S}}_{z}^{(h)}+A_{j,x}^{(h)}\hat{\boldsymbol{I}}_{x}^{(j)}\hat{\boldsymbol{S}}_{x}^{(h)}+A_{j,y}^{(h)}\hat{\boldsymbol{I}}_{y}^{(j)}\hat{\boldsymbol{S}}_{y}^{(h)}\right) \tag{1.11}$$

where this time the coupling constant $A_j^{(h)}$ is anisotropic and is decomposed on the x, y and z directions. The envelope of the hole wavefunction at the location of the nuclei j is denoted $\left|\Psi^{(h)}\left(\vec{r_j}\right)\right|^{2}$ (red dashed line in Fig. 1.18b).

The Fermi contact interaction dominates over the dipole-dipole one: $A_j^{(e)}$ is ten times higher than $A_{j,z}^{(h)}$. The latter constant results from the pure heavy-hole component whereas the relatively smaller terms $A_{j,y}^{(h)}$ and $A_{j,y}^{(h)}$ come from the residual mixing with the light-hole band. As a consequence, the hole spin presents a much longer dephasing time than the electron spin [47].

Dynamics of the hyperfine interaction

The interplay between the spin carrier trapped in a quantum dot and its nuclear spin environment is shown in Fig. 1.19, where the *Overhauser* magnetic field (order of magnitude 15-50 mT) resulting from the randomly oriented and fluctuating nuclei acts on the spin carrier, and the fluctuations of the spin carrier generate in return the relatively smaller *Knight* magnetic field acting on the nuclei[1].

---

[1] Neither this figure nor Fig. 1.18a present realistic spin vector lengths (1/2 for the central spin and 3/2 or 9/2 for nuclei).

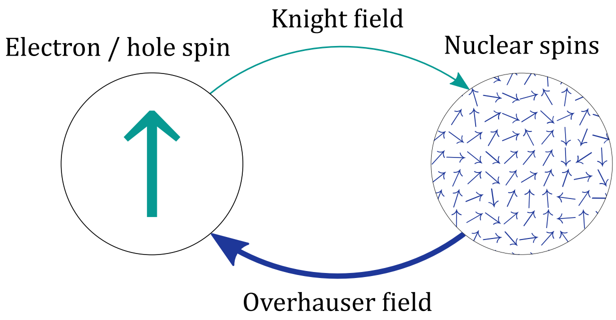

FIGURE 1.19: Magnetic feedback loop between the central electron or hole spin and the nuclear spin ensemble: the Overhauser field is the nuclear field acting on the central spin and the Knight field is the one emerging from the central spin acting on the nuclear spins.

From this feedback loop, three distinct timescales emerge [50, 86]:

- Short timescale: the electron spin precesses about the seemingly frozen Overhauser field in the order of 1 ns. In the case of a hole spin, its decreased sensitivity to the hyperfine interaction increases this precession time to the order of 100 ns.
- Intermediate timescale: the precession of the electron or hole spin, itself creating an inhomogeneous magnetic field (Knight field), causes the precession of the Overhauser field.
- Long timescale: the nuclei outside of the quantum dot but in its vicinity are subject to dipole-dipole interaction, disturbing the Overhauser field in the order of 100 µs.

The contributions of these three phenomena lead to the orders of magnitude of the electron and hole dephasing times given above without an external magnetic field: 0.5 ns for the electron and 10 ns for the hole [50, 54, 55].

1.2.4 Stabilization of the spin qubit

The hyperfine interaction determines the pure dephasing time of spin carriers, but multiple strategies allow this limitation to be circumvented.

Screening the nuclear field with an external magnetic field

Without an external magnetic field, the spin qubit precesses about the Overhauser field, as illustrated in the left panel of Fig. 1.20. When an external magnetic field is applied (in the longitudinal direction for the right panel of the figure), the spin qubit precesses about the total magnetic field, which is much stronger in the direction of the external magnetic field than any other. The spin coherence is therefore preserved over longer delays (i.e., the Bloch vector mostly rotate about z, preserving the superposition states in the s_x and s_y components).

This technique led to an improvement of an electron dephasing time from 0.5 ns without an external magnetic field to 4 ns with a 100 mT field [55]. In another experiment, the dephasing time of a hole spin exceeded 500 ns in a 3 T magnetic field [47, 87].

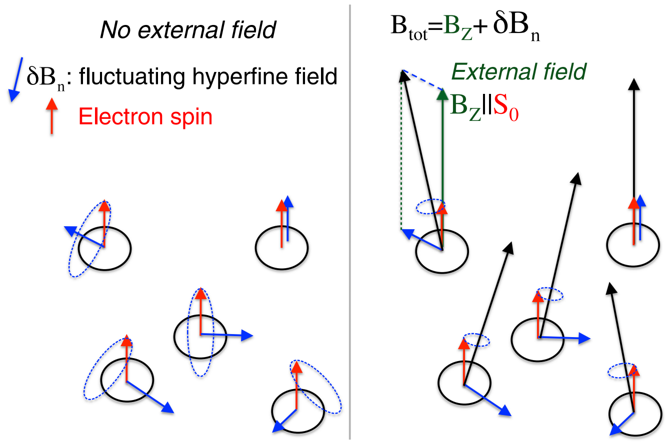

FIGURE 1.20: Magnetic screening of the Overhauser field. **(Left)** Without an external magnetic field, the randomly oriented Overhauser field is the only contribution. **(Right)** The addition of a high external longitudinal magnetic field B_z imposes spin rotations mainly about the z-axis, preserving spin coherence in the s_x and s_y components. Figure from [50].

Reversing the precession about the Overhauser field with spin echo

The spin echo technique makes use of π-pulses which coherently reverse the spin state (describing a π rotation in the Bloch sphere). For a spin initially rotating about the frozen Overhauser field for a time T, a first π pulse reverses the direction of the spin precession, such that after a subsequent delay T and a second π pulse, the spin is brought back to its initial state. This technique decouples the spin from the frozen Overhauser field, and its coherence is preserved as long as the Overhauser field is stable ($\simeq 1\,\mu s$). The spin echo can extend the electron dephasing time to a few microseconds [88, 89], using a transverse magnetic field of 3 T to enable the spin rotation by optical pulses as presented in subsection 1.2.2. This technique is also applicable to a heavy hole spin [90].

Polarizing the nuclei to stabilize the Overhauser field

Since the transverse components of the hyperfine interaction mediate spin flip-flops between the spin carrier and nuclear spins [91], a repeated pumping of the spin carrier (see subsection 1.1.4) might progressively polarize a significant part of the quantum dot nuclei. This phenomenon is called dynamic nuclear polarization (DNP) and was achieved with electron spins [92] and hole spins [93]. About 60 % of the quantum dot nuclei can be polarized, resulting in an additional magnetic field on the spin carrier location that can reach a few Teslas. In the last years, the group of M. Atatüre showed excellent control of the nuclear spin bath by an advanced scheme comparable to dynamic nuclear polarization, demonstrating a tenfold increase in an electron coherence time [94]. They also recently explored the ensemble oscillations of the nuclei as quantum carriers of information, broadening further the scope of the nuclear spin studies in quantum dots [95].

1.2.5 Experimental milestones with single spins in semiconductor quantum dots

We outline two major experimental techniques that demonstrated the potential of quantum dot spins as solid-state qubits.

Spin noise spectroscopy

When illuminated with linearly polarized photons propagating in the z direction, the dynamics of the quantum dot spin is mapped on the polarization of the transmitted[1] photons through the Faraday rotation effect, discussed later in subsection 1.3.4: a single spin in state $|\uparrow\rangle_z$ or $|\downarrow\rangle_z$ imprints a state-dependent polarization rotation to linearly polarized photons, of a few tens of µrad [57, 82]. Measuring the noise in the photonic polarization after the spin-photon interaction therefore translates as a measurement of the spin noise: this is the idea behind the field of spin noise spectroscopy (SNS) [96–98]. Fig. 1.21 presents an illustration of SNS, where a sample under a magnetic field in the z or x direction imprints a certain rotation on the photonic polarization: this rotation fluctuates in time, as shown in the polarization rotation graph in each case. Its characteristic evolution timescale is accessed by analyzing the autocorrelation of the polarization rotation signal, or its Fourier transform called the *spin noise power*.

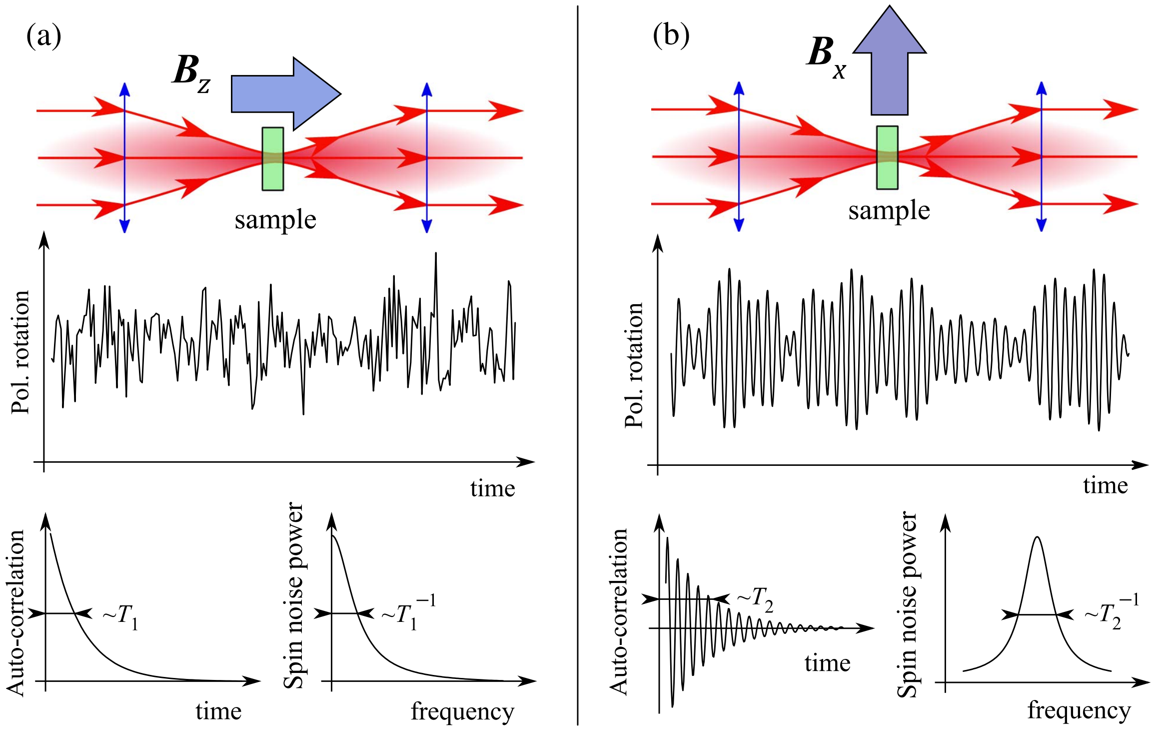

FIGURE 1.21: Principle of SNS. A sample with single spins under an external magnetic field is illuminated with photons, whose polarization is rotated depending on the spin state. The considered magnetic field is longitudinal in **(a)** and transverse in **(b)**. The transmitted signal exhibits a polarization rotation fluctuating in time. Its autocorrelation and its Fourier transform (called spin noise power) both decay in either the relaxation time T_1 for B_z or the dephasing time T_2 for B_x. Figure adapted from [97].

---

[1] Either reflected or transmitted photons, as appropriate in the experimental configuration.

When the magnetic field is along z, the spin eigenstates are $|\uparrow\rangle_z$ and $|\downarrow\rangle_z$, each of which rotates the photonic polarization in one direction or the opposite, so the dynamics imprinted on the polarization rotation is determined only by the spin flips (timescale T_1). However, in the case of a B_x magnetic field, the spin eigenstates become $|\uparrow\rangle_x$ and $|\uparrow\rangle_x$ and the Larmor precession about this axis causes an oscillation between $|\uparrow\rangle_z$ and $|\downarrow\rangle_z$, itself imprinted on the polarization rotation. The Larmor precession is damped in the coherence time T_2.

In semiconductor physics, spin noise spectroscopy was first applied to a macroscopic ensemble of spins to study the dynamics of electrons in bulk GaAs [99]. The technique was later brought to the level of an ensemble of single spins in InGaAs quantum dots [100], and finally to the ultimate limit of a single spin [101]. However, the variability of the experimental configurations makes the comparison of the results difficult.

Pushed to the level of a single spin interacting with single photons, spin noise spectroscopy is envisioned as a type of quantum non-demolition measurement [31, 102] as the measured system (the single spin) is preserved while the measurement only destroys the reflected photons. This regime is experimentally analyzed with photonic correlation measurements in the next chapters. Furthermore, as long as the Faraday rotation angles stay very small, this technique can be viewed as a weak measurement extracting very little information about the spin state, which is useful to measure the dephasing dynamics of the unperturbed spin.

Spin-photon entanglement

The entanglement between a quantum dot spin and an emitted photon arises when a trion state such as $|\Uparrow\Downarrow\uparrow\rangle_x$ decays with equal probabilities to $|\Uparrow\rangle_x$ or $|\Downarrow\rangle_x$ in a Voigt magnetic field (see Fig. 1.9c): the emitted photons are respectively in polarizations H or V, with energy ω_H or ω_V, each possibility corresponding to either ground spin state. The combined spin-photon state after emission is therefore:

$$\left|\Psi_{\text{sp-ph}}\right\rangle = \frac{|\Uparrow, H, \omega_H\rangle + |\Downarrow, V, \omega_V\rangle}{\sqrt{2}} \tag{1.12}$$

One photonic degree of freedom must be erased to achieve spin-photon entanglement: for example by using frequency conversion. In that case, the entanglement persists between the spin and the polarization, in the following inseparable state:

$$\boxed{\left|\Psi_{\text{sp-ph}}\right\rangle = \frac{|\Uparrow, H\rangle + |\Downarrow, V\rangle}{\sqrt{2}}} \tag{1.13}$$

The entanglement between the spin of a single electron trapped in an InGaAs quantum dot and the polarization degree of freedom of a photon was achieved by *De Greve et al. (2012)* [103] in the group of Y. Yamamoto. As explained above, they erased the photon energy information through a frequency down-conversion process, reaching a fidelity higher than 80 % to an entangled state analogous to Eq. 1.13. Similar results were obtained by *Schaibley et al. (2013)* [104] in the group of L. Sham, this time erasing the photon energy information through ultrashort detection times. Finally, *Gao et al. (2012)* [22] in the group of A. Imamoglu demonstrated the spin-photon entanglement by erasing the polarization degree of freedom of photons.

The entanglement procedure described here is limited to a bipartite entanglement: indeed, in the case of an excitation laser tuned to the $|\Uparrow\rangle_x \rightarrow |\Uparrow\Downarrow\uparrow\rangle_x$, repeating the procedure inevitably projects the spin in $|\Uparrow\rangle_x$, thereby projecting the first entangled photon to $|H\rangle$ before entangling a consecutive one. Nevertheless, having multiple devices able to generate an entanglement between a stationary spin and an emitted photon paves the way to the entanglement of distant spins, based on the entanglement swapping scheme successfully achieved by *Delteil et al. (2016)* [105] with distant hole spins and *Stockill et al. (2017)* [106] with electrons.

An ideal spin-photon interface could overcome this limitation, by successively entangling photons impinging on the qubit, based on the spin-dependent Faraday rotation to be described in subsection 1.3.4, which associates the complementary spin states to complementary polarization states. Such a protocol was proposed by *Hu et al. (2008)* [29] to generate *linear cluster states*, a class of highly entangled states useful for quantum computing (more information on which are presented in the perspectives of the manuscript). Efforts are also devoted to entangle a quantum dot spin with the timing of emitted single photons, referred to as *time-bin* encoding, which could be generalized to produce linear cluster states [107].

A major limiting factor of the entanglement rate is the efficient extraction of photons from the solid-state device. This is facilitated by coupling quantum dots to microcavity structures, as described in the next section.

1.3 Coupling the quantum dot to a cavity

This section focuses on the enhancement of the spin-photon interaction by a cavity. First, we lay the groundwork by describing the coupling between a two-level system and a cavity in the formalism of cavity quantum electrodynamics (cQED), through the Jaynes-Cummings model. We follow by explaining the experimental steps leading to such a quantum dot-cavity coupling. Next, the polarization qubit is described in the Poincaré sphere, and the core notion of spin-dependent polarization rotation is physically interpreted. Finally, we give an overview of experimental realizations towards an ideal spin-photon interface.

1.3.1 The Jaynes-Cummings model of cavity quantum electrodynamics

The light-matter interaction between photons and a quantum dot mediated by a cavity is interpreted in the Jaynes-Cummings model [108]. Here, the quantum dot is assimilated to a two-level system and the main results of the model are discussed; the theoretical framework will be extensively developed in section 3.1.

Let the energy of the vacuum serve as a reference. We consider a two-level system between a ground state $|g\rangle$ of null energy and an excited state $|e\rangle$, separated by the energy ω_d (modeling the quantum dot), interacting with photons in a cavity of fundamental mode tuned to the same energy ω_d. The coherent and incoherent cQED phenomena described next are sketched in Fig. 1.22.

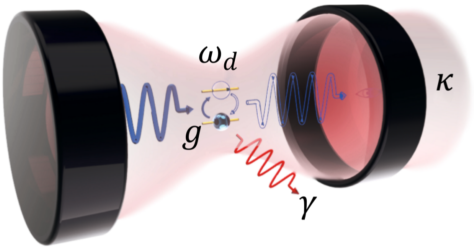

FIGURE 1.22: cQED phenomena included in the Jaynes-Cummings model. Photons interact with a two-level system of energy ω_d by coherent absorption and emission at a rate g; photons escape from the cavity at a rate κ and the two-level system loses photons outside of the cavity mode at a rate γ. Figure adapted from [109].

Coherent quantum dot-photon interaction

- The Hamiltonian giving the energy of the intracavity photons reads $\hat{\boldsymbol{H}}_{cav} = \omega_d \hat{\boldsymbol{a}}^\dagger \hat{\boldsymbol{a}}$, where $\hat{\boldsymbol{a}}$ is the operator annihilating an intracavity photon and its Hermitian conjugate $\hat{\boldsymbol{a}}^\dagger$ creates one.
- The Hamiltonian giving the energy of the quantum dot reads $\hat{\boldsymbol{H}}_d = \omega_d |e\rangle \langle e|$.
- The light-matter interaction is described by the Hamiltonian $\hat{\boldsymbol{H}}_{int} = ig\left(\hat{\boldsymbol{a}}^\dagger \hat{\boldsymbol{\sigma}} - \hat{\boldsymbol{a}} \hat{\boldsymbol{\sigma}}^\dagger\right)$ where $\hat{\boldsymbol{\sigma}} = |g\rangle \langle e|$ is the operator bringing the quantum dot from its excited to its ground state and its Hermitian conjugate $\hat{\boldsymbol{\sigma}}^\dagger$ does the opposite. This interaction coherently exchanges photons between the cavity and the quantum dot at a rate g.

After diagonalization, the total Hamiltonian exhibits an eigenenergy spectrum $E_{n,\pm}$ ($n \in \mathbb{N}^*$), where each couple $(E_{n,+}, E_{n,-})$ originates from the empty cavity level of energy $n\omega_d$. The new eigenstates are called *dressed states*, and their corresponding energy spectrum is given by:

$$\boxed{E_{n,\pm} = n\omega_d \pm \sqrt{n}g} \tag{1.14}$$

The associated eigenstates combine the states $|g, n\rangle$ and $|e, n-1\rangle$ (respectively quantum dot in the ground state with n intracavity photons, and quantum dot in the excited state with $n-1$ photons):

$$\boxed{|E_{n,\pm}\rangle = \frac{|g, n\rangle \pm |e, n-1\rangle}{\sqrt{2}}} \tag{1.15}$$

The lowest energy is $E_0 = 0$, associated to the single state $|E_0\rangle = |g, 0\rangle$. The dressed states compose the *Jaynes-Cummings ladder*, the first few rungs of which are represented in Fig. 1.23. Each (E_+, E_-) doublet is separated by a splitting of $2\sqrt{n}g$.

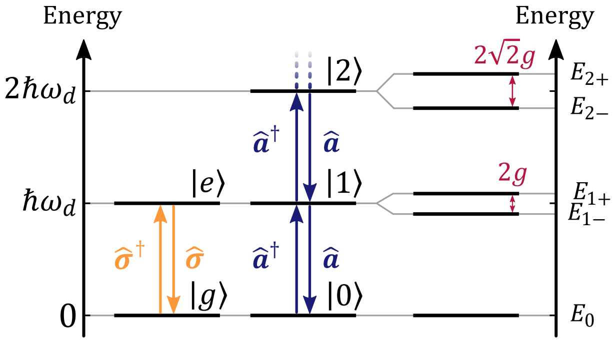

FIGURE 1.23: Eigenstates of the isolated quantum dot **(left)**, the isolated cavity photons **(middle)** and the coupled quantum dot-cavity system in the Jaynes-Cummings model **(right)**.

Incoherent quantum dot-photon interaction

Two incoherent phenomena break the coherent light-matter interaction: first, the loss of photons by the cavity at a rate κ, and second, the loss of coherence by the quantum dot at a rate $\gamma = 1/T_2$ (dephasing rate). These phenomena are theoretically modeled in section 3.1. Two regimes emerge when comparing their relative strength [110]:

- Strong coupling: the losses through κ and γ are lower than the coherent interaction: $\sqrt{\kappa^2 + (2\gamma)^2} < 4g$.
- Weak coupling: the losses are higher than the coherent interaction: $\sqrt{\kappa^2 + (2\gamma)^2} > 4g$.

Notice that the dephasing rate defined here is analogous to $1/T_2$ from subsection 1.2.1, but the considered qubit is now the two-level system with eigenstates $|g\rangle$ and $|e\rangle$, which would replace the states $|\uparrow\rangle_z$ and $|\downarrow\rangle_z$ in the Bloch sphere of a spin qubit. Specifically, pure dephasing now relates to the phase blurring of the superposed states $|g\rangle + e^{i\phi}|e\rangle$ at the rate $\gamma^* = 1/T_2^*$, and relaxation, to T_1 phenomena de-exciting the system from $|e\rangle$ to $|g\rangle$. The latter includes the spontaneous emission in all directions at a rate γ_{sp}, as well as the accelerated spontaneous emission in the cavity mode (known as the Purcell effect), specific to the weak coupling regime, at the rate $\Gamma_0 = 4g^2/\kappa$ [111, 112]. The relaxation time presented in subsection 1.2.1 is therefore redefined as $(T_1)^{-1} = \Gamma = \Gamma_0 + \gamma_{sp}$. On the other hand, the coherence time from Eq. 1.9 now becomes $(T_2)^{-1} = (2T_1)^{-1} + (T_2^*)^{-1}$ (the relaxation contribution is halved since the two level system can only decay from excited to ground state, compared to the two-way relaxation through spin flips). An important figure of merit expressing the relative strength of the coherent and incoherent processes is the cooperativity: $C = g^2/(\kappa\gamma)$. Two other figures of merit give essential information to compare cQED devices together: first, the quality factor $Q = \omega_c/\kappa$ (where ω_c is the cavity energy, different from ω_d in the general case). Cavities with highly reflective mirrors present high quality factors and are suited to work in the strong coupling regime as their losses

κ are very small. Second, the Purcell Factor $F_P = \Gamma_0/\gamma_{sp}$, which compares the spontaneous emission rate of the isolated two-level system γ_{sp} with its Purcell-enhanced emission in the cavity mode Γ_0. A high Purcell factor is crucial to minimize photonic losses in the device.

While the strong coupling regime demonstrated extremely efficient cavity-quantum dot interaction [113], weak coupling finds applications where an increased light-matter interaction is as important as an efficient collection of the photons from the device. Single photon sources and spin-photon interfaces belong to this category. In the scope of this manuscript, we focus especially on the giant Faraday rotation mediated by a cavity with devices of cooperativity of the order of unity (or above).

Optical microcavities

A cQED device confines specific electromagnetic modes around a quantum emitter. Compared to an isolated quantum dot, the consequences are twofold: the emission of the quantum emitter in the cavity modes is accelerated through the Purcell effect and the light-matter interaction is enhanced, leading to strong coupling in extreme cases. Cavities with small mode volumes favor high values of g and those with highly reflective mirrors favor low values of κ and high quality factors.

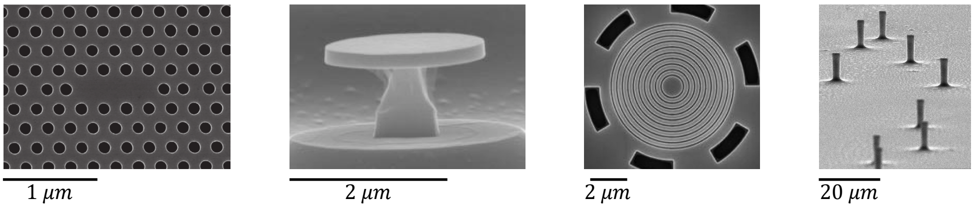

FIGURE 1.24: **(From left to right)** Photonic crystal cavity, microdisk cavity, bullseye cavity and micropillar cavity. Figures from the articles cited below.

The development of high precision lithography and etching techniques led to increasingly detailed solid-state structures. The idea of coupling solid-state emitters to optical microcavities became achievable, expanding cQED from its historical field of atomic physics to the solid-state realm. Despite the incomparably more complex environment surrounding a solid-state emitter compared to those in atomic physics, the benefit of solid-state systems lies in their simpler operation and their scalability. Let us review the most common optical microcavities presented in Fig. 1.24. From left to right:

- Photonic crystal cavities [114–119] are defined by a periodic pattern of nanometric holes in a semiconductor slab with a few holes deliberately skipped to confine light in the corresponding region. Light can be injected in and collected from the cavity either with a free-space beam orthogonal to the surface, or through a 2D waveguide on the slab. In both cases, the spatial profile of the mode is very different from the Gaussian mode of a fiber, hindering the coupling from one to the other. Quality factors can reach $10^5 - 10^6$ in such structures [118].

- Microdisks [120–125]: a suspended semiconductor disk exhibits optical resonances through whispering gallery modes, with quality factors reaching 10^5 [125]. Injection and collection of light usually take advantage of a waveguide tangent to the disk. Deterministic coupling of a single emitter to the cavity is difficult as the precise location of the antinodes of the whispering gallery mode –where the emitter must be placed– are strongly mode-dependent.
- Bullseye cavities [126–128]: light is confined in the center of a pattern of circular Bragg reflectors. Quality factors reach the 10^3 order of magnitude [127]. This design has been drawing attention thanks to its low-cost production and scalability; its broadband cavities and the development of deterministic cavity-quantum dot coupling techniques makes it a good candidate for single-photon sources.
- Micropillar cavities [129–132] are formed by distributed Bragg reflectors (DBR) sandwiching a central layer acting as a cavity. Quality factors reach 10^5 [132]. They are well suited to couple to the spatial mode of a fiber [133]. Devices called nanotrumpets are similar to micropillars, but their name originates from their conic shape with a thinner base [134]. An extension of the micropillar cavity is the open Fabry-Pérot cavity where the top side is replaced with a lens-shaped DBR, and the quantum dot layer and bottom mirror compose a planar structure displaceable relatively to the lens to form a cavity wherever the lens focuses [113, 135]. Quality factors close to 10^6 were achieved.

Purcell acceleration and strong coupling were achieved for photonic crystals [116, 117], microdisks [122, 124] and micropillars [129, 131]. Only Purcell acceleration was reached for bullseye cavities to our knowledge [127]. Our system of choice is the micropillar cavity: its very good coupling to a fiber makes it an excellent candidate for a fiber-based single-photon source, its absence of polarization selectivity is ideal for a spin-photon interface, and its versatility in the design of the heterostructure is key to single out and stabilize the desired charge state in the quantum dot. Next, we continue with a summary of the fabrication process of a micropillar cavity deterministically coupled to a quantum dot.

1.3.2 From a distributed Bragg Reflector to a micropillar cavity

Before being shaped into micropillars, the outcome of the epitaxy is a planar heterostructure composed of distributed Bragg reflectors (DBR) forming a cavity enclosing a quantum dot layer.

Distributed Bragg Reflector

A distributed Bragg reflector is an optical reflector consisting in a sequence of two materials of indices n_1 and n_2 as sketched in the top panel of Fig. 1.25 with layers of GaAs ($n_1 = 3.5$) and AlAs ($n_2 = 2.9$) on a GaAs substrate. An optical beam impinging on the top of the structure encounters a quarter wavelength optical thickness on each layer, of physical length equal to $\lambda/(4n_i)$ ($i \in 1, 2$). As a consequence, the optical path difference between the beam impinging on a material interface and the beam reflected at the next interface is always half a wavelength, and with the alternating phase reversal due to reflection on a higher index surface, all the reflected components interfere constructively while the transmitted parts interfere destructively. Semiconductor DBRs can reach reflectivities higher than $1 - 10^{-6}$ for a wide range of wavelengths known as the *stopband*, as illustrated in the reflectivity spectrum in the figure.

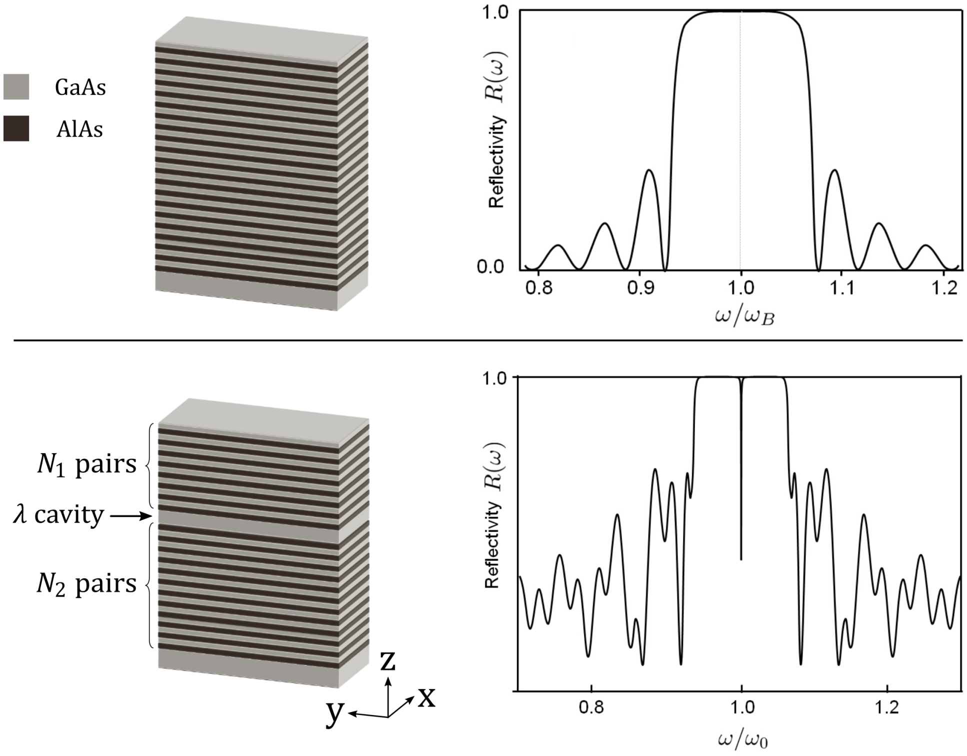

FIGURE 1.25: Planar heterostructure and simulated reflectivity spectrum for **(Top)** a planar DBR with 20 alternating layers of GaAs and AlAs and **(Bottom)** the same structure with a layer of physical thickness λ/n, creating a λ-cavity. ω_B and ω_0 refer respectively to the central energies of the Bragg reflector and of the cavity. Plots adapted from [136].

Planar cavity

Increasing the physical thickness of one of the DBR layers to $L_{cav} = \lambda/n$ creates a Fabry-Pérot cavity associated to a reflectivity dip, as shown in the bottom panel of Fig. 1.25. Photons bounce back and forth between the mirrors, forming a standing wave, before escaping the cavity at the rate κ (giving the width of the dip). Depending on the symmetry of the DBR stacking on the top and bottom sides of the cavity (N_t and N_b pairs respectively), the structure can be fully transmissive on resonance if $N_1 = N_2$ or have a non-zero reflectivity in other configurations. The cavity losses through the top and bottom channels are labeled κ_{top} and κ_{bottom} respectively. The free spectral range of the cavity is high enough to allow only a single Fabry-Pérot mode in the stopband.

It is at the center of the λ-cavity that the quantum dot layer is to be grown, at the antinode of the electromagnetic field, where it is the most intense. Their density can reach 10-100 dots per μm^2, far too high to isolate a single quantum dot in a micropillar of approximately 3 µm in diameter. An annealing step described in subsection 1.1.1 is performed to spectrally shift the energy distribution of quantum dots, so that only one quantum dot per potential micropillar is in the appropriate spectral range to interact properly with the cavity.

Deterministic quantum dot-cavity coupling with in-situ lithography

The planar cavity confines light in the z direction only. Etching a pillar of micrometric radius from this planar cavity leads to the additional confinement in the lateral dimensions, strongly increasing the light-matter interaction. A micropillar cavity should be spatially centered on a single quantum dot and the energy of its optical mode tuned to the desired optical transition. The chances to match these criteria by positioning the micropillars randomly on the planar sample are very low. Accordingly, an *in-situ* lithography technique was designed in the group of P. Senellart by *Dousse et al. (2008)* [23] with the following protocol:

> After the epitaxy of the planar structure, the wafer is coated with a photoresist layer. The lithography process, described in Fig. 1.26, is twofold: first, the sample is excited by an 850 nm laser (in red) and the luminescence (in orange) is analyzed by a spectrometer while the sample is scanned in the lateral plane: this allows to map quantum dots and to select those emitting close to the cavity energy. Once a quantum dot is selected, a 530 nm laser (in green) exposes the photoresist right above the quantum dot, marking a disk shape that will result, after etching, in a micropillar centered on the selected quantum dot with a precision of 50 nm. The diameter of the pillar is set by the exposure time with the green laser, and it in turn tunes the energy of the cavity mode (smaller diameters for higher energy cavities) in the appropriate range for optimal tuning with the quantum dot transition with a spectral precision of 0.35 nm.

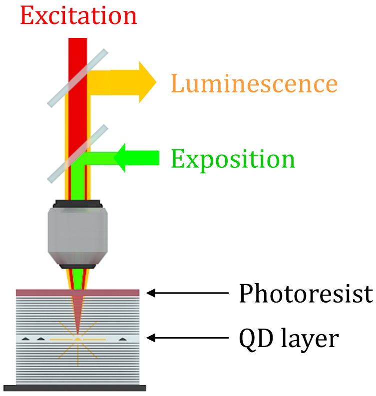

FIGURE 1.26: Experimental configuration to perform in-situ lithography with an excitation laser (in red) impinging on quantum dots, which in turn emit luminescence (in orange), and a green laser exposing the photoresist on top of a selected quantum dot.

The in-situ lithography followed by the etching of the sample completes the fabrication process. A finalized micropillar as seen through an optical microscope is shown in Fig. 1.27: the zoom on one micropillar on the left side evidences the intersection of four ridges constituting the pillar, which is connected to a circular frame, itself joined to a large electrically contacted mesa to which many micropillars are connected. The H and V axes indicate the eigenpolarizations of the cavity that arise from the difference in lateral confinement along those two directions [137]. The energy splitting between the two cavity modes is typically 80 µeV in our samples. A consequence of the ellipticity of the cavity is that it acts as a birefringent medium and rotates the polarization of light [138]. Such an asymmetry can be exploited to accelerate the emission of quantum dots preferentially in one of the modes, by tuning the dots in resonance with this mode and out of resonance with the other. Highly elliptical cavities coupled to quantum dots have shown high performance as sources of polarized single photons [127, 139]. The right part of Fig. 1.27 shows a zoomed-out view of the sample, where many pillars embedded in circular frames are joined to a mesa. The gold cover is connected by wire bonding to apply a voltage to the surface. The ground voltage is applied below the sample. The electrical contact stabilizes the charge environment of the quantum dot and allows a fine-tuning of the transitions' energies through Stark shift [140].

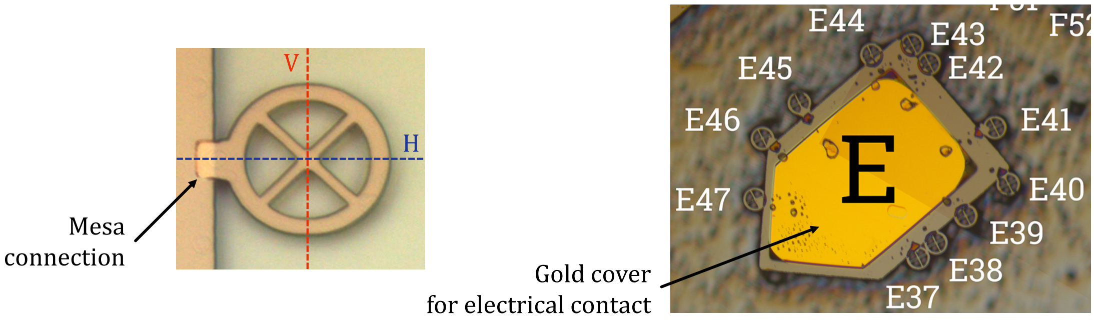

FIGURE 1.27: **(Left)** Micropillar embedded in a circular frame through four ridges. The asymmetry of the lateral confinement makes two eigenpolarizations emerge along the H and V axes. **(Right)** Zoomed out view of a whole electrically contacted mesa (called "E") with attached micropillars. The gold cover is where a wire is bonded to apply a voltage and the ground voltage is applied below the sample.

At this point, the sample is handed from the fabrication team (A. Lemaître, N. Somaschi, I. Sagnes, A. Harouri) to the optics team (L. Lanco, C. Millet, P. Hilaire, E. Mehdi) to analyze the spin-photon interaction in the quantum dot-micropillar structures. The micropillar labeled E46, which we will call the *positively charged device* in this manuscript was extensively studied as a spin-photon interface for chapter 4. Additionally, it was used by J. Loredo and C. Anton to generate non-classical states of light by coherent control of the quantum dot [141], and as a single-photon source in collaboration with the team of H. Eisenberg to generate photonic cluster states [142].

cQED parameters of a micropillar cavity

The different parameters characterizing a quantum dot-micropillar device, described in Fig. 1.28a, are the following:

- The coupling strength g, already described in the Jaynes-Cummings model.
- The cavity losses $\kappa = \kappa_{top} + \kappa_{bottom} + \kappa_{loss}$, distributed between the losses through the top and bottom mirrors and through the sidewall of the micropillar caused by surface roughness (κ_{loss}).
- The dephasing rate of the quantum dot, $\gamma = \gamma_{sp}/2 + \gamma^*$, either through spontaneous emission outside the cavity mode or through pure dephasing.

Three dimensionless parameters commonly characterize a microcavity, as shown in Fig. 1.28b: the efficiency of the input coupling η_{in}, quantifying the overlap between the spatial mode of the input beam and the fundamental mode of the micropillar; the cooperativity C described in subsection 1.3.1; and finally the top mirror output coupling $\eta_{top} = \kappa_{top}/\kappa$, referring to the probability for intracavity photons to escape by the top mirror through the collection port, as opposed to the other channels in which they are definitely lost.

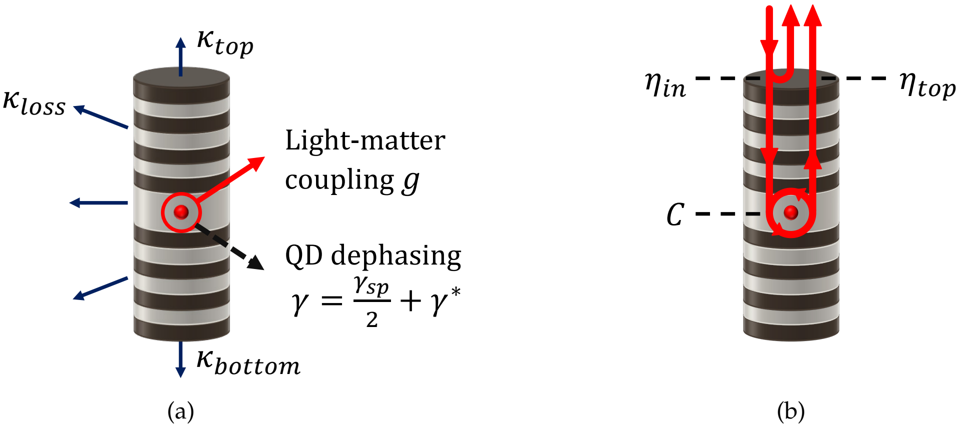

FIGURE 1.28: **(a)** cQED parameters of a micropillar cavity. **(b)** Figures of merit (dimensionless parameters) characterizing a microcavity.

We emphasize that κ relates to purely photonic losses and γ to dephasing of the two-level system (here, the quantum dot), while g quantifies the coherent interaction. In addition, η_{in} pertains only to spatial modes overlap whereas η_{top} compares the output canal of interest with the global photonic losses. In general, we aim at high values of C, η_{in} and η_{top} to reach the best performance of the device as a single-photon source or spin-photon interface.

- Maximizing g requires small optical mode volumes, and thus micropillars of small radii.
- Minimizing κ while keeping η_{top} high is achieved by having high-reflectivity DBRs on each side of the cavity, with a relatively lower value on the top side.
- Minimizing the dephasing is achieved by stabilizing the charge environment of the quantum dot with the electrical bias.

We have now reviewed the deterministic light-matter coupling in a solid-state cavity. In order to better grasp the interaction between the spin qubit and the photonic qubit, let us describe the latter in an analogous manner as we did the former in the Bloch sphere.

1.3.3 Description of the polarization qubit in the Poincaré sphere

Here, we give an overview of the mathematical description of the polarization of light as a wave and its counterpart in quantum optics, where the photon constitutes a polarization qubit.

Classical description in the (H,V) basis

A monochromatic plane wave traveling in the z direction with a wave vector $\vec{k} = (\omega/c)\vec{u_z}$ is described by its electric field that can be written as projections on the horizontal and vertical directions $(\vec{u_H}, \vec{u_V})$, where $(\vec{u_H}, \vec{u_V}, \vec{u_z})$ is an orthonormal basis:

$$\vec{E}(z,t) = \begin{pmatrix} A_H e^{i(kz-\omega t)}\vec{u_H} \\ A_V e^{i(kz-\omega t+\delta)}\vec{u_V} \\ 0 \cdot \vec{u_z} \end{pmatrix} \tag{1.16}$$

where $\vec{E}$ is the complex amplitude of the electric field, and $A_{H/V}$ are the maxima of the H and V components. The electric field oscillates with a phase term $(kz-\omega t)$ and a dephasing δ between its H and V components.

Let us consider normalized electric fields ($A_H^2 + A_V^2 = 1$) and study only the polarization degree of freedom, which refers to the orientation of the oscillatory electric field in the $(\vec{u_H}, \vec{u_V})$ plane. For a classical wave, it takes the form of an ellipse such as that represented in Fig. 1.29a for an arbitrary case. The ellipse describes all the values of the electric field vector in one oscillation period. Let us now simplify the common oscillatory term $e^{i(kz-\omega t)}$. Three specific couples of polarization states are commonly used as bases to describe all polarizations as linear combinations: (H,V), (D,A), (R,L). The first two sets comprise the linear polarizations (horizontal, vertical, diagonal and anti-diagonal), which are found when the H and V components oscillate in phase ($\delta = 0$) and the third basis, the circular polarizations (left and right-handed), this time for an oscillation in opposite phase ($\delta = \pm\pi/2$). In the (H,V) basis, we find:

$$\begin{pmatrix} E_D \\ E_A \end{pmatrix} = \frac{1}{\sqrt{2}} \begin{pmatrix} 1 & 1 \\ 1 & -1 \end{pmatrix} \begin{pmatrix} E_H \\ E_V \end{pmatrix} \qquad \begin{pmatrix} E_R \\ E_L \end{pmatrix} = \frac{1}{\sqrt{2}} \begin{pmatrix} 1 & i \\ 1 & -i \end{pmatrix} \begin{pmatrix} E_H \\ E_V \end{pmatrix} \tag{1.17}$$

In the ellipse representation, the polarization is characterized by an orientation angle Ψ and an ellipticity angle χ, and we find the basis polarizations for the following angles:

$$\begin{array}{llllll} \text{H:} & (\Psi = 0, \quad \chi = 0) & \text{D:} & (\Psi = \pi/4, \quad \chi = 0) & \text{R:} & (\Psi = 0, \quad \chi = \pi/4) \\ \text{V:} & (\Psi = \pi/2, \quad \chi = 0) & \text{A:} & (\Psi = -\pi/4, \quad \chi = 0) & \text{L:} & (\Psi = 0, \quad \chi = -\pi/4) \end{array} \tag{1.18}$$

The transformations of Eq. 1.17 have the same properties as those linking the spin states together in the Bloch representation (Eq. 1.3). This encourages the representation of polarization in a sphere called the Poincaré sphere, where each polarization state is mapped to a point on the surface of the sphere (Fig. 1.29b shows the location of the arbitrary elliptical state from Fig. 1.29a). In this representation, a pure polarization state is described by a Poincaré vector $\boldsymbol{S} = (s_{HV}, s_{DA}, s_{RL})$ of unity length with a longitude angle $\Phi = 2\Psi$ and a latitude angle $\theta = 2\chi$. The (Φ, θ) notations will be used in the rest of this manuscript. In Fig. 1.30, we plot examples of different polarization states in the two representations.

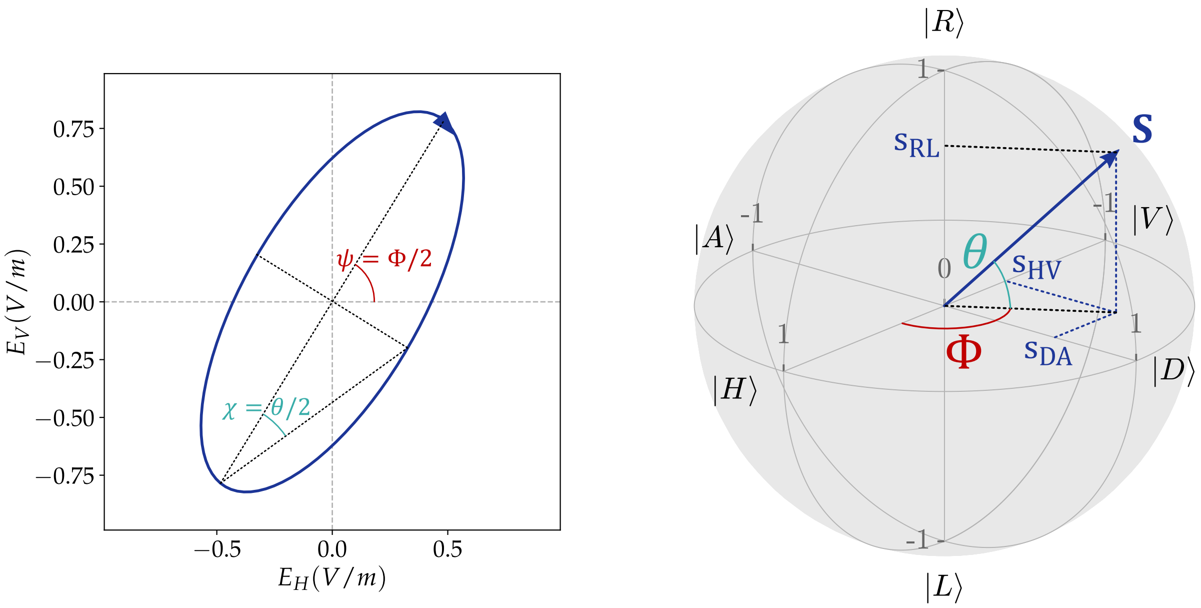

(a) (b)

FIGURE 1.29: Example of a polarization state described by $\Phi = 120°$ and $\theta = 45°$ in two representations: **(a)** ellipse and **(b)** Poincaré sphere. The associated Stokes $\boldsymbol{S}$ vector has the Cartesian coordinates $s_{HV} = -0.35, s_{DA} = 0.61, s_{RL} = 0.71$.

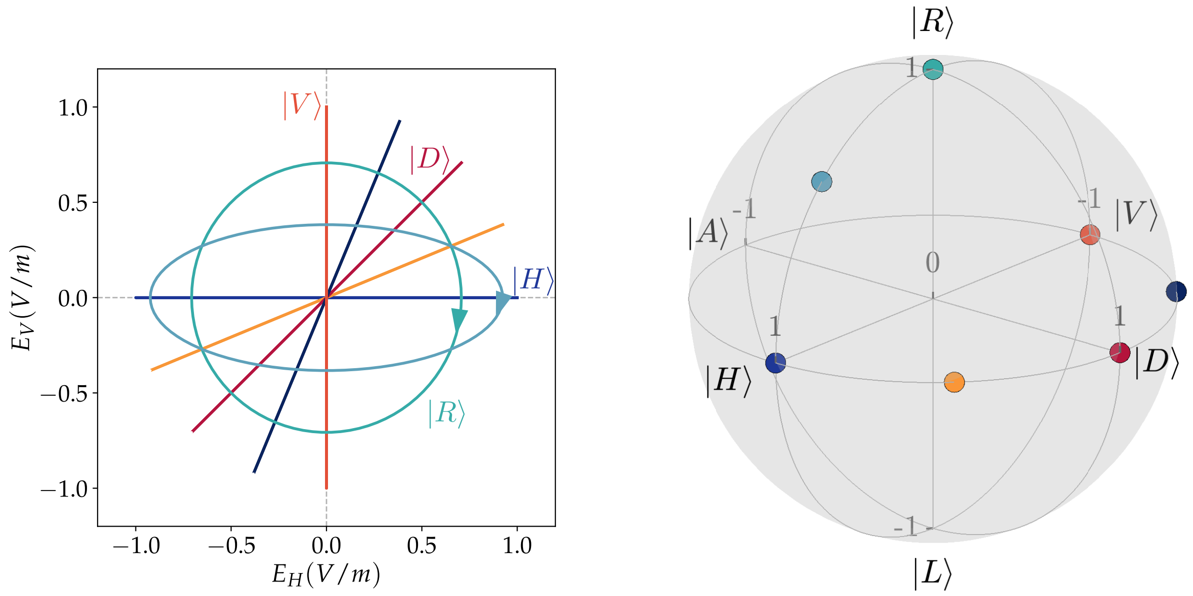

(a) (b)

FIGURE 1.30: Examples of different polarization states with a color mapping between **(a)** the ellipse representation and **(b)** the Poincaré sphere.

The Cartesian coordinates of the Poincaré vector are known as the Stokes parameters, they are expressed as functions of the latitude and longitude angles:

$$\begin{aligned} s_{HV} &= \cos(\Phi)\cos(\theta) \\ s_{DA} &= \cos(\theta)\sin(\Phi) \\ s_{RL} &= \sin(\theta) \end{aligned} \tag{1.19}$$

Quantum description in the (R,L) basis

At the single photon level, the Poincaré sphere describes a polarization qubit. Each photon carries a spin quantized along the propagation axis $\vec{u_z}$, of projection $+1$ or -1 corresponding respectively to the circular polarizations $|R\rangle$ and $|L\rangle$. All the pure polarization states are superpositions of the circular polarizations:

$$|\Psi\rangle = \alpha\,|R\rangle + \beta\,|L\rangle \tag{1.20}$$

where α and β are complex numbers such that $|\alpha|^2 + |\beta|^2 = 1$. The reasoning done with a spin qubit holds for the polarization qubit, albeit with different conventions. Let us examine the consequences.

First, the link between (α, β) and the angular coordinates in the Poincaré sphere is given by the following expressions, translated from Eq. 1.4 and adapted them for $\phi = \varphi$ and $\theta = \pi/2 - \vartheta$:

$$\begin{cases} \alpha = \cos\left(\dfrac{\pi}{4} - \dfrac{\theta}{2}\right) \\ \beta = e^{i\phi}\sin\left(\dfrac{\pi}{4} - \dfrac{\theta}{2}\right) \end{cases} \tag{1.21}$$

The expression of the Stokes parameters of a pure polarization state can be adapted from Eq. 1.4:

$$\begin{aligned} s_{HV} &= 2\,\mathrm{Re}\{\alpha\beta^*\} = \cos(\phi)\cos(\theta) \\ s_{DA} &= 2\,\mathrm{Im}\{\beta\alpha^*\} = \sin(\phi)\cos(\theta) \\ s_{RL} &= \alpha\alpha^* - \beta\beta^* = \sin(\theta) \end{aligned} \tag{1.22}$$

An extra precaution is required when writing the basis change relations with kets like $|R\rangle$ that stand for Fock states with single photons in the given polarization: indeed, we could write $|R\rangle = |1_R\rangle$, and the Fock state would be formed by applying the creation operator to the vacuum state $|1_R\rangle = \hat{\boldsymbol{a}}_R^\dagger\,|0_R\rangle$. Besides, the creation operator being the hermitian conjugate of the electric field, it follows the complex conjugate rules of Eq. 1.17. Therefore in the $(|H\rangle, |V\rangle)$ and $(|R\rangle, |L\rangle)$ bases, we have respectively:

$$\begin{pmatrix} |D\rangle \\ |A\rangle \end{pmatrix} = \frac{1}{\sqrt{2}}\begin{pmatrix} 1 & 1 \\ 1 & -1 \end{pmatrix}\begin{pmatrix} |H\rangle \\ |V\rangle \end{pmatrix} \qquad \begin{pmatrix} |R\rangle \\ |L\rangle \end{pmatrix} = \frac{1}{\sqrt{2}}\begin{pmatrix} 1 & -i \\ 1 & i \end{pmatrix}\begin{pmatrix} |H\rangle \\ |V\rangle \end{pmatrix} \tag{1.23}$$

$$\begin{pmatrix}|H\rangle\\|V\rangle\end{pmatrix}=\frac{1}{\sqrt{2}}\begin{pmatrix}1&1\\i&-i\end{pmatrix}\begin{pmatrix}|R\rangle\\|L\rangle\end{pmatrix}\qquad\begin{pmatrix}|D\rangle\\|A\rangle\end{pmatrix}=\frac{1}{\sqrt{2}}\begin{pmatrix}1+i&1-i\\1-i&1+i\end{pmatrix}\begin{pmatrix}|R\rangle\\|L\rangle\end{pmatrix}\tag{1.24}$$

If a photon is in a statistical mixture of pure polarization states, it is characterized in the Poincaré sphere by a vector that doesn't reach the surface of the sphere. We write this general case $\boldsymbol{S}=(s_{HV},s_{DA},s_{RL})$, and its norm is called the purity $p=\sqrt{s_{HV}^2+s_{DA}^2+s_{RL}^2}$. The coordinates of the mixed polarization state are:

$$\begin{aligned}s_{HV}&=p\cdot\cos(\Phi)\cos(\theta)\\s_{DA}&=p\cdot\cos(\theta)\sin(\Phi)\\s_{RL}&=p\cdot\sin(\theta)\end{aligned}\tag{1.25}$$

This description is analogous to the density matrix approach. A mixed state is the incoherent sum of multiple pure states, each with their own probability. This incoherent summing can have multiple causes:

- Fast variations of the phase ϕ that can't be resolved by the detection apparatus.
- Coherent superposition of pure polarization states associated to other degrees of freedom, such as spatial modes. For example, the state $|\Psi_s\rangle=\frac{|H,m_1\rangle+|V,m_2\rangle}{\sqrt{2}}$ appears as a mixed superposition of $|H\rangle$ and $|V\rangle$ to a detector that cannot resolve the two spatial modes m_1 and m_2.

Experimental polarization tomography

We experimentally access the Stokes parameters by measuring the intensity of the electric field along each polarization X, for X ∈ [H,V,D,A,R,L]. The intensity is $I_X=|E_X|^2$. The Stokes vector is reconstructed with the following expressions, valid for pure and mixed states:

$$s_{HV}=\frac{I_H-I_V}{I_H+I_V}\qquad s_{DA}=\frac{I_D-I_A}{I_D+I_A}\qquad s_{RL}=\frac{I_R-I_L}{I_R+I_L}\tag{1.26}$$

1.3.4 Principle of the spin-dependent polarization rotation

The Faraday rotation, briefly mentioned in subsection 1.2.5 for its potential application in the generation of multipartite entangled states, is now developed. We focus on the case of a single photon interacting with a single spin in a micropillar cavity. The photon polarization is a sum of the left- and right-handed circular polarizations, $|L\rangle$ and $|R\rangle$, respectively associated with a spin projection of the photons of -1 and $+1$ along its propagation direction. When light propagates along the growth axis of the micropillar z, the optical selection rules restrict the spin states it can interact with: as per Fig. 1.7, $|R\rangle$ can only interact with $|\uparrow\rangle_z$ of an electron or $|\Downarrow\rangle_z$ of a hole and the opposites spin projections interact with $|L\rangle$. In fact, the natural quantization axis of spins interacting with light is identical to the light propagation axis z, in the absence of a magnetic field. We now show that a given linearly polarized photonic state undergoes a rotation in one direction or the other depending on the spin state, as sketched in Fig. 1.31.

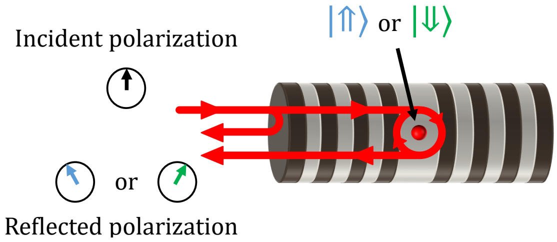

FIGURE 1.31: Principle of the Faraday rotation of a linearly polarized photon by a quantum dot spin coupled to a micropillar cavity.

Let us consider an input photon of polarization $|\Psi_{in}\rangle = |H\rangle = \frac{|R\rangle+|L\rangle}{\sqrt{2}}$ impinging on the device trapping a hole spin is in state $|\Uparrow\rangle_z$. The left-handed circular component of $|H\rangle$ experiences a cavity with a two-level system represented by the $|\Uparrow\rangle_z \to |\Uparrow\Downarrow\uparrow\rangle_z$ transition, also denoted *hot cavity* (loaded with the two-level system), as for the right-handed circular component, it only experiences an empty cavity called *cold cavity* (without a two-level system). The corresponding reflection coefficients can be computed in the semi-classical approximation [143] to model the response of the device under a low power excitation[1]. The hot and cold cavities are characterized by the following complex reflection coefficients, respectively labeled h and c:

$$\boxed{r_h(\omega) = \frac{E_{out}(\omega)}{E_{in}(\omega)} = 1 - 2\eta_{top}\left(1 - 2i\frac{\omega-\omega_c}{\kappa} + \frac{2C}{1 - i\frac{\omega-\omega_d}{\gamma}}\right)^{-1}} \tag{1.27}$$

$$r_c(\omega) = 1 - 2\eta_{top}\left(1 - 2i\frac{\omega-\omega_c}{\kappa}\right)^{-1} \tag{1.28}$$

where ω, ω_c and ω_d stand respectively for the energies of the laser, the cavity and the quantum dot, and η_{top} and C were previously introduced. The cold cavity takes $C = 0$ to remove the light-matter interaction. Notice in the equations that η_{top} brings about the interference between the light that entered the cavity and left through the top mirror and the light directly reflected without entering the cavity, as sketched on Fig. 1.31.

Let us simulate the quantum state of the reflected polarization. The set of parameters used for this simulation is: $g = 15\,\mu\text{eV}$, $\kappa = 375\,\mu\text{eV}$, $\gamma = 0.3\,\mu\text{eV}$, $\eta_{top} = 0.9$, $\omega_d = \omega_c = \omega_0$; it will be studied in-depth in chapter 4 as it constitutes a base model of the device we call *positively charged device*. We denote the reflected polarization state $|\Psi_\Uparrow\rangle$ to indicate the spin state that light has interacted with. It is given by the following expression, as a function of the laser energy ω:

$$|\Psi_\Uparrow(\omega)\rangle = \frac{r_c(\omega)\,|R\rangle + r_h(\omega)\,|L\rangle}{\sqrt{|r_c(\omega)|^2 + |r_h(\omega)|^2}} \tag{1.29}$$

---

[1] This approximation starts from the master equation detailed in section 3.1 and ignores the quantum correlations to find analytical solutions of the reflection coefficient in the steady state.

We can rewrite this expression to highlight the effect of the moduli and phases of the reflection coefficients with $r_{h/c} = \left|r_{h/c}\right| e^{i\phi_{h/c}}$ (the energy dependence is implied for clarity):

$$\boxed{\left|\Psi_{\Uparrow}\right\rangle = \frac{|r_c| e^{i\phi_c} \left|R\right\rangle + |r_h| e^{i\phi_h} \left|L\right\rangle}{\sqrt{|r_c|^2 + |r_h|^2}}} \tag{1.30}$$

The modulus and phase of the two reflection coefficients are plotted in Fig. 1.32 as a function of the laser-quantum dot detuning $\delta\omega = \omega - \omega_0$, as solid green lines for the hot cavity and dashed black lines for the cold cavity. The moduli exhibit a large cavity-induced dip of width κ and depth determined by η_{top}, and a thin dip originating from the quantum dot, of width Γ and depth given by C and η_{top}. The difference between the hot and cold cavities around the quantum dot contribution alters the relative contributions of $\left|R\right\rangle$ and $\left|L\right\rangle$ light in the output. Here, the incident light is $\left|H\right\rangle$ and has equal contributions of $\left|R\right\rangle$ and $\left|L\right\rangle$, but the spin $\left|\Uparrow\right\rangle_z$ interacts only with $\left|L\right\rangle$ so the reflected light has comparably more $\left|R\right\rangle$ than $\left|L\right\rangle$ components. As for the phase of the reflectivity, the hot cavity steeply separates from the slow increase of the cold cavity at the quantum dot contribution. It impacts the reflected light by creating a relative dephasing of $e^{i(\phi_h - \phi_c)}$ between $\left|L\right\rangle$ and $\left|R\right\rangle$: this is equivalent to an increase of ϕ (introduced in Eq. 1.20 and 1.21), which causes a rotation of the reflected polarization from $\left|H\right\rangle$ towards $\left|D\right\rangle$[1].

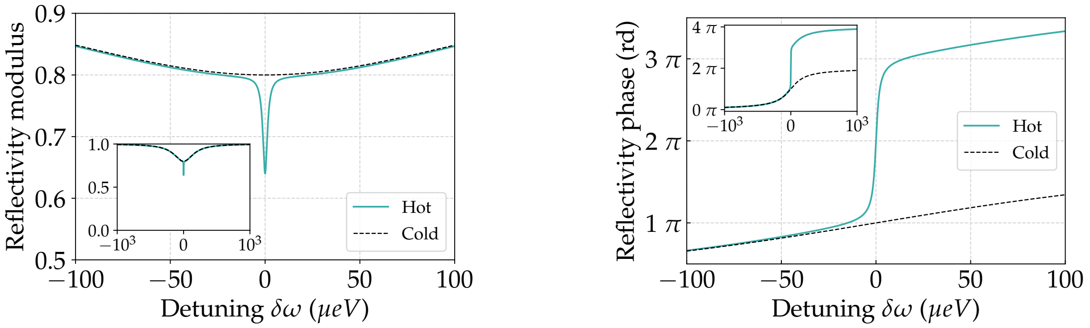

(a) (b)

FIGURE 1.32: Reflection coefficients of the hot and cold cavity (respectively in solid green lines and dashed black lines) as a function of the laser-quantum dot detuning $\delta\omega$: **(a)** in modulus and **(b)** in phase. Insets show a broader range of detunings.

In the same fashion, we can calculate $\left|\Psi_{\Downarrow}\right\rangle$ by inverting $\left|L\right\rangle \leftrightarrow \left|R\right\rangle$ in the previous paragraph and its conclusions. The polarization state $\left|\Psi_{\Downarrow}\right\rangle$ is therefore rotated towards $\left|A\right\rangle$, with a relatively more important $\left|L\right\rangle$ than $\left|R\right\rangle$ contribution in the output.

If we identify the values of α and β from $\left|\Psi_{\Uparrow}\right\rangle$ and $\left|\Psi_{\Downarrow}\right\rangle$ (as in Eq. 1.20) and calculate the Stokes parameters using Eq. 1.22, we can compute their scalar product using Eq. 1.8 and conclude that a value of ω exists where $\left\langle\Psi_{\Uparrow}|\Psi_{\Downarrow}\right\rangle = 0$. This situation is presented in Fig. 1.33 and illustrates the case of an ideal spin-photon interface. Indeed, in that case, any spin state is

---

[1] The rotation angle of the linear polarization is close to $\phi_h - \phi_c$ and it is visibly 0 rad for low detunings, π rad on resonance with the quantum dot, and 2π rad for high detunings. We see next that this consideration is not completely rigorous as the output polarization does not stay perfectly linear but becomes slightly elliptical due to the different reflectivity moduli of the hot and cold cavity applied to $\left|L\right\rangle$ and $\left|R\right\rangle$.

translated to an analogous polarization state:

$$\begin{array}{c} \text{Spin state} \qquad \text{Polarization state} \\ \hline |\Uparrow\rangle \xrightarrow{\hspace{3em}} |\Psi_\Uparrow\rangle \\ |\Downarrow\rangle \xrightarrow{\hspace{3em}} |\Psi_\Downarrow\rangle \\ \alpha\,|\Uparrow\rangle + \beta\,|\Downarrow\rangle \rightarrow \alpha\,|\Psi_\Uparrow\rangle + \beta\,|\Psi_\Downarrow\rangle \end{array} \tag{1.31}$$

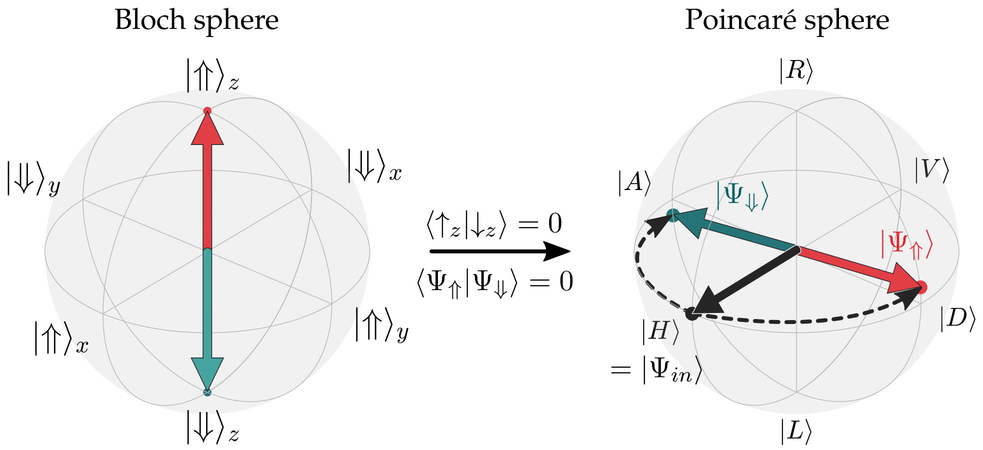

FIGURE 1.33: **(a)** The two hole spin states $|\Uparrow\rangle_z$ and $|\Downarrow\rangle_z$ are represented by arrows in the Bloch sphere. They imprint a spin-dependent rotation of the polarization on photons. **(b)** The Poincaré sphere describes the input state $|\Psi_{in}\rangle = |H\rangle$ and the two reflected states depending on the spin state, $|\Psi_\Uparrow\rangle$ and $|\Psi_\Downarrow\rangle$, chosen at the right detuning $\delta\omega$ so that $\langle\Psi_\Uparrow|\Psi_\Downarrow\rangle = 0$.

The global spin-photon state after the interaction can exhibit entanglement, but only to the extent that the spin is in an equal superposition of the basis states, such as $\left|\Psi_{\text{sp}}\right\rangle = \frac{|\Uparrow\rangle+|\Downarrow\rangle}{\sqrt{2}}$ (or any states on the equator of the Bloch sphere). In that specific case, the global state is maximally entangled:

$$\boxed{\left|\Psi_{\text{sp-ph}}\right\rangle = \frac{|\Uparrow,\Psi_\Uparrow\rangle + |\Downarrow,\Psi_\Downarrow\rangle}{\sqrt{2}}} \tag{1.32}$$

The result of this semi-classical model is quite relevant, as we will see in chapter 3 that a fully quantum model gives very close results (for instance in Fig. 3.6).

1.3.5 Experimental spin-dependent polarization rotation

The first measurements of the spin-dependent polarization rotation induced by charged quantum dots were achieved in the group of D. Awschalom [82] and A. Imamoglu [57] with rotation angles close to 0.01° and 0.001° respectively. They both observed the rotation induced by ensembles of quantum dots with single electron spins in planar cavities. Since then, much higher rotation angles were demonstrated by coupling individual quantum dots to a microcavity. Noticeably, micropillars gave exceptional results: 12° in the team of L. Lanco in C2N [27], and $60 - 120°$ in the group of R. Oulton in Bristol [28] (albeit with a post-selection protocol in the latter case).

To summarize, micropillar cavities coupled to quantum dots are promising candidates as solid-state spin-photon interfaces in a quantum network, thanks to their excellent coupling with the spatial mode of an optical fiber [133], and their absence of polarization selectivity preserving the polarization qubit in and out of the cavity. Achieving complementary spin-dependent polarization states such that $\langle \Psi_{\Uparrow} | \Psi_{\Downarrow} \rangle = 0$ is within reach as we will justify in the rest of the manuscript. In addition, the cavity-quantum dot coupling can be controlled deterministically by in-situ lithography [23]. Many teams have explored the different light-matter coupling regimes in these devices: on the one hand in the weak coupling to engineer high-efficiency single-photon sources [24] and giant Faraday rotation [27, 28], and on the other hand, in the strong coupling [144] with perspectives in photon-photon gates. Other leading groups in this field are led by D. Bouwmeester in Leiden [145], A. Shields in Cambridge [146] and J.-W. Pan in Hefei [63].

1.4 Conclusion

Photons and electrons or holes hold the fundamental property of quantum superposition, in the polarization degree of freedom of the photons and in the spin degree of freedom of the charges. Harnessing the benefits of both types of qubits paves the way towards quantum networks with photons carrying quantum information from one localized spin node to another. The key takeaway of this chapter is the ability to trap single charges in solid-state quantum dots, to control their spin and to fabricate microcavities producing an efficient spin-photon interaction. An ideal spin-photon interface would provide the entanglement between a localized spin and an external photon, a process much sought after for quantum networks and quantum computing in general. Additionally, the remarkable scalability and relative affordability of such devices compared to their cold atom counterparts offer potential for large-scale applications in future photonic quantum technologies. In this chapter, the workings of a spin-photon interface were laid out as generally as possible, and the state-of-the-art experimental implementations were presented. Next, we focus more specifically on the work achieved in the group of L. Lanco and P. Senellart who developed very promising cQED devices in the solid state which we will seek to study as spin-photon interfaces.

Chapter 2

Sample structure and experimental principles

The development of spin-photon interfaces in the solid-state is technologically challenging and their operation requires combining techniques from the fields of optics and solid-state physics. From the fabrication standpoint, a single quantum dot must be isolated, loaded with a single charge carrier, and coupled to a cavity. Specifically, the cavity and the quantum dot need careful spatial and spectral tuning. From the characterization standpoint, an input beam resonant with the optical cavity mode and the selected quantum dot transition must be precisely aligned to the micropillar cavity, with a careful polarization control in the input and output paths.

In this chapter, we first focus on the design of two samples suited to operate as spin-photon interfaces: one in which a single electron can be trapped by electrical control and the other in which a single hole can be optically injected. After detailing the specifications of each sample, we explain how the in-situ lithography technique can be adapted to obtain a deterministic coupling of an identified quantum dot transition with the optical mode of a micropillar cavity.

We then establish the principle of the optical characterization experiments presented along this manuscript: starting with the spectroscopic investigation of the device reflectivity in multiple polarization configurations, to study the effect of the cavity and the quantum dot spin on the reflected light. By combining several of these reflectivity data, the tomography technique developed in previous works at the C2N [133, 147] allows a complete characterization of the reflected polarization state: here, we apply it to the study of the cavity-induced polarization rotation, as it gives insights on the micropillar cavity parameters and the quality of the optical alignment. It will later enable the study of the spin-induced polarization rotation in the steady state. Next, we present the experiments used to evaluate the performance of our devices as spin-based single-photon sources. The first step is to find an excitation protocol to load the charge in the quantum dot, and then to measure the brightness of the source and the lifetime, purity and indistinguishability of the emitted photons: high-quality performance as a spin-based single-photon source ensures the optimal operating conditions of a device as a spin-photon interface. In the last section, we introduce long-term photonic correlation measurements through which we access the dynamic regime of the quantum dot charge and spin states.

The general idea behind each type of measurement is described, leaving the complete theoretical analysis for chapter 3 and the in-depth experimental exploration of two specific devices for chapters 4 and 5, in which they will be characterized as spin-photon interfaces by studying the spin-induced polarization rotation in the continuous and dynamic regimes. The optical characterization experiments presented here were conducted on the *positively charged device* by P. Hilaire and myself. The deterministic fabrication of the quantum dot-cavity devices coupling a trion transition to a micropillar was published in [148] and the results concerning the long-term photonic correlations from subsection 2.4.3 are the object of a publication in preparation.

2.1 Design and properties of the samples

Two different designs of structures coupling a quantum dot to a micropillar cavity are analyzed throughout this work. They are both tailored to operate as spin-photon interfaces, one with the spin of a hole in a positively charged quantum dot and the other with the spin of an electron in a negatively charged quantum dot. These designs inherit the technological knowledge developed by the team of P. Senellart from one generation of samples to the next. The first major step of the fabrication is the epitaxy of the planar heterostructure, which considerably determines the parameters of the optical cavity and how the charge carriers distribute in the structure. We start by presenting the heterostructures of the *positively charged device* and the *negatively charged device* and explaining the principle of the confinement of light in the cavity and of charges in the quantum dot. Then, the modification of the light-matter interaction by an external magnetic field is analyzed, with the aim of identifying the optical transition of the single hole or electron charge state. Subsequently, the in-situ lithography technique [23] produces a micropillar cavity centered on the quantum dot and spectrally tuned to the appropriate optical transition. The additional parameter that is the external bias applied to the structure is discussed as it is the final piece to achieve the fine-tuning of the quantum dot transition with the energy of the cavity mode.

2.1.1 Design of the planar heterostructures

General concepts

In order to fabricate a device comprising a quantum dot coupled to a micropillar cavity, the planar heterostructure is first epitaxially grown (see subsection 1.1.1 and 1.3.2): layers of alternating AlAs/GaAs make up the two distributed Bragg reflectors of a Fabry-Pérot cavity between which a layer of quantum dots is sandwiched. The planar structure sets the fundamental properties of the sample through the different optical indices, energy gaps and dopings of the constitutive layers. Several parameters need to be carefully adjusted to get the desired outcome:

- The number of Bragg mirror pairs of the top and bottom sides of the cavity, which sets the cavity width κ and the top mirror output coupling η_{top}.
- The doping of the layers, which allows an external bias to be applied to the structure [140]. It defines the Fermi level and, if the latter is carefully adjusted, the possibility to electrically inject carriers in the quantum dot. The optical losses caused by the additional free carriers come into play if regions where the optical mode is intense are doped[1] (especially for the p-doped layers [149]).
- The possibility to increase the tunneling time out of the quantum dot for a specific type of carrier, with a barrier in the vicinity of the quantum dot layer [46].

Negatively charged device

The high value of η_{top}, required for an ideal spin-photon interface, is obtained through the asymmetric design of the cavity to favor the collection of intracavity photons from the top mirror, as shown in Fig. 2.1a which represents the heterostructure of the *negatively charged device*.

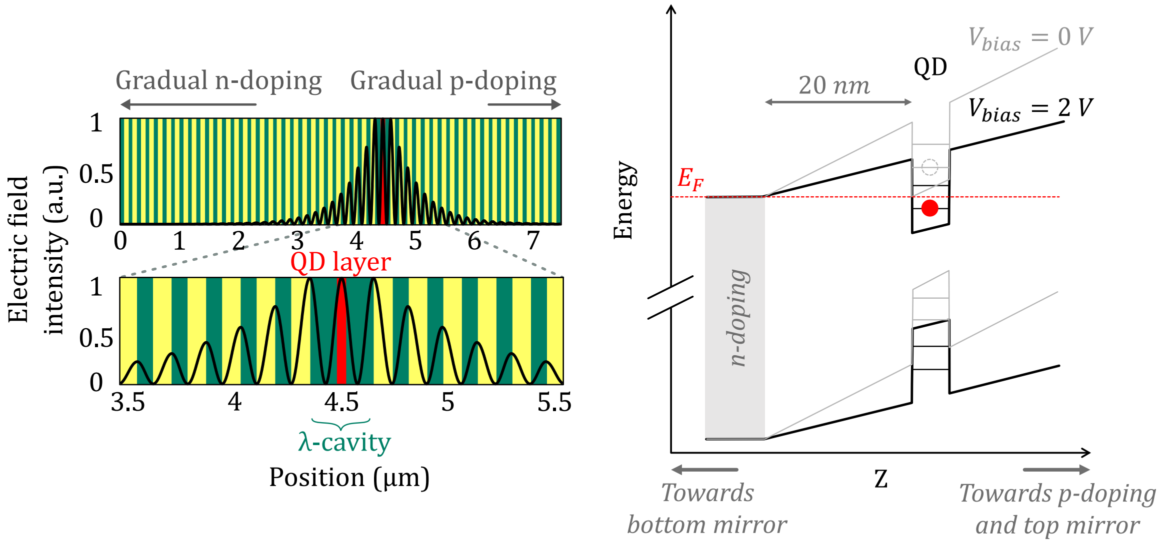

(a) (b)

FIGURE 2.1: **(a)** Heterostructure of the *negatively charged device* with the simulation of the electric field intensity inside the microcavity. A gradual n-doping from the λ-cavity to the bottom side tilts the bands to lower energies whereas the analogous gradual p-doping on the top side tilts the bands to high energies. The QD layer is drawn in red (not to scale). **(b)** Corresponding energy band structure in the vicinity of the quantum dot layer. The proximity of the quantum dot layer to the n-doped area allows an electron to be electrically injected in the quantum dot when an external voltage brings the first conduction-band level of the quantum dot below the Fermi energy E_F.

---

[1] Additional insights are given in [47], especially on the influence of the p-doping on the rest of the epitaxy process, and why it is suitable to place it on the top of the structure and not on the bottom.

The bottom side of the λ-cavity contains 30 mirror pairs, and the top side, 20 (simulations predict $\eta_{top} \simeq 87\,\%$ for a lossless device where $\kappa_{loss} = 0\,\mu\text{eV}$). The simulation of the electromagnetic field inside the cavity shows that it is maximal on the quantum dot layer to maximize the light-matter interaction, extremely weak on the bottom to minimize the losses through the substrate and not too weak on the top to be able to extract photons efficiently.

The energy band structure in the vicinity of the quantum dot layer is sketched in Fig. 2.1b: the sample is designed with an n-doped section so that the Fermi energy E_F is close to the first conduction-band level of the quantum dot and, in such a configuration, an external bias V_{bias} can tilt the bands enough to push this level below E_F, thereby injecting an electron. The electrical control provides access to a wide range of charge states [20, 43] and additionally reduces charge noise. It also allows the tuning of the quantum dot energy by Stark shift [140, 150].

Having a doped area this close to the quantum dot (i.e., to the InAs wetting layer) implies that the optical mode is still intense at this location. In the case of a n-doping, this leads to a moderate absorption, slightly increasing κ_{loss} and decreasing η_{top}.

Positively charged device

The heterostructure of the *positively charged device* is shown in Fig. 2.2a:

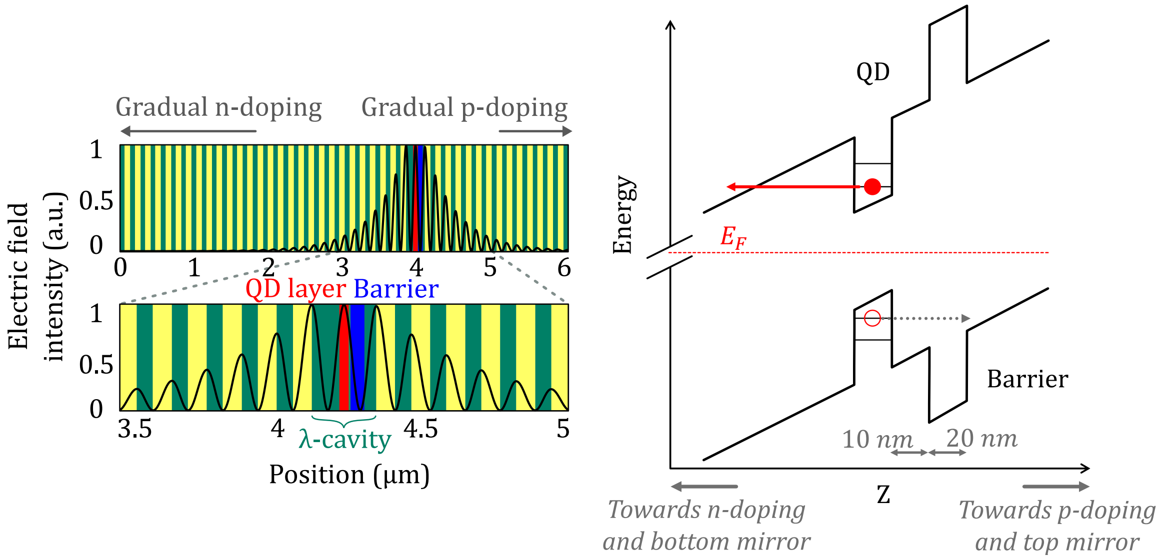

(a) (b)

FIGURE 2.2: **(a)** Heterostructure of the *positively charged device* with the simulation of the electric field intensity inside the microcavity. The QD and barrier layers are drawn in red and blue (not to scale). **(b)** Corresponding energy band structure. The doping is placed far away from the quantum dot layer to avoid optical absorption, which brings the Fermi energy too far away from the quantum dot conduction and valence levels to enable electrical injection. However, the optical injection of the positive charge carriers is facilitated by the presence of a trapping barrier in the vicinity of the quantum dot layer. When an electron-hole pair is optically created in the quantum dot, the electrons can tunnel out whereas the trapping barrier prevents the holes from doing so.

It differs from the previous one in several ways: first, it is adapted for a higher η_{top} with 28 mirror pairs on the bottom and 14 on the top of the λ-cavity (simulations predict $\eta_{top} \simeq 95\,\%$ for a lossless device), second, it should be able to hold positively charged quantum dot states. However, a hole cannot be electrically injected, because the presence of a p-doped layer in the λ-cavity would cause detrimental optical losses. Both the p and n-dopings are therefore placed far away from the quantum dot layer (in the Bragg mirrors). The resulting energy band structure, sketched in Fig. 2.2b, exhibits a Fermi level mid-gap, far from the quantum dot conduction and valence levels. However, electron-hole pairs can be injected optically and a trapping barrier, positioned 10 nm above the quantum dot layer, ensures that electrons can tunnel out rapidly (typically in 10-100 ns) while holes are trapped for a longer time ($\simeq 100\,\mu$s).

2.1.2 Identification of a trion transition by in-plane magnetic field spectroscopy

A fine-tuning between the energy of the trion transition and that of the optical mode of the cavity is required for an optimal spin-photon interaction. To that end, we begin by identifying the energies of the optical quantum dot transitions with their respective charge states.

In order to analyze the charge states of the quantum dot, we experimentally measure its photoluminescence spectrum while scanning the intensity of an in-plane (transverse) magnetic field. The experimental setup is described in Fig. 2.3a: the excitation is a non-resonant (NR) 850 nm laser, injected into the micropillar through a fibered input. Light is absorbed to create electron-hole pairs that recombine by multiple quantum dot transitions. The excitation power is kept reasonably low (around 1 μW on the sample) to avoid the accumulation of carriers in the quantum dot before they can recombine, which would lead to the manifestation of unwanted lines in the resulting spectra. The sample stands in a liquid helium cryostat where an in-plane magnetic field is applied. The PL signal is sent to the collection path through a 90:10 beam splitter (BS) (a low-pass spectral filter eliminates the reflected laser to keep only the PL signal). Finally, a half-waveplate (HWP) and a linear polarizer (LP) can be added before the collection to distinguish polarized lines. The output signal is analyzed with a spectrometer of resolution 25 pm/px.

The result is shown in Fig. 2.3b, for a planar sample, using the heterostructure comprising a tunnel barrier, in which holes can be optically injected (Fig. 2.2). The bottom panel comprises a stack of PL spectra as a function of the emission wavelength (horizontal axis) for different in-plane magnetic fields (vertical axis) from 0 T to 9 T, while collecting all polarizations (no polarization analysis on the output path yet). The lines exhibit Zeeman splitting on top of a diamagnetic shift of approximately –3.3 pm/T^2. The top panel shows the polarization substructure of the lines, which was not visible on the bottom panel: to do so, the in-plane magnetic field in set at 4 T and the reflected PL passes through the polarization analysis, while the HWP is rotated (top vertical axis) so as to resolve doublets of lines that are linearly polarized in two orthogonal directions and hardly split by one pixel of the spectrometer.

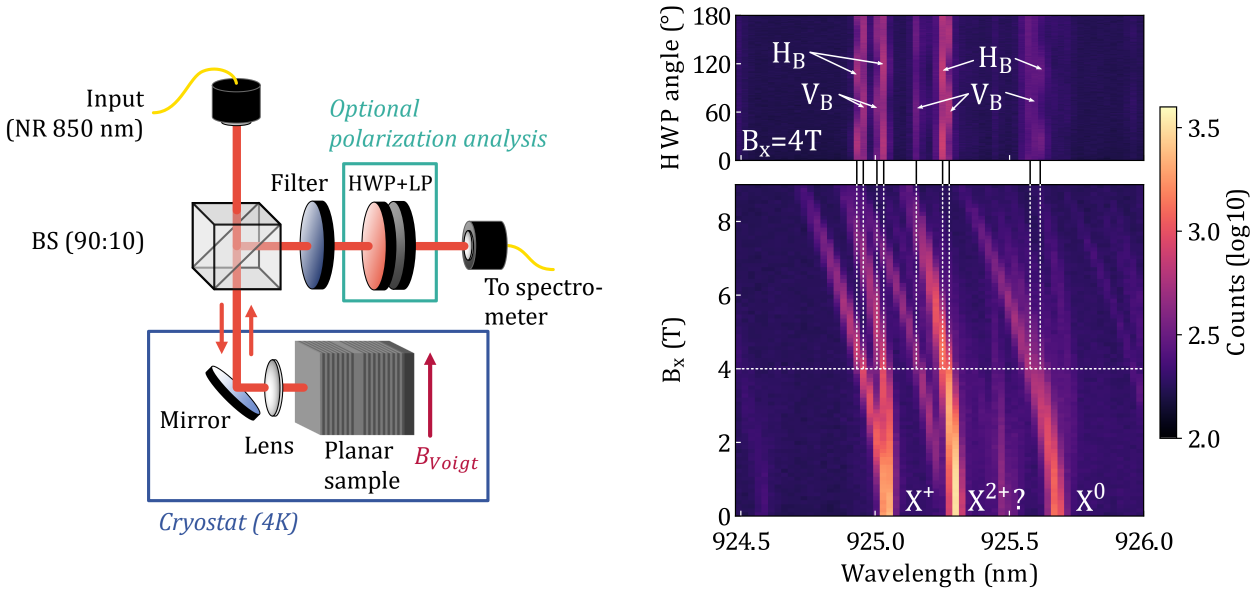

(a)

(b)

FIGURE 2.3: **(a)** Setup of the photoluminescence experiment. BS: beam splitter, HWP: half-waveplate, LP: linear polarizer. **(b)** Study of a typical quantum dot in the planar sample with the heterostructure designed to trap holes: PL spectra as a function of the intensity of the in-plane magnetic field while collecting all polarizations (bottom) and polarization analysis with HWP+LP at 4 T (top). Figure adapted from [148].

We can identify:

- A trion transition on the left side ($\lambda = 925.1\,\mathrm{nm}$): the magnetic scan shows a splitting into two lines that are in fact four linearly polarized transitions orthogonal two by two, as evidenced by the polarization analysis[1].
- An unknown transition in the middle ($\lambda = 925.3\,\mathrm{nm}$), splitting into two $\mathrm{H_B}$ and $\mathrm{V_B}$ lines and with a very close $\mathrm{V_B}$ line that appears around 1 T. The asymmetry in the brightness of the two lines is an indicator of a more complex charge state such as X^{2+} [43].
- A line that behaves as an excitonic transition on the right side ($\lambda = 925.7\,\mathrm{nm}$), comprising two close $\mathrm{H_B}$ and $\mathrm{V_B}$ lines.

Here, the trion transition is the only one that we need to identify beyond any doubt for the purpose of this manuscript.

---

[1] The magnetic scan can't prove if the state in presence is a positive or negative trion, but we are confident that it is positive based on the heterostructure design.

2.1.3 Fabrication of deterministically coupled quantum dot-micropillar devices

The fabrication of the sample relies on the in-situ lithography technique [23] to position a micropillar cavity around a quantum dot and tune the energy of its optical mode to that of a quantum dot transition. This step is carried out in a custom-designed Attocube Attodry 1000 cryostat that currently operates without a magnetic field, so no identification of the charge state is possible during the lithography.

Negatively charged device: in-situ lithography without quantum dot state identification

The lithography of the *negatively charged device* consisted in examining the PL signal from quantum dots without prior identification of the charge states. While scanning the lateral position of the planar sample, the emission lines of a single quantum dot are isolated, and one of the transitions is chosen randomly. The micropillar is then designed around that specific quantum dot and its energy tuned to the designated transition. The outcome was that most of the micropillars of this sample were tuned to a X^0 transition, and only a few of them to X^- (including the one studied in chapter 5). Nevertheless, multiple devices from this wafer achieved exceptional results with X^0 transitions, in terms of single photon emission [24], coherent control [25] and single photon non-linearity [26]. For the next generation sample, a novel idea was experimented in an effort to make the in-situ lithography process more deterministic.

Positively charged device: first attempt at charge-selective in-situ lithography

In order to deterministically engineer micropillars tuned to the X^+ transition, the in-plane magnetic field spectroscopy identification is required to identify the line beforehand: this step is achieved in a separate cryostat. Unfortunately, it is unfeasible to carry out the magnetic identification on a specific quantum dot and to locate it during the lithography step after changing cryostats. An alternative solution is to identify patterns of emission lines from quantum dots on the planar sample, that are recognizable without a magnetic field, such as the one of Fig. 2.3b. It was indeed possible to observe a recurring pattern of three bright lines across multiple quantum dots, separated as follows: $X^+ - 200\,\mathrm{pm} - X^{+2}(?) - 400\,\mathrm{pm} - X^0$. The in-situ lithography was carried out aiming at the X^+ line of the pattern, and was followed by the etching step and the electrical contacting of the sample. The etched micropillars were shown in Fig. 1.27.

The in-plane magnetic field spectroscopy experiment was performed once again on the finalized device in a separate cryostat (Fig. 2.4). This time, the polarization was analyzed at the same time as the magnetic field was scanning, therefore, a modulation between the linearly polarized lines is visible. We can identify the X^+ transition at 925.8 nm. It is centered on the cavity mode, which strongly enhances the emission in the 925.7 – 926 nm range. The X^0 transition is located at 926.5 nm. The Landé factors of the electron and hole can be calculated from the Zeeman splitting of the lines since $Z_{e,\perp} = |g_{e,\perp}\mu_B B_x|$ and $Z_{h,\perp} = |g_{h,\perp}\mu_B B_x|$. Additionally, the diamagnetic factor $\delta_{dia,\perp}$ characterizes the quadratic offset of the lines to high energy as the in-plane magnetic field increases. We estimate the following parameters, in agreement with the findings of other groups studying annealed InGaAs quantum dots [151–153]: $g_{h,\perp} = -0.2$; $g_{e,\perp} = -0.5$; $\delta_{dia,\perp} = 4.8\,\mu\mathrm{eV/T}^2$.

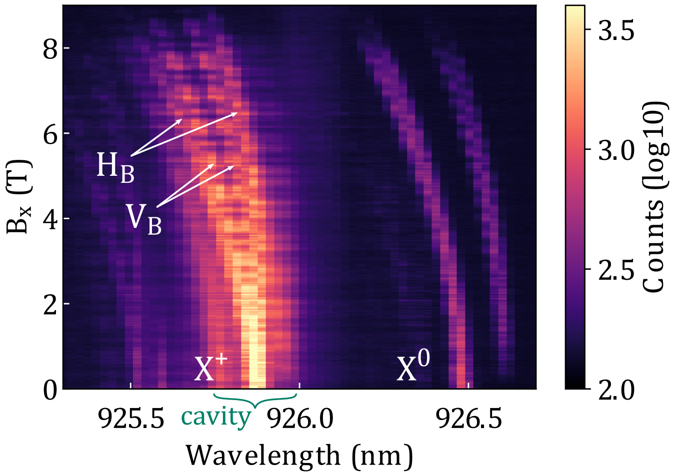

FIGURE 2.4: Photoluminescence spectra of a quantum dot in a micropillar (*positively charged device*) as a function of the intensity of the in-plane magnetic field. The presence of the cavity enhances the emission around 925.8 nm. Here, the polarization analysis is carried out by rotating the collection HWP before a linear polarizer as the magnetic field increases, so the four lines of the X^+ transition are already evidenced. The X^0 transition is also identifiable. Figure adapted from [148].

This novel technique was applied successfully for the *positively charged device*, and for other devices from the same wafer prepared with the same technique, which were involved in various publications [69, 141, 142, 148, 154]. Further improvements of the technique point to a live identification of the transitions during the lithography step without the need for an external magnetic field: either by analyzing the voltage dependence of the transitions (requiring the implementation of the electrical contact beforehand), or by exploring the response to an LA-phonon-mediated excitation [69], both of which show charge-selective behavior.

Next, we delve into the main experimental techniques which made the results of the next chapters possible.

2.2 Coherent laser spectroscopy of quantum dot-cavity devices

The coherent laser spectroscopy is a fundamental tool that we employ in a wide range of characterization experiments, from the analysis of the cavity modes presented in this section, to the spin-induced polarization rotation, explored in the next chapters. The principle is that a laser of varying wavelength probes the reflectivity of the sample using various injection and collection polarizations. The experimental setup is first presented, followed by the reflectivity of the two eigenmodes of the bare cavity. Then, a complete characterization of the reflected polarization in the Poincaré sphere with a tomography technique gives additional insights.

2.2.1 Polarization-resolved reflectivity measurements

The complete characterization of the effect of the device on the input polarization requires a versatile setup, able to inject a given polarization in the micropillar and to collect the reflected intensity in the six polarizations HVDARL, to reconstruct the state in the Poincaré sphere. The input polarization is a pure state $|\Psi_{in}\rangle$ associated to a polarization density matrix $\boldsymbol{\rho}_{in}^{(pol)}$ and a Stokes vector $\boldsymbol{S}_{in}$, defined by:

$$\boldsymbol{\rho}_{in}^{(pol)} = |\Psi_{in}\rangle\langle\Psi_{in}| \qquad \boldsymbol{S}_{in} = \begin{pmatrix} s_{HV}(\Psi_{in}) \\ s_{DA}(\Psi_{in}) \\ s_{RL}(\Psi_{in}) \end{pmatrix} \tag{2.1}$$

The reflected polarization (output state) is denoted with the density matrix $\boldsymbol{\rho}_{out}^{(pol)}$ associated to the Stokes vector $\boldsymbol{S}_{out}$ which may or may not be a pure state.

Optical setup

Let us describe the optical setup presented in Fig. 2.5 from the input fiber to the sample, and back from the sample to the collection:

- The input beam comes from an optical fiber of numerical aperture $NA = 0.13$, from which it is collimated by an aspheric lens ($f = 11\,\mathrm{mm}$, $NA = 0.25$). The NA of the lens is higher than the one of the fiber so that the beam does not cover the whole surface of the lens and goes through it with minimal aberrations. The beam then propagates in freespace (in the horizontal plane) with a waist of typically ⌀1.9 mm. This laser is either pulsed to facilitate alignment or continuous wave (CW) with a scanning wavelength for reflectivity measurements.

- The linear polarizer (LP) sets the polarization of the excitation beam to s (using the standard (s, p) notations for the polarizations respectively parallel and orthogonal to the plane of incidence on the optics). 10 % of the input light is transmitted by the beam splitter (BS).

- The beam size is then adjusted with a telescope ($f_1 = 125\,\mathrm{mm}$, $f_2 = -100\,\mathrm{mm}$) so that it matches the mode of the micropillar (⌀ 2.7 µm, $NA \simeq 0.3$) after passing through the focusing lens right above the sample ($f = 3.1\,\mathrm{mm}$, $NA = 0.7$).

- The excitation polarization is set with the quarter- and half-waveplates QWP1, HWP1 to the state $|\Psi_{in}\rangle$. In the following, it will be linearly polarized along a cavity eigenpolarization H or V to study the spin-induced polarization rotation, or along D or A to study the cavity anisotropy.

- Between these waveplates and the focusing lens, a mirror not shown on the figure makes the beam propagate vertically inside the cryostat. There, the sample lies in an enclosure containing a contact gas (12 mbar helium), which is itself immersed in liquid helium. The sample is mounted on piezoelectric nanopositioners for a fine alignment with the input beam.

- After the interaction with the sample, the beam is reflected with the polarization state $\boldsymbol{\rho}_{out}^{(pol)}$. 90 % of the output light is reflected to the collection path by the BS and then goes through a polarization analysis setup: there, the carefully calibrated waveplates QWP2 and HWP2 transpose the three couples of complementary polarizations HV,DA,RL to the (s, p) directions on which the Wollaston prism projects. The output polarization state is reconstructed in the Poincaré sphere in three sequential steps, one for each basis.
- The intensities in the s and p polarizations after the Wollaston are measured, either by freespace avalanche photodiodes (APDs) or fibered detectors such as single photon APDs (SPAPD, efficiency $\eta_{det} \sim 30\,\%$) and superconducting nanowire single photon detectors (SNSPD, $\eta_{det} \sim 90\,\%$). The freespace APDs have a lower efficiency and give a voltage proportional to the photon flux whereas the fibered detectors give a TTL signal each time they detect a single photon. In the case of the freespace APDs, the input laser can be modulated in intensity and the output voltage treated by a lock-in amplifier to reduce noise.

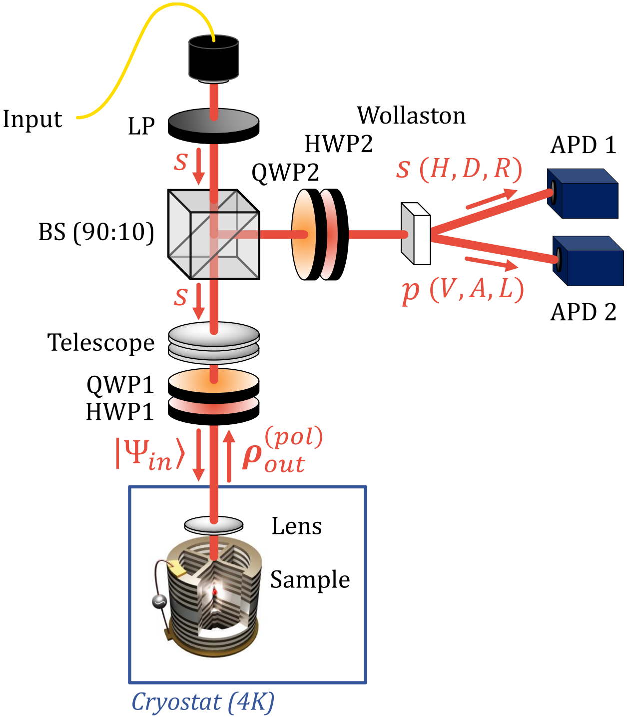

FIGURE 2.5: Setup for the polarization-resolved reflectivity measurements. LP: linear polarizer, BS: beam splitter, QWP: quarter-waveplate, HWP: half-waveplate, APD: avalanche photodiode. The beam comes from the input fiber, its polarization is set to s by LP and then to $|\Psi_{in}\rangle$ by QWP1 and HWP1. The size of the beam is adjusted by the telescope. Upon reflection from the sample, the polarization state is written $\boldsymbol{\rho}_{out}^{(pol)}$: the beam goes through the polarization analysis setup, where QWP2, HWP2 and the Wollaston prism split it in any two polarization bases (HV,DA,RL). The intensity in each polarization is then measured by photodiodes to reconstruct the Stokes vector of the output polarization in the Poincaré sphere, $\boldsymbol{S}_{out}$, or equivalently its density matrix $\boldsymbol{\rho}_{out}^{(pol)}$.

Reflectivity measurement of the cavity eigenmodes

As mentioned in subsection 1.3.2, the anisotropic optical confinement in the micropillar creates two cavity eigenmodes at different energies, for two complementary linear polarizations written H_{cav} and V_{cav} (simply labeled H and V in this manuscript) [138]. Such an effect is better known as birefringence and a complete characterization will in turn provide information to isolate the Faraday rotation induced by a quantum dot when it later comes into play.

We probe the reflectivity of the cavity eigenmodes by using the setup described in Fig. 2.5, exciting along the cavity eigenpolarizations and each time collecting in the same polarization (*parallel* to the excitation). The protocol to prepare the excitation and collection configuration consists in the following steps:

- Starting from the setup of Fig. 2.5, sending a broadband input source on the sample (typically a 3 ps Ti:sapph pulsed laser) and collecting light in one of the outputs after the Wollaston prism.
- Exploring configurations of angles for HWP1, QWP1, HWP2 and QWP2 until the collected light has a minimum of intensity for the whole spectrum of the input source. This indicates that the excitation is aligned to a cavity axis (say H for the example): the reflected light is unaltered (also polarized in H) and the collection is *cross-polarized* (observing in V).
- A rotation of $45°$ of HWP2 aligns the collection to H, the same polarization as the input.
- The input is replaced with a continuous wave laser of scanning wavelength to proceed to the measurement of the reflectivity spectrum and the protocol is repeated to characterize the reflectivity of the V mode.

The experimental reflectivity of the two cavity modes is plotted in Fig. 2.6 and the data are fitted by the semi-classical formula of the reflection coefficient [143], adapted from Eq. 1.28 with specific parameters for each cavity mode:

$$\begin{aligned} r_{c,H}(\omega) &= \frac{E_{H,out}(\omega)}{E_{H,in}(\omega)} = 1 - 2\eta_{top,H}\left(1 - 2i\frac{\omega-\omega_{c,H}}{\kappa_H}\right)^{-1} \\ r_{c,V}(\omega) &= \frac{E_{V,out}(\omega)}{E_{V,in}(\omega)} = 1 - 2\eta_{top,V}\left(1 - 2i\frac{\omega-\omega_{c,V}}{\kappa_V}\right)^{-1} \end{aligned} \tag{2.2}$$

where we introduced individual values of ω_c, κ and η_{top} for each cavity mode. The abscissa of the plot is centered on $\omega_c = \frac{\omega_{c,H}+\omega_{c,V}}{2}$ as will be the case for the following figures of this section. In addition, the APDs measure the intensity of the electric field in a given polarization, so for each cavity eigenpolarization, we plot the reflectivity given by:

$$\frac{I_{out}}{I_{in}} = \left|\frac{E_{out}}{E_{in}}\right|^2 = R_c(\omega) = |r_c(\omega)|^2 \tag{2.3}$$

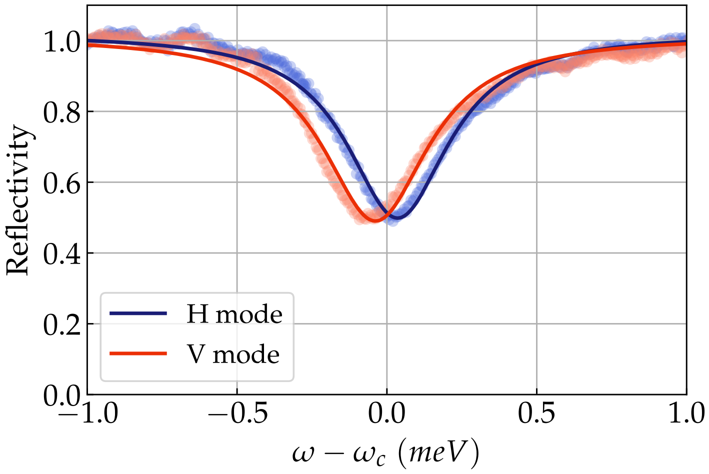

FIGURE 2.6: Reflectivity of a quantum dot-micropillar device of the *positively charged device* while exciting the eigenpolarizations of the cavity, H and V.

The fitting parameters converge to:

$$\begin{cases} \eta_{top,H} = 0.85 \pm 0.1 & \kappa_H = (416 \pm 20)\ \mu\text{eV} \\ \eta_{top,V} = 0.85 \pm 0.1 & \kappa_V = (432 \pm 20)\ \mu\text{eV} \\ \omega_{c,H} - \omega_{c,V} = (74 \pm 10)\ \mu\text{eV} \end{cases} \tag{2.4}$$

This set of parameters will be a starting point, first to model the cavity-induced birefringence in the next paragraph, and to fit the more complex behavior of the system when a quantum dot enters into play in chapter 4.

Here, we implicitly assumed a perfect coupling of the input beam to the micropillar. As was shown in [133], a proper fit of the total reflectivities in H and V exists for multiple values of the input coupling, providing η_{top} is adjusted. We discuss in the next paragraph how a tomography experiment can give definitive and more precise information on the cavity parameters and the quality of the alignment.

2.2.2 Reconstructing the complete reflected polarization state through polarization tomography

Outline of the experiment

The polarization tomography technique makes use of the calibrated configurations of HWP2 and QWP2 in the setup from Fig. 2.5 to measure the reflected intensities in (HV, DA, RL), with which the Stokes parameters are reconstructed (see Eq. 1.26). The result after a wavelength scan of the input laser consists in a succession of Stokes vectors plotted in the Poincaré sphere.

In this experiment, we study the wavelength dependence of the reflected light with an input polarized along D. In fact, the effect of the cavity birefringence is the strongest on the D and A inputs as they fall in the middle of the two cavity eigenpolarizations H and V. In the ideal situation where $\eta_{in} = 1$, the input and output polarization states are given by:

$$\begin{cases} |\Psi_{in}\rangle = |D\rangle = \dfrac{|H\rangle + |V\rangle}{\sqrt{2}} \\ |\Psi_{out}\rangle = \dfrac{r_{c,H}\,|H\rangle + r_{c,V}\,|V\rangle}{\sqrt{|r_{c,H}|^2 + |r_{c,V}|^2}} \neq |D\rangle \end{cases} \tag{2.5}$$

The reflected polarization state associates the reflection coefficients $r_{c,H}$ and $r_{c,V}$ to their respective components in $|\Psi_{in}\rangle$, reasoning analogously to the Faraday rotation from subsection 1.3.4. In the specific case where $\eta_{in} = 1$, the output polarization state is pure, i.e., $\boldsymbol{\rho}_{out}^{(pol)} = |\Psi_{out}\rangle\langle\Psi_{out}|$. However, this is generally not the case when performing free-space experiments where the collected light is a superposition of light coupled to the cavity mode (with the efficiency η_{in}) and light that is not coupled to this mode (efficiency $1 - \eta_{in}$), which is reflected with no polarization change. The influence of η_{in} was studied previously in the C2N by *Hilaire et al. (2018)* [133]: it was shown that $\eta_{in} < 1$ results in a depolarization of $\boldsymbol{\rho}_{out}^{(pol)}$, which cannot be unambiguously characterized by the reflectivities in H and V alone. Indeed, multiple combinations of η_{top} and η_{in} give the same reflectivities for a given polarization. Only with a polarization tomography of the reflected light can the actual combination unequivocally be determined.

The experimental Stokes parameters and tomography data are presented in Figs. 2.7 and 2.8 as a function of the laser-cavity detuning[1]. Fits are superimposed, first with a perfect input coupling and then with an imperfect one, explained in the next two paragraphs. The polarization state is rotated from $|D\rangle$ towards $|L\rangle$ when the laser comes into resonance with the central cavity energy whereas the input polarization is unchanged for high detunings. Additionally, a small depolarization is visible, especially in the Stokes parameters.

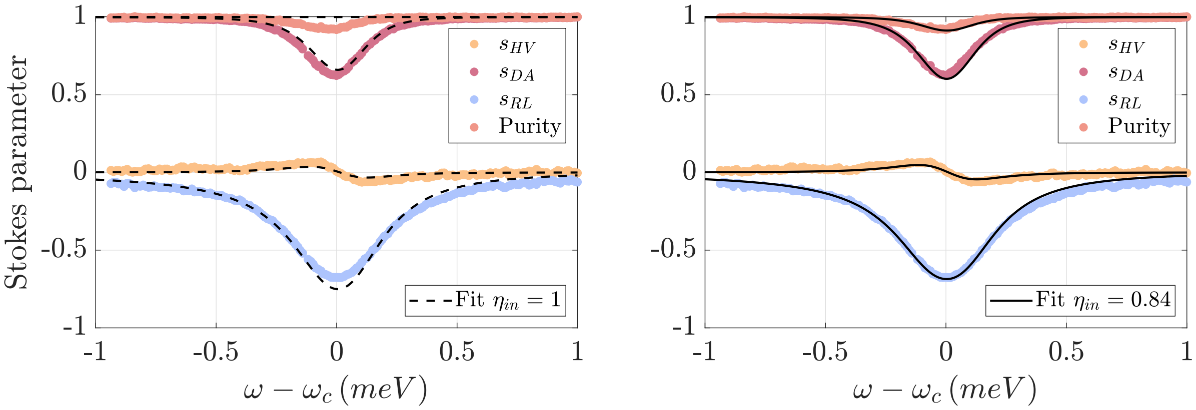

(a) (b)

FIGURE 2.7: Stokes parameters of the light reflected by the bare cavity (freespace collection) with an input polarization $|\Psi_{in}\rangle = |D\rangle$. Experimental points superimposed with fits in black lines. **(a)** Forcing $\eta_{in} = 1$, the purity is always unity (fit in dashed lines). **(b)** Allowing an imperfect input coupling, the fit in solid lines matches the reduced purity of the experimental points.

---

[1] The experimental data shown here were measured in the set of polarizations $[HVDARL]_{coll}$, specific to the collection. A rotation was applied to bring them back to the cavity set of polarization $[HVDARL]_{cav}$, thereby compensating any ellipticity on the collection paths. To do so, the out-of-resonance points were brought to $|D\rangle$ and the orientation of the loop in the Poincaré sphere was aligned with the simulated one.

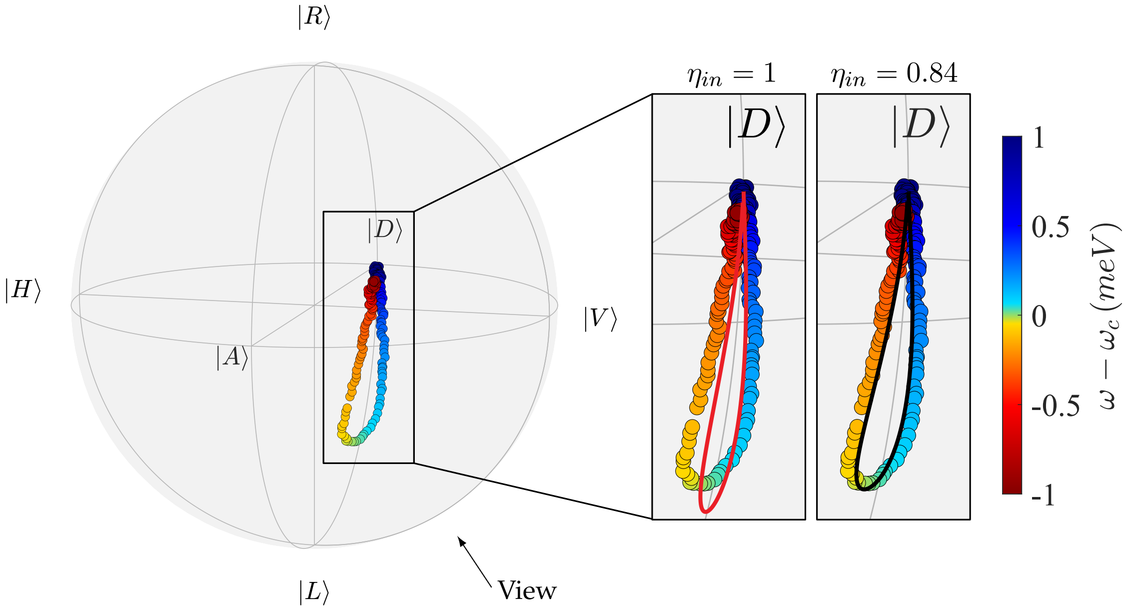

FIGURE 2.8: Polarization tomography based on the Stokes parameters from Fig. 2.8. The whole sphere contains only experimental points and the zoomed windows display the fitting results on top, first with a perfect input coupling (red line), then with an imperfect one (black line). The sphere is viewed from below the (HDVA) plane, placing $|D\rangle$ in the foreground.

Modeling the ideal case $\eta_{in} = 1$

Let us first assume a perfect injection ($\eta_{in} = 1$). In an analogous way as in Eq. 1.22, we can write the Stokes parameters of the reflected polarization state as expressions of the input electric fields and reflection coefficients in the (H,V) basis:

$$\begin{aligned} s_{HV,out} &= \left(|r_H E_{in,H}|^2 - |r_V E_{in,V}|^2\right)\Big/ I \\ s_{DA,out} &= 2\ \mathrm{Re}\left\{r_H E_{in,H} \cdot \overline{r_V E_{in,V}}\right\}/I \\ s_{RL,out} &= 2\ \mathrm{Im}\left\{r_H E_{in,H} \cdot \overline{r_V E_{in,V}}\right\}/I \end{aligned} \tag{2.6}$$

We can arbitrarily fix $I = 1$ and then take $E_{in,H} = E_{in,V} = 1/\sqrt{2}$ to account for the D-polarized input. The fit is computed with the expressions of the reflectivity coefficients from Eq. 2.2 and its outcome is represented by a red line along with the experimental data in the Poincaré sphere in Fig. 2.8 and the associated Stokes parameters are given in Fig. 2.7a (the purity stays at unity). The fitting parameters have been constrained to keep the same values of $\kappa_{H/V}$ and $\omega_{c,H} - \omega_{c,V}$ as in the fitting of the reflectivities of the two cavity modes (see Eq. 2.4). The results are the same as the previous fit, except for the top mirror output coupling of which we get a more precise value: $\eta_{top,H} = \eta_{top,V} = 0.94 \pm 0.02$. The quality of the fit is already high, but it is hindered by the constraint to stay on the surface of the Poincaré sphere ($\eta_{in} = 1$). In such a case, the computed polarization state is pure: $\boldsymbol{\rho}_{out}^{(pol)} = |\Psi_{out}\rangle\langle\Psi_{out}|$.

Modeling the non-ideal case $\eta_{in} < 1$

We can now refine the model by considering an imperfect input coupling ($\eta_{in} < 1$) that should reproduce the depolarization effect. The consequence is that starting from a beam of intensity I_{in}, a portion $\eta_{in} I_{in}$ enters the cavity and undergoes the cavity reflectivity as studied previously, and another portion $(1 - \eta_{in}) I_{in}$ is not coupled in the cavity because its spatial mode has no overlap with the cavity mode: it is therefore reflected in the input polarization. The absence of spatial mode overlap between the coupled and uncoupled light implies that they will not interfere upon reflection[1]. In terms of Stokes parameters of the reflected polarization, this translates as incoherently summing a coupled part (labeled c) and an uncoupled part (labeled u). The Stokes coefficients of the reflected coupled light are given by the expressions of Eq. 2.6 and those of the uncoupled light are simply the coordinates of $|D\rangle$ ($s_{HV,u} = 0$, $s_{DA,u} = 1$, $s_{RL,u} = 0$). According to the calculations from [133], the measured Stokes parameters $s_{XY,refl}$ for XY ∈ [HV, DA, RL] result from the sum of the coupled and uncoupled contributions, with respective weights p and $1 - p$ such that:

$$\begin{gathered} p = \frac{\eta_{in} \times R_m}{(1 - \eta_{in}) + \eta_{in} \times R_m} \\ s_{XY,refl} = p \times s_{XY,c} + (1 - p) \times s_{XY,u} \end{gathered} \tag{2.7}$$

where we introduced the total mode reflectivity R_m, given for a D excitation by the expression $R_m(\omega) = (R_H(\omega) + R_V(\omega))/2$. The final result is represented by black lines on the tomography and Stokes parameters figures and the fitting parameters are given below, were the same constraints as previously were imposed ($\kappa_{H/V}$ and $\omega_{c,H} - \omega_{c,V}$ fixed to match Eq. 2.4). In that case, the fit is closer to the experimental data as the imperfect input coupling introduces depolarization. This set of parameters will be the starting point to model the behavior of the *positively charged device* in chapter 4.

$$\begin{cases} \eta_{in} = 0.84 \pm 0.02 \\ \eta_{top,H} = 0.92 \pm 0.02 \quad \kappa_H = (416 \pm 20)\,\mu\text{eV} \\ \eta_{top,V} = 0.92 \pm 0.02 \quad \kappa_V = (432 \pm 20)\,\mu\text{eV} \\ \omega_{c,H} - \omega_{c,V} = (74 \pm 10)\,\mu\text{eV} \end{cases} \tag{2.8}$$

2.2.3 Complementary considerations on the cavity birefringence

Cavity-induced rotation for different input polarizations

The analytical model lets us simulate the polarization state of the reflected photons for different input polarizations, as seen in Fig. 2.9. On the left sphere, we consider the input polarizations D,L,A and R and the color code corresponds to the wavelength scan: the trajectories present a characteristic "droplet" shape, with the output polarization being identical to the

---

[1] This holds for free-space collection detectors as they collect both coupled and uncoupled light, as opposed to a single-mode fiber that performs a spatial filtering

input one when the laser is far detuned, and rotated to the curved side of the droplet on resonance. The right panel shows similar scans, for linear input polarizations from H to V: the cavity rotation is maximal for D and is null for H and V (if $|\Psi_{in}\rangle = |H\rangle$, then $|\Psi_{out}\rangle = |H\rangle$, and similarly for $|V\rangle$).

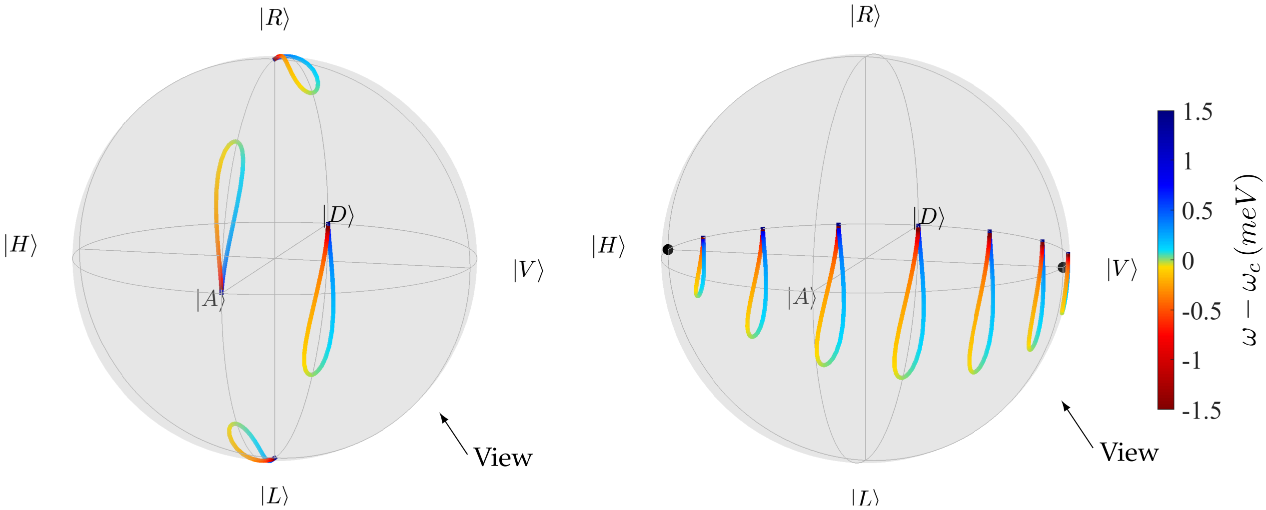

FIGURE 2.9: Examples of trajectories of the polarization state while scanning the wavelength of the input laser, for different input polarizations. The view angle corresponds to $|D\rangle$ in the foreground. The black points on H and V show that the cavity has no effect on these polarizations.

Case of a fibered collection

In realistic experiments such as those presented in chapters 4 and 5, the output light is sent to a fibered single photon detector, which induces a spatial selection that can be modeled by introducing the overlap between the input mode and the collection mode, η_{ic}, and the overlap between the cavity mode m and the collection mode, η_{mc}. It can be demonstrated [155] that the cavity reflectivity coefficient for mode m, written $r_{c,m}$ in Eq. 2.2 becomes:

$$r_{fibered,m} = \sqrt{\eta_{ic}} \cdot r_m^{(eff)} \tag{2.9}$$

where $r_m^{(eff)}$ is an effective reflectivity, with formulae analogous to $r_{c,m}$ modified with an effective output coupling: $\eta_{top}^{(eff)} = \eta_{top}\sqrt{\frac{\eta_{in}\eta_{mc}}{\eta_{ic}}}$. This factor depends on the optical alignment, and becomes close to η_{top} when a good alignment is obtained.

The choice made for the data fitting in the next chapters is to hypothesize a perfect input coupling and to allow a small offset of $\eta_{top}^{(eff)}$ compared to the fitted value with a freespace reflectivity (here, $\eta_{top} = 0.92$ for the *positively charged device*).

2.2.4 Alignment technique using the cavity-induced polarization rotation

Knowing that the cavity rotates in the Poincaré sphere the states that are different from its eigenpolarizations H and V, one can devise an alignment procedure based on the maximization of this "cavity-rotated light" in the collection arm. With that intent, we excite the device with a pulsed laser broader than the cavity width and observe the reflected light in different configurations. The resulting spectra are plotted as solid lines in Fig. 2.10 along with a Gaussian profile (dashed yellow line) representing the spectrum of the input laser of width 550 µeV. The two configurations of interest are the following:

- Exciting H and collecting V (red line): in this configuration, the polarization is left unchanged by the micropillar ($|\Psi_{out}\rangle = |\Psi_{in}\rangle = |H\rangle$), therefore, a collection arm polarizing along V maximally attenuates the collected light, as shown in the inset of the figure.
- Exciting D and collecting A (blue line): here, we collect only the contribution from the light rotated by the cavity, which is produced in a range of around 315 µeV in the present case (corroborating the width of s_{DA} in Fig. 2.7).

Once the cavity-rotated light is isolated, it can be used to match the collection mode of the setup to that of the micropillar by maximizing its contribution in the detected signal. That way, we can ensure that η_{in}, η_{ic} and η_{mc} are maximal. The typical value of the output coupling of the rotated light in the collection fiber is 65 %.

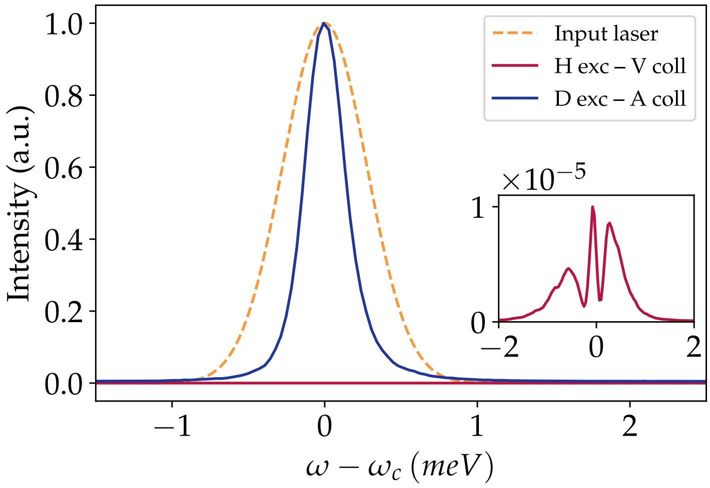

FIGURE 2.10: Spectral shape of the collected light after exciting H and collecting V (solid red line, also in the inset), or exciting D and collecting A (solid blue line). The shape of the input laser is plotted as a Gaussian spectrum of width 550 µeV in a dashed yellow line.

2.3 The quantum dot-cavity device as a single-photon source

In this section, we first explain how the single charge state is created in the quantum dot, and we then proceed to the characterization of the device as a single-photon source. As the charge creation in the *negatively charged device* is straightforward since it relies only on the external bias, we focus on the more complex optical carrier injection for the *positively charged device*.

Then, we characterize the single photon emission, which gives valuable information on the efficiency of the excitation scheme, on the quality of the filtering of the quantum dot-emitted photons in the collection, and on the quantum interaction leading to single photon emission. The figures of merit are the brightness of the source and the lifetime, the purity and the indistinguishability of the emitted photons.

2.3.1 Optical injection of a hole in the positively charged device

The design of the *positively charged device* implies an optical injection of the single hole charge state. This is done with a two-color excitation (see subsection 1.1.5), comprising a quasi-resonant laser to create the single hole charge and a resonant one to probe it. The hole injection scheme is detailed in Fig. 2.11. The considered levels and transition energies are highlighted on the left side of the figure, separating the case of a neutral quantum dot and that of a quantum dot with a single hole, which modifies the electromagnetic environment, and therefore the energy of the quantum dot levels. The excitation sequence is sketched on the right side and proceeds as follows:

- The quantum dot is initially in the neutral state and an electron-hole pair is pumped with the quasi-resonant laser at ω_{QR}.
- Then, the electron rapidly relaxes to the ground state of the valence band. At this point, either the electron-hole pair recombines, emitting a photon at ω_X and restarting the cycle, or the electron tunnels out while the hole is blocked by the barrier.
- After the electron tunnels out, the quantum dot is left with a single hole that can be addressed with a resonant laser at ω_{X^+}. Because the hole modifies the electromagnetic environment, the energy required to add an additional electron-hole pair quasi-resonantly is now $\omega_{QR,1h}$, which cannot be excited by the quasi-resonant laser as it is different from ω_{QR}.

Experimentally, we first explore the response of the trion emission with a scanning non-resonant laser: this is known as a photoluminescence excitation (PLE) experiment. The result gives clues on the energy-level structure of the quantum dots [62, 156, 157]. The PLE spectra are shown in Fig. 2.12 (left) for an excitation power of $P_{NR} = 15\,\mu\text{W}$. The emission of the trion transition is located around 925.9 nm: it shows a modest intensity for a non-resonant laser below 885 nm, that we identify as wetting layer excitation, and a few sharp resonances from 899 nm to 912 nm that can correspond to any quasi-resonant transitions.

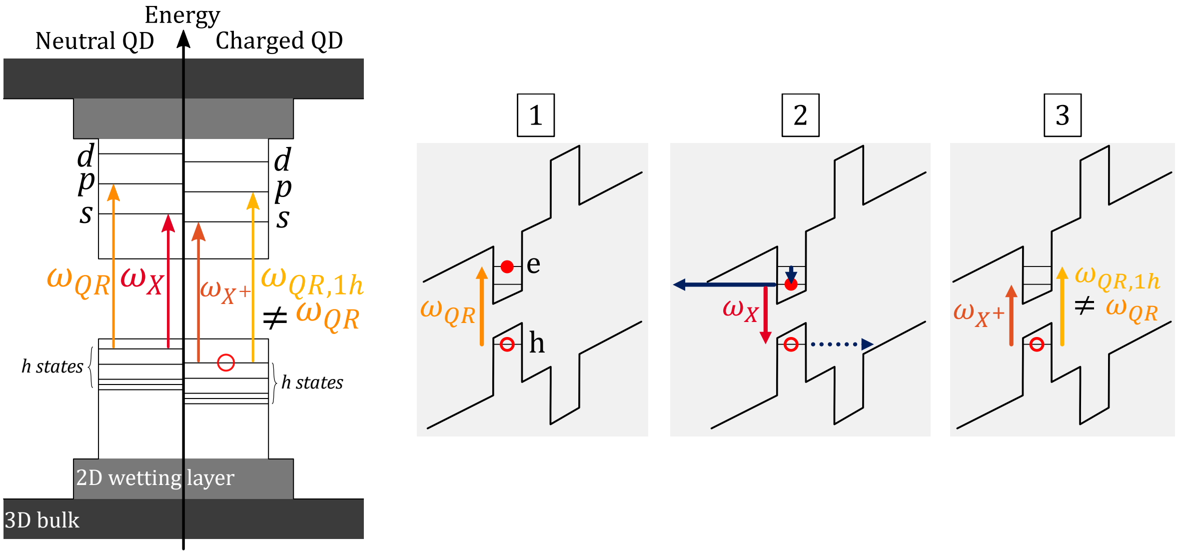

FIGURE 2.11: **(Left)** Schematic electronic structure of the quantum dot and its surroundings, with a separation between the case of a neutral quantum dot and that of a quantum dot charged with a single hole. **(Right)** Excitation sequence, with **(1)** the initial injection of an electron-hole pair by quasi-resonant excitation at ω_{QR}, **(2)** the relaxation of the electron and either recombination with the hole (bringing back the sequence to (1)) or tunneling out of the electron, leaving the quantum dot with a single hole **(3)**. The single hole is addressed with a second laser at ω_{X^+}, and the quasi-resonant laser doesn't create additional e-h pairs since $\omega_{QR,1h} \neq \omega_{QR}$. Figure adapted from [148].

In order to generate single photons from the trion transition, we add a 15 ps pulsed resonant excitation ($P_{NR} = 1\,\mathrm{nW}$) tuned to λ_{X^+} and restart the scan of λ_{NR} as shown on the right side of the figure, this time with a much weaker non-resonant excitation ($P_{NR} = 50\,\mathrm{nW}$) so as to observe only the resonance fluorescence emission and not the PL emission. The pattern of resonances is modified by the presence of the resonant excitation: short wavelengths of the non-resonant laser amplify the emission up to 893 nm and longer wavelengths give rise to multiple narrow resonances. Among all of these, the one for $\lambda_{NR} = 901\,\mathrm{nm}$ was the most promising (intense and narrow). This specific wavelength corresponds to ω_{QR} in Fig. 2.11. The energy difference with the s-shell transition is 35.8 meV, which is very close to the LO-phonon energy[1].

In the following, we explore the performance of such a device as a single-photon source. The excitation scheme will mostly be resonant s-shell excitation with a pulsed laser coupled to a CW non-resonant one. The specific 901 nm resonance that is discussed here will be explored in the long-delay correlation experiments of section 2.4.

---

[1] Depending on the electronic structure of our quantum dots, this resonance could also be a p-shell or d-shell transition.

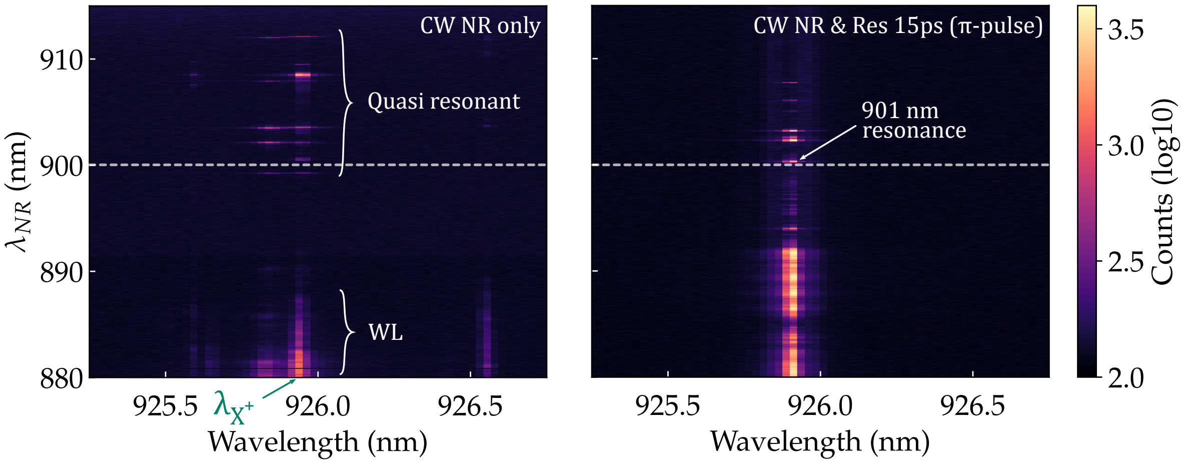

FIGURE 2.12: **(Left)** PLE spectra for a scanning non-resonant laser (P_{NR} $= 15\,\mu\mathrm{W}$). The line $\lambda_{NR} = 900\,\mathrm{nm}$ is highlighted for visualization. **(Right)** Resonance fluorescence spectra with a resonant 15 ps laser ($P_R = 1\,\mathrm{nW}$) coupled to a scanning non-resonant laser ($P_{NR} = 50\,\mathrm{nW}$).

2.3.2 Characterization techniques related to single-photon emission

We explore the experimental methods to quantify the quality of the single photons emitted by the quantum dot-micropillar cavity devices, taking the data measured on the *positively charged device* as an example. Optimizing the single photon operation helps to find the best excitation conditions which in turn leads to a high-quality spin-photon interface. The performance of the sources fabricated at the C2N laboratory was extensively studied by *Ollivier et al. (2020)* [154], especially the reproducibility of the characteristics from one device to the other. The results given in this section pertain to the *positively charged device*, which is studied as a spin-photon interface in chapter 4. Here, the device is addressed with a wetting layer (WL) two-color scheme including a 15 ps pulsed resonant laser ($P_R = 2\,\mathrm{nW}$, repetition rate $f_{rr} = 81\,\mathrm{MHz}$) with an additional CW non-resonant laser in the wetting layer ($\lambda_{NR} = 830\,\mathrm{nm},\ P_{NR} = 0.5\,\mathrm{nW}$); the excitation is polarized along the cavity axis H and the single photons are extracted in the cross-polarized collection.

Measuring the first lens brightness

The brightness of the source is defined as the probability that it emits a single photon when triggered by an excitation pulse. To calculate the first lens brightness, we compensate the detected photon count rate by the losses on the collection path, from the first lens after the micropillar to the single photon detector, and divide this number by the repetition rate of the pulsed excitation laser. By exciting the device with the WL two-color scheme, we obtain a single photon count of $CR = (1.6 \pm 0.2)\,\mathrm{MHz}$ after the collection fiber. To calculate the first lens brightness, we must correct by the detector efficiency $\eta_{det} = 30\,\%$ and the overall transmission of the collection path, evaluated at $T_{setup} = 35\,\%$:

$$B = \frac{CR}{f_{rr} \times T_{setup} \times \eta_{det}} = (19 \pm 2)\,\% \tag{2.10}$$

Measuring the trion lifetime

The temporal shape of the single photon wave packet allows us to infer the emission dynamics and to confirm which type of quantum dot transition the single photons originate from [154]. It is measured by timing the detection events of the single photons after each excitation pulse.

Here, we use SNSPD for the single-photon detection (unlike the other coincidence measurements of this section, which rely on SPAPDs): their very short time jitter minimizes the distortion of the measurement. The timing of the detection events is treated by a time-correlated single photon counting (TCSPC) module. The result for the emission of a X^+ transition is a fast increase and a slow decay as shown in Fig. 2.13. The total lifetime is $T_1 = 200\,\mathrm{ps}$, corresponding to a spectral width of $3.3\,\mu\mathrm{eV}$. It was computed by fitting the data with a Heaviside function modeling the trion decay, convolved with a Gaussian detector response of half width at half maximum (HWHM) 50 ps. We emphasize that the sharp increase of the trion emission comes from the fact that it can emit photons in the cross-polarization as soon as it is excited by the input pulse and the slow decay corresponds to the Purcell-enhanced emission and the spontaneous emission in the cross-polarization. The behavior of an exciton transition is very different as it shows a slow increase and a beating in the decay due to the fine structure splitting [154].

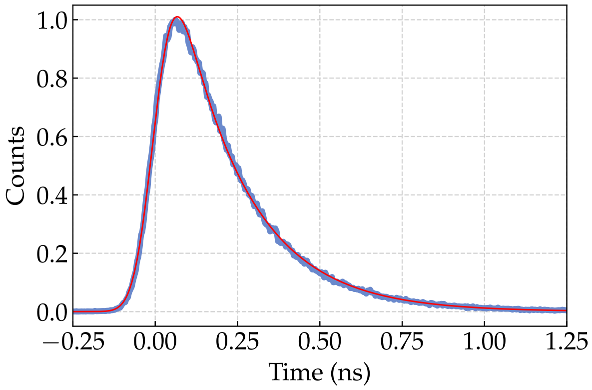

FIGURE 2.13: Lifetime of a trion of the *positively charged device* excited with the WL two-color scheme, measured with an SNSPD synchronized with the clock of the pulsed excitation. The fit comprises a mono-exponential of decay $T_1 = 200\,\mathrm{ps}$ convolved with a Gaussian detector response of HWHM 50 ps.

The lifetime is sensitive to the excitation scheme, as a non-radiative decay before the emission can strongly modify the temporal shape of the single photon emission [62]. It is also sensitive to the Purcell enhancement of the emission, which depends on the detuning of the quantum dot transition relative to the H and V modes of the cavity (see appendix A): the lifetime can therefore significantly vary from one experiment to the other.

Measuring the single photon purity

The purity is the figure of merit evaluating if the source emits one and not more than one photon per triggering pulse. It is described by the second order correlation function [158]:

$$g^{(2)}(\tau) = \frac{\left\langle \hat{\boldsymbol{a}}^{\dagger}(0)\hat{\boldsymbol{a}}^{\dagger}(\tau)\hat{\boldsymbol{a}}(\tau)\hat{\boldsymbol{a}}(0) \right\rangle}{\left\langle \hat{\boldsymbol{a}}^{\dagger}(0)\hat{\boldsymbol{a}}(0) \right\rangle \cdot \left\langle \hat{\boldsymbol{a}}^{\dagger}(\tau)\hat{\boldsymbol{a}}(\tau) \right\rangle} \tag{2.11}$$

The photon statistics translate in the second order correlations. Fig. 2.14 represents the different possibilities: antibunched photons are emitted with a regular time interval between each other, coherent photons with a random interval and bunched photons are emitted by groups with a characteristic duration. For a perfect single-photon source, the photons are antibunched and $g^{(2)}(0) = 0$ whereas $g^{(2)}(0) = 1$ for a coherent source and $g^{(2)}(0) > 1$ for a bunched (thermal) source.

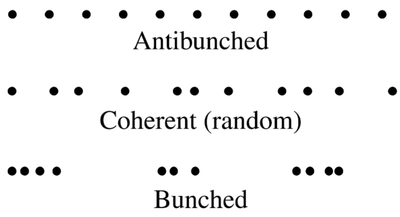

FIGURE 2.14: Typical photon distributions: a single-photon source emits antibunched photons, a laser, coherent photons and a thermal source, bunched photons. Figure from [159].

The second order correlation function is evaluated with the experiment introduced by Hanbury-Brown and Twiss (HBT) [160], in which the stream of photons is sent on a beam splitter and the coincidences between the detection events in the two outputs provide the $g^{(2)}$ function. The principle is shown in Fig. 2.15a in the fibered version. The TCSPC module is triggered by the detection of a photon in APD1, then measures the time before the next detection in APD2 and so on, progressively filling the histogram of time differences. The result in Fig. 2.15b shows the antibunching at zero delay as expected with a source of single photons.

The purity $\mathcal{P}$ is defined as the contrast between the area of the central peak with respect to the neighboring peaks. We find:

$$\begin{gathered} g^{(2)}(0) = 6.5\,\% \\ \mathcal{P} = 93.5\,\% \end{gathered} \tag{2.12}$$

The favored hypotheses for the imperfect purity are the presence in the collection of photons from the excitation pulse that were not completely removed by the cross-polarized output, or multiple excitations of the quantum dot in a single excitation pulse.

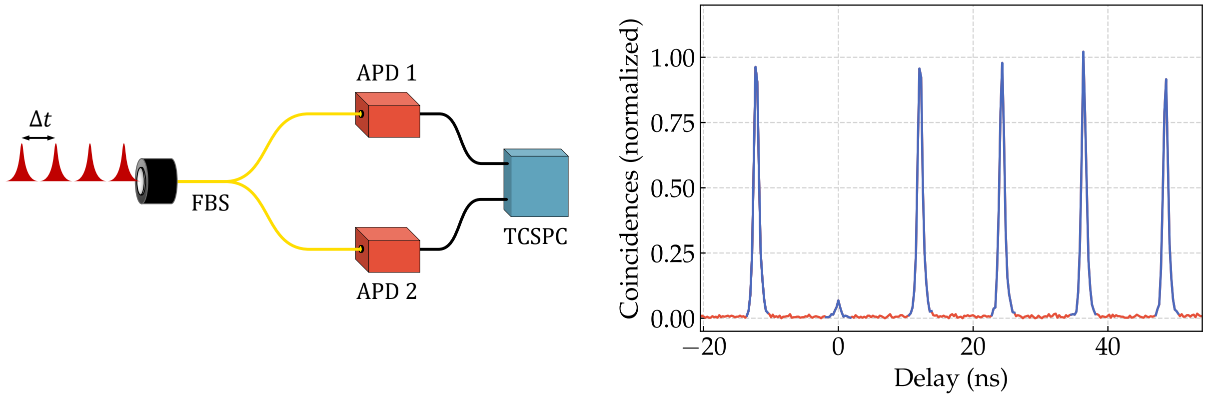

(a) (b)

FIGURE 2.15: **(a)** Fibered version of the HBT experiment with a pulsed excitation (FBS: fibered beam splitter). **(b)** Coincidences measured with the HBT setup. The *positively charged device* is excited with the WL two-color scheme. The blue peaks are integrated to compute the purity while the noise is left out (in orange).

Measuring the indistinguishability of single photons

The measurement of the indistinguishability of single photons relies on the coalescence of identical photons on a beam splitter and was pioneered experimentally by Hong, Ou and Mandel (HOM) [161]. When applied to the emission triggered by a pulsed laser, we measure the "mean wave-packet overlap" M, given by the coincidence rate at zero delay after an imbalanced Mach-Zehnder interferometer, where one path is delayed by the time between two single photon pulses in order to make consecutively emitted photons interfere on a beam splitter (Fig. 2.16). We plot the coincidences between the detection events in the two outputs in Fig. 2.17.

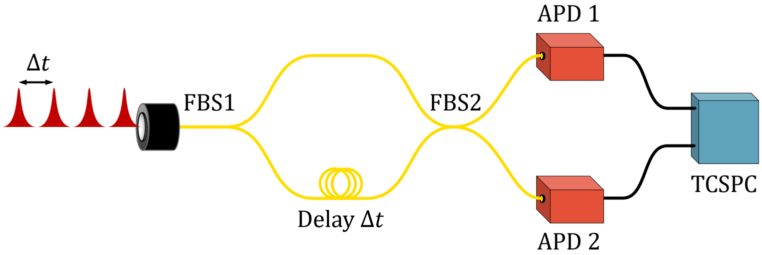

FIGURE 2.16: Fibered version of the HOM experiment for a pulsed single-photon source. The imbalanced Mach-Zehnder interferometer delays one path by the time between two single photon pulses Δt and successively emitted single photons interfere on FBS2.

Here, by the area of the central peak and its contrast with respect to the neighboring peaks, we measure a raw indistinguishability $M_{raw} = 0.77$. This figure of merit can be corrected by the imperfect purity of the source, as demonstrated by *Ollivier et al. (2021)* [162]:

$$M_{corr} = \frac{M_{raw} + g^{(2)}(0)}{1 - g^{(2)}(0)} = 0.89 \tag{2.13}$$

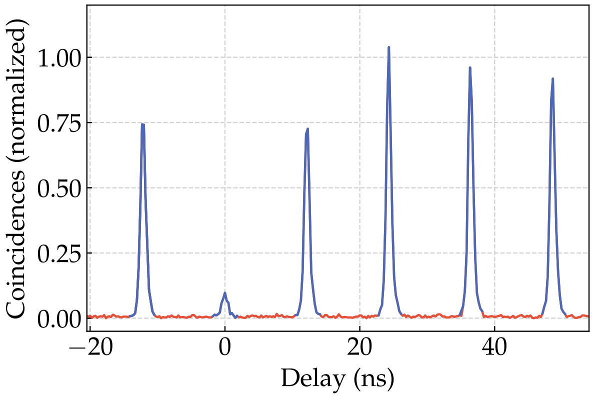

FIGURE 2.17: Coincidences measured after the HOM setup described in Fig. 2.16. The *positively charged device* is excited with the WL two-color scheme. The blue lines are integrated to compute the indistinguishability while the noise is left out (in orange).

We can notice that the indistinguishability measured this way takes into account only the 12 ns delay. Longer delays between interfering photons were studied by *Loredo et al. (2016)* [163] and the decrease in indistinguishability was below 5 % for delays of a few hundred nanoseconds: this translates a good stability of the source at these timescales. Indeed, an imperfect indistinguishability arises from pure dephasing or other sources of noise at fast timescales compared to the temporal separation between the emission of the two photons that interfere.

The results from the current section corroborate those found in [154]. Changing the excitation scheme to a quasi-resonant excitation with $\lambda_{QR} = 901\,\mathrm{nm},\ P_{QR} = 250\,\mu\mathrm{W}$ and the same pulsed resonant laser resulted in a brighter source $B = (27 \pm 3)\,\%$, albeit with a trade-off on the purity: $g^{(2)}(0) = 15\,\%$ and $M_{corr} = 95\,\%$. This scheme will nonetheless be favored for the further experiments as we expect less spectral wandering with a quasi-resonant excitation than a non-resonant one: this phenomenon will be modeled in chapter 3 and we will see how detrimental spectral wandering is to the spin-photon interface, even though its long timescale doesn't impact the measured purity and indistinguishability of the single photon emission. Let us add that a very high-quality single-photon source was reached in the quasi-resonant excitation scheme on the *positively charged device* by filtering the collected light with a Fabry-Pérot etalon of width 30 pm: $g^{(2)}(0) = 1.6\,\%$ and $M_{raw} = 97\,\%$ [148], albeit at the cost of a reduced brightness.

2.4 Long delay photon-photon correlations

The study of the photon-photon correlations on longer timescales than the typical hundreds of nanoseconds of the previous experiments allows us to access the charge and/or spin dynamics of the system. We present the results in two different experimental conditions that separate these effects by detecting photons in different polarization bases.

2.4.1 Principle of the experiment

In the following experiments, we use the time-correlated single photon counting (TCSPC) apparatus in "time-tagging" mode to record all the detection events in the two detectors, from which we calculate the correlations *a posteriori* in order to access the long timescales. In comparison, the short delay data of section 2.3 were measured in real time with a software that only computes the delays between two consecutive detections in 1 and 2, i.e., starting from a triggering event at t_1 on detector 1, the device waits for a detection event in detector 2 at time t_2 and adds the delay $t_2 - t_1$ to the coincidence histogram. Since the photon detection rate is typically in the MHz range, the probability of observing long delays ($\gg 100\,\mathrm{ns}$) is reduced and does not reflect the actual correlations. This technique is appropriate for fast measurements at short delays, but long delay studies must take into account all the detection events to compute the correlations and require more computation time.

Correlations are widely used to uncover the charge dynamics of the system: one can for example correlate different emission lines of a single quantum dot to each other, by spectrally selecting one line per detector: the correlations reveal which charge state comes first and the dynamics of charge creation [164–166]. Another idea is to spectrally split in half a single quantum dot emission line and to correlate the two halves to study spectral diffusion effects [167]. Here, we focus on the single quantum dot in the trion transition with the quasi-resonant two-color excitation scheme devised in subsection 2.3.1 ($\lambda_{QR} = 901\,\mathrm{nm}$). As will be shown theoretically and experimentally in the next chapters, the photons reflected from the device exhibit both the charge dynamics (i.e., the dynamics of electrons and holes being injected in or tunneling out of the quantum dot) and the spin dynamics (resulting from the ground state spin fluctuations). Since these effects are polarization-specific, as will be demonstrated in chapter 3, the detection in the (H,V) basis only exhibits the charge dynamics whereas the detection in the $(|\Psi_\Uparrow\rangle, |\Psi_\Downarrow\rangle)$ basis additionally displays the spin dynamics.

2.4.2 Evaluating the charge state occupation by single photon correlations in the cross-polarization

Experimental implementation

We first study the autocorrelation of the cross-polarized emission, that is the emitted photons detected in polarization V when exciting H, for which we expect only the charge dynamics to manifest. The experimental setup in Fig. 2.18a is based on the HBT configuration for the measurement of the single photon purity: the quantum dot-emitted single photons are isolated in the cross-polarization, and are split by a non-polarizing beam splitter. The *positively charged device* is excited with the quasi-resonant two-color scheme, comprising a 15 ps resonant laser on the π-pulse power and an auxiliary quasi-resonant laser at 901 nm with varying powers. We expect the non-resonant laser power to influence the occupation probability of the charge state (a single hole in the present case). The autocorrelation $g^{(2)}_{VV}$ is plotted as a function of the delay in

Fig. 2.18b, and a zoom on the short delays reproduces Fig. 2.15b, which despite different excitation conditions, shows that the peaks are averaged out on the measurement considered here. Notice that the upper graph represents coincidences normalized by the maximum value and the lower graph is the actual second-order correlation function, normalized at infinite delay.

The on/off fluctuations of the hole state (also called *blinking*) result in the bunching of the autocorrelation curves at short delays, signaling that photons are detected in bunches of characteristic length given by the decay time to unity. One can view the "start" photon detection as the indication that the quantum dot is in the single hole state, which in turn increases the probability to detect a "stop" photon shortly after, coming from the same bunch. Mono-exponential fits are plotted on top of the experimental data; they will be explained by the simple model we develop next.

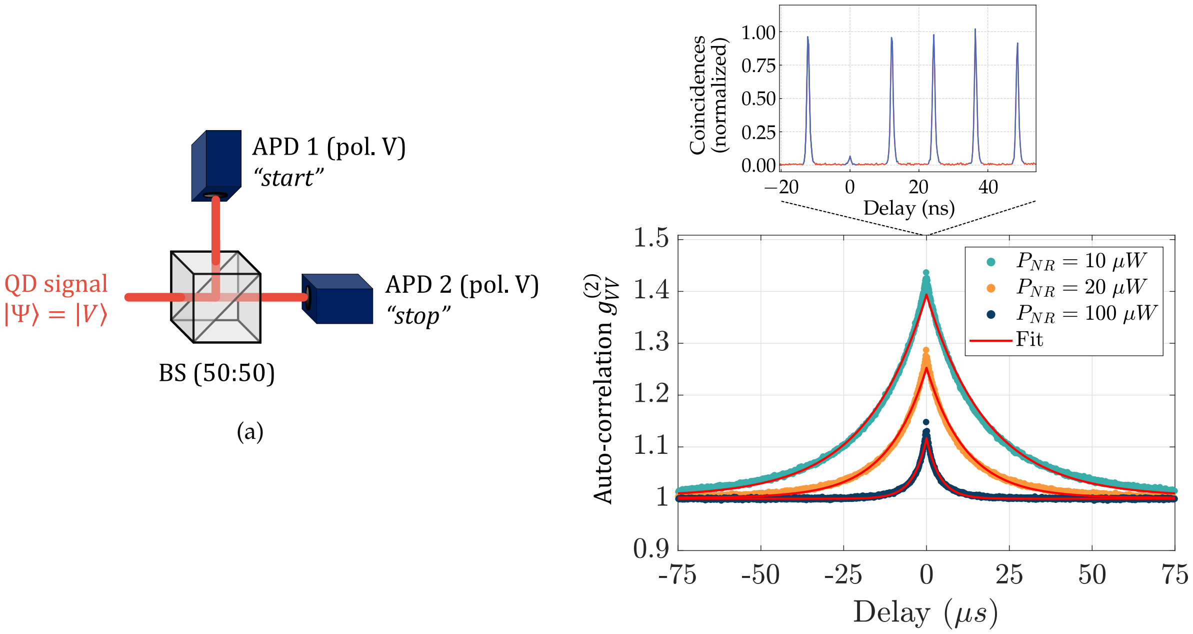

(a)

(b)

FIGURE 2.18: **(a)** Principle of the characterization of the occupation probability through autocorrelation of the cross-polarized emission. **(b)** autocorrelation of the V-polarized photons as a function of the delay for different non-resonant laser power, superimposed with mono-exponential fits (lower graph). The plots were normalized to 1 at a 200 µs delay so any effects at longer timescale are ignored. The upper graph is a reproduction of Fig. 2.15b to remind that the data measured here are a zoom out from the correlation data presented above. This result was published in [148].

Charge escape and capture model

The imperfect occupation probability of the charge can be modeled by a two-state system, with a charged state and an empty state. The latter is denoted $\varnothing$ to symbolize the absence of charge in the quantum dot. The associated probabilities are written P_c and $P_\varnothing$. The autocorrelation that we seek to explain can be written as the conditional probability to detect a "stop" photon at time τ, knowing that a "start" photon was previously detected at time 0, normalized by the unconditioned probability. This mathematically translates as follows:

$$g^{(2)}_{VV}(\tau) = \frac{P(V\,\text{"stop"}, t = \tau | V\,\text{"start"}, t = 0)}{P(V\,\text{"stop"})} \tag{2.14}$$

Since the resonant laser is tuned to the energy of the trion transition, only this charge state will give rise to single photon emission, and therefore to a signal in the cross-polarized collection: this proves that the initial condition of the autocorrelation is $P_c(t = 0) = 1$. The occupation probabilities, and therefore the autocorrelation, will then evolve under the effect of two phenomena: a pumping mechanism (here, the 901 nm laser) that allows the system to capture a charge with a characteristic time τ_{capt}, and an escape mechanism by which the quantum dot loses the charge with a time τ_{esc}. The rate equations in this model read as follows:

$$\frac{\mathrm{d}P_\varnothing(t)}{\mathrm{d}t} = -\frac{P_\varnothing(t)}{\tau_{capt}} + \frac{P_c(t)}{\tau_{esc}} \tag{2.15}$$

$$\frac{\mathrm{d}P_c(t)}{\mathrm{d}t} = +\frac{P_\varnothing(t)}{\tau_{capt}} - \frac{P_c(t)}{\tau_{esc}} \tag{2.16}$$

Exploiting the fact that $P_\varnothing + P_c = 1$, we can combine the two previous equations in:

$$\frac{\mathrm{d}P_c(t)}{\mathrm{d}t} = \frac{1}{\tau_{capt}} - \left(\frac{1}{\tau_{esc}} + \frac{1}{\tau_{capt}}\right) P_c(t) \tag{2.17}$$

Taking the stationary regime gives the average value of P_c:

$$\langle P_c \rangle = \frac{\tau_{esc}}{\tau_{esc} + \tau_{capt}} \tag{2.18}$$

With the initial condition $P_c(t = 0) = 1$, the occupation probability of the charge state therefore reads:

$$P_c(t) = \langle P_c \rangle + \Big(1 - \langle P_c \rangle\Big) e^{-t/T_c} \tag{2.19}$$

where we introduced the effective lifetime of the charge: $T_c = \left(\frac{1}{\tau_{capt}} + \frac{1}{\tau_{esc}}\right)^{-1}$. In this reasoning, according to Eq. 2.14, the second-order autocorrelation is simply given by $P_c(t)$, normalized by its stationary value:

$$\boxed{g^{(2)}_{VV}(t) = \frac{P_c(t)}{\langle P_c \rangle} = \left(\frac{1}{\langle P_c \rangle} - 1\right) e^{-t/T_c} + 1} \tag{2.20}$$

The experimental data in Fig. 2.18b and other analogous experiments at different powers of the quasi-resonant laser were fitted with Eq. 2.20: the $\langle P_c \rangle$ and T_c parameters are aggregated in Fig. 2.19, demonstrating an increasing occupation probability and a decreasing lifetime of the charge when the power of the QR laser is increased. The average occupation probability starts at zero and saturates close to unity for powers higher than 300 µW while the lifetime of the charge is reduced from 50 to 1 µs. This can be interpreted as a single hole charge state more efficiently injected in the quantum dot at high QR laser powers, escaping in a shorter time but present more often in average. Finally, we emphasize that a low occupation probability induces a bunching of the autocorrelation and, in the opposite case, a flat line is obtained if $\langle P_c \rangle = 1$.

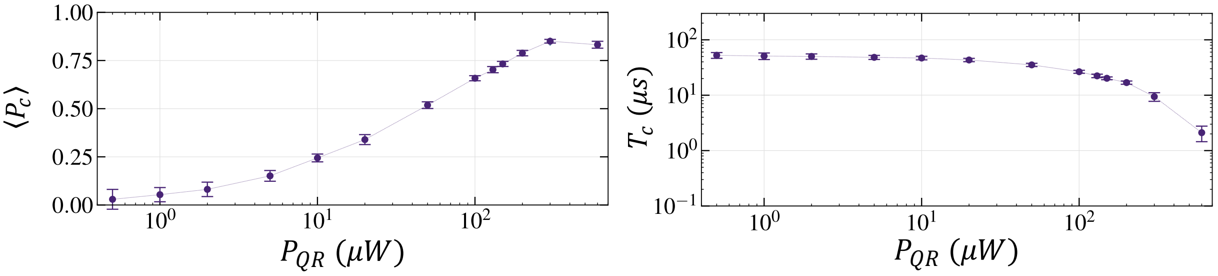

FIGURE 2.19: Fitting parameters of the autocorrelation experiments at different quasi-resonant laser powers using formula Eq. 2.20 to extract the average occupation probability **(left)** and the effective charge lifetime **(right)**. Figure adapted from [133].

2.4.3 Evaluating the spin statistics by single photon cross-correlations

Cross-correlations as spin noise spectroscopy

Our implementation of spin noise spectroscopy (SNS) is to study the spin dynamics through cross-correlations in a spin-sensitive basis. More specifically, we focus on the polarizations $|\Psi_{\Uparrow}\rangle$ and $|\Psi_{\Downarrow}\rangle$ determined by the spin-dependent polarization rotation from the states $|\Uparrow\rangle$ and $|\Downarrow\rangle$ (as first introduced in Fig. 1.33).

The experimental setup is presented in Fig. 2.20a: the whole reflected beam is split in a certain detection basis of orthogonal polarizations $(|\Psi_D\rangle, |\overline{\Psi_D}\rangle)$ close to $(|\Psi_{\Uparrow}\rangle, |\Psi_{\Downarrow}\rangle)$ by waveplates and a polarizing beam splitter. A TCSPC apparatus subsequently measures the cross-correlations between the photon detection events in each collection arm. The result is plotted in Fig. 2.20b: the anti-correlation at short delay is explained by the initial partially projective measurement in $|\Psi_D\rangle \simeq |\Psi_{\Uparrow}\rangle$, leaving the spin in a state that will continue to rotate the polarization to $|\Psi_{\Uparrow}\rangle$ for as long as it has not flipped. The exponential decay of the anti-correlation is interpreted as the lifetime of the spin, T_S before its return to thermal equilibrium. This experiment was achieved by exciting the sample with a CW resonant laser ($P_R = 8\,\mathrm{pW}$) combined with a quasi-resonant excitation ($\lambda_{NR} = 901\,\mathrm{nm}$, $P_{QR} = 2\,\mu\mathrm{W}$) and applying a small longitudinal magnetic field $B_z = 30\,\mathrm{mT}$ to screen the effect of the nuclear spins. The imperfect contrast of the anti-correlation will be interpreted in chapter 4 as a consequence of charge noise [168] on an otherwise high-efficiency spin-photon interface.

These data can be interpreted by the definition of the cross-correlation function in terms of probabilities. Indeed, the second order cross-correlation function is equal to the probability of detecting a $\overline{\Psi_D}$-polarized photon at time τ conditioned by an initial detection of a Ψ_D-polarized photon, normalized by the unconditioned detection probability in Ψ_D:

$$g^{(2)}_{\Psi_D\overline{\Psi_D}}(\tau) = \frac{P(\overline{\Psi_D}, t = \tau | \Psi_D, t = 0)}{P(\overline{\Psi_D})} \tag{2.21}$$

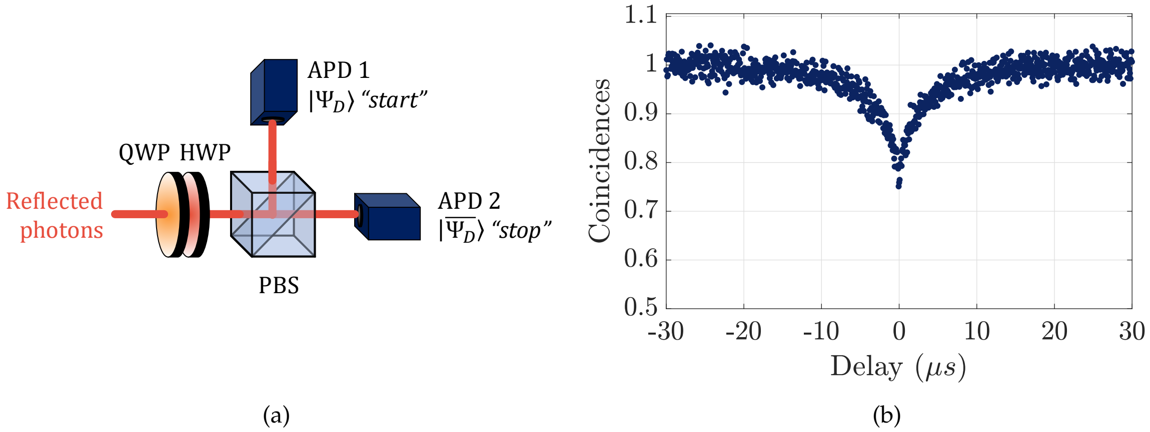

FIGURE 2.20: **(a)** Principle of the characterization of the spin dynamics through cross-correlations in the $(\Psi_D, \overline{\Psi_D})$ basis, determined by the angles of QWP and HWP. **(b)** Coincidences as a function of the delay with an external longitudinal magnetic field $B_z = 30\,\mathrm{mT}$. The data were normalized to unity at a 60 µs delay so any effects at longer timescale are ignored.

General case: interplay between the charge and spin dynamics

In order to explain the interplay between the charge and spin dynamics, we develop a three-level model including the spin states $|\Uparrow\rangle$, $|\Downarrow\rangle$ and the empty state $|\varnothing\rangle$. We ignore the excited levels of the trion transition as the excitation power stays very weak compared to the saturation of the transition. The model is represented in Fig. 2.21.

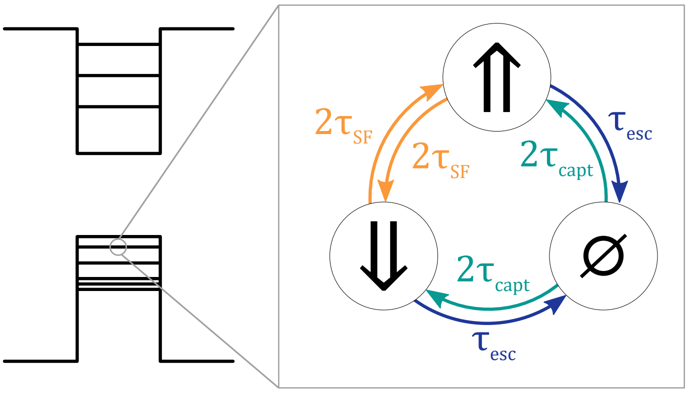

FIGURE 2.21: Three-level model including spin flips and charge escape and capture effects.

The rate equations linking the occupation probabilities in each state are the following:

$$\begin{aligned}
\frac{\mathrm{d}P_{\Uparrow}(t)}{\mathrm{d}t} &= -\frac{P_{\Uparrow}(t) - P_{\Downarrow}(t)}{2\tau_{SF}} - \frac{P_{\Uparrow}(t)}{\tau_{esc}} + \frac{P_{\varnothing}(t)}{2\tau_{capt}} \\
\frac{\mathrm{d}P_{\Downarrow}(t)}{\mathrm{d}t} &= +\frac{P_{\Uparrow}(t) - P_{\Downarrow}(t)}{2\tau_{SF}} - \frac{P_{\Downarrow}(t)}{\tau_{esc}} + \frac{P_{\varnothing}(t)}{2\tau_{capt}} \\
\frac{\mathrm{d}P_{\varnothing}(t)}{\mathrm{d}t} &= -\frac{P_{\varnothing}(t)}{\tau_{capt}} + \frac{P_{\Uparrow}(t) + P_{\Downarrow}(t)}{\tau_{esc}}
\end{aligned} \tag{2.22}$$

where $P_c(t) = P_{\Uparrow}(t) + P_{\Downarrow}(t)$ and $P_{\Uparrow}(t) + P_{\Downarrow}(t) + P_{\varnothing}(t) = 1$. We calculate the dynamics of the charge, given by the same formula as Eq. 2.19, and the dynamics of the spin polarization $s_z(t) = P_{\Uparrow}(t) - P_{\Downarrow}(t)$ (assuming that $s_z(t = \infty) = 0$, corresponding to a thermal equilibrium between $|\Uparrow\rangle$ and $|\Downarrow\rangle$):

$$\begin{aligned} P_c(t) &= \langle P_c \rangle + \Big(1 - \langle P_c \rangle\Big) e^{-t/T_c} \\ s_z(t) &= s_z(0) e^{-t/T_s} \end{aligned} \tag{2.23}$$

where we introduced the following expression of the spin characteristic time, featuring both the charge escape and the spin-flip times:

$$T_s^{-1} = \left(\frac{1}{\tau_{esc}} + \frac{1}{\tau_{SF}} \right)^{-1} \tag{2.24}$$

It is apparent that, while P_c only exhibits the charge dynamics, s_z includes both the spin and charge contributions. A useful expression gives the probability associated to the $|\Uparrow\rangle$ state as a function of the charge probability and spin polarization:

$$P_{\Uparrow}(t) = \frac{P_c(t) + s_z(t)}{2} \tag{2.25}$$

Translated in terms of cross-correlations, these expressions result in the presence of two distinct exponential decays, a complete theoretical and experimental study of which follows in the next chapters.

2.5 Conclusion

We have mapped out the main experimental protocols and applied them for preliminary experiments on the *positively charged device*. The continuous regime offers the possibility to fully characterize the reflected polarization state in the Poincaré sphere, while the dynamic regime reveals the charge and spin dynamics through cross-correlation experiments. Next, the theoretical framework is laid out as it gives an in-depth understanding of the more detailed experiments to follow.

Chapter 3

Theoretical framework and simulations

The theoretical tools to model the quantum dot-micropillar cavity system are introduced in this chapter. The mathematical formalism of the Jaynes-Cummings model is solved numerically by the master equation approach, which includes the incoherent processes that cannot be ignored experimentally. This leads to the description of a wide range of physical phenomena known to play a role in quantum dot-based spin-photon interfaces.

The goal of the simulations lies in the explanation of actual experiments that will be at the center of the next chapters. To do so, the numerical solving is first carried out in the steady state: this allows quantifying how good a spin-photon interface a given device could be, by computing the polarization states $|\Psi_{\Uparrow}\rangle$ and $|\Psi_{\Downarrow}\rangle$ which are reflected from the sample, depending on the spin state: the ideal spin-photon interface criterion is $\langle\Psi_{\Uparrow}|\Psi_{\Downarrow}\rangle = 0$. This criterion is studied with respect to the figures of merit of the device (cavity output coupling and cooperativity) and we show that multiple configurations fulfill it, albeit with very different reflected polarization states.

A second experimental aspect is the dynamics of the system, measured through photonic correlations. We theoretically investigate this principle by disturbing the steady state of the system with the detection of a reflected photon, and by computing the evolution back to equilibrium. This evolution is sensitive, in particular, to the different relaxation mechanisms.

Lastly, we separately introduce the effect of an external magnetic field, charge blinking, pure dephasing and slow charge noise to bring the simulation closer to realistic devices.

3.1 Master equation formalism

The numerical simulation of the quantum dot-micropillar system is based on the theory of the *master equation* (ME), which models a quantum system that can be in a coherent or incoherent superposition of states [169]. The Jaynes-Cummings model detailed in subsection 1.3.1 lays the mathematical description of the coherent light-matter coupling in a cavity [108]. The master equation completes this approach by including the incoherent phenomena caused by the coupling of the quantum system to an environment with a large number of degrees of freedom.

This section starts by extending the Schrödinger equation to the master equation through the description of the incoherent superposition of quantum states with the formalism of the density matrix. Then, the collapse operators modeling the coupling to the environment are introduced: when applied to the density matrix in a specific combination, they constitute the Lindblad superoperators, which govern the incoherent evolution of the quantum system.

Next, the spin-photon interface is progressively described in this framework: starting by the empty cavity, followed by the four-level quantum dot and finally the coherent and incoherent couplings between the two. The results of the numerical simulation in the steady state are given for various cases of cavity and quantum dot configurations, analyzing the requirements of an ideal spin-photon interface.

3.1.1 Evolution of an open quantum system

Let us consider a quantum system coupled to an environment. The quantum system (S) is described by a modest number of degrees of freedom: it constitutes the computation space which must stay within processing capability. By contrast, the environment (E) is a reservoir with many particles interacting with the system (S): even if it could in principle be represented by a quantum state, the sheer number of degrees of freedom prevents any attempt at an exact modeling. A statistical approach is developed instead, based upon the density matrix theory.

Pure quantum states

A pure quantum state is mathematically written as a ket $|\Psi\rangle$, which is a vector in a Hilbert space $\mathcal{H}$. The measurement of a physical quantity of this state is represented by an observable $\hat{\boldsymbol{A}}$, and the theoretical average outcome of the measurement is given by $\langle\hat{\boldsymbol{A}}\rangle = \langle\Psi|\hat{\boldsymbol{A}}|\Psi\rangle$. This measurement can only result in an eigenvalue of $\hat{\boldsymbol{A}}$ with a given probability, and the state of the system is projected onto the corresponding eigenvector upon measurement. We work in the Schrödinger picture that considers state vectors evolving with time and constant operators. In that case, for an isolated quantum system, the evolution of a pure state is given by the Schrödinger equation:

$$\frac{\mathrm{d}\,|\Psi(t)\rangle}{\mathrm{d}t} = -i\hat{\boldsymbol{H}}\,|\Psi(t)\rangle \tag{3.1}$$

where the Hamiltonian operator $\hat{\boldsymbol{H}}$ is the observable for the total energy of the system. This evolution is described as coherent because the state stays pure at all times.

Mixed quantum states

To account for a statistical mixture of quantum states, the density matrix operator $\hat{\boldsymbol{\rho}}$ is introduced: it represents an incoherent superposition of multiple pure quantum states $|\Psi_i\rangle$, each with a probability p_i:

$$\hat{\boldsymbol{\rho}} = \sum_i p_i\,|\Psi_i\rangle\,\langle\Psi_i| \tag{3.2}$$

In that case, the system cannot be described by a single pure state. The time evolution of the density matrix is ruled by the Von Neumann equation:

$$\frac{\mathrm{d}\hat{\boldsymbol{\rho}}(t)}{\mathrm{d}t} = i\left[\hat{\boldsymbol{\rho}}(t), \hat{\boldsymbol{H}}(t)\right] \tag{3.3}$$

The average value of an operator applied to a quantum system in a statistically mixed state is given by tracing over the density matrix:

$$\langle \hat{\boldsymbol{A}} \rangle = \sum_i p_i \langle \Psi_i | \hat{\boldsymbol{A}} | \Psi_i \rangle = \mathrm{Tr}\left\{ \hat{\boldsymbol{A}} \cdot \hat{\boldsymbol{\rho}} \right\} \tag{3.4}$$

Coupling to the environment

So far, we have considered an isolated quantum system. However, in realistic cases, the system under investigation is coupled to an environment with which it interacts and that could only be represented as an extremely complex quantum state. The complete isolated system (C) now comprises the system under investigation (S) and the environment (E). Their interaction causes disturbances that can be approximated by jumps between the quantum states of (S), provided the following hypotheses are met [169]:

- The coupling of (S) with the environment is weak – *Born approximation*.
- The initial state is uncorrelated between (S) and (E). This translates mathematically as the possibility to write the total initial state of the system as the tensor product $\mathrm{C} = \mathrm{S} \otimes \mathrm{E}$.
- The interaction of (S) with the environment does not depend on the history of the complete system – *Markov approximation.*

A first example of an incoherent process is the case of a random jump that can project the system from an initial state $|i\rangle$ onto a final state $|f\rangle$ at a rate γ_{if} (in s^{-1}). This phenomenon is accounted for by the collapse operator $\hat{\boldsymbol{C}}_{if}$ which reads:

$$\hat{\boldsymbol{C}}_{if} = \sqrt{\gamma_{if}}\, |f\rangle \langle i| \tag{3.5}$$

An incoherent jump performs a measurement-like projection, thereby resetting the coherent evolution of the system. To apply a collapse operator to the density matrix, the possible transitions it can cause are described by a Lindblad superoperator (or Lindbladian) defined as:

$$\hat{\boldsymbol{L}}_{if}\left[\hat{\boldsymbol{\rho}}\right] = \hat{\boldsymbol{C}}_{if}\hat{\boldsymbol{\rho}}\hat{\boldsymbol{C}}_{if}^{\dagger} - \frac{1}{2}\left(\hat{\boldsymbol{C}}_{if}^{\dagger}\hat{\boldsymbol{C}}_{if}\hat{\boldsymbol{\rho}} + \hat{\boldsymbol{\rho}}\hat{\boldsymbol{C}}_{if}^{\dagger}\hat{\boldsymbol{C}}_{if}\right) \tag{3.6}$$

When developed, it becomes:

$$\hat{\boldsymbol{L}}_{if}\left[\hat{\boldsymbol{\rho}}\right] = \gamma_{if} P(i)\, |f\rangle \langle f| - \frac{\gamma_{if}}{2}\Big(|i\rangle \langle i|\, \hat{\boldsymbol{\rho}} + \hat{\boldsymbol{\rho}}\, |i\rangle \langle i| \Big) \tag{3.7}$$

The first term of Eq. 3.7 projects the system onto the final state $|f\rangle$ at the rate γ_{if} proportionally to the probability to find the system in the initial state, $P(i)$. The consecutive terms reduce the probability to find the system in the initial state, and ensure that the density matrix stays normalized at all times.

A second example of incoherent process is when, instead of producing a jump from one quantum state to another, the process encompasses multiple initial and final states. It is the case when an intracavity photon is lost: the initial and final states can be any photon number state separated by one unit, as will be detailed later on.

Finally, when combining independent incoherent processes resulting from independent interactions between the system and its environment, the Lindblad superoperators $\hat{\boldsymbol{L}}_k$ associated to each of these processes have to be summed and added to the Von Neumann equation to form the master equation, accounting for both the coherent and incoherent evolution [169]:

$$\boxed{\frac{\mathrm{d}\hat{\boldsymbol{\rho}}(t)}{\mathrm{d}t} = i\left[\hat{\boldsymbol{\rho}}(t), \hat{\boldsymbol{H}}\right] + \sum_k \hat{\boldsymbol{L}}_k\left[\hat{\boldsymbol{\rho}}(t)\right]} \tag{3.8}$$

In the following paragraphs, we model the quantum dot-micropillar cavity system in the master equation framework.

3.1.2 Bare cavity

To begin with, we model a bare cavity coupled to an input beam, from which we observe the reflected light as illustrated in Fig. 3.1, setting aside the polarization degree of freedom.

Description of the electromagnetic fields

The modes of the electromagnetic field involved with the bare cavity are the input and output modes as well as the intracavity mode. Photons can be removed from these modes by the annihilation operator $\hat{\boldsymbol{a}}$ or added by its Hermitian conjugate, the creation operator $\hat{\boldsymbol{a}}^\dagger$. The eigenstates of this operator are the Fock states, also called number states as they are defined by $\{|N\rangle\}_{N\in\mathbb{N}}$ with N the number of photons in the considered mode. The annihilation and creation operators act on the Fock states as follows:

$$\begin{aligned} \hat{\boldsymbol{a}}^\dagger |N\rangle &= \sqrt{N+1}\,|N+1\rangle \\ \hat{\boldsymbol{a}}\,|N\rangle &= \sqrt{N}\,|N-1\rangle \\ \hat{\boldsymbol{a}}\,|0\rangle &= |0\rangle \end{aligned} \tag{3.9}$$

We label $\hat{\boldsymbol{b}}_{in}$, $\hat{\boldsymbol{b}}_{out}$ and $\hat{\boldsymbol{a}}$ the annihilation operators respectively relative to the input, output and cavity modes as shown in Fig. 3.1. The right side of the figure represents the Fock states of the cavity mode at energies $N\omega_c$. The photon number operator for mode a is $\hat{\boldsymbol{n}} = \hat{\boldsymbol{a}}^\dagger\hat{\boldsymbol{a}}$, whose average value $\langle\hat{\boldsymbol{n}}\rangle$ gives the photon flux in the considered mode (in s^{-1}).

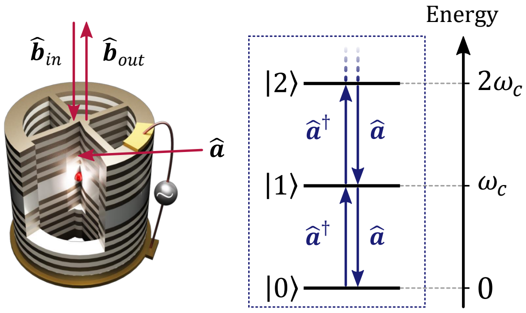

FIGURE 3.1: **(Left)** Annihilation operators of the considered modes of the electromagnetic field (input $\hat{b}_{in}$, output $\hat{b}_{out}$ and intracavity $\hat{a}$). **(Right)** Representation of the Fock state basis for the cavity mode in which a photon can be added by $\hat{a}^\dagger$ or removed by $\hat{a}$.

In the practical simulations, the model is restricted to the fundamental optical mode of the cavity to which the input and output beams couple best. The Hilbert space of the cavity is in principle infinite dimensional, but it is truncated to a value N_{max}. Typically, we choose $N_{max} = 3$, which is valid for low excitation powers (as long as the populations of the intracavity Fock states $|3\rangle$ and above stay small compared to that of the lower number states).

Intracavity Hamiltonian

Let ω_c be the energy of the cavity mode. The operator whose eigenvalues are the energies of the corresponding Fock states $E_N = N\omega_c$ constitutes the Hamiltonian of the intracavity photons and reads [108]:

$$\hat{H}_{cav} = \omega_c \hat{a}^\dagger \hat{a} \tag{3.10}$$

In general, the energy of the input laser ω is detuned from ω_c and the calculations therefore include electric fields oscillating at the sum and the difference of the two energies. We proceed to the *rotating wave approximation* (RWA), by which the fast oscillating terms at $\omega_c + \omega$ are averaged out and the bare cavity Hamiltonian becomes [170]:

$$\hat{H}_{cav} = (\omega_c - \omega)\hat{a}^\dagger \hat{a} \tag{3.11}$$

Pumping Hamiltonian

The coherent transfer of photons from the input field to the cavity is described by the pumping Hamiltonian [171]:

$$\hat{H}_{pump} = -i\sqrt{\kappa_{top}}\left(\hat{b}_{in}\hat{a}^\dagger - \hat{b}_{in}^\dagger \hat{a}\right) \tag{3.12}$$

Reflected field

The output reflected field can be calculated knowing the input and the intracavity fields as they are linked by the *input-output* formula [112, 171]:

$$\hat{b}_{out} - \hat{b}_{in} = \sqrt{\kappa_{top}}\hat{a} \tag{3.13}$$

In general, the operators $\hat{\boldsymbol{b}}_{in/out}$ act on the quantum states of the corresponding electromagnetic fields, which should all be included in the simulated Hilbert space. However, a simplification arises in the case of coherent fields [112]: Eq. 3.13 also applies to reduced operators restricted to the cavity subspace, replacing $\hat{\boldsymbol{b}}_{in/out}$ by $b_{in/out}\hat{\boldsymbol{I}}_{cav}$ where we introduced the identity operator in the cavity subspace. This simplification makes numerical calculations tractable and will be applied from now on. For instance, the value of b_{in} is a scalar linked to the input power P_{in} by: $b_{in} = \sqrt{\eta_{in} P_{in}/(\hbar\omega)}$.

Cavity losses

The cavity losses are accounted for by the collapse operator:

$$\hat{\boldsymbol{C}}_{cav} = \sqrt{\kappa}\hat{\boldsymbol{a}} \tag{3.14}$$

Its effect is to randomly annihilate photons from the cavity at a rate given by κ. The corresponding Lindblad superoperator is labeled $\hat{\boldsymbol{L}}_{cav}$.

Complete model of the bare cavity

The bare cavity coupled to the input and output fields is completely modeled by:

$$\begin{aligned} \hat{\boldsymbol{H}}_{bare} &= \hat{\boldsymbol{H}}_{cav} + \hat{\boldsymbol{H}}_{pump} \\ \frac{\mathrm{d}\hat{\boldsymbol{\rho}}}{\mathrm{d}t} &= i\left[\hat{\boldsymbol{\rho}}, \hat{\boldsymbol{H}}_{bare}\right] + \hat{\boldsymbol{L}}_{cav}\left[\hat{\boldsymbol{\rho}}\right] \end{aligned} \tag{3.15}$$

The result of the simulation at this point is typically the photon flux reflected by a standard Fabry-Pérot cavity in the stationary regime, calculated as a function of the input laser energy:

$$\frac{\mathrm{d}\hat{\boldsymbol{\rho}}(\omega)}{\mathrm{d}t} = 0 \implies \hat{\boldsymbol{\rho}}(\omega) = \hat{\boldsymbol{\rho}}_{ss}(\omega) \tag{3.16}$$

In this stationary regime, the output intensity reads:

$$I_{out}(\omega) = \langle \hat{\boldsymbol{b}}_{out}^{\dagger}\hat{\boldsymbol{b}}_{out}\rangle_{\hat{\boldsymbol{\rho}}_{ss}(\omega)} = \mathrm{Tr}\Big\{\hat{\boldsymbol{b}}_{out}^{\dagger}\hat{\boldsymbol{b}}_{out} \cdot \hat{\boldsymbol{\rho}}_{ss}(\omega)\Big\} \tag{3.17}$$

3.1.3 Elliptical bare cavity

We now add the polarization degree of freedom for all the modes of the electromagnetic field. To that end, the Hilbert space is extended and the operators duplicated in the basis of the cavity modes (H,V) whose energies are $\omega_{c,H}$ and $\omega_{c,V}$, as represented in Fig. 3.2. An arbitrary polarization state is fully modeled by its projections on the (H,V) basis. The figure also shows on the right the double Fock state basis in the general case of an elliptical cavity, for which the modes are not energy-degenerate. The dimension of the photonic Hilbert space now increases to $N_{max} = N_{max,H} \times N_{max,V}$.

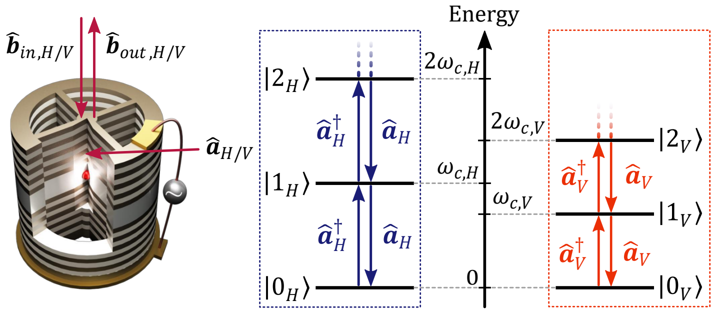

FIGURE 3.2: **(Left)** Annihilation operators of the H- and V-polarized modes of the electromagnetic field considering an elliptical cavity. **(Right)** Representation of the Fock state basis for the intracavity modes in which a photon can be added by $\hat{a}^\dagger_{H/V}$ or removed by $\hat{a}_{H/V}$.

The operators take a new form, as they now include terms acting on the H and V subspaces independently. Those related to the coherent evolution are duplicated within the same operator, as a coherent superposition [108, 170, 171]:

$$\begin{aligned}\hat{H}_{cav} = &(\omega_{c,H} - \omega)\hat{a}_H^\dagger \hat{a}_H \\ &+(\omega_{c,V} - \omega)\hat{a}_V^\dagger \hat{a}_V\end{aligned} \tag{3.18}$$

$$\begin{aligned}\hat{H}_{pump} = &-i\sqrt{\kappa_{top,H}}\left(\hat{b}_{in,H}\hat{a}_H^\dagger - \hat{b}_{in,H}^\dagger \hat{a}_H\right) \\ &-i\sqrt{\kappa_{top,V}}\left(\hat{b}_{in,V}\hat{a}_V^\dagger - \hat{b}_{in,V}^\dagger \hat{a}_V\right)\end{aligned} \tag{3.19}$$

The incoherent cavity losses are summed as Lindblad superoperators:

$$\hat{L}_{cav} = \hat{L}_{cav,H} + \hat{L}_{cav,V} \tag{3.20}$$

for which the two collapse operators are:

$$\hat{C}_{cav,H/V} = \sqrt{\kappa_{H/V}}\hat{a}_{H/V} \tag{3.21}$$

The evolution of the system is still ruled by Eq. 3.15. Unless stated otherwise, this chapter will describe only cavities with energy-degenerate polarization modes ($\omega_c = \omega_{c,H} = \omega_{c,V}$); nevertheless, the duplication of the Hilbert space is mandatory to account for any input and output polarization state.

3.1.4 Four-level system coupled to a cavity

The four-level system constituting the trion transition is now coupled to the cavity. The dimension of the computation space increases to $4N_{max,H} \times N_{max,V}$. The four-level structure and the physical phenomena covered by the model are represented in Fig. 3.3. The ground state is a hole spin: the system comprises a branch with a left hand circularly polarized transition

(L) coupling $|\Uparrow\rangle_z$ to $|\Uparrow\Downarrow\uparrow\rangle_z$ and an analogous R branch coupling $|\Downarrow\rangle_z$ to $|\Downarrow\Uparrow\downarrow\rangle_z$. The two transitions are energy-degenerate in the absence of an applied magnetic field and their energy is written ω_d.

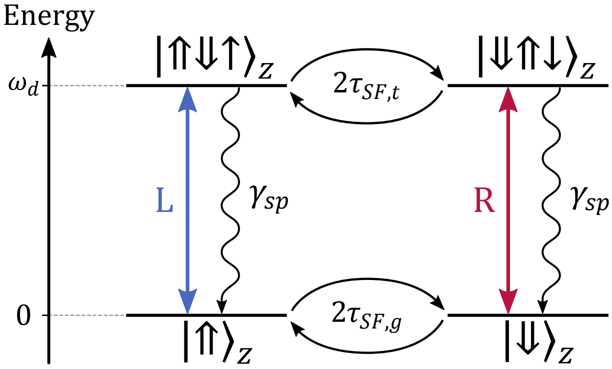

FIGURE 3.3: Four levels of the quantum dot transition from the hole spin in the ground state to the positive trion in the excited state and physical phenomena included in the simulation: coherent interaction in the L and R branches (colored arrows), spontaneous emission at the rate γ_{sp} (wavy black arrows) and ground and trion spin flips at the rates $\tau_{SF,g}$ and $\tau_{SF,t}$ respectively.

The coherent spin-photon interaction is represented by the colored arrows of Fig. 3.3: it is the energy exchange between the excitation laser and the quantum dot, with spin-dependent selection rules through which the Faraday rotation emerges (see subsection 1.1.3 and 1.3.4). The other processes are incoherent, that is they are dissipative in nature:

- The spontaneous emission γ_{sp} causes an incoherent de-excitation from the trion states to the ground states, with an emission of photons in all the modes of the electric field[1]. The spontaneous emission rate in the bulk GaAs is typically $\gamma_{sp} = 0.6\,\mu\text{eV} = 1\,\text{ns}^{-1}$ and this rate can be modified in the range $[0.3; 1.2]\,\mu\text{eV}$ depending on the diameter of the micropillar [172].
- The spin-flip phenomena randomly switch between the two branches. They are caused by the interaction with phonons and nuclear spins [54, 173–175].

The Hamiltonian terms developed below are based on the Jaynes-Cummings model of the light-matter interaction in a cavity [108].

Coherent processes

The operators describing the excitation and de-excitation of the quantum dot are the raising and lowering operators, respectively denoted $\hat{\boldsymbol{\sigma}}^\dagger$ and $\hat{\boldsymbol{\sigma}}$. We define simplified notations for the ground and trion states that we label g or t and index with the helicity of each branch:

$$\begin{aligned} |g_L\rangle &= |\Uparrow\rangle_z & |g_R\rangle &= |\Downarrow\rangle_z \\ |t_L\rangle &= |\Uparrow\Downarrow\uparrow\rangle_z & |t_R\rangle &= |\Downarrow\Uparrow\downarrow\rangle_z \end{aligned} \tag{3.22}$$

---

[1] Notice that it is different from the Purcell-enhanced spontaneous emission in the cavity mode at the rate $\Gamma_0 = 4g^2/\kappa$.

The raising and lowering operators then take the following form:

$$\begin{aligned} \hat{\boldsymbol{\sigma}}_L^\dagger &= \left|t_L\right\rangle \left\langle g_L\right| \quad & \hat{\boldsymbol{\sigma}}_R^\dagger &= \left|t_R\right\rangle \left\langle g_R\right| \\ \hat{\boldsymbol{\sigma}}_L &= \left|g_L\right\rangle \left\langle t_L\right| \quad & \hat{\boldsymbol{\sigma}}_R &= \left|g_R\right\rangle \left\langle t_R\right| \end{aligned} \tag{3.23}$$

We also introduce the $\hat{\boldsymbol{\sigma}}_{z,R/L}$ operators, which represent the population difference between the excited and ground levels of each branch:

$$\hat{\boldsymbol{\sigma}}_{z,R/L} = \left|t_{R/L}\right\rangle \left\langle t_{R/L}\right| - \left|g_{R/L}\right\rangle \left\langle g_{R/L}\right| \tag{3.24}$$

These operators will not be used in this chapter but it is important to note that they correspond to the third Pauli matrices of the subsystems $\left|g_L\right\rangle, \left|t_L\right\rangle$ ("L branch") and $\left|g_R\right\rangle, \left|t_R\right\rangle$ ("R branch"). Taken independently, both subsystems can be viewed as a qubits, in the same fashion as a qubit can be constituted by the $(\left|R\right\rangle, \left|L\right\rangle)$ polarizations of a photon, or by the $(\left|\Uparrow\right\rangle_z, \left|\Downarrow\right\rangle_z)$ components of a spin.

The Hamiltonian of the isolated quantum dot in the RWA reads:

$$\hat{\boldsymbol{H}}_d = (\omega_d - \omega) \left(\hat{\boldsymbol{\sigma}}_R^\dagger \hat{\boldsymbol{\sigma}}_R + \hat{\boldsymbol{\sigma}}_L^\dagger \hat{\boldsymbol{\sigma}}_L\right) \tag{3.25}$$

The interaction with the intracavity photons is given by the following Hamiltonian, that represents the coherent exchange of energy between the intracavity field and the (R,L) branches of the four-level quantum dot at rate g:

$$\hat{\boldsymbol{H}}_{int} = ig\left(\hat{\boldsymbol{a}}_R^\dagger \hat{\boldsymbol{\sigma}}_R - \hat{\boldsymbol{a}}_R \hat{\boldsymbol{\sigma}}_R^\dagger\right) + ig\left(\hat{\boldsymbol{a}}_L^\dagger \hat{\boldsymbol{\sigma}}_L - \hat{\boldsymbol{a}}_L \hat{\boldsymbol{\sigma}}_L^\dagger\right) \tag{3.26}$$

The final expression of the Hamiltonian combines all contributions:

$$\hat{\boldsymbol{H}}_{tot} = \hat{\boldsymbol{H}}_{cav} + \hat{\boldsymbol{H}}_{pump} + \hat{\boldsymbol{H}}_d + \hat{\boldsymbol{H}}_{int} \tag{3.27}$$

Incoherent processes

- First, the spontaneous emission in all modes is described by the following collapse operators:

  $$\hat{\boldsymbol{C}}_{sp,R/L} = \sqrt{\gamma_{sp}}\hat{\boldsymbol{\sigma}}_{R/L} \tag{3.28}$$

  Their effect is to randomly de-excite the corresponding trion state to its ground state at the rate γ_{sp}. The associated Lindblad superoperator reads:

  $$\hat{\boldsymbol{L}}_{sp} = \hat{\boldsymbol{L}}_{sp,R} + \hat{\boldsymbol{L}}_{sp,L} \tag{3.29}$$

- Next, the spin flips are accounted for by the four collapse operators that flip the ground and trion states between the branches R and L:

$$\begin{aligned} \hat{\boldsymbol{C}}_{SF,g_R\to g_L} &= \frac{1}{\sqrt{2\tau_{SF,g}}} \left|g_L\right\rangle \left\langle g_R\right| & \hat{\boldsymbol{C}}_{SF,t_R\to t_L} &= \frac{1}{\sqrt{2\tau_{SF,t}}} \left|t_L\right\rangle \left\langle t_R\right| \\ \hat{\boldsymbol{C}}_{SF,g_L\to g_R} &= \frac{1}{\sqrt{2\tau_{SF,g}}} \left|g_R\right\rangle \left\langle g_L\right| & \hat{\boldsymbol{C}}_{SF,t_L\to t_R} &= \frac{1}{\sqrt{2\tau_{SF,t}}} \left|t_R\right\rangle \left\langle t_L\right| \end{aligned} \tag{3.30}$$

  These operators randomly flip the spin of the hole in the ground states or the electron in the excited states at rates $(2\tau_{SF,g/t})^{-1}$. The spin-flip Lindblad superoperator combines the four contributions:

$$\hat{\boldsymbol{L}}_{SF} = \hat{\boldsymbol{L}}_{g_R\to g_L} + \hat{\boldsymbol{L}}_{g_L\to g_R} + \hat{\boldsymbol{L}}_{t_R\to t_L} + \hat{\boldsymbol{L}}_{t_L\to t_R} \tag{3.31}$$

The master equation of a four-level quantum dot in a micropillar cavity includes the full Hamiltonian (Eq. 3.27) and the Lindblad superoperators of the cavity and quantum dot losses (Eqs. 3.20, 3.29 and 3.31):

$$\hat{\boldsymbol{L}}_{tot} = \hat{\boldsymbol{L}}_{cav} + \hat{\boldsymbol{L}}_{sp} + \hat{\boldsymbol{L}}_{SF} \tag{3.32}$$

$$\boxed{\frac{\mathrm{d}\hat{\boldsymbol{\rho}}(t)}{\mathrm{d}t} = i\left[\hat{\boldsymbol{\rho}}(t), \hat{\boldsymbol{H}}_{tot}\right] + \hat{\boldsymbol{L}}_{tot}\left[\hat{\boldsymbol{\rho}}(t)\right]} \tag{3.33}$$

Conversion to the (H,V) basis

The computation of the photonic polarization state can be implemented in either the (H,V) basis of the cavity eigenmodes or the (R,L) basis of the quantum dot transitions. The choice to work in the (H,V) basis is motivated by the fact that it allows the adiabatic elimination of the cavity to be performed; this approximation reduces the computation Hilbert space by removing the cavity modes, provided that the intracavity photons can adapt fast enough to the changes in the quantum dot state. To do so, we translate to the (H,V) basis the quantum dot operators involved in the photonic subspace through the interaction Hamiltonian of Eq. 3.26 and also through the spontaneous emission.

- The lowering operators follow the same polarization basis change relations as the electric fields (see Eq. 1.17):

$$\begin{pmatrix} \hat{\boldsymbol{\sigma}}_R \\ \hat{\boldsymbol{\sigma}}_L \end{pmatrix} = \frac{1}{\sqrt{2}} \begin{pmatrix} 1 & i \\ 1 & -i \end{pmatrix} \begin{pmatrix} \hat{\boldsymbol{\sigma}}_H \\ \hat{\boldsymbol{\sigma}}_V \end{pmatrix} \tag{3.34}$$

  We can therefore convert the Hamiltonian terms of Eq. 3.26 in the (H,V) basis:

$$\hat{\boldsymbol{H}}_{int} = ig\left(\hat{\boldsymbol{a}}_H^\dagger \hat{\boldsymbol{\sigma}}_H - \hat{\boldsymbol{a}}_H \hat{\boldsymbol{\sigma}}_H^\dagger\right) + ig\left(\hat{\boldsymbol{a}}_V^\dagger \hat{\boldsymbol{\sigma}}_V - \hat{\boldsymbol{a}}_V \hat{\boldsymbol{\sigma}}_V^\dagger\right) \tag{3.35}$$

- For the incoherent processes, only the Lindblad superoperators acting in the photonic subspace need to be translated to the (H,V) basis, so that includes the spontaneous emission but not the spin flips as they are restricted to the quantum dot subspace. When writing the Lindblad superoperator of the spontaneous emission in the (H,V) basis, it appears that the spontaneous emission in the (R,L) branches, each at a rate γ_{sp}, is equivalent to the emission of H- and V-polarized photons from each trion state at a rate $\gamma_{sp}/2$, giving a total rate of emission of γ_{sp} in polarization H and the same in V. Eq. 3.29 becomes:

$$\hat{\boldsymbol{L}}_{sp} = \hat{\boldsymbol{L}}_{sp,H} + \hat{\boldsymbol{L}}_{sp,V} \tag{3.36}$$

where the superoperators in the (H,V) basis are defined with the collapse operators:

$$\hat{\boldsymbol{C}}_{sp,H/V} = \sqrt{\gamma_{sp}}\hat{\boldsymbol{\sigma}}_{H/V} \tag{3.37}$$

Though the model will later be enriched with other loss phenomena (charge blinking, pure dephasing and slow electric noise), we now proceed to simulate the behavior of realistic devices as spin-photon interfaces.

3.2 Numerical simulation of the reflected polarization in the steady state

3.2.1 Outline of the numerical simulation

Steady-state density matrix

The numerical calculations are performed either with the Quantum Optics Toolbox for Matlab [176] or with the QuTiP library for Python [177, 178]. The steady state value of the density matrix is computed by numerically solving the master equation (Eq. 3.33) in the steady state:

$$\frac{\mathrm{d}\hat{\boldsymbol{\rho}}(t)}{\mathrm{d}t} = 0 \iff \hat{\boldsymbol{\rho}} = \hat{\boldsymbol{\rho}}_{ss} \tag{3.38}$$

Simulated Stokes parameters and occupation probabilities

The average value of the intensity in each output polarization is computed as the average of the operator $\hat{\boldsymbol{b}}^{\dagger}_{out}\hat{\boldsymbol{b}}_{out}$ in the steady state, i.e., for polarization X:

$$I_X = \langle \hat{\boldsymbol{b}}^{\dagger}_{out,X}\hat{\boldsymbol{b}}_{out,X}\rangle_{\hat{\boldsymbol{\rho}}_{ss}} = \mathrm{Tr}\Big\{\hat{\boldsymbol{b}}^{\dagger}_{out,X}\hat{\boldsymbol{b}}_{out,X}\cdot\hat{\boldsymbol{\rho}}_{ss}\Big\} \tag{3.39}$$

where $\hat{\boldsymbol{b}}_{out,X} = \hat{\boldsymbol{b}}_{in,X} + \sqrt{\kappa_{top}}\hat{\boldsymbol{a}}_X$. The Stokes parameters are deduced from the output intensities in order to reconstruct the complete output polarization state in the Poincaré sphere, which we study as a function of the energy of the input laser, ω:

$$s_{XY}(\omega) = \frac{I_X(\omega) - I_Y(\omega)}{I_X(\omega) + I_Y(\omega)} \tag{3.40}$$

where $XY \in [HV, DA, RL]$. The Stokes parameters are the coordinates of the Stokes vector $\boldsymbol{S}$, representing the polarization density matrix in the Poincaré sphere.

As for the quantum dot, the occupation probabilities of each state of the four-level system are computed by averaging the spin operators of the appropriate branch:

$$\begin{aligned} P(g_L) &= \langle \hat{\boldsymbol{\sigma}}_L \hat{\boldsymbol{\sigma}}_L^\dagger \rangle_{\hat{\boldsymbol{\rho}}_{ss}} \qquad & P(g_R) &= \langle \hat{\boldsymbol{\sigma}}_R \hat{\boldsymbol{\sigma}}_R^\dagger \rangle_{\hat{\boldsymbol{\rho}}_{ss}} \\ P(t_L) &= \langle \hat{\boldsymbol{\sigma}}_L^\dagger \hat{\boldsymbol{\sigma}}_L \rangle_{\hat{\boldsymbol{\rho}}_{ss}} \qquad & P(t_R) &= \langle \hat{\boldsymbol{\sigma}}_R^\dagger \hat{\boldsymbol{\sigma}}_R \rangle_{\hat{\boldsymbol{\rho}}_{ss}} \end{aligned} \tag{3.41}$$

Spin state initialization

By excluding some spin-flip processes from the total Lindbladian, it is possible to simulate an initialization of the quantum dot in any of the charge states. We call $\hat{\boldsymbol{L}}_{SF}^{(\Uparrow)}$ the total Lindbladian forcing the initialization of the spin in state $|\Uparrow\rangle$ (L branch) and use similar notations for $|\Downarrow\rangle$ (R branch). The spin initialization is accounted for by removing from the general expression of Eq. 3.31 the spin-flip terms that end up in the unwanted branch; the spin-flip contributions to the total Lindbladian become:

$$\begin{aligned} \hat{\boldsymbol{L}}_{SF}^{(\Uparrow)} &= \hat{\boldsymbol{L}}_{g_R \to g_L} + \hat{\boldsymbol{L}}_{t_R \to t_L} \\ \hat{\boldsymbol{L}}_{SF}^{(\Downarrow)} &= \hat{\boldsymbol{L}}_{g_L \to g_R} + \hat{\boldsymbol{L}}_{t_L \to t_R} \end{aligned} \tag{3.42}$$

The steady state simulation with these Lindblad superoperators results in density matrices written for instance $\hat{\boldsymbol{\rho}}_{ss}^{(\Uparrow)}$ for a spin initialized in $|\Uparrow\rangle$. The consecutive intensities and Stokes parameters are labeled $I_X^{(\Uparrow)}$ and $s_{XY}^{(\Uparrow)}$ (pointing to the Stokes vector $\boldsymbol{S}^{(\Uparrow)}$ in the Poincaré sphere).

Common parameters

We take default parameters for the following simulations that are similar to the actual specifications of the samples studied in chapters 4 and 5, although with simplifications (no cavity splitting, no cavity-quantum dot detuning, no charge blinking). This set of parameters will be effective for the rest of the current chapter unless stated otherwise:

$$\left|\begin{aligned} P_{in} &= 1\,\mathrm{pW} \\ |\Psi_{in}\rangle &= |H\rangle \\ \eta_{in} &= 1 \\ P_c &= 1 \end{aligned}\right. \quad \left|\begin{aligned} \omega_c &= 1.3392\,\mathrm{eV} \\ \omega_{c,H} &= \omega_c + \Delta_{HV}/2 \\ \omega_{c,V} &= \omega_c - \Delta_{HV}/2 \\ \Delta_{HV} &= 0\,\mu\mathrm{eV} \\ \omega_d &= \omega_c \end{aligned}\right. \quad \left|\begin{aligned} g &= 15\,\mu\mathrm{eV} \\ \gamma_{sp} &= 0.6\,\mu\mathrm{eV} \\ \gamma^* &= 0\,\mu\mathrm{eV} \\ \gamma &= 0.3\,\mu\mathrm{eV} \\ \tau_{SF,g} &= 2\,\mu\mathrm{s} \\ \tau_{SF,t} &= 100\,\mathrm{ns} \end{aligned}\right. \tag{3.43}$$

- The input laser is CW, H-polarized and has a low power P_{in} to avoid saturation of the quantum dot transition. The input coupling η_{in} is assumed to be perfect as well as the charge occupation probability P_c.
- The cavity splitting Δ_{HV} is null and the energy of the quantum dot transition matches that of the cavity.
- We consider an absence of pure dephasing $\gamma^* = 0\,\mu\mathrm{eV}$ and therefore a total dephasing rate $\gamma = \gamma^* + \gamma_{sp}/2 = 0.3\,\mu\mathrm{eV}$.

The cavity width κ and the top mirror output coupling η_{top} will be adjusted for each example. In particular, κ will be calculated to match the desired cooperativity: $\kappa = g^2/(\gamma C)$. For the following example, we choose the parameters $\kappa = 375\,\mu\mathrm{eV}$ and $\eta_{top} = 0.9$, close to the specifications of the *positively charged device* studied later in chapter 4. In the next sections, we compute the reflected polarization states, first with initialized spin states to model the spin-dependent polarization rotation, then without spin initialization to understand the effect of spin averaging, followed by an explanation of the effect of cavity splitting and finally, a study of the influence of the two figures of merit C and η_{top}.

3.2.2 Reflected polarization state with an initialized quantum dot spin

Spin initialized in $|\Uparrow\rangle$

We first focus on the case where the quantum dot is initialized in the state $|\Uparrow\rangle$ using the spin-flip Lindbladian $\hat{\boldsymbol{L}}_{SF}^{(\Uparrow)}$ from Eq. 3.42, instead of the general expression $\hat{\boldsymbol{L}}_{SF}$. The reflected intensities denoted $I_X^{(\Uparrow)}$ in polarization X are plotted in Fig. 3.4 as a function of the normalized laser-quantum dot detuning $\Delta_d = (\omega - \omega_d)/\Gamma$, the total emission rate being $\Gamma = 4g^2/\kappa + \gamma_{sp}$, equal in the present case to $(220\,\mathrm{ps})^{-1}$, equivalent to $3\,\mu\mathrm{eV}$. The computed intensities are normalized by the incident one so the result is analogous to the reflectivity measured in Fig. 2.6.

The $I_H^{(\Uparrow)}$ component is produced by the interference of the photons reflected by the empty cavity (forming a large Lorentzian dip) with the photons that have interacted with the quantum dot (deep narrow dip on top of the cavity one). On the other hand, the $I_V^{(\Uparrow)}$ component corresponds to the polarization orthogonal to the excitation and contains only photons resulting from the quantum dot cross-polarized emission.

A zoom on the quantum dot to the horizontal axis range $\Delta_d \in [-6, 6]$ is plotted in Fig. 3.5, where the reflected intensities in each polarization (in solid lines) are superimposed with the intensities that would be reflected by a cold cavity (in dashed lines). As the quantum dot is initialized in $|\Uparrow\rangle$ (L branch), the intensity $I_R^{(\Uparrow)}$ corresponds to the response of the bare cavity whereas $I_L^{(\Uparrow)}$ undergoes the quantum dot phase shift (hot cavity), exactly as discussed in subsection 1.3.4.

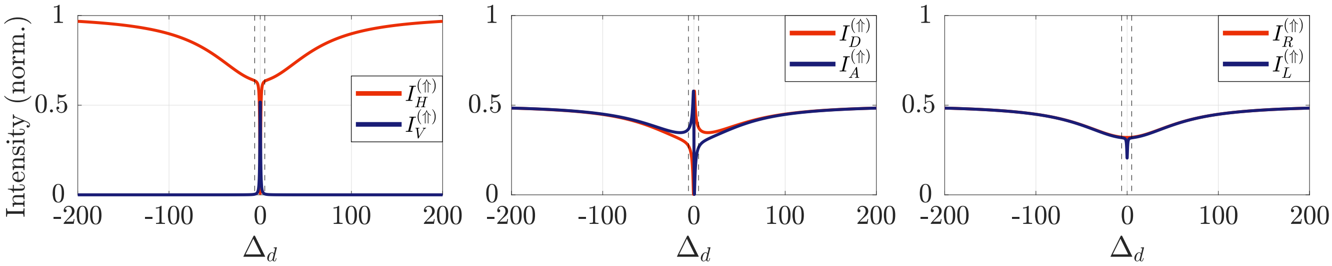

FIGURE 3.4: Normalized reflected intensities in the H,V;D,A;R,L polarizations as a function of the normalized laser-quantum dot detuning $\Delta_d = (\omega - \omega_d)/\Gamma$ with an H-polarized input and a quantum dot charge state initialized in $|\Uparrow\rangle$. The broad cavity dip in H,D,A,R,L is superimposed with narrow quantum dot features. A zoom on the central energy range (dashed lines) is shown in the next figure.

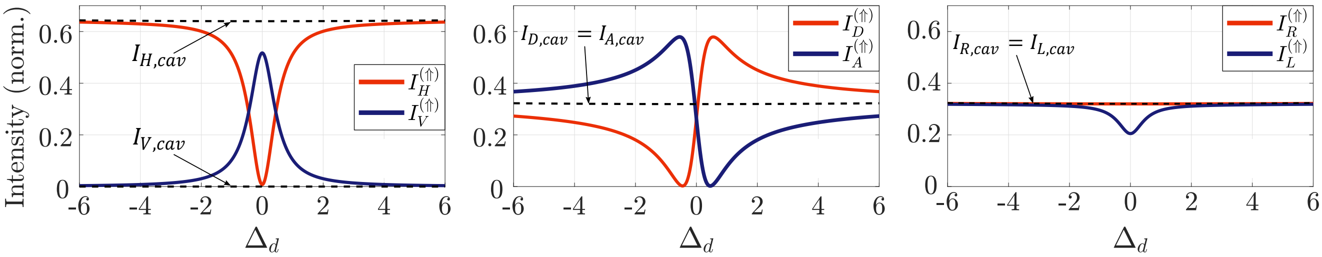

FIGURE 3.5: Normalized reflected intensities as a function of the normalized laser-quantum dot detuning as presented in the previous figure, focused on the central detuning range. The intensities for a quantum dot initialized in the $|\Uparrow\rangle$ state, $I_X^{(\Uparrow)}$, are plotted with solid lines along with those for an empty cavity in dashed lines.

Finally, the Stokes parameters $s_{XY}^{(\Uparrow)}$ defining the coordinates of the Stokes vector $\boldsymbol{S}^{(\Uparrow)}$ in the Poincaré sphere are calculated from the previous intensities using Eq. 3.40; they are plotted in Fig. 3.6a and aggregated as Stokes vectors in Fig. 3.6b. In the current case of an initialization in the $|\Uparrow\rangle$ state, the reflected polarization state is pure and the Stokes vector is equal to $|\Psi_{\Uparrow}\rangle$. Here, the arrows point to specific values of the Stokes vector for different detunings.

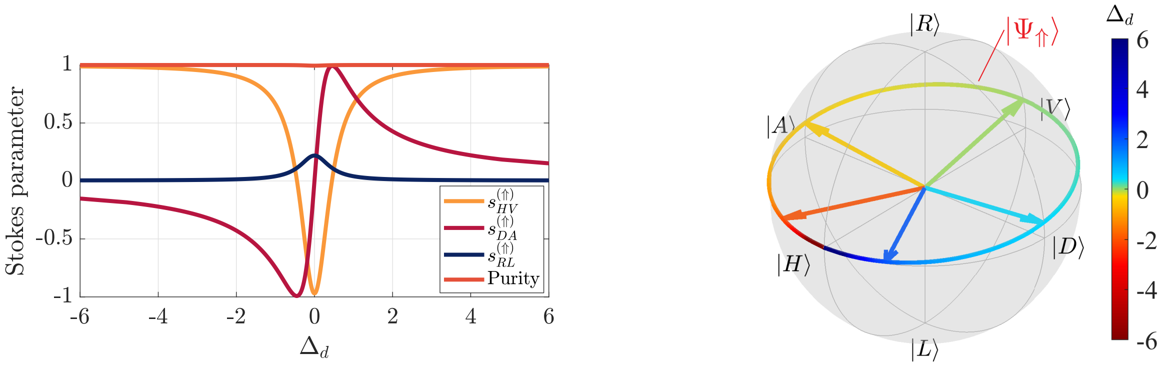

(a) (b)

FIGURE 3.6: **(a)** Stokes parameters of the reflected polarization state when the quantum dot is initialized in $|\Uparrow\rangle$, $s_{XY}^{(\Uparrow)}$, calculated from the reflected intensities shown in Fig. 3.5. **(b)** Trajectory of $\boldsymbol{S}^{(\Uparrow)} = |\Psi_{\Uparrow}\rangle$ in the Poincaré sphere as a function of the normalized laser-quantum dot detuning. The solid arrows point to the values of $|\Psi_{\Uparrow}\rangle$ for different color-coded detunings.

Spin initialized in $|\Downarrow\rangle$

Next, we detail the case of a quantum dot initialized in the $|\Downarrow\rangle$ state, enabled by using the spin-flip Lindbladian $\hat{\boldsymbol{L}}_{SF}^{(\Downarrow)}$. The reflected intensities are plotted in Fig. 3.7. As compared to the initialization in $|\Uparrow\rangle$, we find that:

$$\begin{aligned} I_H^{(\Downarrow)} &= I_H^{(\Uparrow)} & I_V^{(\Downarrow)} &= I_V^{(\Uparrow)} \\ I_D^{(\Downarrow)} &= I_A^{(\Uparrow)} & I_A^{(\Downarrow)} &= I_D^{(\Uparrow)} \\ I_L^{(\Downarrow)} &= I_R^{(\Uparrow)} & I_R^{(\Downarrow)} &= I_L^{(\Uparrow)} \end{aligned} \tag{3.44}$$

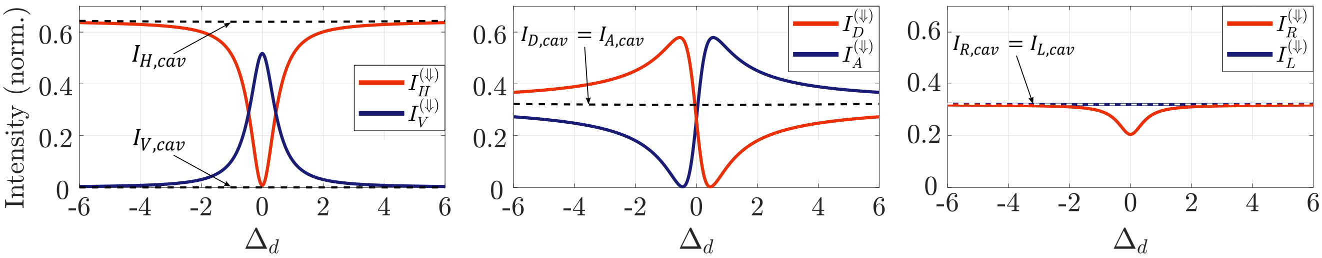

FIGURE 3.7: Normalized reflected intensities as a function of the normalized laser-quantum dot detuning. The intensities for a quantum dot initialized in the $|\Downarrow\rangle$ state, $I_X^{(\Downarrow)}$, are plotted with solid lines along with those for an empty cavity in dashed lines.

By consequence, $s_{HV}^{(\Downarrow)} = s_{HV}^{(\Uparrow)}$, $s_{DA}^{(\Downarrow)} = -s_{DA}^{(\Uparrow)}$ and $s_{RL}^{(\Downarrow)} = -s_{RL}^{(\Uparrow)}$. The Stokes parameters and the Poincaré sphere are plotted in Fig. 3.8. The dashed arrows point to specific values of the Stokes vector for the same detunings as before. The symmetry relations developed here show not only that $|\Psi_\Downarrow\rangle$ is the symmetrical of $|\Psi_\Uparrow\rangle$ with respect to the (HVDA) plane, but also with respect to the (HRVL) plane: this is why as Δ_d increases, $|\Psi_\Uparrow\rangle$ describes a circle in the clockwise direction starting from H whereas $|\Psi_\Downarrow\rangle$ goes counterclockwise.

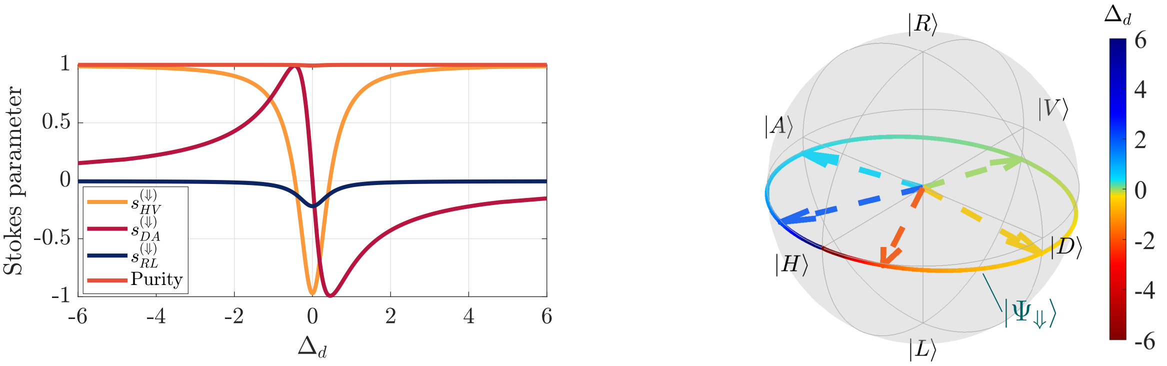

(a) (b)

FIGURE 3.8: **(a)** Stokes parameters of the reflected polarization state when the quantum dot is initialized in $|\Downarrow\rangle$, $s_{XY}^{(\Downarrow)}$, calculated from the reflected intensities shown in Fig. 3.7. **(b)** Trajectory of $\boldsymbol{S}^{(\Downarrow)} = |\Psi_\Downarrow\rangle$ in the Poincaré sphere as a function of the normalized laser-quantum dot detuning The dashed arrows point to the values of $|\Psi_\Downarrow\rangle$ for different color-coded detunings.

Working points for an ideal spin-photon interface

In Fig. 3.9, we show the two Stokes vectors $\boldsymbol{S}^{(\Uparrow)}$ and $\boldsymbol{S}^{(\Downarrow)}$ as a function of Δ_d in order to evidence the existence of particular detuning values that allow $\langle\Psi_\Uparrow|\Psi_\Downarrow\rangle = 0$, the criterion for an ideal spin-photon interface. The scalar product is defined in the Poincaré sphere for pure or mixed states by:

$$\boxed{\left|\left\langle \boldsymbol{S}^{(1)} \middle| \boldsymbol{S}^{(2)} \right\rangle\right|^2 = \frac{1 + s_{HV}^{(1)} s_{HV}^{(2)} + s_{DA}^{(1)} s_{DA}^{(2)} + s_{RL}^{(1)} s_{RL}^{(2)}}{2}} \tag{3.45}$$

Therefore, orthogonal Stokes vectors are parallel and pointing in opposite directions in the Poincaré sphere. The noticeable values of the detuning that meet the condition of the ideal spin-photon interface are $\Delta_{opt} = \pm 0.45$ (here equivalent to $\omega - \omega_d = \pm 1.35\,\mu\text{eV}$), and are highlighted in light blue and yellow in the figure. The arrows corresponding to $|\Psi_{\Uparrow}\rangle$ and $|\Psi_{\Downarrow}\rangle$ at the optimal detunings indeed point in opposite directions.

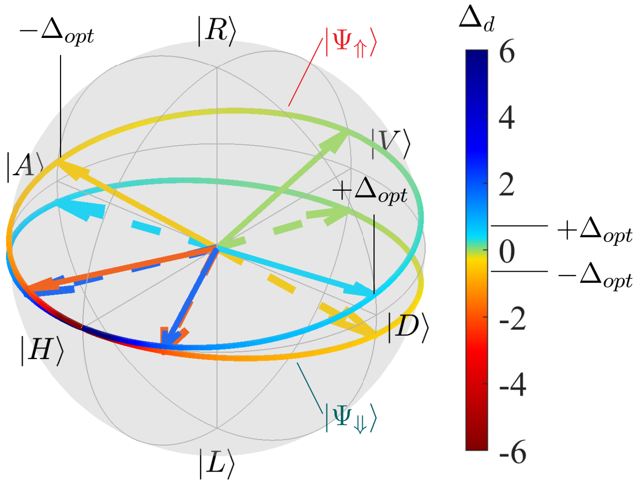

FIGURE 3.9: Trajectories of $|\Psi_{\Uparrow}\rangle$ and $|\Psi_{\Downarrow}\rangle$ in the Poincaré sphere as a function of the normalized laser-quantum dot detuning $\Delta_d = (\omega - \omega_d)/\Gamma$. The solid arrows point to $|\Psi_{\Uparrow}\rangle$ and the dashed arrows to $|\Psi_{\Downarrow}\rangle$ for different detunings. The optimal detunings to have $\langle \Psi_{\Uparrow} | \Psi_{\Downarrow} \rangle = 0$ are indicated at $\pm\Delta_{opt}$.

3.2.3 Averaging of the spin states

In a situation where the spin state in not initialized, the states $|\Uparrow\rangle$ and $|\Downarrow\rangle$ are equally likely and the resulting reflected intensities become the average of the initialized intensities: $I_X^{(avg)} = \left(I_X^{(\Uparrow)} + I_X^{(\Downarrow)}\right)/2$. The symmetries between the two initialized states described in Eq. 3.44 let us infer that:

$$s_{HV}^{(avg)} = \frac{s_{HV}^{(\Uparrow)} + s_{HV}^{(\Downarrow)}}{2} \qquad\qquad s_{DA}^{(avg)} = s_{RL}^{(avg)} = 0 \tag{3.46}$$

The Stokes vector in the non-initialized case, represented in Fig. 3.10, therefore stays on the (HV) axis of the Poincaré sphere. The condition $\langle \Psi_{\Uparrow} | \Psi_{\Downarrow} \rangle = 0$ is reached for detunings $\pm\Delta_{opt}$: at these points, $\boldsymbol{S}^{(avg)} = 0$, as shown in Fig. 3.11. In fact, the ideal spin-photon interface criterion can be met only if $s_{HV}^{(avg)}(\Delta_d = 0) \leq 0$. A critical experimental step is therefore to measure the dip of $s_{HV}^{(avg)}$ and to try to maximize its contrast.

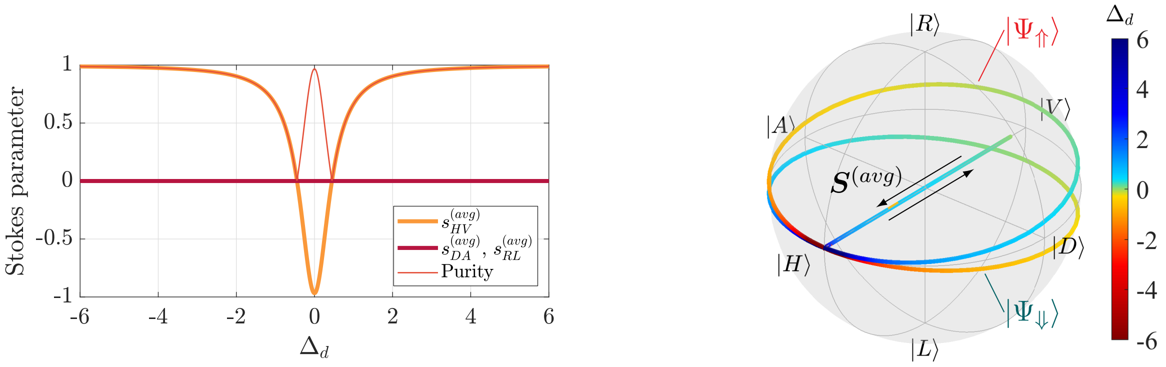

(a)

(b)

FIGURE 3.10: Effect of the averaging of $|\Psi_\Uparrow\rangle$ and $|\Psi_\Downarrow\rangle$ when the spin is not initialized: **(a)** Stokes parameters of the average state $S^{(avg)}$ and **(b)** Poincaré sphere representation.

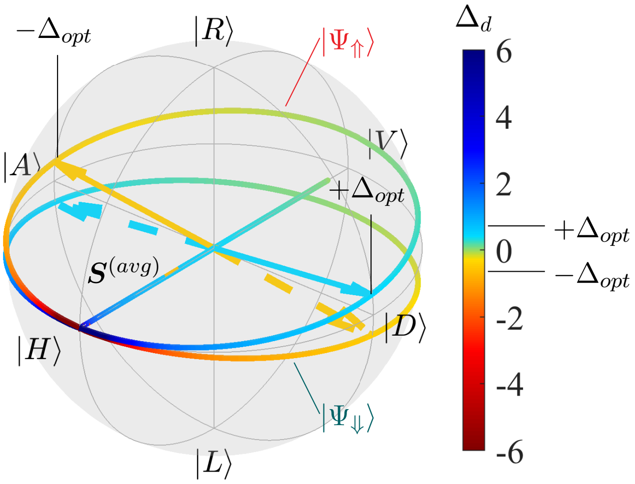

FIGURE 3.11: Trajectories of $|\Psi_\Uparrow\rangle$, $|\Psi_\Downarrow\rangle$ and $S^{(avg)}$ in the Poincaré sphere as a function of the normalized laser-quantum dot detuning. The solid arrows point to $|\Psi_\Uparrow\rangle$ and the dashed arrows to $|\Psi_\Downarrow\rangle$ for the specific detunings $\pm\Delta_{opt}$ achieving $\langle\Psi_\Uparrow|\Psi_\Downarrow\rangle = 0$.

3.2.4 Influence of the cavity splitting

The previous simulations supposed a null cavity splitting. Introducing this energy difference between the two modes of the cavity only rotates the trajectories of $|\Psi_\Uparrow\rangle$ and $|\Psi_\Downarrow\rangle$ about the (HV) axis of the Poincaré sphere, as shown in Fig. 3.12 for the case of a cavity splitting $\Delta_{HV} = 70\,\mu\text{eV}$. The averaged Stokes vector $S^{(avg)}$ is identical to the case without cavity splitting, owing to its rotational symmetry about (HV).

The optimal detunings $\pm\Delta_{opt}$ to get $\langle\Psi_\Uparrow|\Psi_\Downarrow\rangle = 0$ are detailed in Fig. 3.13: they are identical to those found without cavity splitting, but the values of $|\Psi_\Uparrow\rangle$ and $|\Psi_\Downarrow\rangle$ are changed. In the rest of this chapter, the splitting will be ignored for clarity but it will become relevant when studying realistic samples in the next chapters.

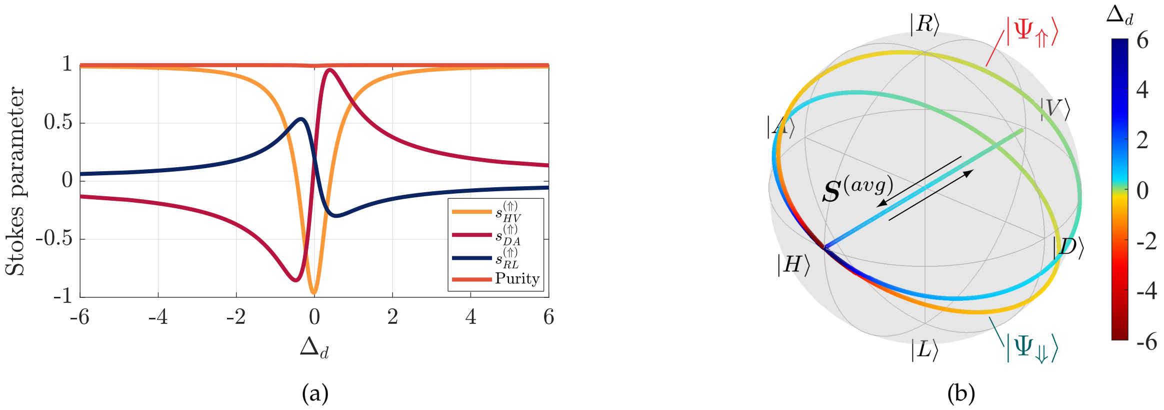

(a) (b)

FIGURE 3.12: **(a)** Stokes parameters for a spin initialized in $|\Uparrow\rangle$, $s_{XY}^{(\Uparrow)}$, with a cavity splitting $\Delta_{HV} = 70\,\mu\text{eV}$. **(b)** Poincaré sphere representation of $|\Psi_\Uparrow\rangle$, $|\Psi_\Downarrow\rangle$ and $\boldsymbol{S}^{(avg)}$ with a cavity splitting.

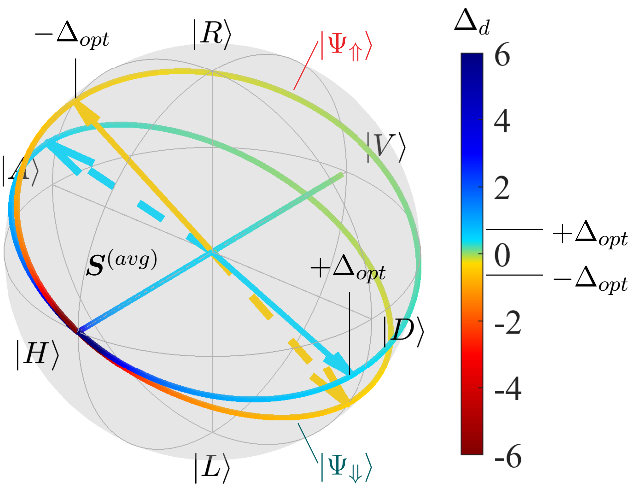

FIGURE 3.13: Trajectories of $|\Psi_\Uparrow\rangle$, $|\Psi_\Downarrow\rangle$ and $\boldsymbol{S}^{(avg)}$ in the Poincaré sphere with a cavity splitting $\Delta_{HV} = 70\,\mu\text{eV}$. The solid arrows point to $|\Psi_\Uparrow\rangle$ and the dashed arrows to $|\Psi_\Downarrow\rangle$ for the specific detunings $\pm\Delta_{opt}$ achieving $\langle\Psi_\Uparrow|\Psi_\Downarrow\rangle = 0$.

3.2.5 Influence of the top mirror output coupling and cooperativity

The efficiency of the spin-photon interaction is governed by the cooperativity $C = g^2/(\kappa\gamma)$ and the top mirror output coupling $\eta_{top} = \kappa_{top}/\kappa$. We study the effect of these two figures of merit on the trajectories of $|\Psi_\Uparrow\rangle$ and $|\Psi_\Downarrow\rangle$ in the Poincaré sphere (Fig. 3.14). The detunings for which $\langle\Psi_\Uparrow|\Psi_\Downarrow\rangle = 0$ (if they exist) are highlighted by black dots on $|\Psi_\Uparrow\rangle$ and $|\Psi_\Downarrow\rangle$ and linked by dashed lines. We start from the figures of merit of three real samples:

(1)	$C = 0.2$	$\eta_{top} = 0.4$	Sample similar to *Arnold et al. (2015)* [27]
(2)	$C = 2$	$\eta_{top} = 0.9$	*positively charged device*
(3)	$C = 4$	$\eta_{top} = 0.7$	*negatively charged device*

We then proceed to simulate all the possible combinations of the two figures of merit. The value of κ is varied to adjust C, and η_{top} is changed independently. To obtain $C = 0.2$, 2 and 4, the cavity losses are taken at $\kappa = 3.75\,\text{meV},\ 375\,\mu\text{eV}$ and $187.5\,\mu\text{eV}$.

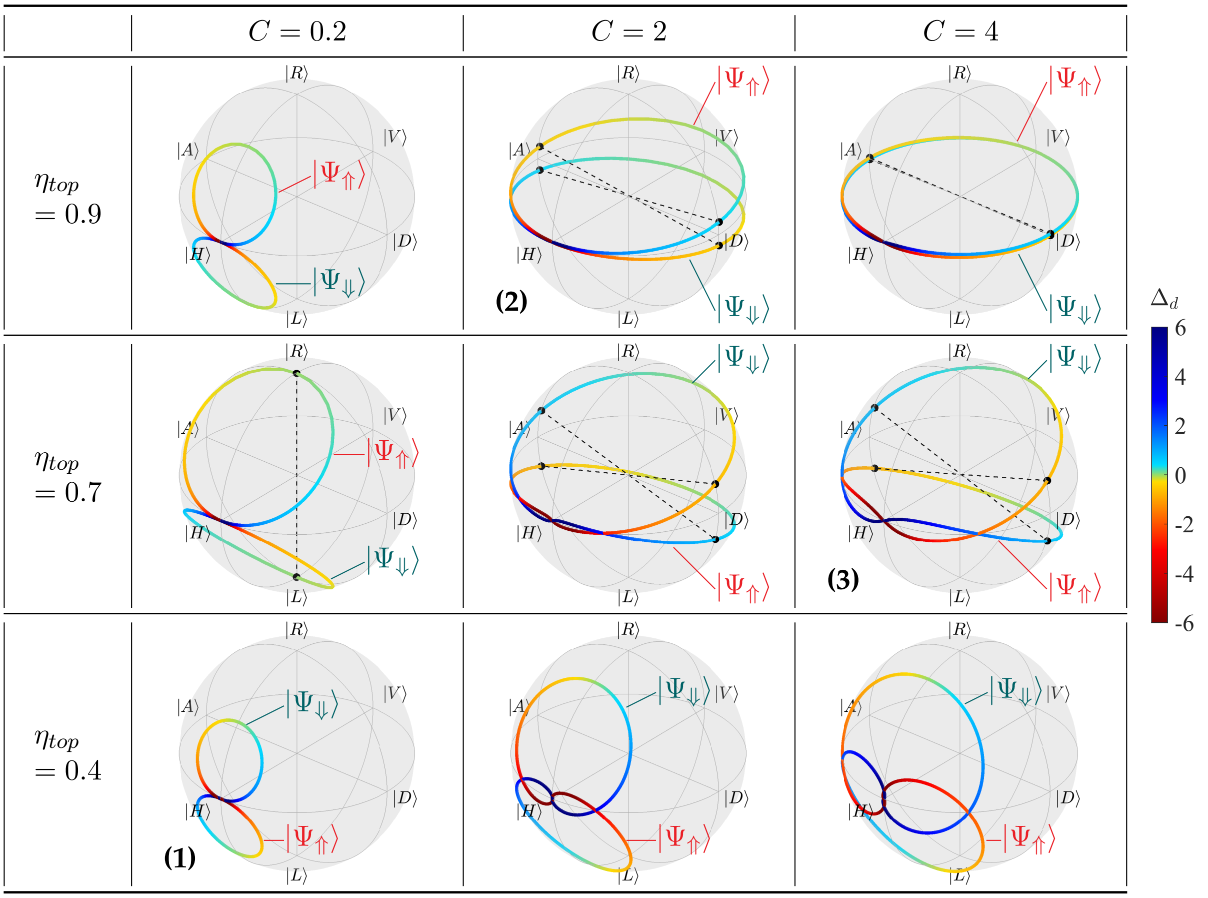

FIGURE 3.14: Trajectories of $|\Psi_\Uparrow\rangle$ and $|\Psi_\Downarrow\rangle$ as a function of the normalized laser-quantum dot detuning $\Delta_d = (\omega - \omega_d)/\Gamma$, for different values of the top mirror output coupling and of the cooperativity. Black dots show the values of $|\Psi_\Uparrow\rangle$ and $|\Psi_\Downarrow\rangle$ if they achieve $\langle\Psi_\Uparrow|\Psi_\Downarrow\rangle = 0$ at certain detunings. **(1)** is similar to the sample from [27], **(2)** to the *positively charged device* and **(3)** to the *negatively charged device*.

For $C = 0.2$, only the case $\eta_{top} = 0.7$ achieves $\langle\Psi_\Uparrow|\Psi_\Downarrow\rangle = 0$ at $|\Psi_\Uparrow\rangle = |R\rangle$ and $|\Psi_\Downarrow\rangle = |L\rangle$. Incidentally, there is a reverse of $|\Psi_\Uparrow\rangle$ and $|\Psi_\Downarrow\rangle$ with respect to the equatorial plane when passing from $\eta_{top} = 0.4$ to $\eta_{top} = 0.7$ and higher.

For $C = 2$ and $C = 4$, it is possible to find $\langle\Psi_\Uparrow|\Psi_\Downarrow\rangle = 0$ for $\eta_{top} = 0.7$ and $\eta_{top} = 0.9$, but not for $\eta_{top} = 0.4$. This time, the inversion of $|\Psi_\Uparrow\rangle$ and $|\Psi_\Downarrow\rangle$ with respect to the equatorial plane happens between $\eta_{top} = 0.7$ and $\eta_{top} = 0.9$.

This study shows how a quantum dot coupled to a micropillar cavity can constitute an ideal spin-photon interface provided that device parameters are carefully adjusted to obtain the appropriate values of C and η_{top}. In the next section, the dynamics of the system is explored with an emphasis on the experimentally measured quantities, which are the reflected intensities in the different polarizations and their time correlations.

3.3 Effect of a photon detection on the quantum dot system

The study of the quantum measurement is of particular interest for a spin-photon interface as its fundamental objective is to imprint the state of a spin on the state of a photon or vice versa: its performance can therefore be assessed by the quality of the projective measurement it allows (i.e., how efficiently the spin can be projected by a photonic measurement). In this section, we use the numerical simulation to predict the evolution of the quantum dot spin and of the polarization of the reflected photons after a photon is detected in a specific state. We study the indirect effect of this evolution in the correlations between detected photons in two complementary polarizations as it will be the experimentally measured quantity in the framework of spin-noise spectroscopy. In this regard, we introduce the following notations, in the general case of a first detected photon in the X polarization and a second one in Y: the conditioned intensity $\widetilde{I_{Y|X}}(t)$ stands for the photon flux in polarization Y at time t when an X-polarized photon is detected at time $t = 0$, and the cross-correlation function, giving the conditioned intensity normalized by the unconditioned one:

$$g^{(2)}_{XY}(\tau) = \frac{\widetilde{I_{Y|X}}(\tau)}{I_Y}$$

3.3.1 Time-resolved numerical simulations

Principle of the calculation

Before the measurement of a photon, the system comprising the quantum dot and the cavity field is in its stationary state $\hat{\boldsymbol{\rho}}_{ss}$ and the measured quantities are calculated by tracing operators over this density matrix (Eq. 3.4). For instance, the intensity reflected in polarization X is defined as follows, dropping the *out* subscript for $\hat{\boldsymbol{b}}_X$ and using the invariance of the trace operation under a circular permutation:

$$I_X = \langle \hat{\boldsymbol{b}}_X^\dagger \hat{\boldsymbol{b}}_X \rangle_{\hat{\boldsymbol{\rho}}_{ss}} = \mathrm{Tr}\Big\{ \hat{\boldsymbol{b}}_X^\dagger \hat{\boldsymbol{b}}_X \cdot \hat{\boldsymbol{\rho}}_{ss} \Big\} = \mathrm{Tr}\Big\{ \hat{\boldsymbol{b}}_X \cdot \hat{\boldsymbol{\rho}}_{ss} \cdot \hat{\boldsymbol{b}}_X^\dagger \Big\} \tag{3.47}$$

where $\hat{\boldsymbol{b}}_X = \hat{\boldsymbol{b}}_{in,X} + \sqrt{\kappa_{top}}\hat{\boldsymbol{a}}_X$.The measurement of a photon in polarization X at time $t = 0$ projects the density matrix along the measured polarization. We translate this phenomenon mathematically with operators that are conditioned by this measurement, and symbolically by writing them with a tilde. The density matrix is transformed from $\hat{\boldsymbol{\rho}}_{ss}$ into the conditional density matrix labeled $\widetilde{\hat{\boldsymbol{\rho}}_X}$ defined at a time $t = 0^+$ right after the photon detection in X at $t = 0$, which we write $(t = 0^+|X, 0)$ [81, 179]:

$$\boxed{\widetilde{\hat{\boldsymbol{\rho}}_X}(t = 0^+) = \widetilde{\hat{\boldsymbol{\rho}}}\left(t = 0^+|X, 0\right) = \frac{\hat{\boldsymbol{b}}_X \cdot \hat{\boldsymbol{\rho}}_{ss} \cdot \hat{\boldsymbol{b}}_X^\dagger}{\mathrm{Tr}\Big\{ \hat{\boldsymbol{b}}_X \cdot \hat{\boldsymbol{\rho}}_{ss} \cdot \hat{\boldsymbol{b}}_X^\dagger \Big\}} = \frac{\hat{\boldsymbol{b}}_X \cdot \hat{\boldsymbol{\rho}}_{ss} \cdot \hat{\boldsymbol{b}}_X^\dagger}{I_X}} \tag{3.48}$$

The numerical simulation computes the temporal evolution of the density matrix, it therefore propagates from $\widetilde{\hat{\boldsymbol{\rho}}_X}(t = 0^+)$ to $\widetilde{\hat{\boldsymbol{\rho}}_X}(t)$, and when $t \to \infty$, the density matrix evolves back to $\hat{\boldsymbol{\rho}}_{ss}$.

Calculation of the reflected intensities

We now deal with the probabilities to detect photons in a detector, which are proportional to the average intensity in the associated polarization: $P(X) \propto I(X)$. The average[1] intensity in detector Y at time t, conditioned by the detection of a photon in X at $t = 0$, is calculated in the Schrödinger representation by letting the density matrix evolve: $\widetilde{\hat{\boldsymbol{\rho}}_X}(t)$ is computed and the intensity is calculated as in Eq. 3.47:

$$\boxed{\widetilde{I_{Y|X}}(t) = \langle \hat{\boldsymbol{b}}_Y^\dagger \hat{\boldsymbol{b}}_Y \rangle_{\widetilde{\hat{\boldsymbol{\rho}}_X}(t)} = \mathrm{Tr}\Big\{ \hat{\boldsymbol{b}}_Y^\dagger \hat{\boldsymbol{b}}_Y \cdot \widetilde{\hat{\boldsymbol{\rho}}_X}(t) \Big\}} \tag{3.49}$$

A similar calculation is carried out to compute the population of the ground and trion states, conditioned by the detection of an X-polarized photon at time $t = 0$, by replacing the operator $\hat{\boldsymbol{b}}_Y^\dagger \hat{\boldsymbol{b}}_Y$ by the appropriate population operator ($\hat{\boldsymbol{\sigma}}_{R/L}^\dagger \hat{\boldsymbol{\sigma}}_{R/L}$ for the trion state populations $|t_{L/R}\rangle$ and $\hat{\boldsymbol{\sigma}}_{R/L} \hat{\boldsymbol{\sigma}}_{R/L}^\dagger$ for the ground state populations $|g_{L/R}\rangle$).

Calculation of the cross-correlations

The cross-correlations in the (X,Y) basis can be defined by the ratio between the probability of detecting a photon in polarization Y at a delay τ after a photon was detected in polarization X at delay 0, divided by the unconditioned probability. We translate this formula in experimental terms by replacing the probabilities with intensities to which they are proportional :

$$\boxed{g_{XY}^{(2)}(\tau) = \frac{\widetilde{P(Y|X)}(\tau)}{P(Y)} = \frac{\widetilde{I_{Y|X}}(\tau)}{I_Y}} \tag{3.50}$$

It is worth noticing that as $\tau \to \infty$, the system loses the memory of the measurement event and $\widetilde{\hat{\boldsymbol{\rho}}_X} \to \hat{\boldsymbol{\rho}}_{ss}$, so the cross-correlation tends to unity.

This definition of the cross-correlation is equivalent to the usual one written with the field operators in the Heisenberg representation:

$$g_{XY}^{(2)}(\tau) = \frac{\Big\langle \hat{\boldsymbol{b}}_X^\dagger(0) \hat{\boldsymbol{b}}_Y^\dagger(\tau) \hat{\boldsymbol{b}}_Y(\tau) \hat{\boldsymbol{b}}_X(0) \Big\rangle_{\hat{\boldsymbol{\rho}}_{ss}}}{\Big\langle \hat{\boldsymbol{b}}_X^\dagger(0) \hat{\boldsymbol{b}}_X(0) \Big\rangle_{\hat{\boldsymbol{\rho}}_{ss}} \cdot \Big\langle \hat{\boldsymbol{b}}_Y^\dagger(\tau) \hat{\boldsymbol{b}}_Y(\tau) \Big\rangle_{\hat{\boldsymbol{\rho}}_{ss}}} = \frac{\mathrm{Tr}\Big\{ \hat{\boldsymbol{b}}_X^\dagger(0) \hat{\boldsymbol{b}}_Y^\dagger(\tau) \hat{\boldsymbol{b}}_Y(\tau) \hat{\boldsymbol{b}}_X(0) \cdot \hat{\boldsymbol{\rho}}_{ss} \Big\}}{I_X I_Y} \tag{3.51}$$

Indeed, by a circular permutation, the density matrix after a photon detection in X, $\hat{\boldsymbol{\rho}}_X$, can be identified in the numerator (using Eq. 3.48):

$$\begin{aligned} &\mathrm{Tr}\Big\{ \hat{\boldsymbol{b}}_X^\dagger(0) \hat{\boldsymbol{b}}_Y^\dagger(\tau) \hat{\boldsymbol{b}}_Y(\tau) \hat{\boldsymbol{b}}_X(0) \cdot \hat{\boldsymbol{\rho}}_{ss} \Big\} \\ =& \mathrm{Tr}\Big\{ \hat{\boldsymbol{b}}_Y^\dagger(\tau) \hat{\boldsymbol{b}}_Y(\tau) \hat{\boldsymbol{b}}_X(0) \cdot \hat{\boldsymbol{\rho}}_{ss} \cdot \hat{\boldsymbol{b}}_X^\dagger(0) \Big\} \\ =& I_X \, \mathrm{Tr}\Big\{ \hat{\boldsymbol{b}}_Y^\dagger(\tau) \hat{\boldsymbol{b}}_Y(\tau) \cdot \widetilde{\hat{\boldsymbol{\rho}}_X}(t = 0^+) \Big\} \end{aligned} \tag{3.52}$$

---

[1] This is the average over many repetitions of the experiment.

The two definitions of $g^{(2)}_{XY}(\tau)$ are thus equivalent, and simply correspond to a choice of representation:

$$\text{Heisenberg representation: } g^{(2)}_{XY}(\tau) = \mathrm{Tr}\left\{\hat{\boldsymbol{b}}^{\dagger}_{Y}(\tau)\hat{\boldsymbol{b}}_{Y}(\tau)\cdot\widetilde{\hat{\boldsymbol{\rho}}_{X}}(t=0^{+})\right\}\Big/ I_Y \tag{3.53}$$

$$\text{Schrödinger representation: } g^{(2)}_{XY}(\tau) = \mathrm{Tr}\left\{\hat{\boldsymbol{b}}^{\dagger}_{Y}\hat{\boldsymbol{b}}_{Y}\cdot\widetilde{\hat{\boldsymbol{\rho}}_{X}}(\tau)\right\}\Big/ I_Y = \frac{\widetilde{I_{Y|X}(\tau)}}{I_Y}. \tag{3.54}$$

In our numerical simulations, the cross-correlations are processed in the Schrödinger representation by computing the density matrix evolving with time and using it to calculate the average value of constant operators.

3.3.2 Choice of an optimal configuration for perfect spin measurement with a single detected photon

Let the sample properties be that of example **(2)** of Fig. 3.14 ($C = 2$, $\eta_{top} = 0.9$) and the input laser be CW, H-polarized with a power of 1 pW and tuned to the optimal detuning $-\Delta_{opt}$ such that $\langle\Psi_{\Uparrow}|\Psi_{\Downarrow}\rangle = 0$. The working point (WP) is illustrated in Fig. 3.15.

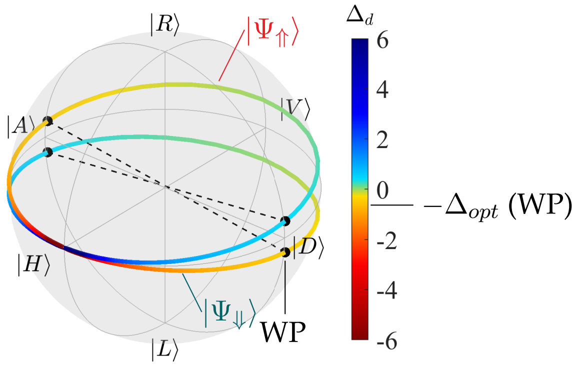

FIGURE 3.15: Trajectories of $|\Psi_{\Uparrow}\rangle$ and $|\Psi_{\Downarrow}\rangle$ in the case $C = 2$ and $\eta_{top} = 0.9$, corresponding to configuration **(2)** of Fig. 3.14. The working point (WP) for this section is $\Delta_d = -\Delta_{opt}$.

We measure the reflected photons in polarization bases that we call $(\theta, \overline{\theta})$: these orthogonal polarization vectors are defined in Fig. 3.16, they are located on the meridian circle comprising (D,R,A,L) and determined by their latitude angle θ (their longitude is always $\Phi = \pi/2$). In this example, the basis characterized by $\theta = \theta_{opt} = -6.4°$ is called the *optimal basis*, since it gives the following match:

$$\begin{aligned} |\theta_{opt}\rangle &= |\Psi_{\Downarrow}\rangle\ (\Delta_d = -\Delta_{opt}) \\ |\overline{\theta_{opt}}\rangle &= |\Psi_{\Uparrow}\rangle\ (\Delta_d = -\Delta_{opt}) \end{aligned} \tag{3.55}$$

A perfect projective measurement is therefore expected when measuring a photon in $|\theta_{opt}\rangle$ or $|\overline{\theta_{opt}}\rangle$ since $\langle\theta_{opt}|\overline{\theta_{opt}}\rangle = 0$. The experimental setup in Fig. 3.16 shows how cross-correlations are measured in the $(\theta_{opt}, \overline{\theta_{opt}})$ basis:

1. First, a photon is detected in $|\theta_{opt}\rangle = |\Psi_{\Downarrow}\rangle$. The measurement projects the spin on the associated state $|\Downarrow\rangle$.

2. After a delay τ, a detection event is registered in $\left|\overline{\theta_{opt}}\right\rangle = |\Psi_{\Uparrow}\rangle$. The histogram of the delays constitutes the cross-correlations $g^{(2)}_{\theta_{opt}\overline{\theta_{opt}}}(\tau)$. The deeper the anti-correlation dip at short delays, the better the measurement-induced spin projection.

The description of the measurement in terms of spin unfolds in the following simplified sequence:

- Before the measurement ($t = 0^-$), the spin is not initialized, so it has a 50 % probability of being in state $|\Uparrow\rangle$ (thus rotating the output polarization to $|\Psi_{\Uparrow}\rangle$) and the same probability of being in state $|\Downarrow\rangle$ (thus rotating the output polarization to $|\Psi_{\Downarrow}\rangle$). The density matrix of the system is approximately equal to $0.5\,|\Uparrow\rangle\langle\Uparrow| + 0.5\,|\Downarrow\rangle\langle\Downarrow|$ (if we neglect the occupations of the trion states $|\Uparrow\Downarrow\uparrow\rangle$ and $|\Downarrow\Uparrow\downarrow\rangle$).
- After the measurement of a photon in $|\theta_{opt}\rangle = |\Psi_{\Downarrow}\rangle$ at time $t = 0^+$, the spin is expected to be mainly in the state $|\Downarrow\rangle$, (again, provided that the population of the trion states can be neglected).
- Then, the spin state goes back to equilibrium after the spin-flip mechanisms have averaged it out.

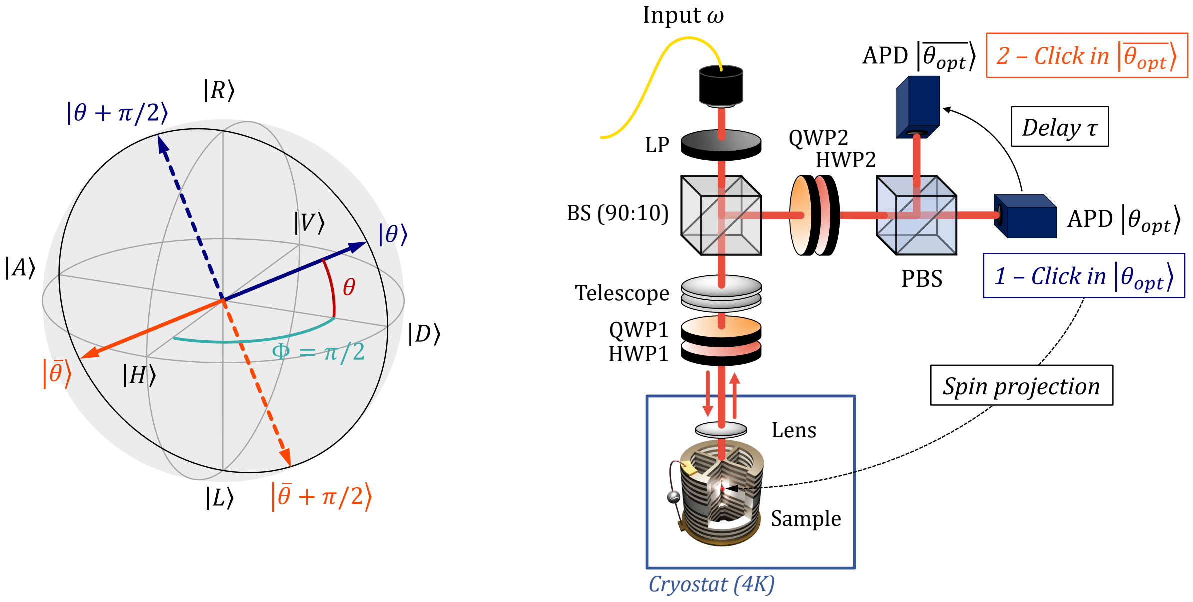

FIGURE 3.16: **(Left)** Definition of the polarization bases $(\theta, \overline{\theta})$, comprising couples of orthogonal polarization states contained in the (DRAL) plane, where θ is the angle of the first polarization state with respect to the (DA) axis. **(Right)** Experimental setup for the study of the cross-correlations in the $(\theta_{opt}, \overline{\theta_{opt}})$ basis. (1) The measurement of a photon ('click') by the $|\theta_{opt}\rangle$ detector projects the spin; (2) then after a delay τ, the detection of a photon in $\left|\overline{\theta_{opt}}\right\rangle$ is registered as a correlation event.

3.3.3 Master equation simulation of the conditional occupation probabilities

Evolution of the occupation probabilities of the ground and excited states

In the following, the complete evolution of the system is computed from the stationary regime (for $t < 0$) that is disturbed by the detection of a photon in $|\theta_{opt}\rangle$ at time $t = 0$. The excitation laser is CW, polarized along H and has a low power of 1 pW at a detuning $\Delta_d = -\Delta_{opt}$ to match $|\theta_{opt}\rangle = |\Psi_\Downarrow\rangle$ and $|\overline{\theta_{opt}}\rangle = |\Psi_\Uparrow\rangle$ (working point from Fig. 3.15). In the master equation simulation, we compute $\hat{\boldsymbol{\rho}}_{ss}$ and $\widetilde{\hat{\boldsymbol{\rho}}_{\theta_{opt}}}(t)$ and use the first density matrix for negative times and the second one for positive times.

For the rest of this section, we adopt the simplified notations for the four levels of the trion transition defined in Eq. 3.22. The occupation probability of the ground states and the trion states are plotted respectively in Figs. 3.17a and 3.17b. We note that the trion population is much smaller than that of the ground states, owing to the low excitation power; still, it plays a significant role in the evolution of the cross-correlation at short delays, and we do not neglect it. Additionally, the total population is normalized: $P(g_L) + P(g_R) + P(t_L) + P(t_R) = 1$.

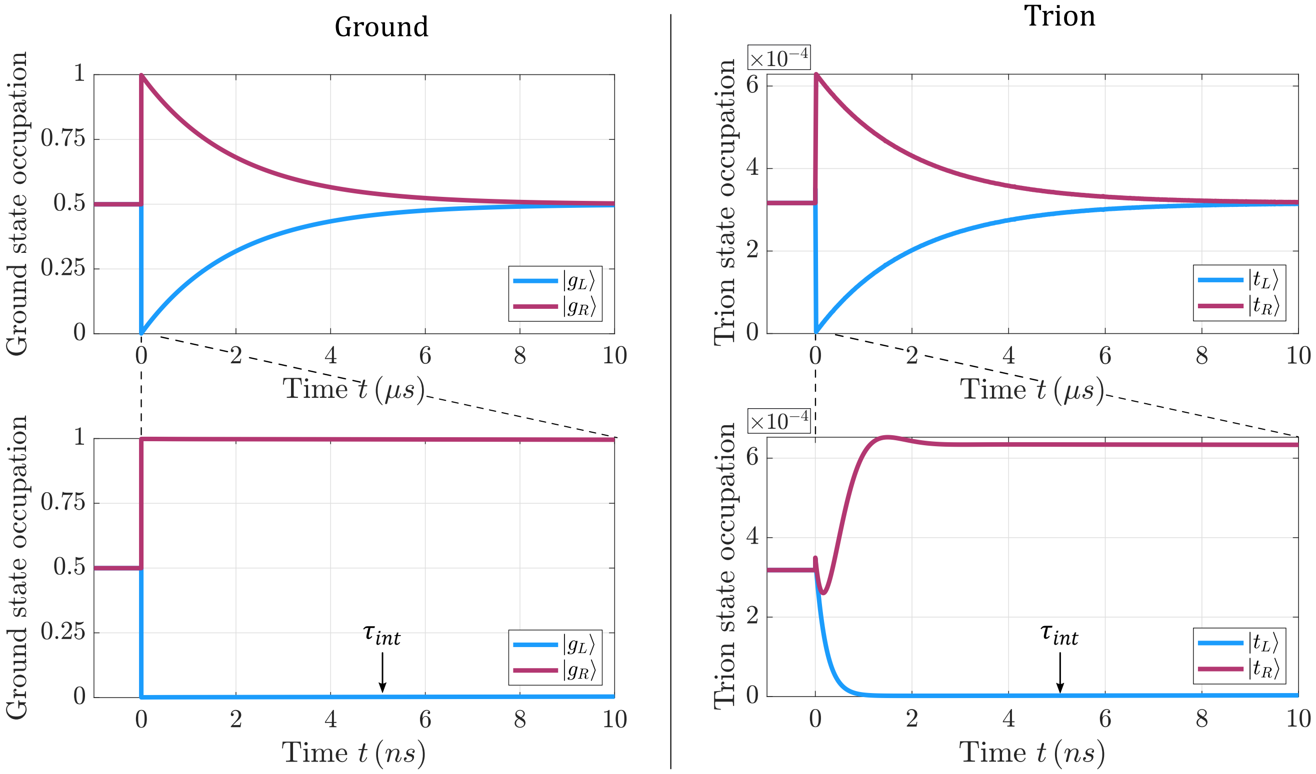

(a) (b)

FIGURE 3.17: **(a)** Occupation probability of the ground states $|g_{R/L}\rangle$ as a function of the time t after a click in $|\theta_{opt}\rangle$, which matches $|\Psi_\Downarrow\rangle$ ($\Delta_d = -\Delta_{opt}$). The photon measurement at $t = 0$ causes a spin projection in $|g_R\rangle = |\Downarrow\rangle$. Long timescale on the top, short timescale on the bottom. **(b)** Corresponding populations of the excited state, which follow an analogous evolution as the ground state, with visible damped Rabi oscillations on short timescale.

The panels of this figure comprise a long timescale view on the top, and a short timescale view on the bottom. A separation of the timescales is useful to distinguish between a transient regime dominated by radiative relaxation and one where spin relaxation is prominent [179]:

- Long timescale ($t \simeq$ µs): upon the measurement of the photon, the ground state is projected in $|g_R\rangle$ and goes back to equilibrium after a few µs. The populations of the trion states are much smaller than that of the ground states (by four orders of magnitude) but follow a similar evolution. The exponential decay of the contrast is due to the spin flips: in this example, $\tau_{SF,g} = 2\,\mu\mathrm{s}$, $\tau_{SF,t} = 100\,\mathrm{ns}$.
- Short timescale ($t \simeq \mathrm{ns}$): right after the photon is detected ($t = 0^+$), the occupations of both the ground states and the excited states are quickly rebalanced by damped Rabi oscillations, with a magnitude around 10^{-4} as the excitation power is very low. The damping happens on the timescale of the excited level lifetime ($\simeq 200\,\mathrm{ps}$). These oscillations are negligible with respect to the difference of population between the two ground states but they are significant for the trion states.

As also visible on the bottom panels of the figure, we introduce an intermediate time $\tau_{int} = 5\,\mathrm{ns}$ after which the radiative relaxation has settled but before which the spin flips happen.

Dynamics of the branch populations and excitation ratios

The short-timescale behavior is explained by the interplay between the spin projection and the short radiative dynamics of the system. To interpret this effect, we introduce in Fig. 3.18 the populations in the left and right branches $P_{R/L} = P(g_{R/L}) + P(t_{R/L})$ and the excitation ratios $\varepsilon_{R/L}$ corresponding to the occupation ratios between excited and ground states of each branch:

$$\varepsilon_{R/L} = \frac{P(t_{R/L})}{P(g_{R/L})} \tag{3.56}$$

The population of each state is given in Fig. 3.18 as a function of these new variables, whose values are given for different times with respect to the initial projective measurement on Table 3.1.

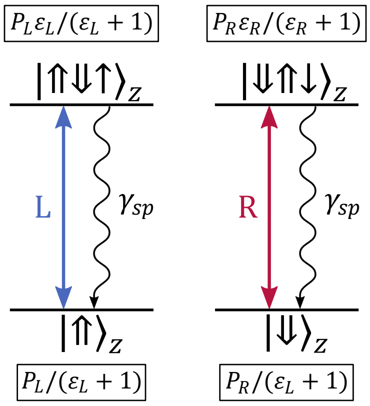

FIGURE 3.18: Definitions of the total populations of each branch $P_{R/L}$ and the excitation ratios $\varepsilon_{R/L}$ for each branch of the four-level system, as new variables to express the populations of each level (in the boxes).

	$t = 0^-$	$t = 0^+$	$t = \tau_{int}$	$t = \tau_{SF,g}$	$t = 5\tau_{SF,g}$
P_R	0.5	0.999	0.997	0.681	0.503
P_L	0.5	0.001	0.003	0.319	0.497
ε_R ($\times 10^{-4}$)	6.4	3.5	6.4	6.3	6.3
ε_L ($\times 10^{-4}$)	6.4	2500	8.9	6.3	6.3

TABLE 3.1: Populations of each branch $P_{R/L}$ and corresponding excitation ratio $\varepsilon_{R/L}$ in the stationary regime ($t = 0^-$), right after a photon is detected ($t = 0^+$), at $t = \tau_{int} = 5\,\text{ns}$, and after spin relaxation at $t = \tau_{SF,g} = 2\,\mu\text{s}$ and $t = 5\tau_{SF,g} = 10\,\mu\text{s}$.

- Before the photon is detected ($t = 0^-$), the system is in the steady state regime, with a radiative equilibrium. In the absence of spin initialization, the L and R branches have populations of one half ($P_R = P_L = 0.5$) with excited state populations close to 0 due to the low excitation power ($\varepsilon_R = \varepsilon_L = 6.4 \times 10^{-4} \ll 1$).
- The detection of the photon creates a discontinuity at $t = 0$ which instantly projects the ground state in $|\Downarrow\rangle$. At $t = 0^+$, the populations are almost exclusively in the R branch, with $P(g_R) \simeq 1$ and $P(g_L) \simeq 0$. This sudden imbalance affects the excitation ratios $\varepsilon_{R/L}$. In particular, the absolute population in $|t_L\rangle$ is still very low but is now comparable with the (also low) population in state $|g_L\rangle$ (with $\varepsilon_L = 0.25$, much higher than the value at radiative equilibrium). This imbalance initiates Rabi oscillations back to equilibrium.
- In each branch, the damped Rabi oscillations are mostly settled at $t = \tau_{int}$: the quantities $\varepsilon_{R/L}$ are back close to their values imposed by the radiative equilibrium. In particular, the population in state $|t_L\rangle$ has further decreased since both P_L and ε_L are very small at $t = \tau_{int}$ (a population $P(t_L) = 2.7 \times 10^{-6}$ is observed at $t = \tau_{int}$). The spin projection is still effective.
- At longer timescales (of the order of $\tau_{SF,g}$), the spin relaxes and the values of $P_{R/L}$ evolve back to one half. Since this is a very slow process compared to τ_{int}, the excitation ratios stay very close to their values at radiative equilibrium, with the occupations of $|t_L\rangle$ and $|t_R\rangle$ adiabatically following those of $|g_L\rangle$ and $|g_R\rangle$.

Overall, the transient regime before τ_{int} can be thought of as a quick rebalancing of the populations between the ground and the excited states through Rabi oscillations that arise in the return to radiative equilibrium of the system after the disturbance of the ground spin projection.

A distinction must be drawn between this transient regime, which affects the equilibrium between $|t_{R/L}\rangle \leftrightarrow |g_{R/L}\rangle$ on the 100 ps timescale, and the damping of the ground spin occupation, which affects the equilibrium between $|g_R\rangle \leftrightarrow |g_L\rangle$ on the µs timescale.

3.3.4 Evolution of the reflected polarization and cross-correlations in the optimal basis

The measurement-induced spin projection changes in return the subsequent output polarization. To study it, we continue to address the system with a CW excitation laser polarized along H, at a power of 1 pW and a detuning $\Delta_d = -\Delta_{opt}$ to match $|\theta_{opt}\rangle = |\Psi_{\Downarrow}\rangle$ and $|\overline{\theta_{opt}}\rangle = |\Psi_{\Uparrow}\rangle$ (working point from Fig. 3.15 with $\theta_{opt} = -6.4°$).

To characterize the reflected polarization state, we begin by plotting in Fig. 3.19a the Stokes parameters of the output polarization, perturbed by the measurement of a photon in $|\theta_{opt}\rangle$ at $t = 0$. These Stokes parameters are computed using the conditioned intensities for each polarization $X \in [H, V, D, A, R, L]$, taking $\widetilde{I_{X|\theta_{opt}}}(t)$ for positive times, and the stationary state values I_X for negative times. The top graph shows the long timescales, where the polarization state right after the photon is measured coincides with $|\Psi_{\Downarrow}\rangle = |\theta_{opt}\rangle$ and decays exponentially to a depolarized state (i.e., $s_{HV} = s_{DA} = s_{RL} = 0$) as the spin flips average out the reflected polarization. A zoom on the short timescales is shown on the bottom graph: the Rabi oscillations of the spin result in short damped oscillations in the reflected polarization before the output state coincides with $\boldsymbol{S}^{(\Downarrow)}$ (the Stokes vector associated to $|\Psi_{\Downarrow}\rangle$), typically at $t = \tau_{int}$.

The cross-correlations between the photon detections in $|\theta_{opt}\rangle$ and $|\overline{\theta_{opt}}\rangle$ are presented in Fig. 3.19b for negative and positive delays τ (this simulation is purely dynamic and negative delays are not stationary regime as in previous figures). They are defined by:

$$g^{(2)}_{\theta_{opt}\overline{\theta_{opt}}}(\tau \geq 0) = \frac{\widetilde{I_{\overline{\theta_{opt}}|\theta_{opt}}}(\tau)}{I_{\overline{\theta_{opt}}}} \qquad g^{(2)}_{\theta_{opt}\overline{\theta_{opt}}}(\tau \leq 0) = \frac{\widetilde{I_{\theta_{opt}|\overline{\theta_{opt}}}}(-\tau)}{I_{\overline{\theta_{opt}}}} \tag{3.57}$$

Here, a positive τ stands for a detection in $|\theta_{opt}\rangle$ followed by one in $|\overline{\theta_{opt}}\rangle$, and conversely for a negative τ. Most prominently, the data exhibit the spin relaxation on the timescale of a few µs:

- On the long delay plot (upper panel), the cross-correlations dip to zero at short delay before losing contrast and increasing to unity for long delays. The cause of this perfect contrast resides in the optimal measurement of the spin state $|\Downarrow\rangle$, as the photon detected in $|\theta_{opt}\rangle = |\Psi_{\Downarrow}\rangle$ at $\tau = 0$ prevents any detection in $|\overline{\theta_{opt}}\rangle = |\Psi_{\Uparrow}\rangle$, until a spin-flip has occurred. The spin state returning to thermal equilibrium is the signature of the decay in the µs timescale.

- Zooming on the short delays, we notice a transient regime behavior by which the cross-correlation is unity for zero delay and takes its minimal value only around the time $\tau = \tau_{int}$. This is the direct counterpart of the quick rebalancing of the trion and ground populations to reach back the radiative equilibrium. In particular, the residual occupation of the trion state $|\Downarrow\Uparrow\downarrow\rangle = |t_L\rangle$ has to strongly decay between $t = 0$ and $t = \tau_{int}$, which can happen through the emission of an L-polarized photon. Such a photon can be detected by the detector in $|\theta_{opt}\rangle$ as well as the one in $|\overline{\theta_{opt}}\rangle$ (since these two polarization states are nearly linear), which explains the unity value of $g^{(2)}_{\theta_{opt}\overline{\theta_{opt}}}$ at very short delays ($\tau = 0^+$ or 0^-).

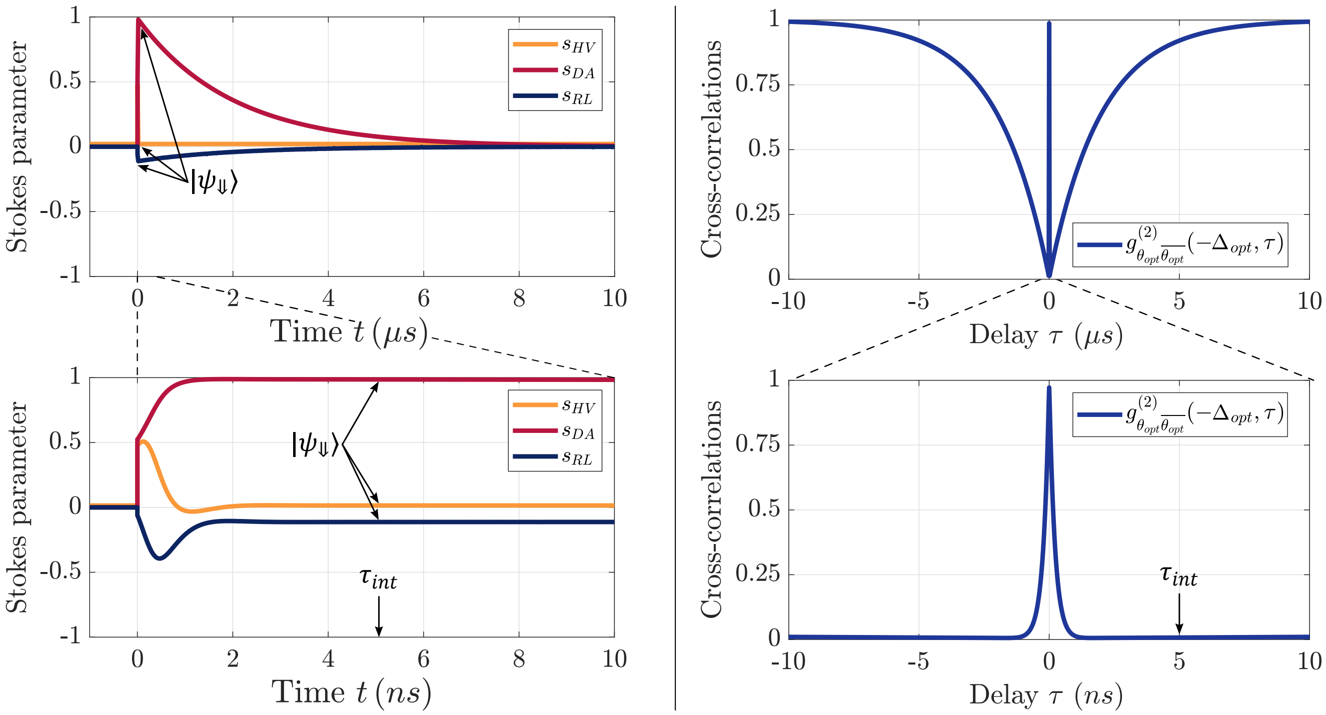

(a) (b)

FIGURE 3.19: **(a)** Stokes parameters of the reflected polarization state as a function of the time t after a click in $|\theta_{opt}\rangle = |\Psi_{\Downarrow}\rangle$. The top figure shows the long timescale while the bottom figure zooms on the short timescale. We notice the stabilization in $|\Psi_{\Downarrow}\rangle$ after the radiative transitory regime lasting for a few ns and the decay to a depolarized state on the µs timescale due to spin flips. **(b)** Corresponding cross-correlations between $|\theta_{opt}\rangle$ and $|\overline{\theta_{opt}}\rangle$ for negative and positive delays τ.

Influence of the measurement basis and laser-quantum dot detuning

In section 3.2, we showed that $\langle\Psi_{\Uparrow}|\Psi_{\Downarrow}\rangle = 0$ could be obtained for two values of the detuning $\Delta_d = \pm\Delta_{opt}$, achieving an ideal spin-photon interface. Then we introduced the measurement bases $(\theta, \overline{\theta})$ in Fig. 3.16, and we have shown that $\theta_{opt} = -6.4°$ allows a perfect measurement back action when $\Delta_d = -\Delta_{opt}$.

Here, we start from this optimal situation and study the dependence of the cross-correlations at intermediate timescale, for different values of the detuning Δ_d. We expect the contrast of the cross-correlations to be perfect at $\Delta_d = -\Delta_{opt}$ and $\theta = \theta_{opt}$ as shown above, and to degrade when deviating from these conditions (see Fig. 3.15 for reference). The result is plotted in Fig. 3.20. The cross-correlations are calculated by two different means: first with the full model described above, by taking the value $g^{(2)}_{\theta_{opt}\overline{\theta_{opt}}}(\Delta_d, \tau_{int})$, and second by a semi-analytical method elaborated in the next paragraph. In Fig. 3.20a, we see that regarding to the cross-correlations in the optimal basis $(\theta_{opt}, \overline{\theta_{opt}})$:

- The cross-correlation is null at $\Delta_d = -\Delta_{opt}$ since $\langle\Psi_{\Uparrow}|\Psi_{\Downarrow}\rangle = 0$.
- At $\Delta_d = 0$, $|\Psi_{\Uparrow}\rangle$ and $|\Psi_{\Downarrow}\rangle$ are very close to $|V\rangle$, and are thus equally distant from the detection polarizations $|\theta_{opt}\rangle$ and $|\overline{\theta_{opt}}\rangle$. This causes the cross-correlation to rise to unity.

- At $\Delta_d = +\Delta_{opt}$, $|\Psi_{\Uparrow}\rangle$ is actually equal to $|-\theta_{opt}\rangle$ and $|\Psi_{\Downarrow}\rangle$ to $\left|\overline{-\theta_{opt}}\right\rangle$: the small difference between the reflected polarizations $(-\theta_{opt}, \overline{-\theta_{opt}})$ and the measurement basis $(\theta_{opt}, \overline{\theta_{opt}})$ explain the non-zero cross-correlation.
- At large detunings, both $|\Psi_{\Uparrow}\rangle$ and $|\Psi_{\Downarrow}\rangle$ are equal to $|H\rangle$ and the cross-correlation is unity.

We now explore the angular dependence of $g^{(2)}_{\theta\overline{\theta}}(-\Delta_{opt}, \tau_{int})$ in Fig. 3.20b, as a function of the measurement basis angle θ, for a detuning equal to $\Delta_d = -\Delta_{opt}$. We see that a sine squared dependence of the cross-correlation contrast is expected when changing the measurement basis in the (DRAL) plane. This dependence arises from the varying scalar products $\langle\Psi_{\Uparrow}|\theta\rangle$ and $\left\langle\Psi_{\Downarrow}|\overline{\theta}\right\rangle$ when θ is varied. The angle θ_{opt} gives a perfect contrast since $\langle\Psi_{\Uparrow}|\theta_{opt}\rangle = 0$ and $\left\langle\Psi_{\Downarrow}|\overline{\theta_{opt}}\right\rangle = 0$ (i.e., a click in $|\theta_{opt}\rangle$ can only be obtained if the spin is $|\Downarrow\rangle$, and a click in $\left|\overline{\theta_{opt}}\right\rangle$ if the spin is $|\Uparrow\rangle$). On the contrary, choosing $\theta = \theta_{opt} \pm \pi/2$ removes the effect completely as such a polarization basis cannot discriminate between $|\Psi_{\Uparrow}\rangle$ and $|\Psi_{\Downarrow}\rangle$, since the scalar products between spin states and detection polarizations are all equal to $1/2$.

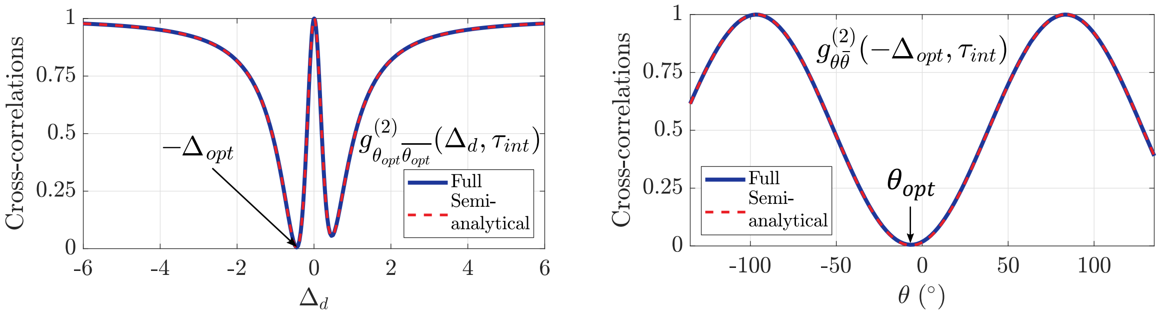

(a) (b)

FIGURE 3.20: **(a)** Cross-correlations at the intermediate time τ_{int} as a function of the normalized laser-quantum dot detuning Δ_d, setting $\theta = -\theta_{opt}$. The best contrast is found for $\Delta_d = -\Delta_{opt}$. The full model simulation is plotted as a solid line and the semi-analytical result as a dashed line. **(b)** Same quantity, this time setting $\Delta_d = -\Delta_{opt}$ and varying the basis angle θ. The best contrast is found for $\theta_{opt} = -6.4°$.

3.3.5 Semi-analytical calculation of the cross-correlations at intermediate delay

The cross-correlations between photons detected in polarizations X and Y, $g^{(2)}_{XY}$, is defined by Eq. 3.50 for any delay τ. Here, we use the results of the simulation in the continuous wave regime to compute the cross-correlations at the intermediate delay $\tau_{int} = 5\,\mathrm{ns}$, $g^{(2)}_{XY}(\tau_{int})$. This method saves a significant amount of computation time and gives insight on the mechanisms at play. Not only does it confirm the numerical calculations presented above but also the correct interpretation of the results. The match between the numerical calculation in the master equation framework and the semi-analytical method developed here is only possible if the timescales of the radiative and spin relaxations are indeed separable with τ_{int} between the two.

Let us first discard the delay and consider only probabilities. We start from the simplified formula of the cross-correlations, which is defined by the normalized probability of detecting a Y-polarized photon conditioned by the detection of an X-polarized photon:

$$g^{(2)}_{XY} = \frac{P(Y|X)}{P(Y)} \tag{3.58}$$

The data we simulate in the steady-state regime are the reflected intensities in the different polarizations (X and Y), with the charge state initialized in each configuration ($s \in [\Uparrow, \Downarrow]$) and the occupation probability for each of these charge states. The intensity in polarization X when the spin is initialized in the state s is written as $I_X^{(s)}$ and the occupation probability of s is written $P(s)$. In order to use these data to calculate the cross-correlations, we perform the following calculation steps:

- According to the definition of $I_X^{(s)}$, we can assume that it is proportional to $P(X|s)$.
- We initially develop the conditional probability $P(Y|X)$ on the basis of the quantum dot states: $s \in [\Uparrow, \Downarrow]$:

$$g^{(2)}_{XY} = \sum_{s\in[\Uparrow,\Downarrow]} \frac{P(Y|s)P(s|X)}{P(Y)} \tag{3.59}$$

- Then, we use the Bayesian inference to invert the probabilities of spin states conditioned by photon detection (which are not simulated directly):

$$P(s|X) = \frac{P(X|s)P(s)}{P(X)} \tag{3.60}$$

- Finally, we write the unconditioned probability by taking into account all possible quantum dot states:

$$P(X) = \sum_{s\in[\Uparrow,\Downarrow]} P(X|s)P(s) \propto \sum_{s\in[\Uparrow,\Downarrow]} I_X^{(s)} P(s) \tag{3.61}$$

After this last step, we can write the cross-correlations $g^{(2)}_{XY}$ as a function of the simulated data, and regroup the denominator terms in the total intensities I_X and I_Y:

$$\boxed{g^{(2)}_{XY} = \frac{\sum_s I_Y^{(s)} I_X^{(s)} P(s)}{\sum_s I_Y^{(s)} P(s) \cdot \sum_s I_X^{(s)} P(s)} = \frac{\sum_s I_Y^{(s)} I_X^{(s)} P(s)}{I_Y I_X}} \tag{3.62}$$

This semi-analytical expression shows a good agreement with the full simulation as was demonstrated in Fig. 3.20. As the starting hypothesis is the existence of an *intermediate steady state*, the result is valid as long as the spin-flip-times and charge characteristic times are much longer than the intermediate timescale[1]: $\tau_{SF,g};\ \tau_{SF,t} \gg \tau_{int}$.

---

[1] Although the charge escape and capture mechanisms are not taken into account here, we explore later in this chapter how they impact the cross-correlations. In that case, the simulation and the semi-analytical calculation must include the initialized states $|\Uparrow\rangle$, $|\Downarrow\rangle$ and $|\varnothing\rangle$.

Fig. 3.21 shows one value of the semi-analytical cross-correlations in the basis $(\theta_{opt}, \overline{\theta_{opt}})$, for $\Delta_d = -\Delta_{opt}$ (red dot) and compares it with the cross-correlations as a function of the delay obtained with the full simulation for different spin-flip times of the ground state. The semi-analytical model matches the simulation as long as $\tau_{SF,g} \gtrsim 1\,\mu\mathrm{s}$, which is to say that no spin flip happens before the transient regime has stabilized to radiative equilibrium[1]. The ideal cross-correlation contrast is also preserved for a very short window of time when $\tau_{SF,g} = 0.1\,\mu\mathrm{s}$, but it is strongly degraded for $\tau_{SF,g} \leq 10\,\mathrm{ns}$ as the separation of timescales is not met anymore.

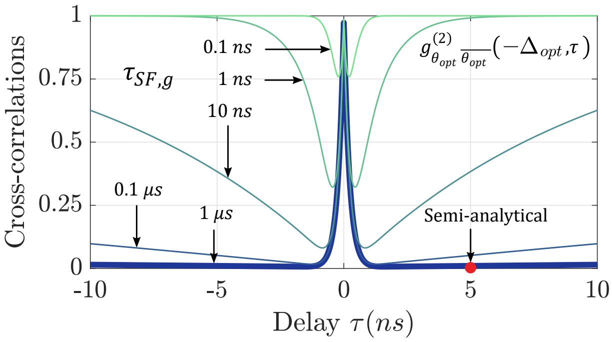

FIGURE 3.21: Cross-correlations in the $(\theta_{opt}, \overline{\theta_{opt}})$ basis as a function of the delay, for an input laser in polarization H and tuned to $-\Delta_{opt}$ (working point from Fig. 3.15). Comparison between the semi-analytical value (red dot at $\tau_{int} = 5\,\mathrm{ns}$) and the full simulation for different spin-flip times of the ground state ($\tau_{SF,g}$ from 0.1 ns to 1 μs). The semi-analytical formula is valid for $\tau_{SF,g} \gtrsim 1\,\mu\mathrm{s}$.

So far, the measurement effect was studied as a function of the energy of the excitation laser, the measurement basis and the delay between photon detections. For each parameter, an optimum was found to achieve a perfect working point, and accordingly a perfect measurement basis. Next, we explore other phenomena occurring in quantum dots that impact the operation of the devices as spin-photon interfaces.

3.4 Effect of a magnetic field

In this section, the Hamiltonian description of an arbitrary external magnetic field interacting with the quantum dot charge is developed. We simulate the consequences of an external longitudinal magnetic field on the experimentally measured quantities.

3.4.1 Hamiltonian of the magnetic interaction

The interaction between a charge carrier of angular momentum $\vec{S}$ and a magnetic field $\vec{B}$ is usually described by the Hamiltonian:

$$\hat{\boldsymbol{H}}_{mag} = g\mu_B \vec{S} \cdot \vec{B} \tag{3.63}$$

where g is the Landé factor and μ_B is the Bohr magneton.

---

[1] This model is also not valid in the presence of a transverse magnetic field, which induces the Larmor precession of the spin and thus prevents from initializing the spin in $|\Uparrow\rangle$ or $|\Downarrow\rangle$.

The scalar product can be decomposed in the spatial basis (x,y,z), here with z parallel to the growth axis of the micropillar device (longitudinal or Faraday magnetic field) and x,y in the orthogonal plane (transverse or Voigt magnetic field):

$$\begin{aligned}\vec{S} &= \hat{\boldsymbol{S}}_x \vec{u_x} + \hat{\boldsymbol{S}}_y \vec{u_y} + \hat{\boldsymbol{S}}_z \vec{u_z} \\ \vec{B} &= B_x \vec{u_x} + B_y \vec{u_y} + B_z \vec{u_z}\end{aligned} \tag{3.64}$$

where we introduced the spin components $\hat{\boldsymbol{S}}_i$ ($i \in [x, y, z]$) which we now label $\hat{\boldsymbol{S}}_i^{(h)}$ for the hole pseudospin or $\hat{\boldsymbol{S}}_i^{(e)}$ for the electron spin, both being spin 1/2. They are defined by:

$$\begin{aligned}
\hat{\boldsymbol{S}}_x^{(h)} &= \frac{1}{2}\big(\left|\Downarrow\right\rangle_z \left\langle\Uparrow\right|_z + \left|\Uparrow\right\rangle_z \left\langle\Downarrow\right|_z \big) & \hat{\boldsymbol{S}}_x^{(e)} &= \frac{1}{2}\big(\left|\downarrow\right\rangle_z \left\langle\uparrow\right|_z + \left|\uparrow\right\rangle_z \left\langle\downarrow\right|_z \big) \\
\hat{\boldsymbol{S}}_y^{(h)} &= \frac{i}{2}\big(\left|\Downarrow\right\rangle_z \left\langle\Uparrow\right|_z - \left|\Uparrow\right\rangle_z \left\langle\Downarrow\right|_z \big) & \hat{\boldsymbol{S}}_y^{(e)} &= \frac{i}{2}\big(\left|\downarrow\right\rangle_z \left\langle\uparrow\right|_z - \left|\uparrow\right\rangle_z \left\langle\downarrow\right|_z \big) \\
\hat{\boldsymbol{S}}_z^{(h)} &= \frac{1}{2}\big(\left|\Uparrow\right\rangle_z \left\langle\Uparrow\right|_z - \left|\Downarrow\right\rangle_z \left\langle\Downarrow\right|_z \big) & \hat{\boldsymbol{S}}_z^{(e)} &= \frac{1}{2}\big(\left|\uparrow\right\rangle_z \left\langle\uparrow\right|_z - \left|\downarrow\right\rangle_z \left\langle\downarrow\right|_z \big)
\end{aligned} \tag{3.65}$$

Here, the (x,y,z) basis refers to the spin basis and is not to be confused with the (HV,DA,RL) basis of the polarization states in the Poincaré sphere.

Since the quantum dots are not spherical but flattened in the z direction, they impose an anisotropic confinement to the trapped charged particles. On that account, the sensitivity to a magnetic field depends on its orientation, especially for the hole [151]. Therefore, different Landé factors are attributed to the contributions of $\vec{B}$ parallel to the growth axis ($g_{\|}$) and in the orthogonal plane ($g_{\perp}$). The complete Hamiltonian then reads as follows, for the hole (h) and the electron (e):

$$\hat{\boldsymbol{H}}_{mag}^{(h)} = g_{h,\|} \times \mu_B B_z \hat{\boldsymbol{S}}_z^{(h)} + g_{h,\perp} \times \mu_B \Big(B_x \hat{\boldsymbol{S}}_x^{(h)} + B_y \hat{\boldsymbol{S}}_y^{(h)} \Big) \tag{3.66}$$

$$\hat{\boldsymbol{H}}_{mag}^{(e)} = g_{e,\|} \times \mu_B B_z \hat{\boldsymbol{S}}_z^{(e)} + g_{e,\perp} \times \mu_B \Big(B_x \hat{\boldsymbol{S}}_x^{(e)} + B_y \hat{\boldsymbol{S}}_y^{(e)} \Big) \tag{3.67}$$

The effect of the magnetic field on the four-level system is to split the ground and excited doublets in energy and to possibly initiate a precession of the spin about the Zeeman-split eigenstates. Moreover, we choose to account for the diamagnetic shift, not with a Hamiltonian term, but by shifting in bulk the energy of the transition manually to an effective value $\omega_d^{(eff)}$:

$$\omega_d^{(eff)} = \omega_d + \delta_{dia,\|} \times B_z^2 + \delta_{dia,\perp} \times \big(B_x^2 + B_y^2 \big) \tag{3.68}$$

The experimental Landé and diamagnetic factors in the case of the *positively charged device* (experimentally studied in chapter 4) are compiled in Table 3.2. These values were measured from the splitting at high magnetic fields in the Faraday and Voigt configurations (the latter is presented in subsection 2.1.3 and the former is derived from an experiment not shown), and we assume that the electron Landé factor is isotropic and negative [152].

Orientation	Landé factor	Diamagnetic factor
Voigt ($B_\perp$)	$g_{h,\perp} = -0.2$ $g_{e,\perp} = -0.5$	$\delta_{dia,\perp} = 4.8\,\mu\mathrm{eV/T^2}$
Faraday ($B_\parallel$)	$g_{h,\parallel} = 0.3$ $g_{e,\parallel} = -0.5$	$\delta_{dia,\parallel} = 12\,\mu\mathrm{eV/T^2}$

TABLE 3.2: Experimentally measured magnetic properties of the *positively charged device* according to the orientation of the magnetic field.

3.4.2 Effect of a longitudinal magnetic field on the simulated quantities

A magnetic field can help stabilizing the spin qubit by screening the environmental fluctuations (see subsection 1.2.4) and has important consequence on the workings of a spin-photon interface. Here, we simulate the effect of a longitudinal magnetic field, which is experimentally explored in the next chapters. Transverse magnetic fields notably come into play in modeling the hyperfine interaction with the nuclei (see subsection 1.2.3), which will not be investigated further in this manuscript.

Zeeman splitting with a non-initialized spin

In Fig. 3.22, the reflected intensity in the V polarization while exciting H (CW, $P_{in} = 1\,\mathrm{pW}$) is simulated for different longitudinal magnetic fields B_z and an absence of spin initialization, so as to evidence the Zeeman splitting. In this situation, the quantum dot state is averaged over $|\Uparrow\rangle$ and $|\Downarrow\rangle$, so the reflected intensity in V (denoted $I_V^{(avg)}$) contains photons from both R and L branches, as per Fig. 1.9b. When the magnetic field increases, the two quantum dot spin states are separated in energy by the Zeeman splitting:

$$\delta_Z = \left|(g_{e,\parallel} - g_{h,\parallel})\mu_B B_z\right| \tag{3.69}$$

Two sub-peaks appear at $\omega_d^{(\Uparrow)} = \omega_d^{(eff)} + \delta_Z/2$ and $\omega_d^{(\Downarrow)} = \omega_d^{(eff)} - \delta_Z/2$, they become visible when δ_Z is larger than the quantum dot linewidth; in addition, the diamagnetic shift of $\omega_d^{(eff)}$ becomes slightly visible in the 200 mT curve, centered at $\Delta_d \simeq 0.16$.

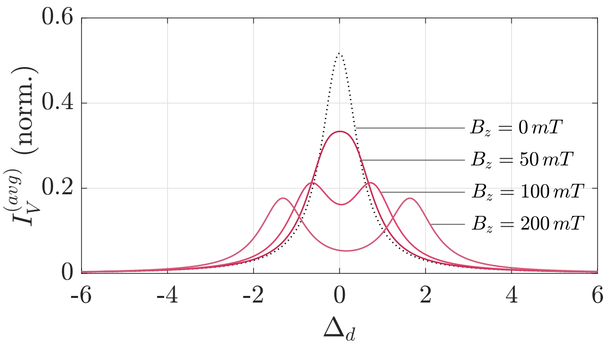

FIGURE 3.22: Reflected intensity in polarization V as a function of the normalized laser-quantum dot detuning $\Delta_d = (\omega - \omega_d)/\Gamma$, while exciting H (CW, $P_{in} = 1\,\mathrm{pW}$) and applying a longitudinal magnetic field from $B_z = 0\,\mathrm{mT}$ to 200 mT.

Shift of the spin-induced polarization rotation

The longitudinal magnetic field also influences the polarization rotation induced by the initialized spin. In Fig. 3.23, numerical simulations are implemented with a spin initialized in branch L, corresponding to the ground spin state $|\Uparrow\rangle$. The behavior of $\boldsymbol{S}^{(\Uparrow)}$ in terms of Stokes parameters and Poincaré vector is plotted, at $B_z = 0\,\mathrm{mT}$ and $50\,\mathrm{mT}$, with arrows representing the value of $\boldsymbol{S}^{(\Uparrow)}$ for detunings $\delta\omega = 0, \pm 0.45\,\mu\mathrm{eV}$, i.e., $\Delta_d = 0, \pm 0.15$. As the Stokes parameters are shifted in energy by the Zeeman splitting, the curves in Fig. 3.23 (left panels) are translated horizontally when B_z is increased, because the resonance with the transition $|\Uparrow\rangle \leftrightarrow |\Uparrow\Downarrow\uparrow\rangle$ occurs at the energy $\omega_d^{(\Uparrow)} > \omega_d$. As a result, the trajectory of the Stokes vector remains similar, but the points are energy-shifted. Therefore, for a fixed detuning between the laser and the quantum dot energy at $B_z = 0\,\mathrm{mT}$, the Stokes vector $\boldsymbol{S}^{(\Uparrow)}$ is shifted in the presence of a magnetic field.

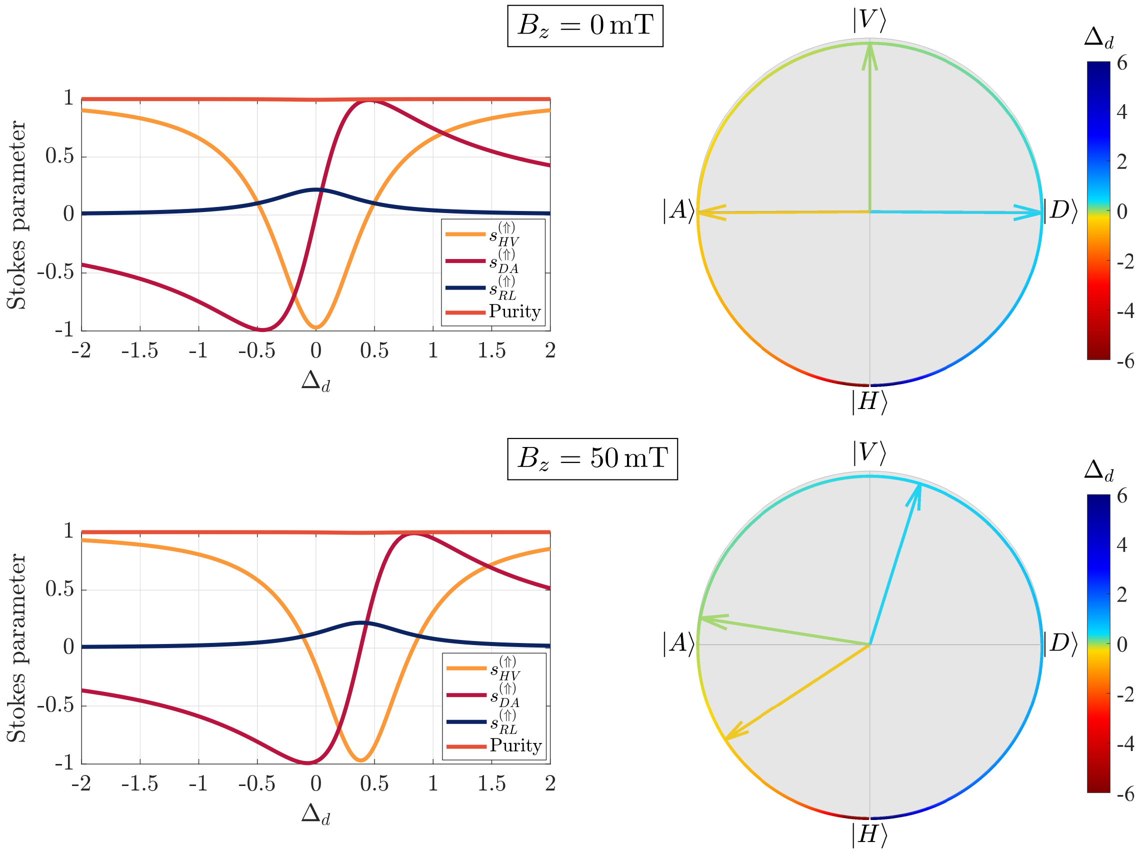

FIGURE 3.23: Evolution of the Stokes vector $\boldsymbol{S}^{(\Uparrow)}$ as a function of the normalized laser-quantum dot detuning $\Delta_d = (\omega - \omega_d)/\Gamma$ (centered on the QD energy in the absence of a magnetic field) **(Top)** for $B = 0\,\mathrm{mT}$ and **(Bottom)** $B = 50\,\mathrm{mT}$. **(Left)** Stokes components; **(Right)** Stokes vector in the Poincaré sphere as seen from the top of the sphere through the (RL) axis. Solid arrows indicate the values of $\boldsymbol{S}^{(\Uparrow)}$ for the detunings $\Delta_d = 0, \pm 0.15$.

Consequence for a spin-photon interface

It is useful to examine if a perfect spin-photon interface can hold with a longitudinal magnetic field: in Fig. 3.24, we plot the $\boldsymbol{S}^{(\Uparrow)}$ trajectory with solid arrows pointing at its value for $\Delta_d = 0, -0.15, 0.37$ (resp. in green, yellow and blue), superimposed with dashed arrows showing $\boldsymbol{S}^{(\Downarrow)}$ for the same detunings. The simulation is plotted for $B_z = 0, 20, 50\,\mathrm{mT}$: without a magnetic field, we immediately see the orthogonality of $\boldsymbol{S}^{(\Uparrow)}$ and $\boldsymbol{S}^{(\Downarrow)}$ for $\Delta_d = -0.15$ (parallel yellow arrows pointing away from each other); when increasing the magnetic field to 20 mT, the two arrows are roughly orthogonal, and with a higher magnetic field, the orthogonality is clearly not preserved. In any case, the measurement basis $(\theta_{opt}, \overline{\theta_{opt}})$ that is optimal at $B_z = 0\,\mathrm{mT}$ is not optimal when a longitudinal magnetic field is present, as we examine next.

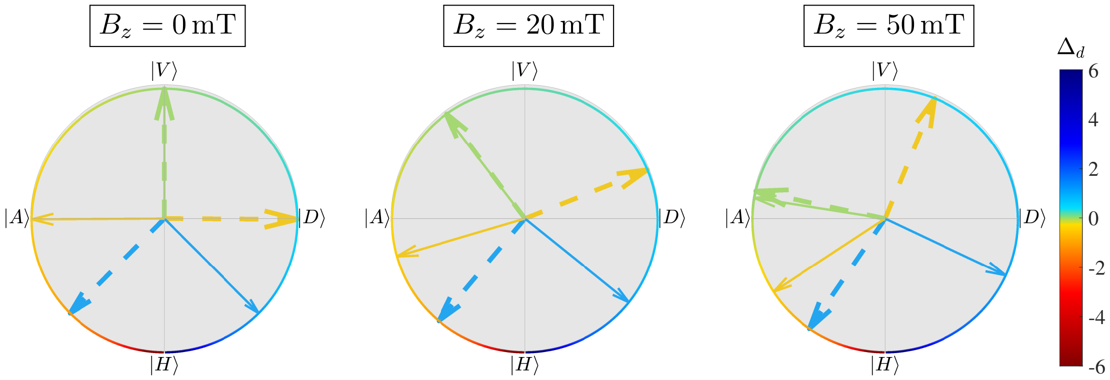

FIGURE 3.24: Effect of a longitudinal magnetic field of 0 mT, 20 mT and 50 mT on the reflected polarization vector. The solid line is the full $|\Psi_{\Uparrow}\rangle$ trajectory as a function of the normalized detuning Δ_d. The solid arrows correspond to $|\Psi_{\Uparrow}\rangle$ and the dashed arrows to $|\Psi_{\Downarrow}\rangle$ for detunings $\Delta_d = 0, -0.15, 0.37$ (resp. green, yellow and blue arrows). The green arrows on resonance with the quantum dot are almost superimposed.

We can surmise that the cross-correlation contrast in the optimal conditions found above at zero magnetic field (basis $(\theta_{opt}, \overline{\theta_{opt}})$, detuning $-\Delta_{opt}$) will be degraded in the same conditions when adding a longitudinal magnetic field. To support this point, we start from the detuning dependence of the cross-correlations at intermediate delay in the optimal basis $(\theta_{opt}, \overline{\theta_{opt}})$ found in Fig. 3.20a, and we study their dependence with an external magnetic field in Fig. 3.25. As B_z increases, the cross-correlation minimum rises and the width of the effect is increased by the Zeeman splitting. We can notice that the cross-correlation at the central detuning stays at unity because the Stokes vectors $\boldsymbol{S}^{(\Uparrow)}$ and $\boldsymbol{S}^{(\Downarrow)}$ on resonance with the quantum dot stay close to identical (as seen in Fig. 3.24 with the green arrows). In addition, the plots are horizontally shifted at high magnetic fields due to the diamagnetic effect.

The sensitivity of our implementation of a spin-photon interface to a longitudinal magnetic field will thus be weighed against its benefit in protecting from the hyperfine inetraftion. Nevertheless, let us describe further its impact, focusing on the states population.

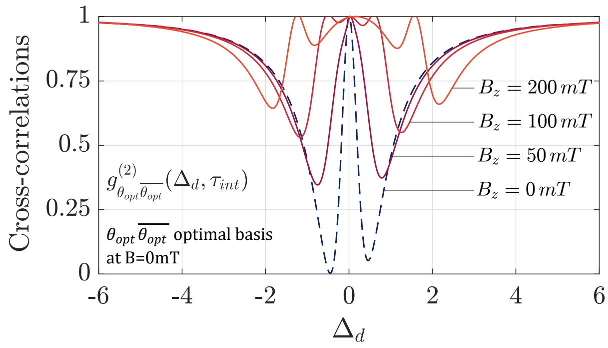

FIGURE 3.25: Effect of a longitudinal magnetic field on the cross-correlations in the optimal basis found without an external magnetic field ($\theta_{opt}, \overline{\theta_{opt}}$), as a function of the normalized laser-quantum dot detuning.

3.4.3 Optical spin pumping with a longitudinal magnetic field

Physical principle

We now develop the spin pumping approach presented in subsection 1.1.4 for the hole spin with a focus on the effect of a longitudinal magnetic field, supported with results from the master equation simulations. To start with, let us first review the principle in depth: a magnetic field changes the populations in the R and L branches, depending on the wavelength and polarization of the excitation laser. The four-level system of the positive trion transition is represented in Fig. 3.26 for a non-zero longitudinal magnetic field.

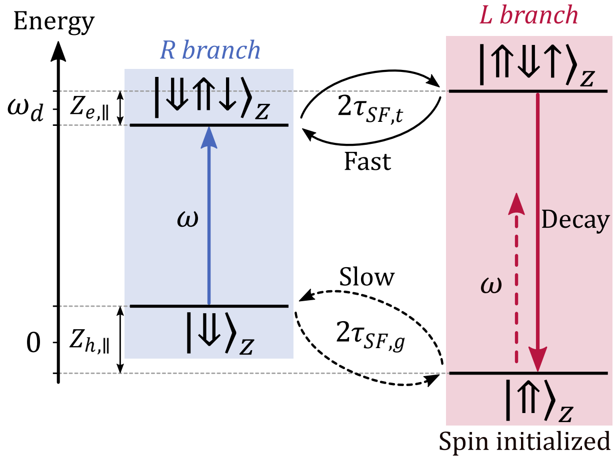

FIGURE 3.26: Optical spin pumping of the hole state with a longitudinal magnetic field and a linearly polarized excitation laser: depending on the excitation energy ω, the hole is pumped in one of the ground states (here, $|\Uparrow\rangle_z$) owing to the asymmetric spin-flip rate of the excited and ground states. The linearly polarized laser could address the two transitions as it contains both R and L components but the Zeeman splitting prevents it, as the laser cannot be in resonance with both transitions simultaneously.

The relatively fast spin flip of the excited levels with respect to the ground levels is the feature we rely on for spin pumping. It can be achieved without an external magnetic field: when pumping selectively the R or L branch, the spin gets trapped in the ground state of the other branch [20] (see subsection 1.1.4). Here, we consider a system excited by a linearly polarized laser, so that at 0 mT, both branches are symmetrically pumped and remain identically populated. However, when the longitudinal magnetic field splits the energy levels as represented in Fig. 3.26, each branch becomes energy-selective. As a consequence, the pumping can work even with a linearly polarized laser containing both R and L components: when exciting resonantly with one branch (the R branch in the figure), the excitation laser is detuned from the other transition and therefore, the spin is trapped in the ground state of the other branch (here L), even if the excitation laser has an L-polarized component.

Influence on the simulated quantities

The spin initialization is most evident in the populations of the ground spin states $P(g_L) = P(|{\Uparrow}\rangle_z)$ and $P(g_R) = P(|{\Downarrow}\rangle_z)$, defined in Eq. 3.41. In Fig. 3.27, we plot their simulated values respectively as solid orange and red lines (or as dashed black lines when they are both constant and equal to 0.5), as a function of the normalized laser-quantum dot detuning. The excitation is still a CW laser polarized along H. The two graphs independently present the effect of the two parameters that influence the spin pumping, namely the intensity of the longitudinal magnetic field B_z (Fig. 3.27a) and the spin-flip ratio $r_{SF} = \tau_{SF,g}/\tau_{SF,t}$ (Fig. 3.27b). Each curve is labeled with the value of the varying parameter. An efficient pumping results in a high contrast between the occupations $P(g_L)$ and $P(g_R)$ and an absence of spin pumping brings them both to 0.5.

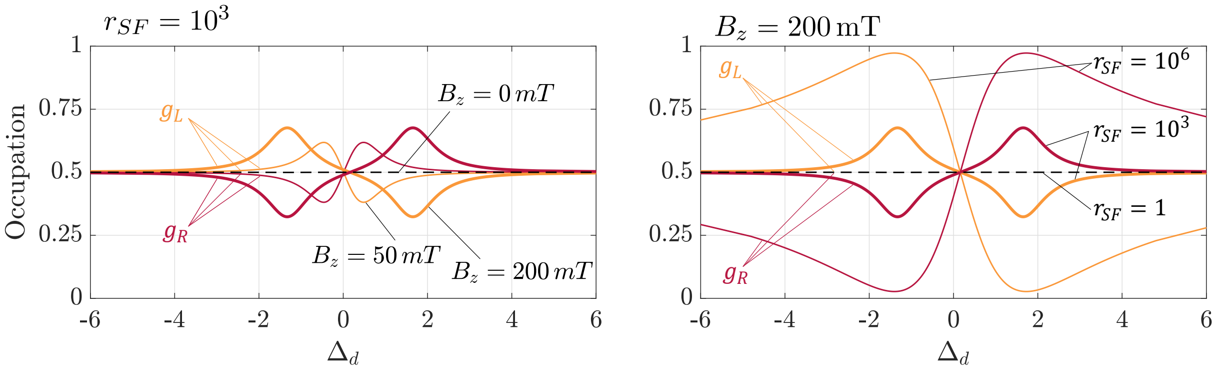

(a) (b)

FIGURE 3.27: Occupation of the ground spin states with $\tau_{SF,t} = 100\,\mathrm{ns}$ **(a)** for different magnetic fields at $r_{SF} = 10^3$ and **(b)** for different values of r_{SF} at $B_z = 200\,\mathrm{mT}$. A high magnetic field and a high spin-flip ratio both improve the quality of the spin pumping.

The first feature to notice is that the spin pumping is only efficient when the input laser is tuned to the energy of one of the branches: on the contrary, at the particular value $\Delta_d = 0$, no asymmetry arises between the population of the two ground states as the two branches are equally addressed by the H-polarized excitation, thus $P(g_L) = P(g_R) = 0.5$. Incidentally, the dashed black lines at 0.5 evidence that the absence of a magnetic field or a unity spin-flip ratio preclude any spin pumping. The spin pumping becomes more efficient when the magnetic field increases (higher Zeeman splitting, so less crosstalk between the two transitions) or when the spin-flip ratio increases[1] (higher asymmetry between the fast trion and the slow hole spin-flip rates).

This change in the populations of the ground hole spin states implies a modified average density matrix, and thus a different Stokes vector of the reflected polarization state when the spin is not initialized, $\boldsymbol{S}^{(avg)}$. It is plotted in Fig. 3.28 as a function of the laser-quantum dot detuning, at $B_z = 50\,\mathrm{mT}$, for different spin-flip ratios from $r_{SF} = 1$ (no spin pumping) to $r_{SF} = 10^6$ (very efficient spin pumping). Here, the Stokes vector $\boldsymbol{S}^{(avg)}$ is the average between the trajectories of $|\Psi_{\Uparrow}\rangle$ and $|\Psi_{\Downarrow}\rangle$ at 50 mT seen in Fig. 3.24, with weights corresponding to the occupation probabilities of states $|\Uparrow\rangle_z$ and $|\Downarrow\rangle_z$ analogous to Fig. 3.27b. Specific points of $|\Psi_{\Uparrow}\rangle$ and $|\Psi_{\Downarrow}\rangle$ take identical values regardless of the spin-pumping:

- $\Delta_d = 0$: both $|\Psi_{\Uparrow}\rangle$ and $|\Psi_{\Downarrow}\rangle$ are equal to $\boldsymbol{S}^{(avg)}(\Delta_d = 0)$ because the weights of $P(g_L)$ and $P(g_R)$ are always 0.5.
- $|\Delta_d| \gg 1$: both $|\Psi_{\Uparrow}\rangle$ and $|\Psi_{\Downarrow}\rangle$ are equal to $|H\rangle$ because the spin is too far in energy to affect on the reflected polarization.

However, the change is quite drastic in between these anchoring points, with an efficient pumping "straightening" the trajectory in the Poincaré sphere (obtained for $r_{SF} \gg 1$). This behavior will help measuring the spin-flip ratios of the real devices.

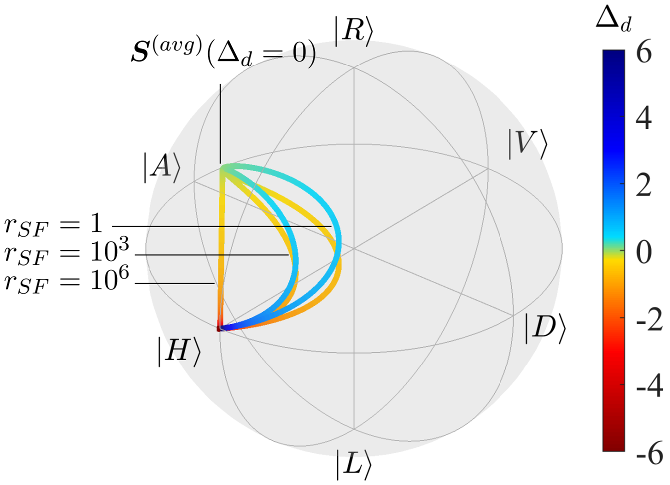

FIGURE 3.28: Effect of the spin flip ratio r_{SF} on the average polarization state $\boldsymbol{S}^{(avg)}$ under a longitudinal magnetic field of 50 mT. Each trajectory goes from $|H\rangle$ to $\boldsymbol{S}^{(avg)}(\Delta_d = 0)$ when Δ_d increases from -6 to 0 and then back to $|H\rangle$ when Δ_d increases to +6.

---

[1] Increasing the power of the input laser results in a similar dependence as increasing the spin-flip ratio since it also favors the spin flip to the branch detuned from the excitation laser through fast electronic spin flip in the excited state.

3.5 Effect of the quantum dot charge blinking: escape and capture mechanisms

In this section, we take into account the possibility that the resident spin carrier is not always present in the quantum dot, causing a blinking effect in the emission. This phenomenon arises when the charge creating mechanism is imperfect or the charge state is unstable. In that regard, we studied in subsection 2.4.2 the case of the optical injection which gets more efficient as the quasi-resonant excitation increases (leading to a higher charge occupation probability). We also mentioned in subsection 2.3.1 that a high-energy non-resonant excitation could create additional charges, thereby resulting in an unwanted charge state. A simple way to describe such phenomena is to include a fifth "empty" level in our model, as well as charge capture and escape mechanisms by the quantum dot.

3.5.1 Complete theoretical model

As the quantum dot is not always in the desired charge state (here, the single hole), we account for the "empty" state of the dot $|\varnothing\rangle$. The updated energy diagram is shown in Fig. 3.29, introducing the charge capture and escape phenomena that populate and depopulate the ground states. We remind from the rate equations of the simple model in subsection 2.4.2 that the average charge occupation probability which we now write P_c is linked to the charge escape and capture times by: $P_c = \tau_{esc}/(\tau_{esc} + \tau_{capt})$.

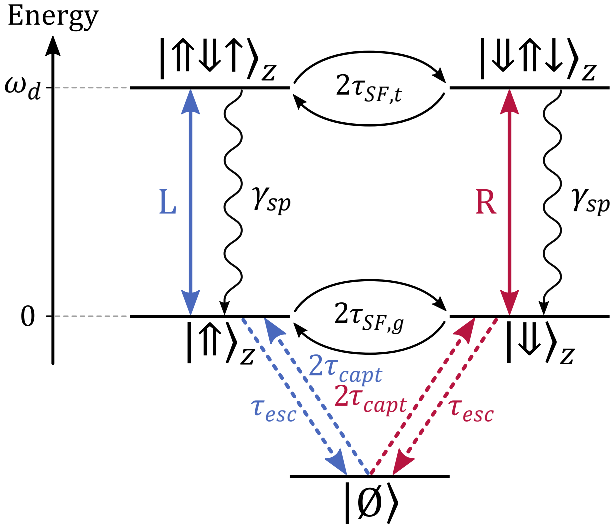

FIGURE 3.29: Quantum dot levels and physical phenomena present in the five-level simulation: coherent spin-photon interaction in the L and R branches (colored arrows), spontaneous emission (wavy arrows), spin flips, and capture / escape mechanisms.

The escape and capture mechanisms are incoherent processes that take the form of four collapse operators that randomly deplete $|g_L\rangle$ and $|g_R\rangle$ at a rate $1/\tau_{esc}$ and populate them at a rate $1/2\tau_{capt}$:

$$\hat{C}_{esc,R/L} = \frac{1}{\sqrt{\tau_{esc}}} |\varnothing\rangle \langle g_{R/L}| \qquad \hat{C}_{capt,R/L} = \frac{1}{\sqrt{2\tau_{capt}}} |g_{R/L}\rangle \langle\varnothing| \tag{3.70}$$

The associated Lindblad operator modeling the blinking phenomenon, $\hat{\boldsymbol{L}}_{blink}$, comprises the contributions of the four collapse operators:

$$\hat{\boldsymbol{L}}_{blink} = \hat{\boldsymbol{L}}_{esc,R} + \hat{\boldsymbol{L}}_{esc,L} + \hat{\boldsymbol{L}}_{capt,R} + \hat{\boldsymbol{L}}_{capt,L} \tag{3.71}$$

and the total Lindbladian from Eq. 3.32 now includes this new term:

$$\hat{\boldsymbol{L}}_{tot} = \hat{\boldsymbol{L}}_{cav} + \hat{\boldsymbol{L}}_{sp} + \hat{\boldsymbol{L}}_{SF} + \hat{\boldsymbol{L}}_{blink} \tag{3.72}$$

If we seek to initialize the system in the empty state, we can remove the capture components of the blinking Lindbladian, which becomes $\hat{\boldsymbol{L}}^{(\varnothing)}_{blink} = \hat{\boldsymbol{L}}_{esc,R} + \hat{\boldsymbol{L}}_{esc,L}$. Conversely, keeping only the capture terms initializes the system in the single hole charge state.

3.5.2 Numerical simulation

Effect on the Stokes parameters and detuning-dependent cross-correlations

The imperfect occupation of the ground state materializes in a new Stokes vector of the output polarization when the spin is not initialized, written $\boldsymbol{S}^{(avg)}$, plotted in the Poincaré sphere for $P_c = 0.56$ and $|\Psi_{in}\rangle = |H\rangle$ in Fig. 3.30. Compared to the four-level case where $P_c = 1$ and the trajectory of $\boldsymbol{S}^{(avg)}$ is the average only between $|\Psi_{\Uparrow}\rangle$ and $|\Psi_{\Downarrow}\rangle$ with equal weights (Fig. 3.10), the average is now between $|\Psi_{\Uparrow}\rangle$ and $|\Psi_{\Downarrow}\rangle$ with a probability $P_c/2$ and $|\Psi_{\varnothing}\rangle = |\Psi_{in}\rangle$ with a probability $1 - P_c$. The result is that the trajectory does not go all the way from H to V. Here, we chose $P_c = 0.56$ as an example; this specific value results in $s_{HV}(\Delta_d = 0) = 0$.

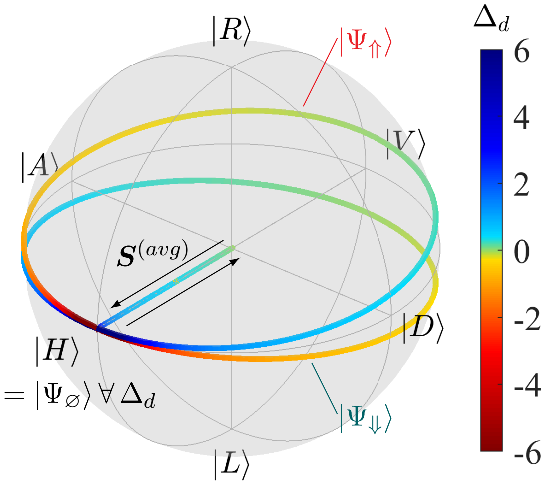

FIGURE 3.30: Effect of the imperfect occupation probability of the charge state through $P_c = 0.56$ on the trajectory of the average Stokes vector $\boldsymbol{S}^{(avg)}$. This non-initialized spin state is now the average of $|\Uparrow\rangle$, $|\Downarrow\rangle$ and $|\varnothing\rangle$, respectively with probabilities $P_c/2$; $P_c/2$; $1 - P_c$, leading to an average of the Stokes vector of the output polarization between $|\Psi_{\Uparrow}\rangle$, $|\Psi_{\Downarrow}\rangle$ and $|\Psi_{\varnothing}\rangle$ with the same respective probabilities.

The effect on the HV Stokes parameter and on the cross-correlations on the optimal basis as a function of the normalized detuning is shown in Fig. 3.31. The imperfect occupation probability results in a loss of contrast in both cases: the value on resonance of s_{HV} goes from -1 for

$P_c = 1$ to 0 when $P_c = 0.56$, as was visible in the Poincaré sphere, while the cross-correlation at $-\Delta_{opt}$ goes from 0 to 0.5 (as highlighted by the dashed lines). An ideal spin-photon interface is still within reach as long as $\langle \Psi_\uparrow | \Psi_\downarrow \rangle = 0$ is verified for a given laser-quantum dot detuning, but a post-selection scheme might be implemented to discard the detected events when the desired charge is not present.

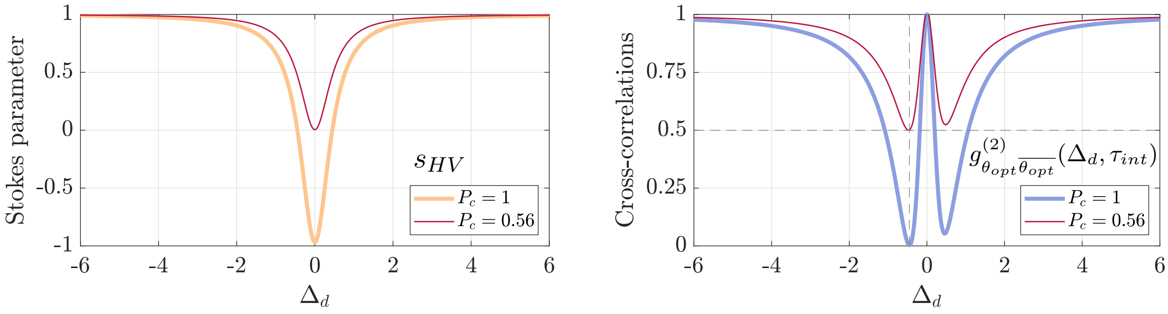

(a) (b)

FIGURE 3.31: Effect of the imperfect occupation probability **(a)** on the Stokes parameter s_{HV} of $\boldsymbol{S}^{(avg)}$ and **(b)** on the cross-correlations in the ideal basis $(\theta_{opt}, \overline{\theta_{opt}})$ at the intermediate delay τ_{int}: $g^{(2)}_{\theta_{opt}\overline{\theta_{opt}}}(\tau_{int}, \Delta_d)$. The ideal working point for $\Delta_d = -\Delta_{opt}$ is highlighted with dashed lines, the cross-correlation at this detuning goes from 0 when $P_c = 1$ to 0.5 when $P_c = 0.56$.

Effect on time-dependent cross-correlations in the optimal basis

Let us now examine the effect of the imperfect charge occupation on the cross-correlations. In Fig. 3.32, the simulations in the optimal basis and for an input laser tuned to $-\Delta_{opt}$ are shown. The characteristic times are $\tau_{SF,g} = 2\,\mu s$; $\tau_{SF,t} = 100\,ns$; $T_c = 20\,\mu s$.

On the left panel, the charge characteristic time is fixed at 20 µs and its occupation probability is changed: although the exponential decay is similar for all cases, caused by the spin relaxation in the timescale of $\tau_{SF,g} = 2\,\mu s$, we observe the loss of contrast of the dip[1] owing to the photons reflected in H when the charge is absent, which the detectors in the optimal basis measure equally, causing a higher number of coincidence events.

In Fig. 3.32b, we investigate the effect of modifying T_c while P_c is fixed at 0.56 and the rest of the parameters are kept identical. The reducing of the decay time when decreasing T_c shows that the dynamics is imposed by the smallest timescale between $\tau_{SF,g} = 2\,\mu s$ and $\tau_{esc} = T_c/(1 - P_c)$; the contrast of the dip can even be diminished if T_c becomes close to the radiative timescale (not shown here, but in a similar fashion as in Fig. 3.21). The combined effect of spin and charge dynamics was first hinted while describing the spin polarization with a simple model in Eqs. 2.23 and 2.24.

---

[1] The radiative relaxation at the ns timescale as seen in Fig. 3.19b is still present but was removed from the plots in this paragraph for clarity.

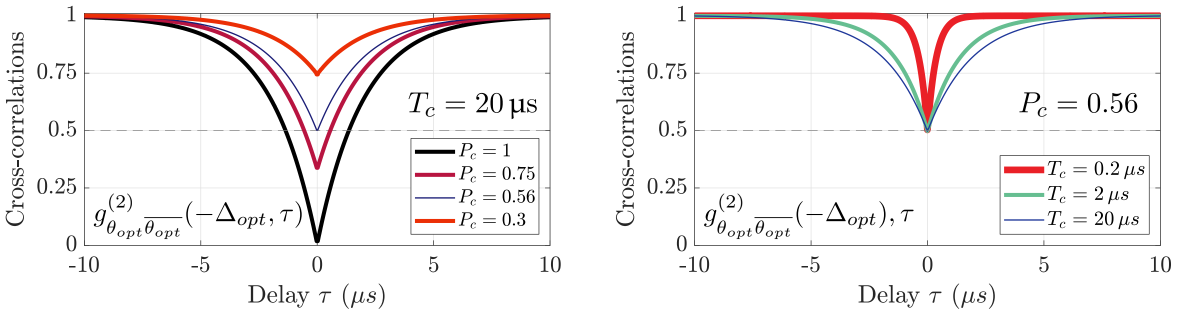

(a) (b)

FIGURE 3.32: Cross-correlations in the optimal basis for an excitation laser of detuning $-\Delta_{opt}$, as a function of the delay. The case $P_c = 0.56$, $T_c = 20$ µs studied in Fig. 3.31b corresponds to the thin blue line, and its cross-correlation value of 0.5 at intermediate timescale $\tau = \tau_{int}$ is highlighted with a dashed line. **(a)** Exploring different occupation probabilities of the charge state P_c, with a fixed $T_c = 20$ µs and **(b)** different charge characteristic times T_c, with a fixed $P_c = 0.56$.

Effect on time-dependent cross-correlations in the (H,V) basis

We now turn to the effect of the charge occupation and characteristic time on the cross-correlations in the (H,V) basis, exploring the exact same parameters as in the last paragraph. The result is presented in Fig. 3.33. As described in section 2.4, this basis is particularly suited to study the charge capture and escape processes, and is blind to the spin-flip mechanisms measured in the $(\theta_{opt}, \overline{\theta_{opt}})$ basis. This is due to the fact that, when $|\Psi_{in}\rangle = |H\rangle$, a photon detection in polarization $|V\rangle$ retrieves no information regarding the spin state, indeed: $\langle V|\theta_{opt}\rangle \simeq \left\langle V\middle|\overline{\theta_{opt}}\right\rangle \simeq 0.5$. Yet, since the V photon was emitted after a trion decay, we know that the quantum dot could not have been in the empty state $|\varnothing\rangle$.

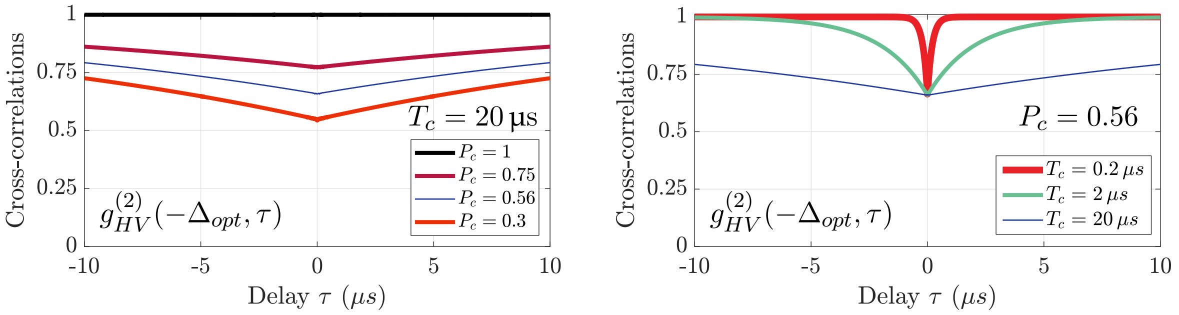

(a) (b)

FIGURE 3.33: Cross-correlations in the (H,V) basis for an excitation laser of detuning $-\Delta_{opt}$, as a function of the delay. **(a)** Exploring different occupation probabilities of the charge state, with a fixed $T_c = 20$ µs and **(b)** different charge characteristic times, with a fixed $P_c = 0.56$.

In Fig. 3.33a, we first display $g^{(2)}_{HV}(-\Delta_{opt}, \tau)$ for different values of the occupation probability P_c. We observe an absence of cross-correlation dip when $P_c = 1$ and a cross-correlation dip of increasing depth when P_c is reduced. In all cases, the decay time is given by $T_c = 20$ µs. Then, in Fig. 3.33b, we show the evolution of the cross-correlation when the value of T_c is changed from 0.2 µs to 20 µs proving that the decay time only depends on T_c and is not limited by the spin-flip time $\tau_{SF,g} = 2\,\mu\text{s}$. This figure illustrates that the (H,V) basis is sensitive only to the charge state since and not the spin state.

3.6 Effect of pure dephasing and slow charge noise

In this section, we compare two sources of noise: pure dephasing and spectral wandering. They both model the effect of environmental fluctuations on the system but they differ on the timescale of these fluctuations. Pure dephasing represents fluctuations faster than any dynamics of the system (i.e., radiative decay, spin-flip, charge capture and escape): the resulting measurement is fundamentally blurred out and no measurement apparatus could overcome this noise source. In our system, this would correspond to fluctuations happening on the timescale shorter than the nanosecond. By opposition, spectral wandering pertains to fluctuations that are slow enough that the system can adiabatically adapt, leading to a measurement constituted by the average over the system's response to different configurations of the environment. Therefore, a measurement apparatus fast enough could in principle overcome such a noise. In our system, the slow noise timescale is of the order of milliseconds or higher.

Pure dephasing is introduced in the numerical simulation with a collapse operator, blurring out the quantum state ahead of the density matrix calculation, whereas spectral wandering is modeled by the Gaussian averaging of the density matrix. This type of slow noise is frequent in solid-state quantum devices [168]. The fundamental difference between pure dephasing and spectral wandering is explored in this section regarding their footprint on the reflected polarization state and cross-correlation measurements. They will be applied to the simulations of real devices in the next chapters to establish which phenomena are at play.

3.6.1 Pure dephasing

We first examine the effect of the pure dephasing. It is caused by interactions with phonons and charge carriers on short timescales compared to the lifetime of the excited level [159]. Its effect is to blur out the energy of the excited levels. The pure dephasing is modeled by a phase reset of the coherent evolution of the trion state at a rate γ^*, and is mathematically translated by the following collapse operator:

$$\begin{aligned}\hat{\boldsymbol{C}}_{deph} &= \sqrt{2\gamma^*}\Big(\,|t_R\rangle\langle t_R| + |t_L\rangle\langle t_L|\,\Big)\\ &= \sqrt{2\gamma^*}\left(\hat{\boldsymbol{\sigma}}_R^\dagger\hat{\boldsymbol{\sigma}}_R + \hat{\boldsymbol{\sigma}}_L^\dagger\hat{\boldsymbol{\sigma}}_L\right)\end{aligned} \tag{3.73}$$

Here, we account for an in-phase pure dephasing, which can be seen as a fast electric noise[1]. In Fig. 3.34a, we examine the case of a pure dephasing $\gamma^* = 1.2\,\mu\text{eV}$ on the Stokes parameter s_{HV} of the stationary state density matrix. This value of γ^* results in $s_{HV}(\Delta_d = 0) = 0$. A reduction of the contrast and a moderate widening of the dip are visible. The effect on the

---

[1] A fast magnetic noise results in an opposite phase pure dephasing and is modeled by the collapse operator $\hat{\boldsymbol{C}}_{deph,m} = \sqrt{2\gamma_m^*}\Big(\,|t_R\rangle\langle t_R| - |t_L\rangle\langle t_L|\,\Big)$

cross-correlations is shown in Fig. 3.34b: the contrast is reduced by the pure dephasing (much more than in the case of the spectral wandering examined next), the value on resonance is unity with and without noise, and the value at $\Delta_d = -\Delta_{opt}$ (highlighted with dashed lines) goes from 0 without noise to 0.8 with noise. The temporal evolution of the cross-correlations for $\Delta_d = -\Delta_{opt}$ is shown in Fig. 3.35: the reduction of the contrast seen in the detuning dependence is also visible, with no change in the evolution back to equilibrium.

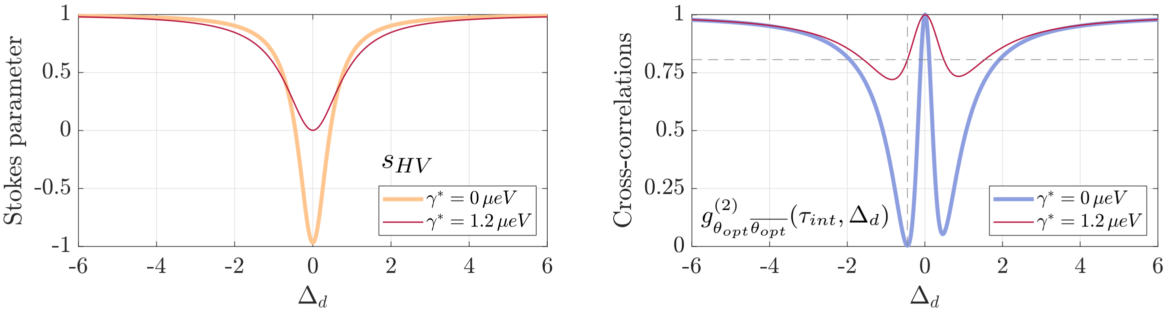

(a)

(b)

FIGURE 3.34: Effect of pure dephasing **(a)** on the Stokes parameter of the stationary state density matrix $\hat{\boldsymbol{\rho}}_{ss}$ and **(b)** on the cross-correlations at intermediate timescale in the optimal measurement basis, plotted as a function of the normalized laser-quantum dot detuning Δ_d.

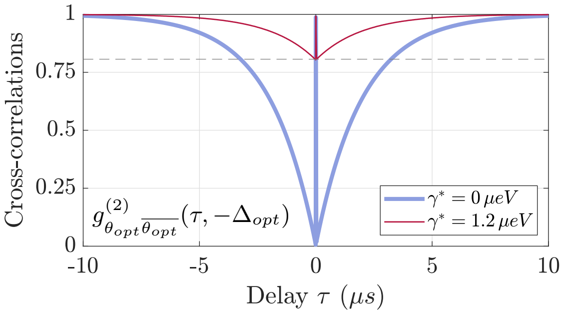

FIGURE 3.35: Effect of pure dephasing on the cross-correlations versus delay. The value at intermediate timescale $\tau = \tau_{int}$ is highlighted with a dashed line as it goes from 0 at $\gamma^* = 0\,\mu\text{eV}$ to 0.8 at $\gamma^* = 1.2\,\mu\text{eV}$, as is the case in Fig. 3.34b.

3.6.2 Slow spectral wandering induced by electric fluctuations

The case of charge noise inducing slow electrical fluctuations is modeled by a fluctuating Stark shift of the energy of the quantum dot transition. It is computed by first defining a probability density function, characterizing the normalized probability that the quantum dot energy is shifted by $\delta\omega_d$ around its average value $\overline{\omega_d}$. It is taken as a Gaussian distribution of width σ_{elec} (in µeV):

$$P(\delta\omega_d) = \frac{1}{\sqrt{2\pi}\sigma_{elec}} e^{-\frac{1}{2}\left(\frac{\delta\omega_d}{\sigma_{elec}}\right)^2} \tag{3.74}$$

Let $\hat{\boldsymbol{\rho}}_{ss}(\overline{\omega_d} + \delta\omega_d)$ be the density matrix at stationary state corresponding to a quantum dot of energy shifted by $\delta\omega_d$. We calculate the average density matrix by summing over a selected range of fluctuations $\delta\omega_d \in [-N, N] \times \mathrm{d}\omega$ where N and $\mathrm{d}\omega$ set the range and the step of the distribution of samples to average. The averaged density matrix is calculated with the formula:

$$\hat{\boldsymbol{\rho}}_{s,avg} = \sum_{k=-N}^{+N} \hat{\boldsymbol{\rho}}_{ss}(\overline{\omega_d} + k\mathrm{d}\omega) P(k\mathrm{d}\omega) \times \mathrm{d}\omega \tag{3.75}$$

The expectation value of the observables are computed on this averaged density matrix. Moreover, the cross-correlations can be computed either this way or by an extended semi-analytical approach developed in appendix B.

Averaging over a charge noise of width $\sigma_{elec} = 2.1\,\mu\mathrm{eV}$ results in the Stokes parameter s_{HV} of the stationary state density matrix presented in Fig. 3.36a: this specific width of the spectral wandering widens the dip and reduces the contrast so that $s_{HV}(\Delta_d = 0) = 0$. On the other side, the cross-correlations at intermediate delay are shown in Fig. 3.36b: the loss of contrast is apparent, as wells as the convolution between the non-averaged cross-correlation curve and the Gaussian noise, resulting in a single large dip. The value on resonance is drastically reduced while the value at $-\Delta_{opt}$ (highlighted with dashed lines) goes from 0 without noise to 0.4 with spectral wandering. The time dependence of the cross-correlations for $\Delta_d = -\Delta_{opt}$ is simulated in Fig. 3.37; it features the same loss of contrast at short delays as the one seen in Fig. 3.36b, without any change in the evolution back to equilibrium.

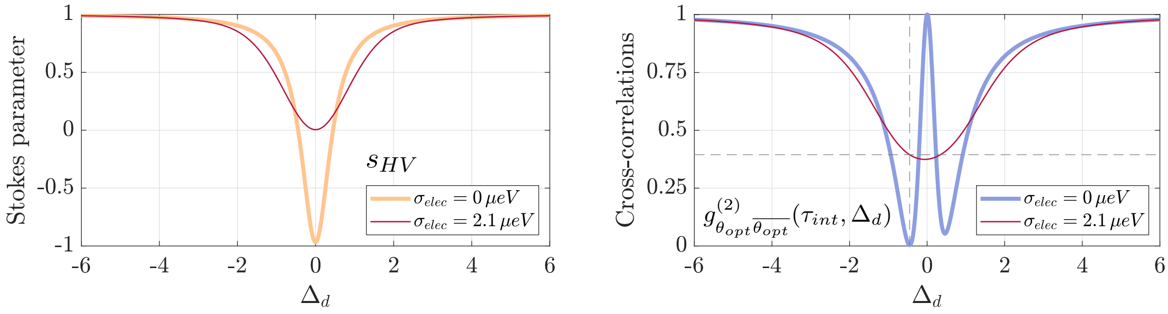

(a) (b)

FIGURE 3.36: Effect of slow electric fluctuations **(a)** on the Stokes parameter of the stationary state density matrix $\hat{\boldsymbol{\rho}}_{ss}$ and **(b)** on the cross-correlations at intermediate timescale in the optimal measurement basis, plotted as a function of the normalized laser-quantum dot detuning $\Delta_d = (\omega - \omega_d)/\Gamma$. The value at $\Delta_d = -\Delta_{opt}$ is highlighted with a dashed line as it goes from 0 at $\sigma_{elec} = 0\,\mu\mathrm{eV}$ to 0.4 at $\sigma_{elec} = 2.1\,\mu\mathrm{eV}$.

The case of the spectral wandering is very similar to that of the pure dephasing in its consequence on the Stokes parameters: one cannot distinguish the two sources of noise with such a measurement. However, the cross-correlations are impacted very differently by these two phenomena, owing to their different physical origin, in particular, the value of the cross-correlation on resonance ($\Delta_d = 0$) is unchanged by pure dephasing but drastically reduced by spectral wandering. Such a cross-correlation measurement can therefore give relevant information on the sources of noise present in a device.

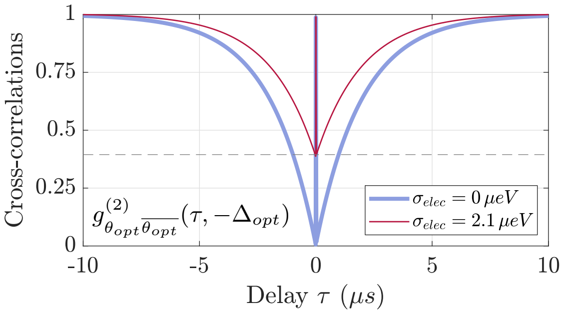

FIGURE 3.37: Effect of slow electric fluctuations on the cross-correlations versus delay. The value at intermediate timescale $\tau = \tau_{int}$ is highlighted with a dashed line as it goes from 0 at $\sigma_{elec} = 0\,\mu\text{eV}$ to 0.4 at $\sigma_{elec} = 2.1\,\mu\text{eV}$, as is the case in Fig. 3.36b.

3.7 Conclusion

A rigorous modeling of the spin-photon interface was developed in the theoretical framework of the master equation. The steady state simulation revealed the way that the spin states rotate the polarization of the reflected photons and the influence of the cooperativity and the top mirror output coupling. The dynamic simulation showed how the detection of a reflected photon could modify the system's density matrix, to the point of a perfect measurement, and characterized the footprint of this effect in the photonic correlation measurements. Finally, we explored the impacts of an external magnetic field, charge blinking, pure dephasing and slow charge noise that are common in quantum dots. In the next chapters, we characterize the real devices and use the modeling tools developed in this chapter to understand the phenomena at play.

Chapter 4

Measuring the spin noise of a single hole spin with single detected photons

This chapter presents experiments conducted on the positively charged micropillar - quantum dot device (presented in section 2.1), leading to the observation of single spin noise through the measurement of single photons reflected from the device. To that end, we evaluate both in the steady-state and dynamic regimes the giant spin-dependent Faraday rotation effect, which is at the core of a quantum dot-based spin-photon interface. We rely on the experimental principles laid out in chapter 2 to characterize the imprint of the spin-photon interaction on the reflected polarization, and fit the measurements with the master equation simulation following the analysis of chapter 3. The simulations provide the cQED parameters of the device by fitting, in the steady state, the Faraday rotation of the reflected polarization, and then, in the dynamic regime, the spin measurement induced by the detection of single photons. Furthermore, the latter allows to access the spin dynamics and to discriminate between different types of noise sources. We eventually suggest solutions to circumvent the noise that would pave the way to achieving a close to ideal spin-photon interface. The experiments were conducted with P. Hilaire [155], and I present here a detailed theoretical analysis of the data.

4.1 Overview of the conducted measurements

The first series of measurements reported in this chapter probes the reflected photons in the steady state with reflectivity and polarization tomography measurements. To that end, we take advantage of the optical setup presented in Fig. 2.5 to inject an H-polarized laser in the device and monitor the reflected intensities in the (H,V,D,A,R,L) output polarizations while the energy of the input laser is scanned. The full polarization state is reconstructed in the Poincaré sphere, and reveals the Faraday rotation induced in average by the single hole spin in thermal equilibrium between states up and down.

Secondly, the measurement of intensity cross-correlations is operated on the same setup, where this time the energy of the input laser is fixed, and the statistics of the photonic detection events are analyzed in different polarization bases with single photon detectors through cross-correlations. The basis where the spin state is optimally imprinted on the reflected polarization state is identified (see subsection 3.3.2). We then proceed to study the effect of the input power and of a longitudinal magnetic field on the cross-correlations and demonstrate that a 30 mT field corresponds to an optimum for the operation as a spin-photon interface, where the spin is partially shielded from the Overhauser field. The simulation matches best the experimental data for a specific combination of noise sources. In addition, a discrepancy at low magnetic fields is interpreted through the lack of a simulated hyperfine interaction.

We recall from the previous chapters that the heterostructure of the *positively charged device* facilitates the optical injection of a single hole in the quantum dot by quasi-resonant excitation (see Fig. 2.2 for the structure and Fig. 2.11 for the excitation scheme). Consequently, in the whole chapter and unless stated otherwise, we address the device with the two-color CW excitation scheme comprising an H-polarized, 8 pW resonant laser and a 2 µW, 901 nm quasi-resonant laser.

4.2 Optical characterization in the steady state with tomography measurements

The spin-dependent polarization rotation occurring in the *positively charged device* is now characterized in the steady state through reflectivity and polarization tomography measurements. In the absence of spin initialization, the quantum dot state naturally evolves in time between a single hole in states spin up $|\Uparrow\rangle$ or spin down $|\Downarrow\rangle$ and the empty state $|\varnothing\rangle$, leading to an average of the reflected polarization states. Its measurement and modeling in the master equation framework gives valuable information on the device cQED parameters and indicates its strengths and weaknesses regarding the operation as a spin-photon interface.

4.2.1 Reflectivity of the quantum dot-microcavity device

As a preliminary experiment, we follow up on the empty cavity characterization of the *positively charged device* presented in section 2.2. In particular, we explore further the reflectivity spectra of the device with a focus on the quantum dot contribution. Reflectivity spectra were first analyzed with the polarization-resolved reflectivity setup presented in Fig. 2.5 and aiming at the characterization of the cavity modes detailed in Fig. 2.6. At this time, a high-power resonant laser polarized along the cavity modes H and V was exciting the device and the reflected light was collected in the parallel polarization with freespace detectors to observe the characteristic dip associated to each cavity mode. Here, the experiment is carried out again with much more sensitive detectors (fibered single photon APDs) so as to carry out the reflectivity measurement with an input power below quantum dot saturation and evidence the quantum dot contribution.

On the left panel of Fig. 4.1 is shown a wide view of cavity and quantum dot reflectivity spectra (or *normalized reflected intensity*), and on the right panel, a zoomed view focusing on the quantum dot contribution. Two sets of lines are visible: first, we plot in light red and blue the cavity modes reflectivity spectra, obtained by exciting the device in H and V with the resonant laser only and collecting the reflected light in the parallel polarization. The corresponding plots are labeled "$I_H(cav)$ (exc. H)" and "$I_V(cav)$ (exc. V)". These scans cover the resonances of the two cavity eigenmodes, split by 74 µeV. Second, on top of the light curves, we add in bright red and blue the reflectivity scans including the quantum dot feature, activated by adding the auxiliary quasi-resonant excitation. This time, the reflected light following an H excitation is observed in the parallel (H) and cross (V) polarizations, respectively labeled "$I_H(QD)$ (exc. H)" and "$I_V(QD)$ (exc. H)". These plots are centered on the spectral region where the quantum dot is active, respectively forming a narrow dip or peak very close to the center of the H cavity mode. The quantum dot effect perceived in this experiment is a reduction of the number of reflected H-polarized photons and an increase in the V polarization.

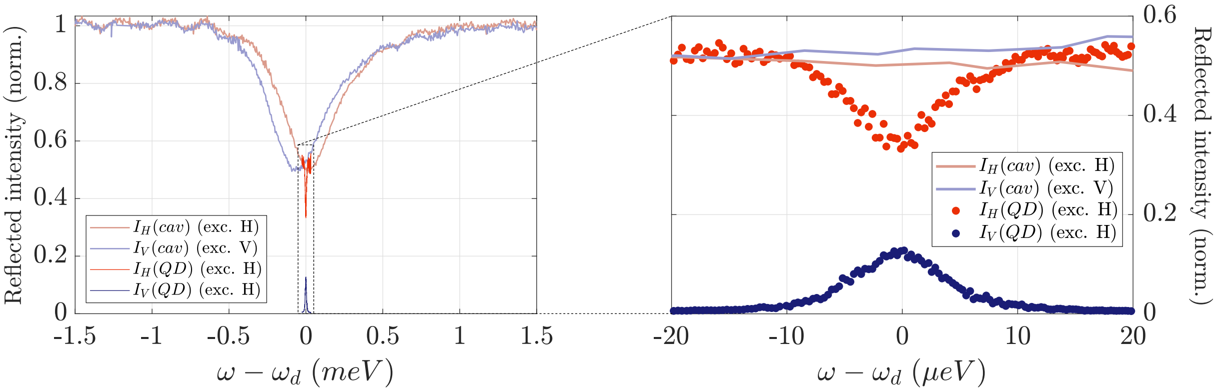

FIGURE 4.1: Reflected intensity normalized by the input one, in the H and V collection polarizations, as a function of the detuning between the resonant laser and the quantum dot, $\omega - \omega_d$. The light-colored curves relate to the cavity modes reflectivity with a collection in the parallel polarization. The bright-colored curves relate to the quantum dot reflectivity, with an H excitation and a collection in H or V. The right panel shows a zoom on the central detuning range to focus on the quantum dot contribution.

Even though the charge state occupation is yet to be determined, the 10 µeV linewidth of the quantum dot feature can give information on the amount of noise by comparing it to the Fourier-limited width. The latter is estimated at $\Gamma = 3.3\,\mu\text{eV}$, corresponding to the measurement of a 200 ps radiative lifetime presented in Fig. 2.13. The measured linewidth is almost three times wider than the Fourier limit, suggesting the presence of a noise mechanism such as pure dephasing or slow electric or magnetic fluctuations. At this point, it is only possible to assert that the noise averages out the signal with a characteristic time smaller than the typical acquisition time of 10 ms for each measured reflectivity point.

4.2.2 Polarization tomography and effect of a longitudinal magnetic field

The successive reflectivity scans while exciting in H and collecting in (H,V,D,A,R,L) enable us to compute the Stokes vector of the reflected photons in order to get the complete picture of the quantum dot-induced polarization transformation through its analysis in the Poincaré sphere. Moreover, we study its dependence to a longitudinal magnetic field as it will later prove relevant in shielding the quantum dot spin from environmental fluctuations.

The Stokes parameters of the reflected polarization are first computed as defined in Eq. 1.26 using the reflectivity spectra, and are plotted in Fig. 4.2 for the longitudinal magnetic fields $B_z = 0, 30, 200\,\text{mT}$, as a function of the laser-quantum dot detuning $\omega - \omega_d$, focusing on the detuning range close to the quantum dot contribution. The device is accordingly excited with the two-color scheme to activate the quantum dot. Then, the associated Stokes vectors are plotted in the Poincaré sphere in Fig. 4.3 as their 3D coordinates are simply defined by the Stokes parameters. There, we introduce the polarizations $|\theta_o\rangle$ and $|\overline{\theta_o}\rangle$ in which the cross-correlation experiments to come exhibit the best contrast: these are the optimal measurement polarizations as introduced in Fig. 3.16, defining the best working point of the device as a spin-photon interface. Here, the raw experimental data were corrected by a rotation in the Poincaré sphere to bring the out-of-resonance points to the input polarization H, as detailed in appendix C.

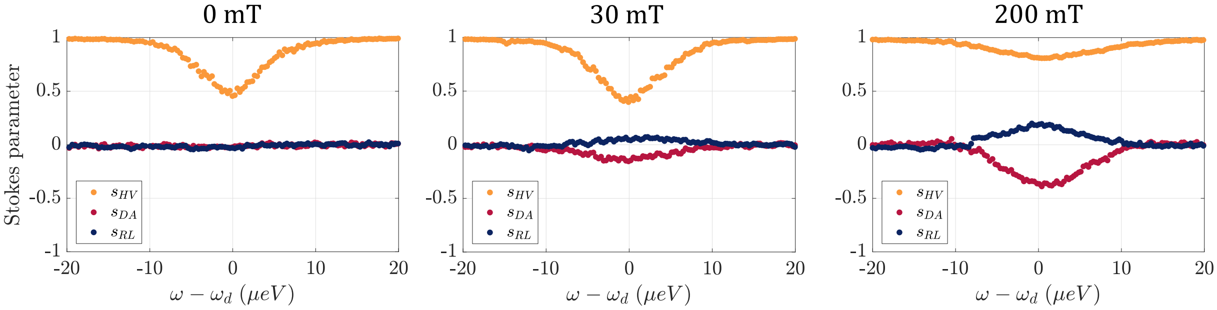

FIGURE 4.2: Detuning dependence of the Stokes parameters characterizing the reflected polarization while exciting the *positively charged device* with the two-color scheme. The data are plotted as a function of $\omega - \omega_d$, for longitudinal magnetic fields of $0,\ 30, 200\,\mathrm{mT}$.

The 0 mT data exhibits a dip in the Stokes parameter s_{HV} (expected from Fig. 4.1) while s_{DA} and s_{RL} are constantly null. This behavior is explained by the averaging of the spin state fluctuating in time between $|\Uparrow\rangle$, $|\Downarrow\rangle$ and $|\varnothing\rangle$, resulting in an average of the reflected Stokes vector between the polarization states $|\Psi_\Uparrow\rangle$, $|\Psi_\Downarrow\rangle$ and $|\Psi_\varnothing\rangle$, associated to the initialized spin states. More details can be found in the simulation from Fig. 3.11 with a unity charge occupation probability and from Fig. 3.30 with charge blinking. Here, the trajectory of the Stokes vector evidences the expected depolarization, as it is brought to the center of the sphere when entering in resonance with the quantum dot. The noiseless simulation with an ideal charge occupation predicts that $s_{HV}(\omega = \omega_d) \simeq -1$ at 0 mT: the value reported here is significantly different, around 0.5. In section 3.5 and 3.6, we showed that this diminished quantum dot contribution could come from charge blinking, pure dephasing as well as slow electric fluctuations. The on-resonance value of s_{HV} observed here implies an average Faraday rotation angle of ±60° in the Poincaré sphere, depending on the spin state, which is a major improvement with respect to the previous generation of devices [27] (±12°), comparable with the current state of the art in the group of R. Oulton [28] who demonstrated rotation amplitudes of $60 - 122°$ using a type of post-selection scheme (the ideal spin-photon interface requires at least a ±90° rotation). When adding a longitudinal magnetic field of 30 mT or 200 mT, the dip in s_{HV} loses contrast and the s_{DA} and s_{RL} parameters stray from their previously null value. This effect is expected when the contributions of the spin states (and thus of $|\Psi_\Uparrow\rangle$ and $|\Psi_\Downarrow\rangle$) are brought out of balance by the magnetic field (as simulated in Fig. 3.28). Furthermore, it is apparent that the trajectories of the Stokes vectors are contained in the $(H\theta_o V\overline{\theta_o})$ plane with $\theta_o = -24°$. As indicated by the simulation, this is the symmetry plane between the $|\Psi_\Uparrow\rangle$ and $|\Psi_\Downarrow\rangle$ trajectories, which is tilted due to cavity splitting as seen in Fig. 3.12.

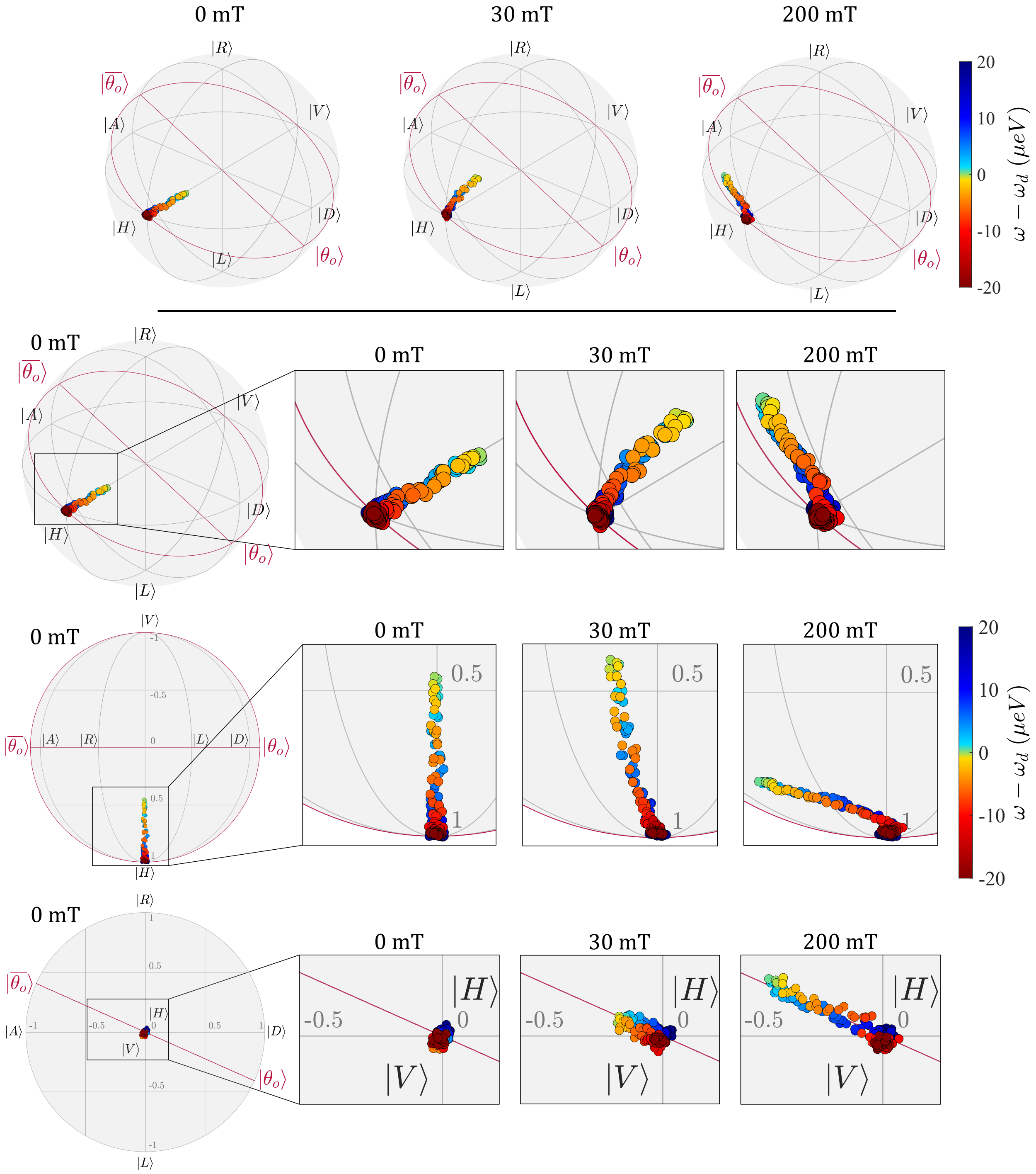

FIGURE 4.3: Polarization tomography of the *positively charged device* excited with the two-color scheme, scanning the detuning between the resonant laser and the quantum dot, $\omega - \omega_d$, for different values of the longitudinal magnetic field. The $(H\theta_o V\overline{\theta_o})$ circle is highlighted in red. The top row contains the full Poincaré spheres while the next three rows display zoomed views, first with the initial viewpoint, then as seen from the top of the $(H\theta_o V\overline{\theta_o})$ plane (with R in the foreground) and second as seen from the (H,V) axis (facing H).

4.2.3 Master equation fitting of the tomography data

The master equation (ME) approach developed throughout chapter 3 is carried out to simulate the experimental results of the *positively charged device* in order to interpret the tomography data from this section as well as the cross-correlation data of the next. Let us introduce the complete set of parameters which corroborates the measurements best:

$$\left|\begin{array}{l}\eta_{in}=1\\ \eta_{top,H}=\eta_{top,V}=0.90\\ \kappa_H=416\,\mu\mathrm{eV}\\ \kappa_V=432\,\mu\mathrm{eV}\\ \omega_{c,H}-\omega_{c,V}=74\,\mu\mathrm{eV}\end{array}\right| \begin{array}{l}g=17.5\,\mu\mathrm{eV}\\ \gamma_{sp}=0.9\,\mu\mathrm{eV}\\ \gamma^*=0.7\,\mu\mathrm{eV}\\ \sigma_{elec}=2.6\,\mu\mathrm{eV}\end{array}\left| \begin{array}{l}P_c=0.75\\ T_c=100\,\mu\mathrm{s}\\ \tau_{SF,t}=36\,\mathrm{ns}\\ \tau_{SF,g}/\tau_{SF,t}=10^3\end{array}\right| \begin{array}{l}g_{h,\parallel}=0.3\\ g_{e,\parallel}=-0.5\\ \delta_{dia,\parallel}=12\,\mu\mathrm{eV}/\mathrm{T}^2\end{array} \tag{4.1}$$

This set was built with the following premise:

- The first column relates to the bare cavity, which was fitted analytically in section 2.2, leading to the parameters from Eq. 2.8. Here, this preliminary experiment imposes the values of cavity widths and splitting, but we hypothesize a perfect input coupling and allow a small offset of η_{top} due to the fibered collection (see subsection 2.2.3 for more details).

- The second and third columns pertain to the light-matter interaction, the noise sources and the charge and spin dynamics: their values will be justified throughout the current chapter.

- The fourth column characterizes the magnetic sensitivity of the system: the Landé factors and the diamagnetic shift were measured in a separate experiment not shown here, under a high longitudinal magnetic field.

We now examine the agreement between the ME simulation and the experimental reflectivity and tomography observations for different magnetic fields. The experimental points will be superimposed with the fits as solid red lines, and only the value of B_z is to be adapted in the simulation from one dataset to the other.

The reflectivity data are first analyzed in Fig. 4.4 where R_H and R_V recall the normalized reflected intensities first measured in Fig. 4.1 and R_{tot} is their sum.

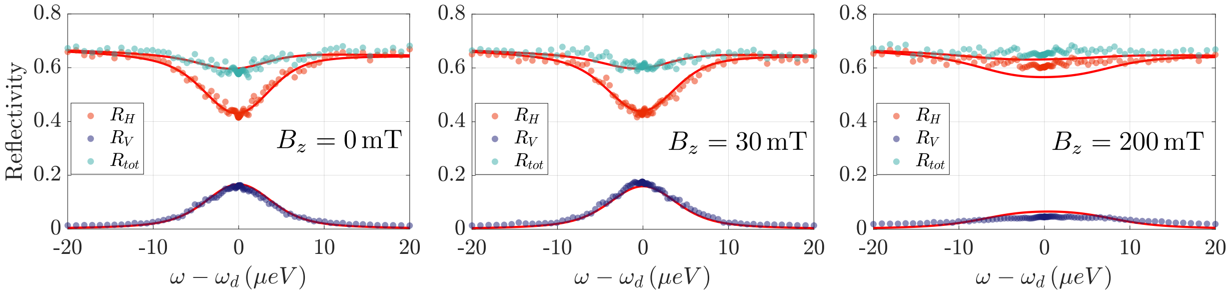

FIGURE 4.4: Experimental reflectivities in H, V and sum of the two, for the longitudinal magnetic fields 0 mT, 30 mT and 200 mT along with fits in solid red lines.

We highlight that the proportion of H and V photons in the reflected field is qualitatively influenced by the chosen couple of (g, γ_{sp}), which is itself constrained by the radiative lifetime of the transition (see Eq. A.1). Even though multiple combinations of (g, γ_{sp}) allow an acceptable fit of R_H and R_V provided an adaptation of the charge occupation probability P_c, we find the best fit of R_H, R_V and R_{tot} simultaneously for $g = 17.5\,\mu\text{eV}$, $\gamma_{sp} = 0.9\,\mu\text{eV}$ and $P_c = 0.75$. Cross-correlation experiments to come in subsection 4.3.2 also agree with this estimation of P_c. It is worth mentioning that the spontaneous emission rate in a micropillar cavity can undergo a scaling up or down by a factor 2 compared to its value in bulk GaAs, $\gamma_{sp,bulk} = 0.6\,\mu\text{eV}$, depending on the exact pillar geometry (radius, shape, etc.) [172].

The Stokes parameters follow in Fig. 4.5 for multiple magnetic fields, and finally the deduced Poincaré vectors in Fig. 4.6 where the viewpoint is set from the top of the $(H\theta_o V\overline{\theta_o})$ plane that contains the experimental and simulated points. The fits agree well with the tomography data for most explored magnetic fields.

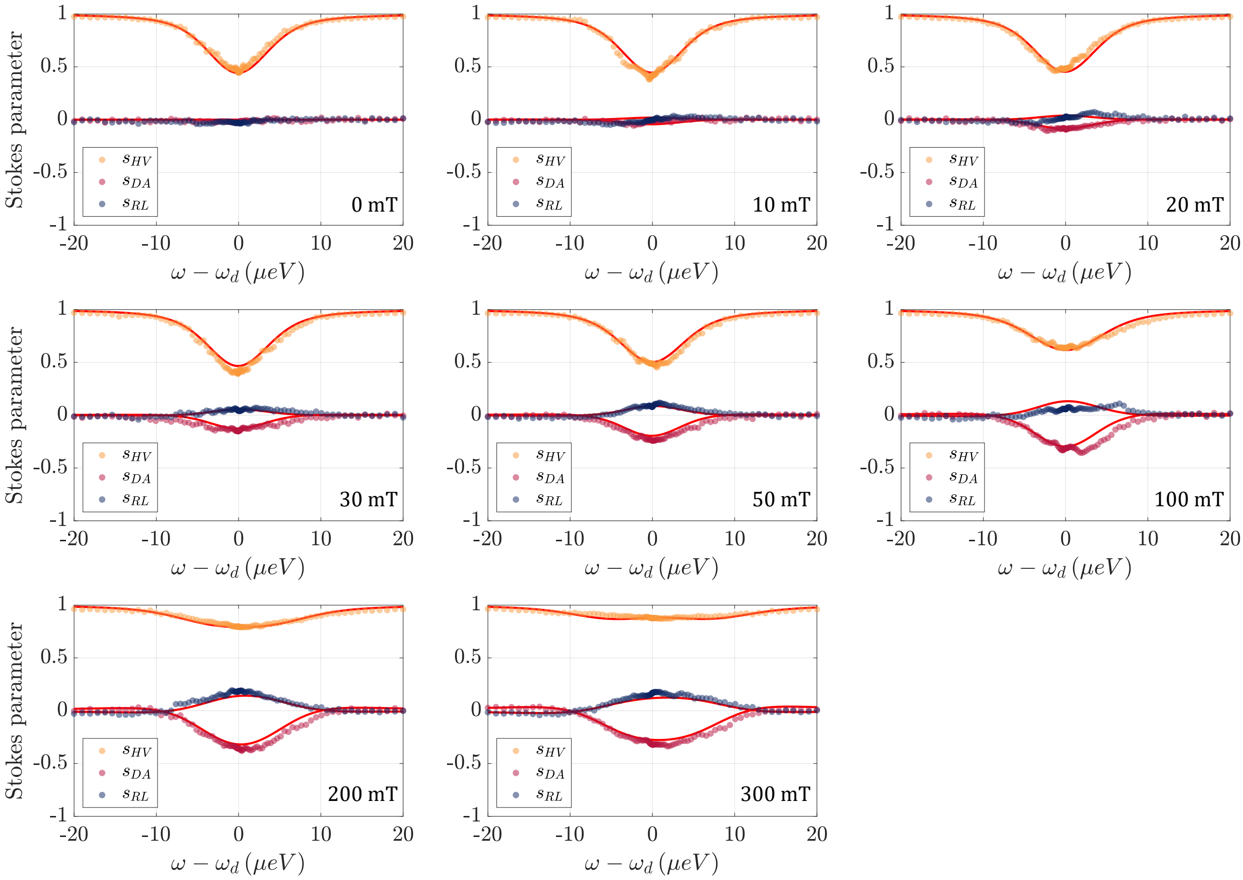

FIGURE 4.5: Experimental Stokes parameters for the multiple values of the longitudinal magnetic field along with fits in solid red lines.

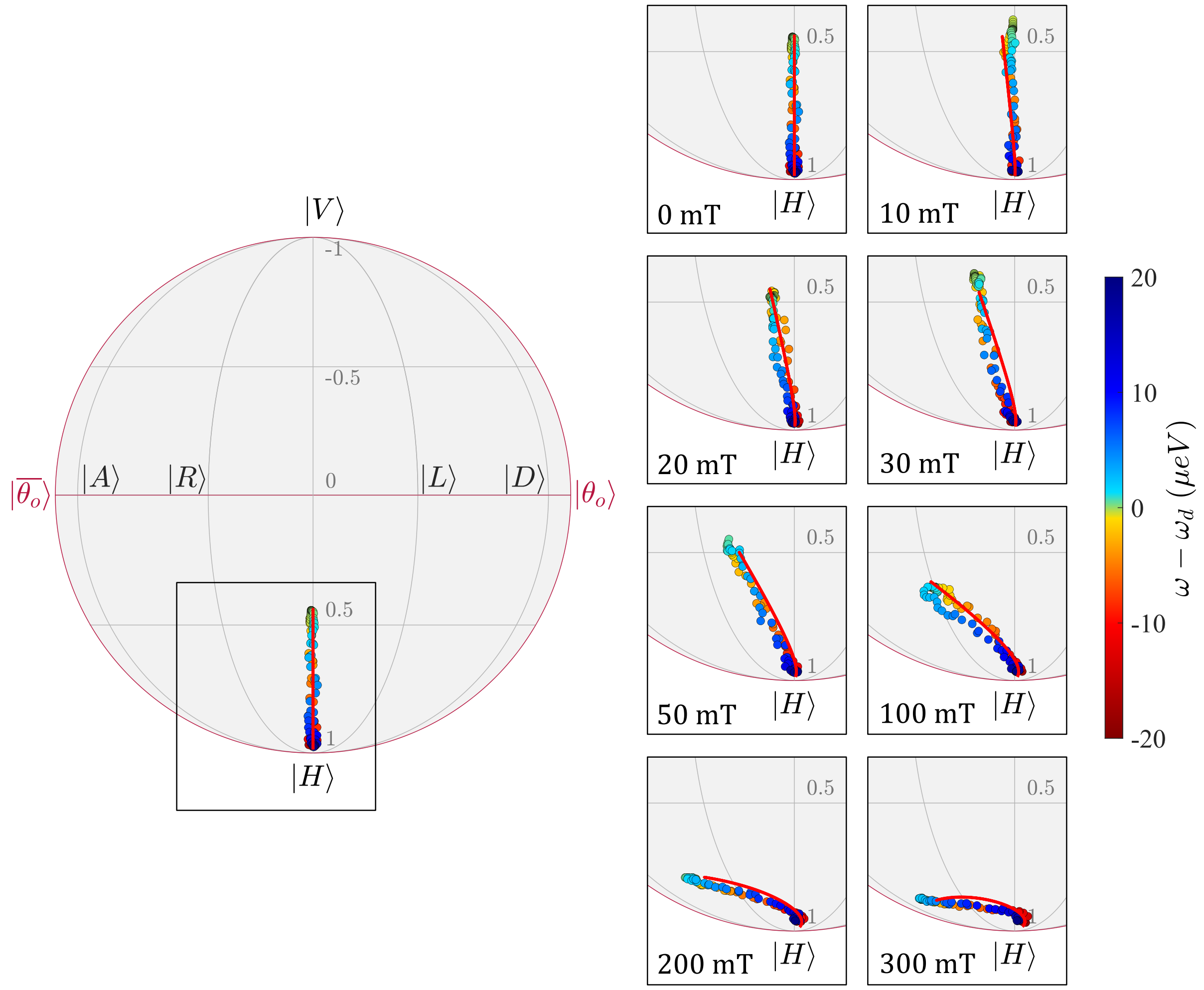

FIGURE 4.6: Experimental Stokes vectors for multiple values of the longitudinal magnetic field along with fits in solid red lines, as seen from the top of the $(H\theta_o V\overline{\theta_o})$ plane. The frame isolates a portion of the sphere plotted at each magnetic field on the right side.

4.2.4 Fitting the tomography data with different noise sources

As far as the tomography data are concerned, both pure dephasing and slow electric noise induce a broadening of the quantum dot contribution (see section 3.6). Therefore, the set of fitting parameters from Eq. 4.1 maintains a proper agreement with the experiment when varying γ^* and σ_{elec} in a complementary way. Let set A be the starting parameters from Eq. 4.1 and sets B and C the ones respectively taking only slow electric fluctuations or pure dephasing while still properly fitting the tomography data. We find the following values:

Set A	$\gamma^* = 0.7 \pm 0.1\,\mu\text{eV}$ $\sigma_{elec} = 2.6 \pm 0.3\,\mu\text{eV}$	Set B	$\gamma^* = 0\,\mu\text{eV}$ $\sigma_{elec} = 3.3 \pm 0.3\,\mu\text{eV}$	Set C	$\gamma^* = 2.0 \pm 0.2\,\mu\text{eV}$ $\sigma_{elec} = 0\,\mu\text{eV}$

The simulated Stokes parameters in the three configurations are shown in Fig. 4.7, demonstrating an accurate fitting in the three cases across the different longitudinal magnetic fields. The reflectivities R_H, R_V, R_{tot} are properly fitted as well (not shown here).

Set A: $[\gamma^* = 0.7\,\mu\text{eV},\ \sigma_{elec} = 2.6\,\mu\text{eV}]$

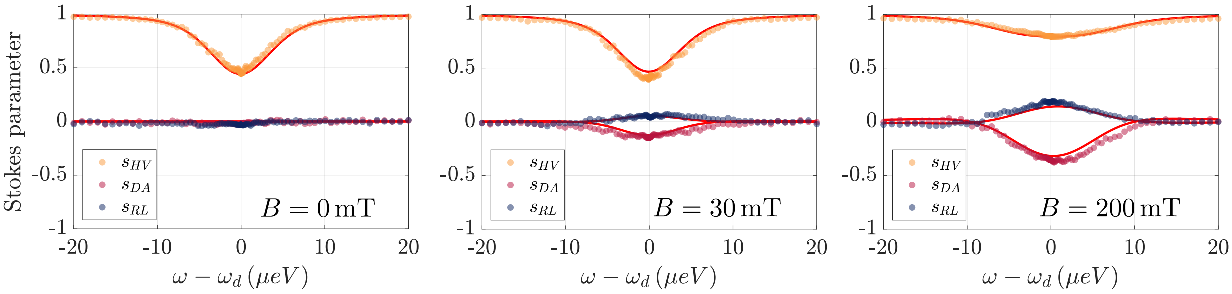

Set B: $[\gamma^* = 0\,\mu\text{eV},\ \sigma_{elec} = 3.3\,\mu\text{eV}]$

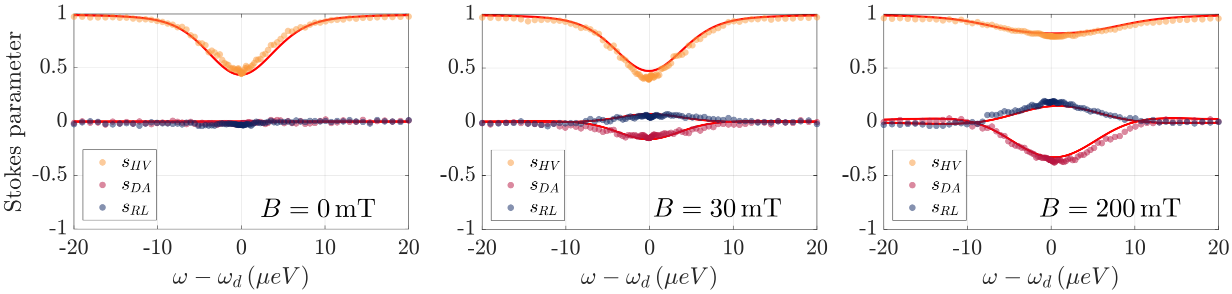

Set C: $[\gamma^* = 2\,\mu\text{eV},\ \sigma_{elec} = 0\,\mu\text{eV}]$

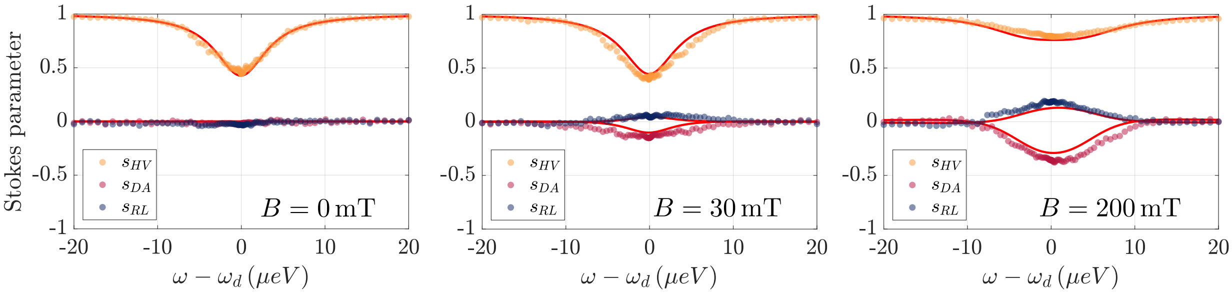

FIGURE 4.7: Experimentally measured Stokes parameters superimposed with ME simulations for longitudinal magnetic fields 0, 30 and $200\,\text{mT}$ (across columns) and for the sets of parameters A, B, C (across rows).

Moreover, as we explore different combinations of pure dephasing and slow electric fluctuations, a multitude of sets is found to fit the Stokes parameters, provided that the total broadening is preserved, as reported in Fig. 4.8. The plotted total cost function represents the difference between the simulation and the experimental data, including the Stokes parameters and the total reflectivity, for all explored magnetic fields. The values of the total cost function are arbitrarily normalized to $[0; 1]$. The black dots on the figure introduce a series of $(\gamma^*,\ \sigma_{elec})$ couples that all fit the tomography data and which we come back to later on, when simulating the magnetic field dependence of the cross-correlation data. Until then and unless stated otherwise, set A is applied in all presented simulations.

At this point, the parameters are almost completely constrained: the values left to justify concern the noise sources $(\gamma^*,\ \sigma_{elec})$ and the spin and charge dynamics (T_c, $\tau_{SF,t}$ and $\tau_{SF,g}$) for which we turn to cross-correlation measurements and the study of charge noise and spin noise.

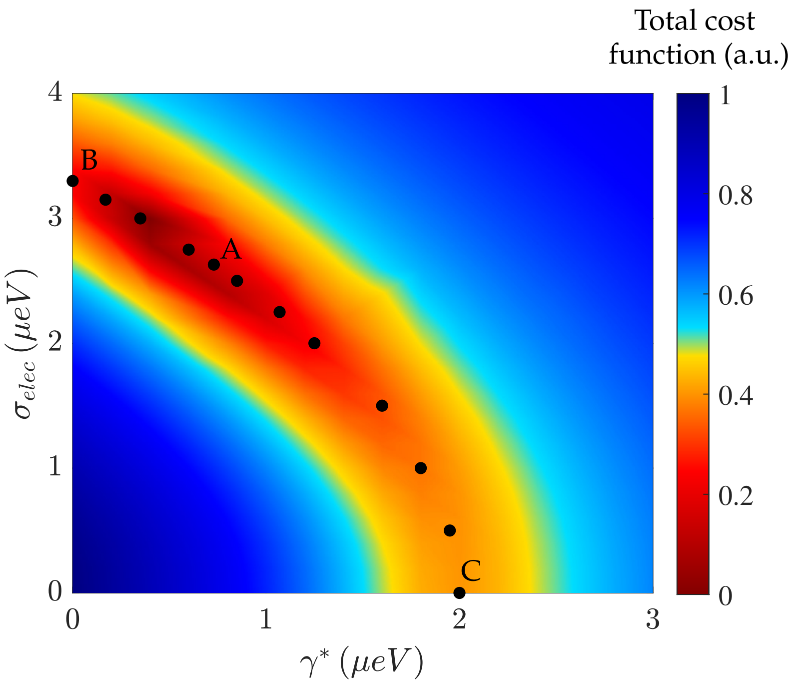

FIGURE 4.8: Total cost function relative to the quality of the simulation of Stokes parameters and reflectivities for all explored magnetic fields, plotted in an arbitrary unit for different (γ^*, σ_{elec}) couples. The black points are the sets of parameters that will be explored in the cross-correlation section up next, and the sets A,B,C introduced above are labeled.

4.3 Cross-correlation measurements: spin noise spectroscopy with single detected photons

The measurement of reflected photons is now used as a tool to investigate the dynamics of the hole, disturbed by the photonic measurement, on its way back to equilibrium. The statistics of the reflected photons detected in different measurement bases allow the separation of the charge and spin dynamics. In the (H,V) basis, sensitive only to the presence or absence of a charge, we evaluate the occupation of the single hole charge state. Then, in the spin-sensitive bases contained in the (DRAL) plane, we study how the detection of a reflected photon partially measures the spin state. The quality of the measurement strongly depends on the basis, and in this regard, the optimal spin-sensitive basis ($\theta_o, \overline{\theta_o}$), exhibits the most contrasted anti-correlation effect and constitutes the best (although not ideal) working point for this device as a spin-photon interface. Finally, these cross-correlations reveal the nature of the noise sources and the limitations of the model.

In the whole section, the device is addressed with the two-color excitation scheme (CW, H-polarized, 8 pW resonant laser and 2 µW, 901 nm quasi-resonant laser), where this time the resonant laser is constantly tuned to ω_d.

4.3.1 Cross-correlations protocol

The cross-correlation measurements consist in splitting the light reflected from the device into two complementary polarizations X and Y, in which the photon detection events are recorded for further statistical analysis. We first described such experiments in subsection 2.4.3 and the complete optical setup in Fig. 3.16.

The cross-correlations are defined as the normalized coincidences between a measured photon in X at time 0 and one measured in Y at time τ. They are computed as the histogram of the time delays between events recorded in one output and the other, with a binning time T_{bin} of a few hundred ns, normalizing the result at unity for delays considered infinite (longer than the dynamic timescales of interest). In mathematical terms, the second order cross-correlation function is experimentally defined as:

$$g_{XY}^{(2)}\left(\tau = kT_{bin}\right) = \frac{N_{XY}\left(kT_{bin}\right)}{N_{\infty}} \tag{4.2}$$

where k is an integer, $N_{XY}\left(kT_{bin}\right)$ stands for the number of events including a photon detection in Y at t_Y and one in X at t_X such that $(k-1)T_{bin} \leq t_Y - t_X \leq kT_{bin}$, and N_{∞} is the empirical normalization factor.

4.3.2 Charge sensitive cross-correlations

The fact that the reflected polarization state without an external magnetic field is contained in the (HV) axis of the Poincaré sphere (see Fig. 4.3) validates the hypothesis that the effects of the quantum dot states $|\Uparrow\rangle$ and $|\Downarrow\rangle$ are averaged over time: the cross-correlations in the (H,V) basis should in principle result only from the presence or absence of the charge state, as extensively studied in section 3.5. Indeed, either the quantum dot does not contain a single hole and the reflected polarization is unchanged (H) or it does and the average reflected polarization $S^{(avg)}$ is brought from H towards V.

Here, the experiment is carried out with the two-color excitation scheme, in the absence of an external magnetic field. In Fig. 4.9, we plot the cross-correlations in the (H,V) measurement basis with a binning time $T_{bin} = 512\,\mathrm{ns}$ per point, revealing especially long timescales. The anti-correlation dip evolves back to unity in a characteristic time on the order of 100 µs. The contrast of the dip is determined by the charge occupation: since the laser is resonant with ω_d, an H-polarized photon can be converted to V by the single hole state, leading to a decrease in H-V correlations. If a V photon is detected, the system is for sure in the single hole state, which is maintained for a time set by the interplay between the charge escape and capture mechanisms of respective timescales τ_{esc} and τ_{capt}. The H-V cross-correlations achieve charge noise spectroscopy with single photons and proved to be a valuable tool to characterize and optimize P_c in everyday experiments.

The current result firstly relates to the analogous characterization from subsection 2.4.2, where the autocorrelations of the V-emitted photons lead to peaks whose contrast and decay time exposed respectively the charge occupation and dynamics, as explained with a simple

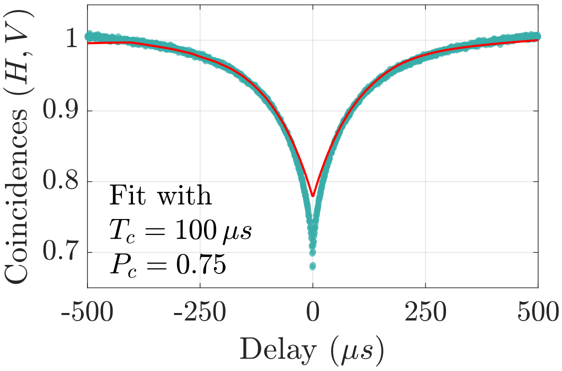

FIGURE 4.9: Cross-correlations in the (H,V) basis without an external magnetic field, as a function of the delay between the photonic detection in each polarization. Each experimental point includes a 512 ns time bin. The solid red line is the ME simulation with the set of parameters A.

analytical charge capture and escape model; in this previous experiment, the resonant laser was pulsed and the autocorrelation showed peaks instead of the dip observed now, with contrast inversely proportional to P_c. Secondly, the effect of the charge occupation probability and its characteristic time were theoretically investigated in the master equation framework in Fig. 3.33, which corroborated the fact that the contrast of the cross-correlations decreases when P_c increases, and that the decay time was set by T_c, even in the presence of shorter spin dynamics[1].

Here, we fit the data with the ME simulation under the set of parameters A (Eq. 4.1), comprising $T_c = 100\,\mu\text{s}$, $P_c = 0.75$ and an the noise sources $(\gamma^* = 0.7\,\mu\text{eV},\, \sigma_{elec} = 2.6\,\mu\text{eV})$. The subsequent charge capture and escape times are $\tau_{capt} = 133\,\mu\text{s}$ and $\tau_{esc} = 400\,\mu\text{s}$, resulting in the decay of the anti-correlations dip on a timescale around 100 µs. The simulation matches the experimental data for the most part, with a discrepancy at short delays that we attribute to experimental imperfections (most likely an offset of the measurement basis compared to the true (H,V) basis, which introduces residual spin effects on the cross-correlations). A more elaborate scenario involving the dynamics between the single hole and states with multiple holes could be considered for a better agreement with the experiment: it should bring about multiple exponential decays owing to the specific capture and escape timescales of each state.

4.3.3 Implementation of spin noise spectroscopy with cross-correlations

We now turn to the main result of this chapter, i.e., spin-sensitive cross-correlations, measured with single photons for the first time to our knowledge: the measurement of a single photon effectively modifies the spin density matrix (see section 3.3), thereby achieving the first step towards the operation as a spin-photon interface.

---

[1] This previous simulation in Fig. 3.33 was carried out in the absence of noise sources and at the specific laser-quantum dot detuning for a perfect spin-photon interface, but the qualitative interpretation holds.

The steady-state polarization tomography measurements demonstrate, in agreement with the simulations, that the spin-dependent polarization rotation is symmetrical with respect to the (HV) axis for very low magnetic fields. To isolate the spin contribution in cross-correlations, we then explore the measurement bases included in the (DRAL) plane, which we call $(\theta, \overline{\theta})$ as defined in Fig. 3.16. Detecting single photons in such bases partially measures the spin, leading to an anti-correlation dip. Its contrast is expected to depend on the laser-quantum dot detuning and the angle defining the measurement basis, θ, as simulated in Fig. 3.20 in the noise-free case.

Experimentally, the photon detection times are recorded in the bases $(\theta, \overline{\theta})$, exciting the device with the two-color scheme, under a 30 mT longitudinal magnetic field stabilizing the spin: these conditions resulted in the highest contrast of the anti-correlation dip. The cross-correlations are determined with Eq. 4.2 using a binning time of 128 ns, and the result is shown in Fig. 4.10: the graph on the left contains the cross-correlations with the best contrast for $\theta_o = -24°$ and the worst for an angle close to $\theta_o + \pi/2$, superimposed with the ME simulation using the set of parameters A (Eq. 4.1). The graph on the right sums up the dependence of the anti-correlation dip as the angle θ of the measurement basis is scanned. The figure also includes the ME simulation of the cross-correlation at intermediate time $g^{(2)}_{\theta_o\overline{\theta_o}}(t = \tau_{int})$: in the current experiment, $\tau_{int} = 5$ ns is considered "zero delay" as the 128 ns binning smooths out the fast radiative transient regime. The relevance of the simulation parameters is supported by the good agreement with the experiment.

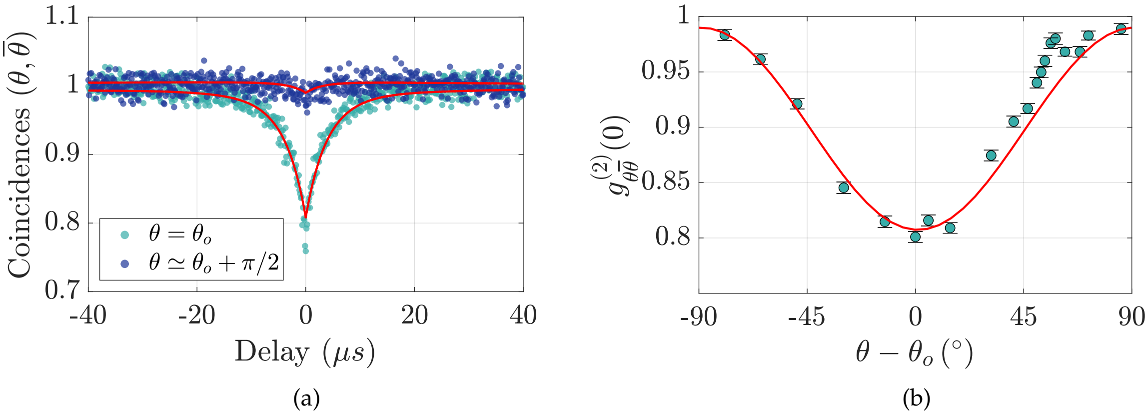

(a)

(b)

FIGURE 4.10: **(a)** Cross-correlations as a function of the delay with a 128 ns binning, in the optimal basis $(\theta_o, \overline{\theta_o})$ and the complementary one. The continuous red lines are ME simulations in both graphs. **(b)** Zero-delay value of the cross-correlations as a function of θ, centered on θ_o.

We emphasize that the anti-correlation was best when the resonant laser was tuned to ω_d. Despite the absence of an experimental study with a varying detuning, this feature can be explained by examining the trajectories of $|\Psi_\Uparrow\rangle$ and $|\Psi_\Downarrow\rangle$ in the Poincaré sphere, as presented in Fig. 4.11. In the absence of noise, the resonance values of $|\Psi_\Uparrow\rangle$ and $|\Psi_\Downarrow\rangle$ are perfectly symmetrical with respect to the $(\theta_o, \overline{\theta_o})$ basis: the cross-correlation contrast should therefore be null. However, slow electrical fluctuations shift the reference value of ω_d in time around an average value $\overline{\omega_d}$ by the fluctuating amount $\delta\omega_d$ such that $\omega_d = \overline{\omega_d} + \delta\omega_d$. In Fig. 4.11, we plot the trajectories of $|\Psi_{\Uparrow}\rangle$ and $|\Psi_{\Downarrow}\rangle$ as a function of $\delta\omega$, along with the optimal cross-correlation basis just determined. Notice that $|\Psi_{\Uparrow}\rangle$ and $|\Psi_{\Downarrow}\rangle$ are by definition not affected by the noise nor by imperfect charge occupation. The figure shows that the measurement in the $(\theta_o, \overline{\theta_o})$ basis can discriminate the two spin states depending on the sign of a non-zero $\delta\omega_d$: indeed when $\delta\omega_d > 0$, the Stokes vector $|\Psi_{\Uparrow}\rangle$ is shifted towards $|\overline{\theta_o}\rangle$ and $|\Psi_{\Downarrow}\rangle$ towards $|\theta_o\rangle$, and vice versa when $\delta\omega_d < 0$. As such, the excitation on resonance with the average quantum dot energy $\overline{\omega_d}$ and detection in the $(\theta_o, \overline{\theta_o})$ basis can indeed partially measure the spin state in the presence of slow electrical fluctuations, without indicating whether the spin is projected in $|\Uparrow\rangle$ or $|\Downarrow\rangle$ since we can't know the value of $\delta\omega_d$ when the photon was detected. However, the cross-correlation dip proves a partial spin projection either in $|\Uparrow\rangle$ or $|\Downarrow\rangle$, induced by the measurement of single photons.

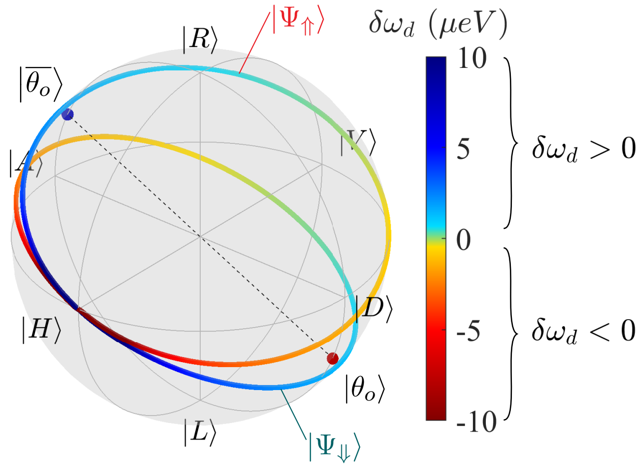

FIGURE 4.11: Poincaré representation of $|\Psi_{\Uparrow}\rangle$ and $|\Psi_{\Downarrow}\rangle$, along with the optimal spin-sensitive measurement basis $(\theta_o, \overline{\theta_o})$ determined experimentally. The excitation laser is set to $\overline{\omega_d}$ and the quantum dot energy shift $\delta\omega_d$ is varied, as shown by the color scale. The quantum dot shifts $\delta\omega_d > 0$ and $\delta\omega_d < 0$ refer to situations where a photon detection in $|\theta_o\rangle$ or $|\overline{\theta_o}\rangle$ partially measures the spin state.

4.3.4 Identification of the noise sources

Although multiple combinations of pure dephasing and slow electric noise properly fit the tomography data (see Fig. 4.8), the unique ways these noise sources manifest in cross-correlations are easily identified. Indeed, as detailed in section 3.6, pure dephasing decreases the cross-correlation contrast whatever the energy of the resonant laser, while slow electric noise mixes the contributions of different detunings. In particular, when the excitation laser is on resonance with $\overline{\omega_d}$, the cross-correlation contrast is always null when only pure dephasing is present, and the anti-correlation dip appears with slow electric noise. This behavior is noticeable in Fig. 4.12 that includes the experimental cross-correlations in the optimal conditions, and simulations in the sets of parameters A ($\gamma^* = 0.7\,\mu\text{eV}$, $\sigma_{elec} = 2.6\,\mu\text{eV}$), B ($\gamma^* = 0\,\mu\text{eV}$, $\sigma_{elec} = 3.3\,\mu\text{eV}$) and C ($\gamma^* = 2.0\,\mu\text{eV}$, $\sigma_{elec} = 0\,\mu\text{eV}$) which all fit the tomography data properly. Only set A with a specific mixture of the two noise sources agrees with the experimental cross-correlations, while set B with only slow electric noise is overcontrasted and set C with only pure dephasing exhibits no anti-correlation dip whatsoever.

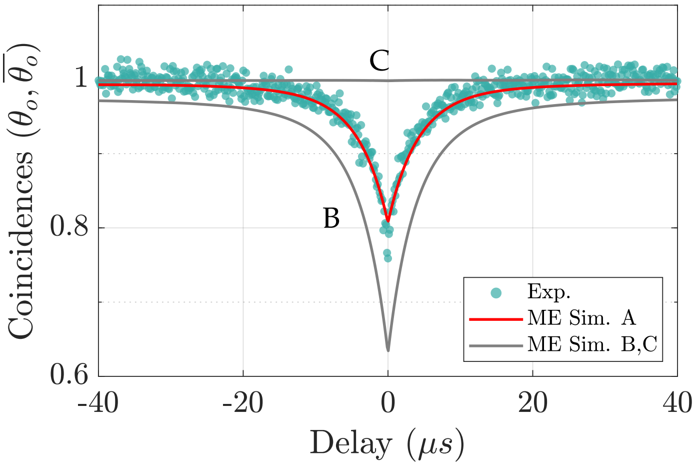

FIGURE 4.12: Cross-correlations in the $(\theta_o, \overline{\theta_o})$ basis with the two-color excitation scheme and a 30 mT longitudinal magnetic field. The scattered points are experimental data, each encompassing a binning time of 128 ns, and the solid lines are the ME simulations: set A in red, sets B and C in gray.

4.4 Spin dynamics and noise sources probed by spin noise spectroscopy

Let the spin noise spectroscopy experiment in the optimal basis be the starting point of two final experiments aiming at confirming the remaining cQED parameters of the device laid out in set A (Eq. 4.1). First, we access the spin-flip timescales by exploring the input power degree of freedom. Second, the longitudinal magnetic field dependence of the cross-correlations confirms the choice of the $(\gamma^*, \sigma_{elec})$ couple but points out a limitation of our model, which doesn't include hyperfine interaction.

4.4.1 Power dependence of the cross-correlations and spin dynamics

Modeling the effect of the spin and charge dynamics on the cross-correlations in the optimal basis has demonstrated that the effective decay time of the contrast was dictated by the shortest timescale between spin flips and charge escape and capture mechanisms (see Fig. 3.32b). Here, the long charge lifetime $T_c = 100\,\mu s$ can hardly be mistaken with the much shorter decay time of the cross-correlations, on the order of 10 µs. In our quantum dots, the spin-flip phenomena can be dominated by electronic spin flips, as electrons are much more sensitive than holes to a fluctuating magnetic field (see subsection 1.2.3). For a positive trion system, spin flips therefore arise from the electron-in-trion, with a rate proportional to the trion occupation that is determined by the input power of the resonant laser.

The typical spin-flip ratio for a positive trion is on the order of $r_{SF} = \frac{\tau_{SF,g}}{\tau_{SF,t}} = 10^3$ [50, 54, 55]. Its value shapes the trajectory of the average reflected polarization state in the Poincaré sphere when an external magnetic field is applied (see Fig. 3.28), a high value of r_{SF} straightening the trajectory and a low value giving it a curved shape. The agreement between our simulation with $r_{SF} = 10^3$ and the tomography data shown in Fig. 4.6 confirms the order of magnitude of the spin-flip ratio, leaving only the value of $\tau_{SF,t}$ to be assessed.

The power dependence of the cross-correlations in the optimal basis is displayed in Fig. 4.13, superimposed with the ME simulation in set A (Eq. 4.1). Only the power of the resonant laser is scanned, from 4 pW to 0.56 nW (8 pW being the standard value in the rest of the chapter), while the power of the quasi-resonant laser is fixed at 2 µW. The external magnetic field of 30 mT is maintained. As the power increases, the trion state is more and more populated, giving rise to fast electron spin flips in the excited state before de-excitation: the consequence is a faster decay of the anti-correlation dip, to the point of even decreasing its contrast at high powers. The agreement between the experimental data and the simulation confirms the value of $\tau_{SF,t} = 36\,\text{ns}$. As for the ground spin flip time, only a lower bound can be surmised, about $\tau_{SF,g} \gtrsim 10\,\mu\text{s}$, since the charge dynamics might come into play at such a long timescale. This is compatible with the order of magnitude of the spin-flip ratio $r_{SF} = 10^3$.

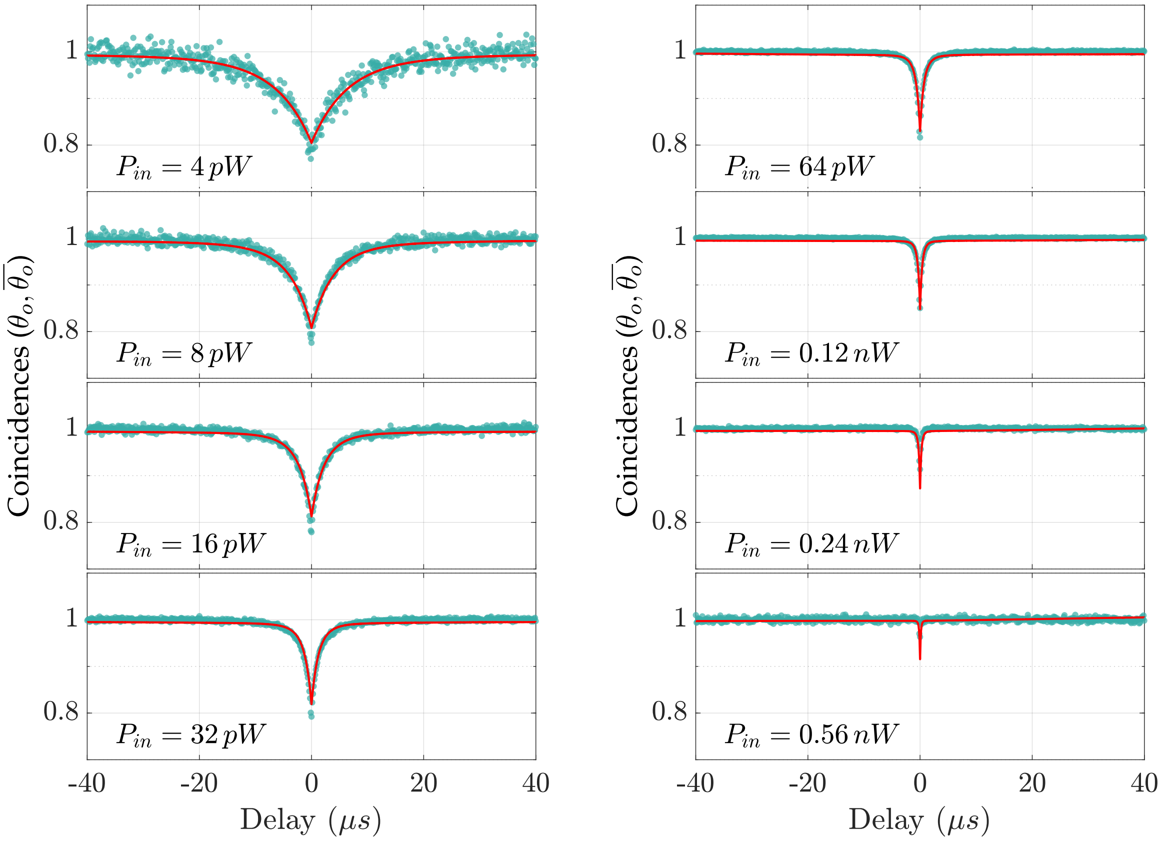

FIGURE 4.13: Cross-correlations in the optimal basis $(\theta_o, \overline{\theta_o})$ as a function of the delay, for different powers of the resonant laser, ranging from 4 pW to 0.56 nW. A 30 mT longitudinal magnetic field stabilizes the spin. Each experimental point includes a 128 ns time bin. The continuous red lines are ME simulations in set A.

This result concludes the full characterization of the *positively charged device* in the cQED framework, proving the consistency of the simulation with the set of parameters A. Next, we present one of its limitations concerning the interpretation of the magnetic field dependence.

4.4.2 Effect of a longitudinal magnetic field and limitations of the model

An external longitudinal magnetic field has two competing effects in regard to the operation of our system as a spin-photon interface: on the one hand, it stabilizes the spin by shielding it from the Overhauser field, which improves the quality of the spin-photon interface, but, on the other hand, it splits the energy of the two spin states $|\Uparrow\rangle$ and $|\Downarrow\rangle$, which degrades the performance, especially for an excitation laser which energy is fixed at $\overline{\omega_d}$, in the middle of the Zeeman-split energies (see subsections 1.2.4 and 3.4.2). A trade-off is expected at moderate magnetic fields, and more precisely around 30 mT, which led to the best contrast of the cross-correlations in the previously presented experiments.

In Fig. 4.14, we show the cross-correlations in the $(\theta_o, \overline{\theta_o})$ basis with an increasing longitudinal magnetic field. The 30 mT configuration demonstrates the highest anti-correlation contrast (despite a slightly worse value here than in previous experiments, probably due to a lesser occupation probability of the charge state in this specific experiment). The ME simulation is plotted in red along with mono-exponential fits (in dark blue), which help quantifying the contrast and decay time of the experiments. The ME simulation now starts from set A at 30 mT but takes a varying trion spin-flip time $\tau_{SF,t}(B)$ to account for its magnetic field dependence. To that end, the value of $\tau_{SF,t}$ was manually set in the simulation to match the decay of the experimental cross-correlation τ_{eff} (resulting from the mono-exponential fits), with the following formula:

$$\tau_{SF,t}(B) = 36\,\mathrm{ns} \times \frac{\tau_{eff}(B)}{\tau_{eff}(30\,\mathrm{mT})} \tag{4.3}$$

This way, the value $\tau_{SF,t}(30\,\mathrm{mT}) = 36\,\mathrm{ns}$ is preserved while empirically accounting for its increase induced by the magnetic field. For simplicity, we keep applying a fixed spin-flip ratio $r_{SF} = 10^3$, though its value does not significantly impact the outcome. The results of the mono-exponential fits are presented in Fig. 4.15, first in terms of zero-delay value of the cross-correlations and then in terms of decay time of the anti-correlation (combining the current experiment and that of Fig. 4.12). It reveals the best contrast at 30 mT, the loss of contrast at small magnetic fields where the random Overhauser field becomes prominent and the loss of contrast at high magnetic field where the Zeeman splitting spectrally separates the effect of each spin state while the excitation laser stays on the central energy. Additionally, the effective decay time τ_{eff} increases with the magnetic field and saturates around 45 µs above 200 mT. We surmise that this saturation of τ_{eff} at high magnetic fields comes from a limitation not by the spin-flip time, which should continue to increase, but by the charge escape time. Indeed, as the magnetic field increases, the quasi-resonant excitation gets less efficient, which might decrease the occupation probability P_c as well as the charge characteristic time T_c, leading to a reduced charge escape time which could become the limiting factor for τ_{eff}.

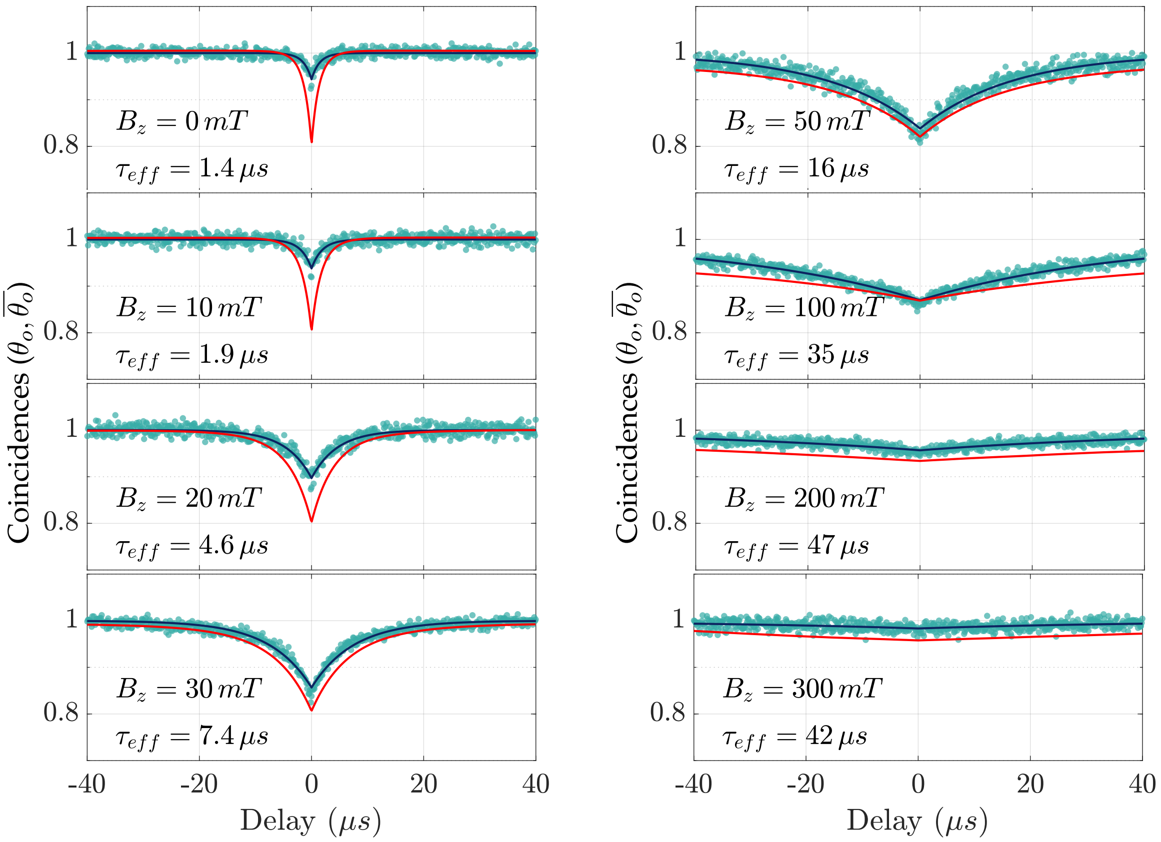

FIGURE 4.14: Cross-correlations in the optimal basis $(\theta_o, \overline{\theta_o})$ for different longitudinal magnetic fields, ranging from 0 mT to 300 mT. Each experimental point includes a 128 ns time bin. The dark blue lines are mono-exponential fits of effective decay times τ_{eff}, and the red lines are ME simulations in set A (adapting the trion spin-flip time to the value of τ_{eff} using Eq. 4.3).

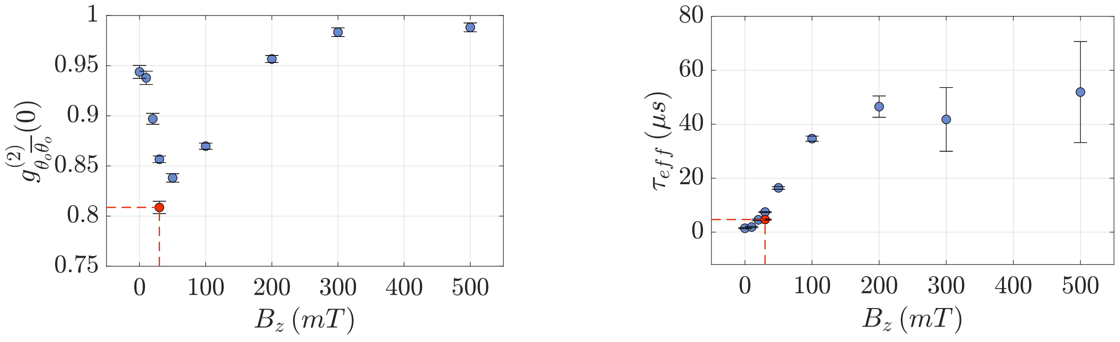

(a)

(b)

FIGURE 4.15: Results of the mono-exponential fits: **(a)** zero-delay value of the cross-correlations $g^{(2)}_{\theta_o\overline{\theta_o}}(0)$ and **(b)** decay time τ_{eff} as a function of the longitudinal magnetic field, B_z. The red point at 30 mT was measured in a previous experiment (Fig. 4.12) and the points at 500 mT were not shown in the previous figure.

This kind of saturation was also observed in the spin noise spectroscopy of a single hole by the group of M. Oestreich [101], but at lower magnetic fields (around 30 mT) and for an effective decay time of 180 µs.

In Fig. 4.16, we show the magnetic field dependence of the zero-delay value of the cross-correlation, with experimental points resulting from the mono-exponential fits and the ME simulation gradually changing the noise source from pure dephasing to electric noise while always fitting the tomography data properly: the explored configurations correspond to the black points of Fig. 4.8. The set A indeed fits the experimental data best. However we notice that no set of parameters matches the lowest magnetic fields. The explanation lies in the fact that the spin-flip phenomena included in the simulation can't account for a magnetic field slowly fluctuating in all directions such as the Overhauser field. In an effort to properly fit the magnetic field dependence, an ongoing work focuses on integrating hyperfine interaction in the model as the average between multiple orientations and intensities of the nuclear magnetic field.

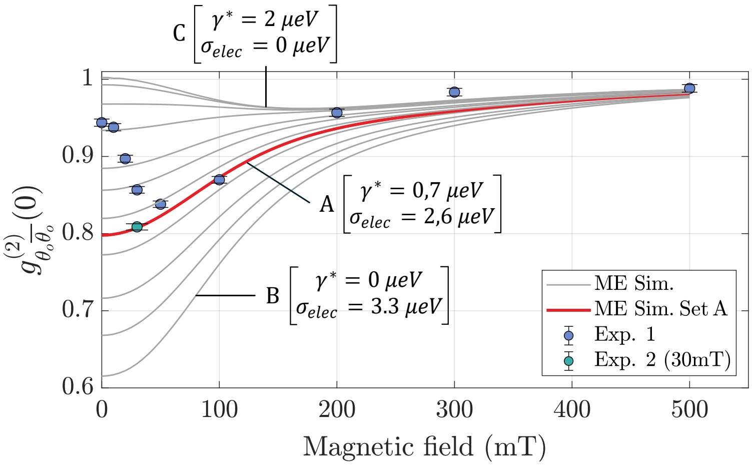

FIGURE 4.16: Zero-delay value of the cross-correlation as a function of the longitudinal magnetic field. Experimental points along with the ME simulations agreeing with the tomography data. Exp. 1 relates to the measurements from Fig. 4.15 and Exp. 2 to that from Fig. 4.12. The simulated curves correspond to the $(\gamma^*, \sigma_{elec})$ couples found to fit the tomography data in Fig. 4.8 and only the best agreement with the cross-correlations is highlighted in red for set A.

4.5 Efficiency of the spin measurement induced by photonic detection: towards the ideal spin-photon interface

In conclusion, we have successfully measured and simulated the imprint of the spin-induced Faraday rotation on the polarization state reflected by our system. We have shown that the fluctuating nuclear magnetic field might be circumvented to a certain degree by applying a longitudinal field of 30 mT, but also that the electric noise present in the device prevents the operation as a proper spin-photon interface. A solution to address this problem would be to use a feedback loop based on the gate voltage of the sample to compensate the slow electrical fluctuations and effectively reduce σ_{elec} [180, 181].

Let us explore the prospects of reducing the noise sources by extrapolating the simulation results. To do so, we simulate the conditional occupation probabilities, denoted $\widetilde{P(\Uparrow)}$ and $\widetilde{P(\Downarrow)}$, defined as the conditional spin state probabilities induced after a time $\tau_{int} = 5\,\mathrm{ns}$ after the initial detection of a photon in $|\theta_o\rangle$. At such a timescale, the radiative relaxation has settled but the spin flips have not yet come into play (see section 3.3). In Fig. 4.17, we present the cross-correlations and the conditional occupation probabilities as a function of the laser-quantum dot detuning, for different noise configurations: first in the set of parameters A (in dark blue), then in the absence of slow electric fluctuations (in red) and finally without any noise source (in light blue). Even in the presence of noise and with quite a low cross-correlation contrast, the detuning dependence of the conditional occupation probabilities shows a partial spin initialization induced by the photonic measurement. The contrast of the spin probabilities is, however, limited by the imperfect charge occupation $P_c = 0.75$ and by the magnetic field $B_z = 30\,\mathrm{mT}$ from which the dip in $\widetilde{P(\Uparrow)} + \widetilde{P(\Downarrow)}$ originates. This result encourages to look for a reduction of the noise sources, but also an exploration of the detuning degree of freedom, to maximize the photonic-induced spin projection even in the presence of noise.

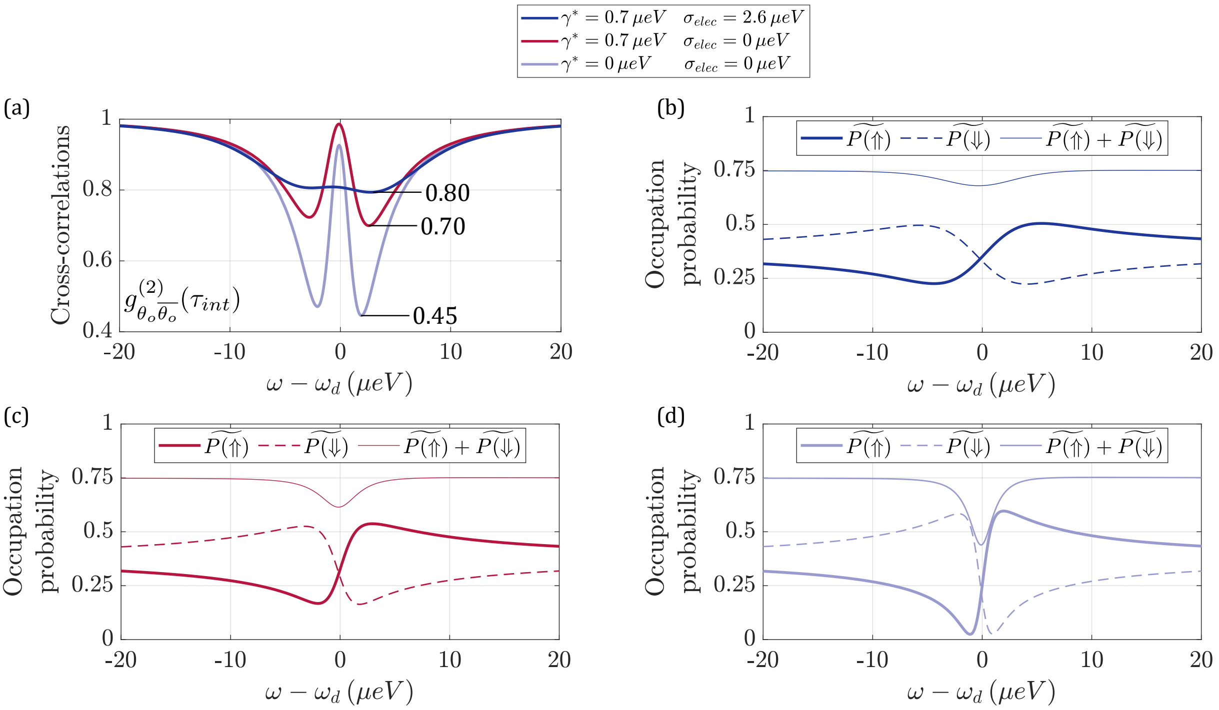

FIGURE 4.17: ME simulations of the detuning dependence of **(a)** the cross-correlations in the $(\theta_o, \overline{\theta_o})$ basis and **(b,c,d)** the conditional occupation probabilities of the spin states. All quantities are computed at the intermediate delay $\tau_{int} = 5\,\mathrm{ns}$ after the detection of a photon in the polarization $|\theta_o\rangle$, and with an external magnetic field of 30 mT. Three configurations of noise sources are color-coded: starting from set A in dark blue, removing the slow electric fluctuations in red and removing all noise sources in light blue.

The outcome of these simulations indicates the direction of future experiments: first, a partial measurement-induced spin projection might be obtained by detuning the excitation laser from ω_d, even in the presence of noise sources. This could be achieved with a time-resolved experiment where the conditional polarization tomography would be monitored as a function of delay a few nano- or microseconds after the projective measurement. Second, all the noise sources have to be reduced. What we modeled as pure dephasing in this chapter may in fact be hyperfine interaction; this kind of noise could be tackled by technological improvements within reach, such as an adaptation of the annealing process, which strongly determines the sensitivity of the spin states to magnetic fluctuations [38]. Finally, the occupation probability of the charge state should be further improved to make the device ideal, by adapting the two-color excitation scheme or designing heterostructures suited for electrical injection.

Chapter 5

Partial measurement of a single electron spin with single detected photons

The experimental techniques with which the hole-based device was investigated in the previous chapter are implemented again, this time to characterize the electron-based (*negatively charged*) device. The change of sample structure and charge type comes with required adaptations of the experimental protocol, and yields complementary results, predominantly determined by the particular sensitivity of the electron to environmental noise [50, 55].

Specifically, the photons reflected from the device are first analyzed in the steady state by polarization tomography, demonstrating large Faraday rotations from which we infer a drastic reduction of the charge noise with respect to the *positively charged device*. Secondly, the cross-correlation experiments reveal the photon dynamics: with the interpretation through the master equation simulations, we indirectly observe the spin fluctuations by measuring photons in the appropriate basis. The efficiency of the partial spin projection, induced by the detection of a single photon, is discussed based on the comparison between experiments and numerical simulations.

Finally, extrapolating the simulations to the ideal case leads to a deeper understanding of the impact of experimental imperfections and designate the major limiting factor to be the fast reset of the electron spin, stemming either from the hyperfine interaction with the quantum dot nuclei or from the fast cotunnelling phenomenon whereby electrons are swapped between the quantum dot and the Fermi sea.

5.1 Steady state measurements and modeling

The purpose of steady-state measurements is to characterize the optical response of the device; more precisely, to measure the reflected polarization state in the Poincaré sphere under specific excitation conditions. Before all else, the cavity-induced polarization shift is investigated so as to separate its effect from the Faraday rotation in further experiments. Then, the tomography technique is applied to the photons reflected by a non-initialized spin, averaging contributions from all the possible quantum dot states. This measurement answers the question of whether the device is suited to operate as an ideal spin-photon interface. It is eventually substantiated by the numerical simulation, indicating the optimal condition for further characterization: that is, the polarization basis to which spin states are optimally imprinted on polarization states and the associated photon energy.

5.1.1 Bare cavity tomography

We remind that our micropillar cavities are slightly birefringent, owing to the ellipticity of the pillar from which two orthogonal eigenaxes emerge, respectively associated to the linear polarizations H and V – see subsection 1.3.2. The aim of characterizing the bare cavity is threefold:

- First, determining the H and V cavity axes offers two choices of input polarizations unperturbed by the cavity, for further experiments where we focus on the quantum dot-induced Faraday rotation;
- Second, the (HV) axis of the Poincaré sphere is oriented to match the cavity polarizations and DALR are determined accordingly (see Eq. 1.23);
- Third, extracting the cavity parameters through analytical fits and injecting them in further simulations account for their impact on the behavior of the spin-dependent polarization rotation (see for example Fig. 3.14), which is valuable to choose the appropriate photonic measurement basis and detuning.

The cavity tomography is conducted by exciting the sample with a resonant CW laser of scanning energy in the diagonal polarization, which undergoes the maximal cavity-induced shift of all polarizations. Here, the excitation is of relatively high power so that the quantum dot is saturated and the majority of the reflected photons are only affected by the cavity. The reflected light is measured in the polarizations (H,V,D,A,R,L) to reconstruct the full polarization state in the Poincaré sphere. The experimental setup was presented in Fig. 2.5 and the analytical theoretical model is detailed in section 2.2 in its application to the *positively charged device*. Here, the collection photodiodes are freespace APDs of moderate efficiency.

In Fig. 5.1, the measured reflected polarization states are plotted in the Poincaré sphere as a function of the laser-cavity detuning $\omega - \omega_c$, where ω_c is halfway between the energies of the two eigenmodes, $\omega_{c,H}$ and $\omega_{c,V}$. The two spheres contain the same experimental points but different fits in continuous lines: on the left, the model is constrained to a unity input coupling $\eta_{in} = 1$ (red line) so the simulated points can only explore the surface of the sphere, whereas on the right, this constraint is lifted and the fit converges to a value $\eta_{in} = 0.96$: the purity of the output states is therefore decreased. The rest of the fitting parameters are the same for both cases and are displayed in Eq. 5.1. The experimental and fitted Stokes parameters are presented in Fig. 5.2 where the experimental points are superimposed with the fit constraining $\eta_{in} = 1$ on the left and the unconstrained one on the right. As in the case of the *positively charged device*, the quality of the simulation is improved when lifting the constraint on the input coupling, owing to the presence in the reflected beam of light not coupled to the cavity, which degrades the overall polarization purity.

$$\begin{cases} \eta_{in} = 0.96 \pm 0.02 \\ \eta_{top,H} = 0.63 \pm 0.02 \quad \kappa_H = (183 \pm 15)\,\mu\text{eV} \\ \eta_{top,V} = 0.59 \pm 0.02 \quad \kappa_V = (199 \pm 15)\,\mu\text{eV} \\ \omega_{c,H} - \omega_{c,V} = (147 \pm 10)\,\mu\text{eV} \end{cases} \tag{5.1}$$

The cavity parameters found here are the starting point for numerically simulating the rest of the experiments in this chapter. However, some differences in the experimental conditions might justify a certain deviation from the current results, in particular for κ and η_{top}.

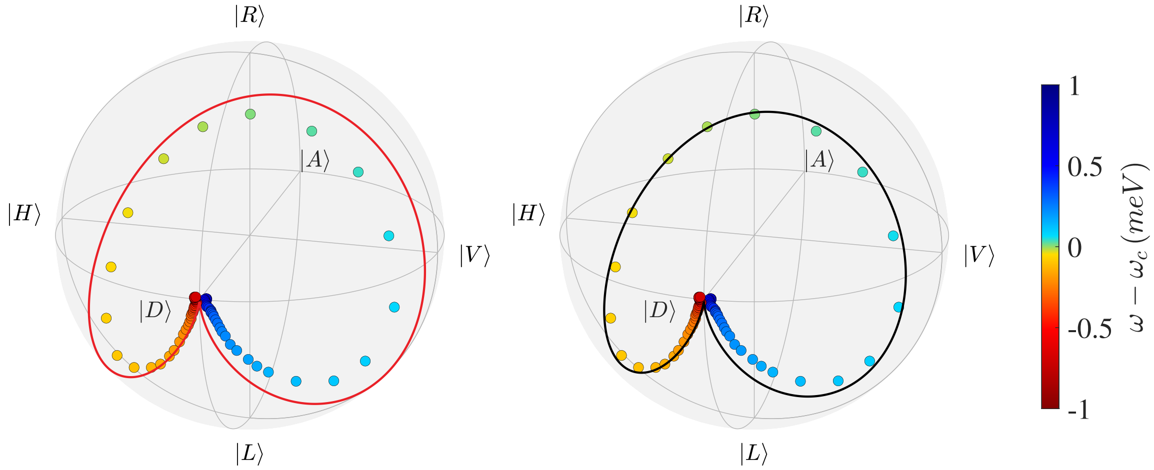

FIGURE 5.1: Polarization tomography of the bare cavity of the *negatively charged device* with a D excitation, as a function of the laser-cavity detuning, $\omega - \omega_c$. **(Left)** The red line is the fit constrained to $\eta_{in} = 1$. **(Right)** The solid line is the unconstrained fit, converging to $\eta_{in} = 0.96$. The view angle sets $|D\rangle$ in the foreground.

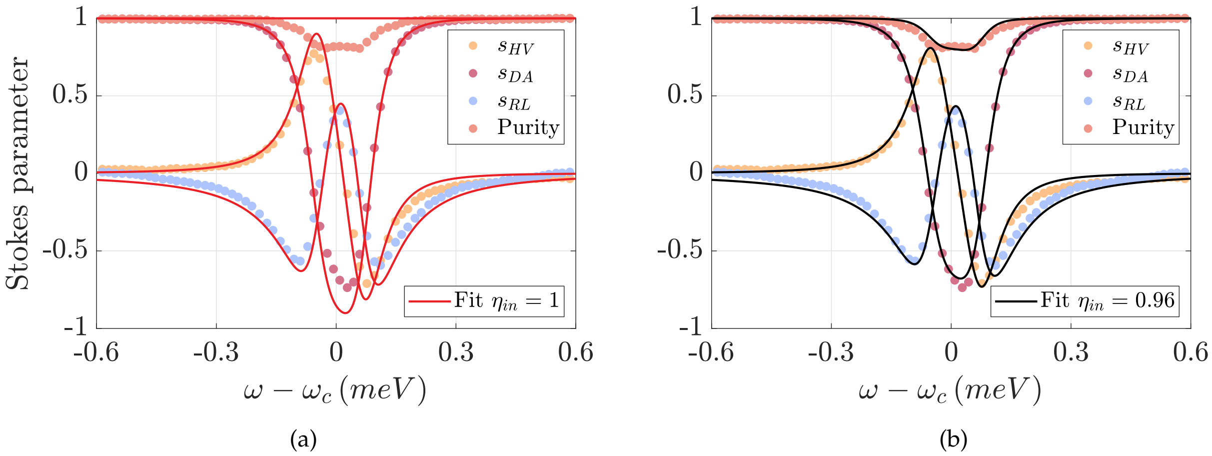

(a) (b)

FIGURE 5.2: Stokes parameters and purity of the tomography data from Fig. 5.1 with **(a)** the fit constrained to $\eta_{in} = 1$ and **(b)** the unconstrained fit converging to $\eta_{in} = 0.96$. It is noticeable that the purity stays at unity for the constrained fit, and is reduced with the unconstrained one, improving the agreement between simulation and experiment.

5.1.2 Quantum dot tomography

The quantum dot tomography addresses the spin-induced polarization rotation: in the same manner as with the *positively charged device*, no spin initialization is implemented, and the measurement characterizes the average output state between the optical responses of the quantum dot states $|\uparrow\rangle$, $|\downarrow\rangle$ and $|\varnothing\rangle$. Here, the excitation laser is polarized along H so that the cavity has no impact on the reflected polarization, and its power is dimmed down to 3 pW (below quantum dot saturation). The detection apparatus is accordingly switched to the very sensitive fibered SNSPDs. Contrary to the *positively charged device* that relies on optical charge injection, the *negatively charged device* structure is designed to achieve electrical injection so the resonant laser is sufficient to probe the quantum dot without any auxiliary input (see the heterostructure design in Fig. 2.1). To ensure that the considered quantum dot transition is indeed that of a negative trion, a separate photoluminescence experiment in a transverse magnetic field was carried out, similarly as in Fig. 2.4.

Let us first examine the reflectivity measurements in Fig. 5.3, where the reflected light was projected in the H and V polarizations. The left graph contains a wide scan encompassing the whole cavity and the area inside the dashed frame is zoomed in on the right side. The V reflectivity R_V is cross-polarized from the excitation so it only contains the narrow quantum dot contribution, while R_H also includes the wide Fabry-Pérot dip of the H cavity mode. Both graphs superimpose the experimental points with the numerical simulation whose parameters are detailed in Eq. 5.2.

$$\begin{array}{|l|l|l}
 & g = 12.7\,\mu\text{eV} & \\
\eta_{top,H} = \eta_{top,V} = 0.70 & \gamma_{sp} = 0.4\,\mu\text{eV} & P_c = 1 \\
\kappa_H = \kappa_V = 168\,\mu\text{eV} & \gamma^* = 0\,\mu\text{eV} & \tau_{SF,g} = 1.5\,\text{ns} \\
\omega_{c,H} - \omega_{c,V} = 147\,\mu\text{eV} & \sigma_{elec} = 0\,\mu\text{eV} & \tau_{SF,t}/\tau_{SF,g} = 10^3 \\
 & \sigma_{mag} = 0\,\mu\text{eV} &
\end{array} \tag{5.2}$$

The full tomography is presented as Stokes parameters and in the Poincaré sphere[1] in Fig. 5.4. The trajectory is contained in the (HV) axis as s_{DA} and s_{RL} stay null, confirming that the non-initialized spin reflects an averaged polarization state arising from the optical responses of the $|\uparrow\rangle$, $|\downarrow\rangle$ and $|\varnothing\rangle$ states, as first introduced in Fig. 3.10. The large increase in contrast of s_{HV} with respect to the *positively charged device* indicates a considerable reduction of the noise in the current device (see Fig. 4.6 to compare the experimental tomography and section 3.6 for the effect of noise on s_{HV}). We can infer a ±130° Faraday rotation, higher than the requirement for an ideal spin-photon interface.

The fitting parameters presented in Eq. 5.2 were found starting from the bare cavity results (Eq. 5.1), by adjusting them manually according to the differences in the experimental setups. Indeed, whereas the bare cavity tomography was recorded with freespace APDs, the fibered output to SNSPDs in the current experiment imposes an effective top mirror output

---

[1] The raw experimental data were processed to compensate a unitary rotation undergone in the collection path, so as to bring the out-of-resonance points on H, as mentioned in appendix C relative to the *positively charged device*.

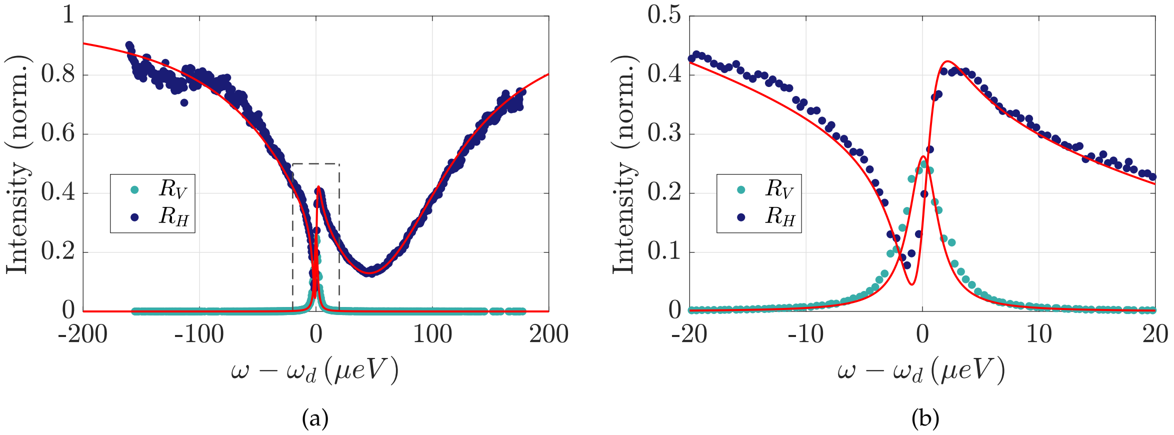

(a) (b)

FIGURE 5.3: **(a)** Normalized reflected intensities in the H and V polarizations while exciting the *negatively charged device* with a scanning 3 pW laser (H-polarized), as a function of the laser-quantum dot detuning $\omega - \omega_d$. The red line is the numerical simulation with parameters from Eq. 5.2. The dashed square delineates the area shown on the right side. **(b)** Same data zoomed on the quantum dot contribution.

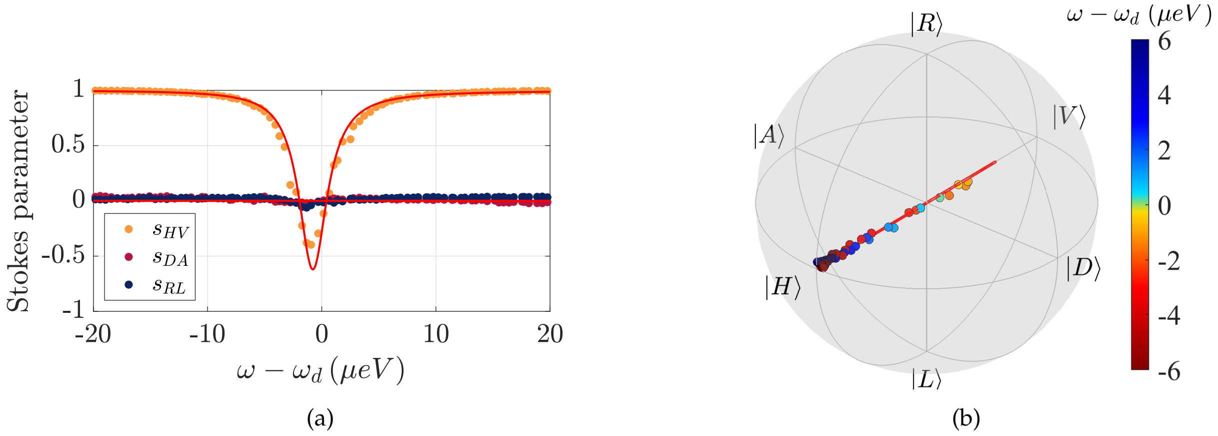

(a) (b)

FIGURE 5.4: **(a)** Experimental Stokes parameters of the reflected photons along with the simulation taking the parameters from Eq. 5.2. **(b)** Poincaré sphere representation of the reflected polarization state. The far-detuned points are close to H and the points enter in the sphere along the (HV) axis when the laser comes into resonance with the quantum dot.

coupling that might slightly differ from the actual η_{top}. In addition, the detector non-linearity at high count rates leads to small distortions in the effective cavity width. These experimental imperfections are not compensated in the post-treatment of the data, but as a consequence, we tolerate a deviation from the bare cavity values of $\kappa_{H/V}$ and $\eta_{top,H/V}$.

Concerning the quantum dot parameters, the selected couple of g and γ_{sp} is linked through the lifetime expression found in Eq. A.1 of appendix A, for a quantum dot lifetime of 230 ps measured separately. This corresponds to a Fourier limited width of 2.9 µeV, quite close to that of R_V of approximately 3.6 µeV. Such a narrow quantum dot contribution ascertains that the noise is indeed far inferior here than in the case of the *positively charged device*, and as such, we decided to ignore noise sources in this simulation. Finally, the last two parameters include the charge occupation probability (assumed to be perfect thanks to the very efficient electrical injection), and the spin flip of the ground and trion states, which will be commented later in the cross-correlation section.

The tomography data might be best fitted by including an electrical noise of width $\sigma_{elec} \sim 1\,\mu\text{eV}$ to the simulation, which would broaden the quantum dot contribution spectrally. Adjusting the (g, γ_{sp}) couple and including a slightly decreased P_c could help to improve the simulation even further. In any case, we adopt the current parameters of Eq. 5.2 a satisfying fit of the steady-state regime.

5.1.3 Stabilizing the single electron charge state with the external bias

Let us take a detour to examine the effect of the external bias on the *negatively charged device*, monitoring it through the quantum dot-induced dip in s_{HV}, knowing its shape in the single electron state (Fig. 5.4a). We remind that the electrical carrier injection relies on the bias applied to the sample (Fig. 2.1), which creates a strong electric field inside the micropillar. The efficiency of the electrical injection can be monitored by plotting s_{HV} for different bias voltages, as shown in Fig. 5.5. The optimal voltage pointed out on the figure is when the quantum dot-induced dip in s_{HV} is the deepest and narrowest. The widening of the line at other bias values might come from a mixture of multiple charge states in the quantum dot. The tight range of optimal voltage differs from that presented in Fig. 1.5 and might originate from the voltage-sensitive cotunnelling processes (electron swap between the quantum dot and the Fermi sea). This measurement proves that the single electron state is stabilized by the bias control, provided the system is operated at the optimal voltage.

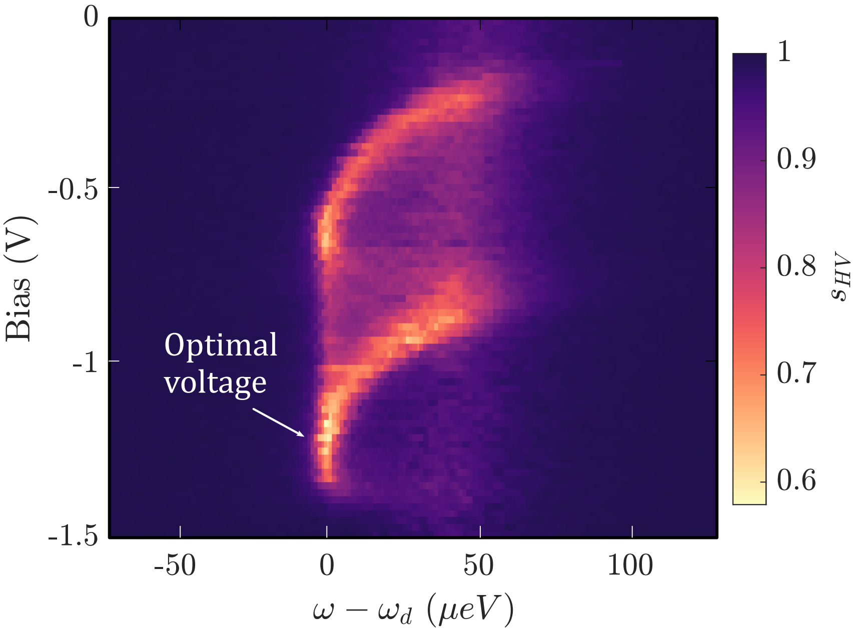

FIGURE 5.5: Evolution of the Stokes parameter s_{HV} of the reflected polarization state as a function of the laser-quantum dot detuning $\omega - \omega_d$ (horizontal axis) when the sample bias is varied (vertical axis). The optimal voltage is pointed out.

5.1.4 Extending the steady-state model to find the best operating conditions

Starting from the numerical model fitting the tomography data in Fig. 5.4, two working points for the device as an ideal spin-photon interface can be deduced through the condition $s_{HV} = 0$, met for $\omega - \omega_d = -2.1\,\mu\mathrm{eV}$ and $0.42\,\mu\mathrm{eV}$. As explained theoretically in section 3.2, this condition ensures the possibility to find complementary spin-dependent polarizations $|\Psi_\uparrow\rangle$ and $|\Psi_\downarrow\rangle$ such that $\langle\Psi_\uparrow|\Psi_\downarrow\rangle = 0$. In the following, the positive-detuning point, $\omega - \omega_d = 0.42\,\mu\mathrm{eV}$, is favored as its higher reflectivity produces more photons on the output, hence a better signal-to-noise ratio. We note, however, that any uncertainty on the s_{HV} measurement has repercussions on the precision of the working point, which in fact impaired the experiments presented in the next section.

Let us extrapolate the polarizations on which the spin states are imprinted when the device operates as an ideal spin-photon interface. To do so, we use the fitting parameters of the quantum dot tomography from Eq. 5.2 to simulate the behavior of the device. We focus on the reflected polarization states $|\Psi_\uparrow\rangle$ and $|\Psi_\downarrow\rangle$, when the excitation laser is H-polarized: these correspond to the pure polarization states that are reflected when the quantum dot is perfectly initialized in states $|\uparrow\rangle$ or $|\downarrow\rangle$. The Stokes parameters of $|\Psi_\uparrow\rangle$ are plotted as a 2D graph in Fig. 5.6a, and in the Poincaré sphere in Fig. 5.6b along with the trajectory of $|\Psi_\downarrow\rangle$. The color scale maps the laser-quantum dot detuning $\omega - \omega_d$, and two sets of points of interest are highlighted: first, the S1 basis including $\mathrm{S1} = \Psi_\uparrow(\delta_{opt,1})$ connected to $\overline{\mathrm{S1}} = \Psi_\downarrow(\delta_{opt,1})$, and second the S2 basis with $\mathrm{S2} = \Psi_\downarrow(\delta_{opt,2})$, connected to $\overline{\mathrm{S2}} = \Psi_\uparrow(\delta_{opt,2})$. Following the simulations, the criterion $\langle\Psi_\uparrow|\Psi_\downarrow\rangle = 0$ should be met[1] in bases S1 and S2, with the respective laser-quantum dot detunings $\delta_{opt,1}$ and $\delta_{opt,2}$. The measurement of photonic correlations in these two bases and at the associated detunings should bring about perfect spin projection, and therefore a perfect anti-correlation, as simulated in section 3.3. The bases S1 and S2 are characterized by the following parameters:

$$\text{Basis S1}\;\left|\;\begin{array}{l}\delta_{opt,1} = -2.1\,\mu\mathrm{eV}\\ \Phi = 90^\circ\\ \theta = 83^\circ\end{array}\right.\qquad\text{Basis S2}\;\left|\;\begin{array}{l}\delta_{opt,2} = 0.42\,\mu\mathrm{eV}\\ \Phi = 90^\circ\\ \theta = 60^\circ\end{array}\right.\tag{5.3}$$

In order to find the best operating conditions, our experimental cross-correlation protocol will explore the measurement bases located on the (DRAL) circle as well as the different laser-quantum dot detunings. We shall, however, keep in mind that the uncertainty in the experimental measurement of s_{HV} will propagate to the calibration of these bases: the simulations will then be adapted accordingly.

---

[1] We remind that the orthogonality in the Poincaré sphere characterizes vectors of opposite directions.

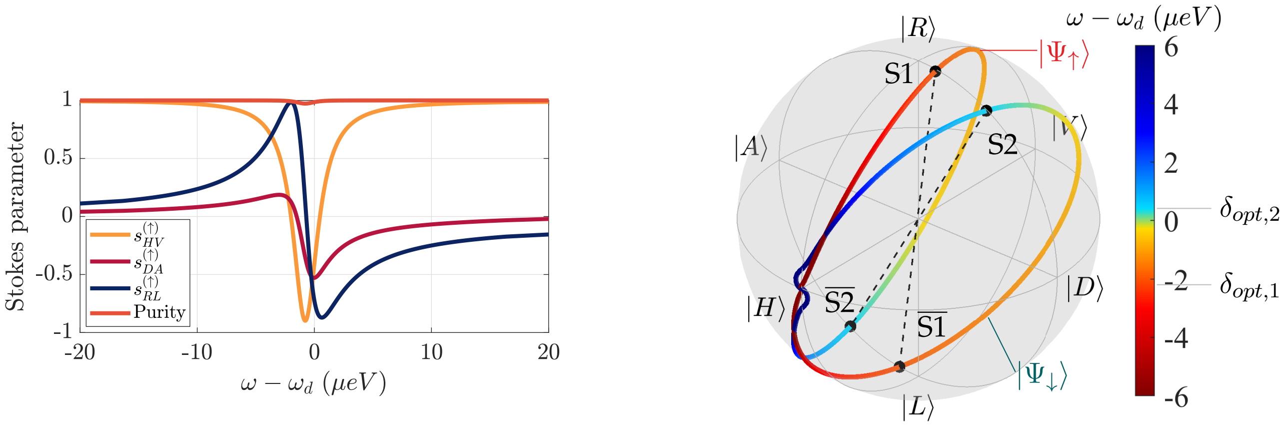

(a) (b)

FIGURE 5.6: Simulated polarization states of $|\Psi_\uparrow\rangle$ and $|\Psi_\downarrow\rangle$ reflected from the device when the spin is in state $|\uparrow\rangle$ or $|\downarrow\rangle$. **(a)** Stokes parameters of $|\Psi_\uparrow\rangle$. **(b)** Poincaré representation of $|\Psi_\uparrow\rangle$ and $|\Psi_\downarrow\rangle$. Two measurement bases are pointed out as black dots linked by dashed lines: (S1,$\overline{\text{S1}}$) and (S2,$\overline{\text{S2}}$). In these bases, a perfect interface between the spin state and the reflected polarization state is expected, since the condition $\langle\Psi_\uparrow|\Psi_\downarrow\rangle = 0$ is met when the excitation laser is tuned respectively to $\delta_{opt,1}$ and $\delta_{opt,2}$.

5.2 Time-resolved cross-correlation measurements and modeling

The cross-correlation experiment is carried out so as to probe the quality of the spin-photon interface: by measuring photon correlation in bases close to S1 or S2 and at the appropriate detunings, we expect the spin state to be properly imprinted on the reflected polarization state, which is indirectly characterized by an anti-correlation dip. This dip indicates a partial measurement-induced spin projection that prevents a photon to be reflected in the complementary polarization immediately after a first detection event, as it can only happen once a spin flip occurred. We start by presenting experimental data and follow by a master equation simulation of the best case. Then, we extend the simulation to test it against the measured basis and detuning dependence. Finally, we show that the electron spin flip is the main limiting factor and simulate the hypothetical performance of a similar device with a longer spin-flip time.

5.2.1 Experimental cross-correlations

The experimental cross-correlations are measured in multiple bases and for different laser-quantum dot detunings, in the absence of an external magnetic field. In Fig. 5.7, we show the experimentally explored bases: they were initially designed to be located on the (DRAL) circle, as intended in the protocol from subsection 3.3.2 and like the experiments from subsection 4.3.3. However, an ulterior calibration shed light on a detection flaw, an imbalance between the collection paths that offset the detection bases to non-zero values of s_{HV} (up to $s_{HV} = 0.35$) instead of the ideal $s_{HV} = 0$. The same experimental flaw has offset the experimental working point in terms of laser-quantum dot detuning, to the value $\omega - \omega_d = 1\,\mu\text{eV}$, compared to the optimal value of $\delta_{opt,2} = 0.42\,\mu\text{eV}$ that was deduced a posteriori. We will take these imperfections into account in the simulation.

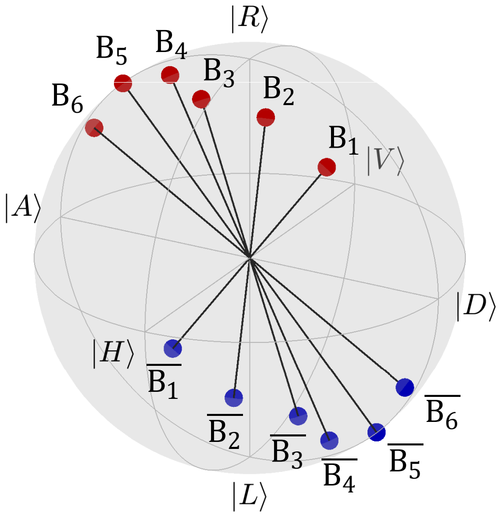

FIGURE 5.7: Experimentally explored measurement bases, labeled from B1 to B6. The red point is the first polarization state of the basis and the blue point is the orthogonal polarization state. The cross-correlations will be measured between the two polarization states of each basis.

In Fig. 5.8 we show the cross-correlation data in three of the measurement bases from Fig. 5.7, for which the excitation laser was set to $\omega - \omega_d = 1\,\mu\text{eV}$. Two main features are visible:

- A fast transient regime on the 100 ps timescale, caused by the radiative relaxation. This phenomenon was extensively studied in subsection 3.3.3, where we introduced the *intermediate* timescale $\tau_{int} = 5\,\text{ns}$ after which the radiative relaxation has settled (see for example Fig. 3.19b). As a reminder, this fast transient corresponds to the rebalancing of the ratios between each ground state population and its corresponding excited state. We also notice that this evolution first leads to a decrease of the cross-correlation contrast (hence the zero-delay peak).
- An anti-correlation dip is expected for a partial spin measurement induced by photon detection. This dip is damped on the ns timescale, which is compatible with the expected spin relaxation induced by the hyperfine interaction. This damping is much faster than what was studied in the previous chapters, decreasing the cross-correlation contrast before the radiative relaxation is over. This induces a mixing of radiative and spin relaxation, preventing any direct analysis of the partial spin measurement's efficiency through the measured cross-correlation contrast.

Among the explored measurement bases, the one labeled B2 gave the best cross-correlation contrast, with an anti-correlation dip as low as 0.25, while many other bases gave intermediate contrasts, such as bases B4 and B6 also presented here. We remind from our simulations that we could expect the basis S2 to give the best contrast, provided an optimal laser-quantum dot detuning $\delta_{opt} = 0.42\,\mu\text{eV}$ (a value that was found a posteriori, and that slightly differs from the chosen value $\omega - \omega_d = 1\,\mu\text{eV}$ that we initially thought as being optimal). The one labeled B2 is the closest to S2 and is extensively studied next.

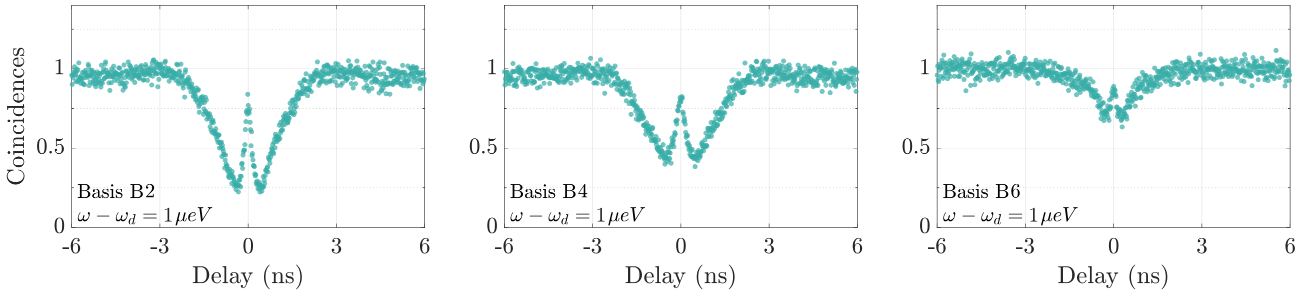

FIGURE 5.8: Cross-correlations in the measurement bases labeled B2, B4 and B6, with the energy of the excitation laser set to $\omega - \omega_d = 1\,\mu\text{eV}$. The experimental basis B2 gives the highest anti-correlation contrast unlike bases B4 and B6 that are not as optimal. Only the contrast of the anti-correlation dip seems to be impacted whereas the maximum of the short delay radiative peak doesn't change.

In Fig. 5.9, we now explore different laser-quantum dot detunings in the experimental basis B2. By changing the energy of the input laser, not only is the contrast of the dip reduced, the relative height of the short-delay peak is also impacted. We expected the detuning to decrease the spin measurement induced by the photon detection, and therefore the contrast of the dip. Nevertheless, the anti-correlation dip is maintained for a surprisingly wide range of detunings, as will be seen in the comparison with numerical simulations in the next section.

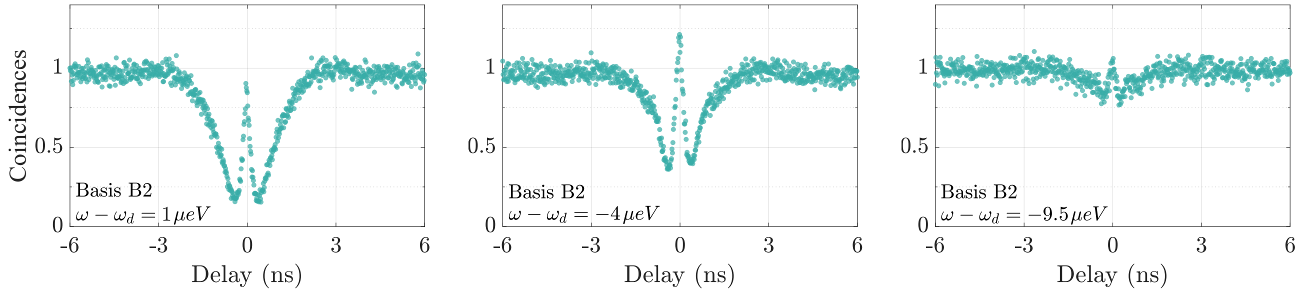

FIGURE 5.9: Detuning dependence of the experimental cross-correlations in basis B2. Both the contrast of the dip and the height of the short delay peak evolve.

5.2.2 Simulated cross-correlations

In this section, we simulate the cross-correlations in the experimental basis B2, in which the anti-correlation contrast was the highest of all the measured bases. In Fig. 5.10a, we show the cross-correlation data in B2, for $\omega - \omega_d = 1\,\mu\text{eV}$, and the simulation using the parameters from Eq. 5.2 as a red line. The ground spin-flip time $\tau_{SF,g} = 1.5\,\text{ns}$ is apparent in the decay time of the dip, while the trion spin flip time is much higher ($\simeq 1\,\mu\text{s}$) and does not influence the results. In the Poincaré sphere, illustrated in Fig. 5.10b, the measurement basis B2 is located at $\Phi = 38°$ and $\theta = 63°$ and we also show the already computed trajectories of $|\Psi_\uparrow\rangle$ and $|\Psi_\downarrow\rangle$ as a function of the laser-quantum dot detuning.

Let us examine the difference between the best experimental measurement basis B2 and the best theoretical one, S2. In Fig. 5.11, we plot, under the same viewing angle, the trajectories of $|\Psi_\uparrow\rangle$ and $|\Psi_\downarrow\rangle$ along with the basis vectors (B2,$\overline{\text{B2}}$) on the left and (S2,$\overline{\text{S2}}$) on the right, and the values of $|\Psi_\uparrow\rangle$ and $|\Psi_\downarrow\rangle$ at the corresponding detunings as solid and dashed arrows respectively. On the left sphere, we notice that even if B2 is very close to $|\Psi_\downarrow\rangle\,(1\,\mu\text{eV})$, the value of $|\Psi_\uparrow\rangle\,(1\,\mu\text{eV})$ is far from orthogonal to $|\Psi_\downarrow\rangle$ at this detuning, so its distance from $\overline{\text{B2}}$ results in an imperfect match between spin state and polarization state: this is limiting the contrast of the anti-correlation dip in this basis. On the right sphere, we show the ideal case with the two orthogonal vectors $\text{S2} = |\Psi_\downarrow\rangle\,(0.42\,\mu\text{eV})$ and $\overline{\text{S2}} = |\Psi_\downarrow\rangle\,(0.42\,\mu\text{eV})$, leading to a perfect spin-photon interface.

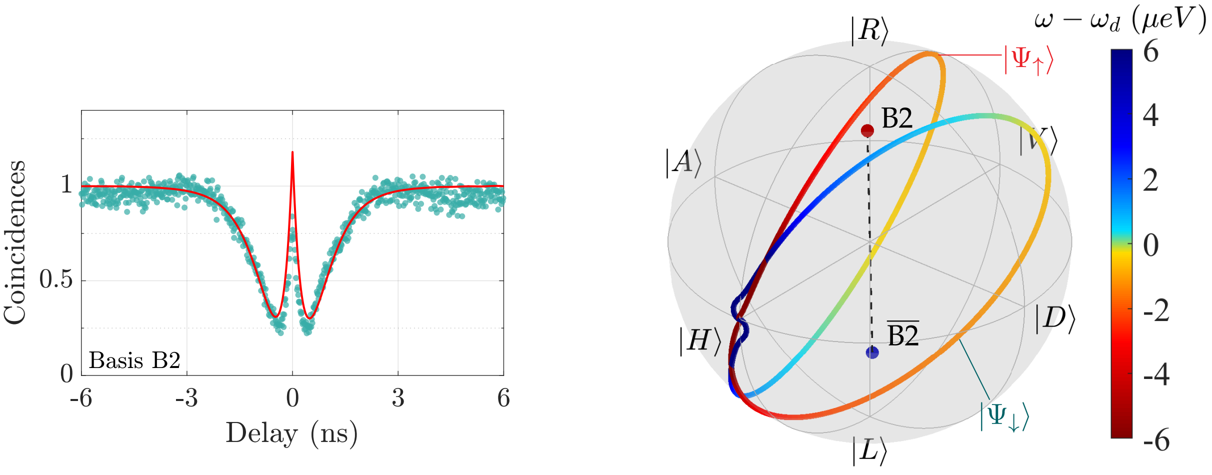

(a) (b)

FIGURE 5.10: **(a)** Experimental cross-correlations measured at $\omega - \omega_d = 1\,\mu\text{eV}$, in basis B2 ($\Phi = 38°$ and $\theta = 63°$). The fit is superimposed as a solid red line. **(b)** Poincaré representation of the simulated $|\Psi_\uparrow\rangle$ and $|\Psi_\downarrow\rangle$, also showing the basis vectors (B2,$\overline{\text{B2}}$).

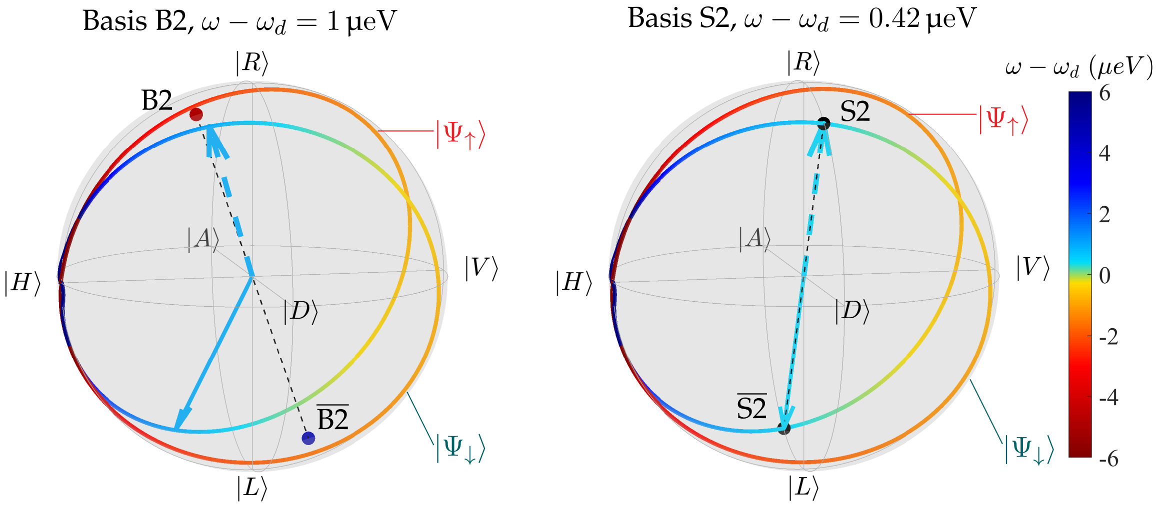

FIGURE 5.11: **(Left)** Trajectories of $|\Psi_\uparrow\rangle$ and $|\Psi_\downarrow\rangle$ as a function of the laser-quantum dot detuning, along with basis states of B2 as red and blue points, and blue arrows representing the specific values of $|\Psi_\uparrow\rangle$ and $|\Psi_\downarrow\rangle$ for the detuning $\omega - \omega_d = 1\,\mu\text{eV}$: B2 is aligned with $|\Psi_\downarrow\rangle$ but $\overline{\text{B2}}$ is offset from $|\Psi_\uparrow\rangle$. **(Right)** Basis S2, $\omega - \omega_d = 0.42\,\mu\text{eV}$: each basis vector is perfectly superimposed either with $|\Psi_\uparrow\rangle$ or $|\Psi_\downarrow\rangle$.

5.2.3 Extending the model to the basis and detuning dependence

Let us compare the experimental and simulated cross-correlations in the bases B1 to B6 with an excitation tuned to $\omega - \omega_d = 1\,\mu\text{eV}$, with every parameter fixed in the simulation except for the measurement basis determined by its location in the Poincaré sphere (see Fig. 5.7). The results are compiled in Fig. 5.12: the simulation reproduces the experimental trend of a lower contrast when the measurement basis is far from B2, but it also shows that the maximum of the short delay radiative peak should not change much and that the spin-flip timescale on which the anti-correlation dip loses contrast should be constant. The disagreements between simulation and experiment could be attributed to complex phenomena slowly changing $\tau_{SF,g}$ between experimental recordings. Indeed, the spin-flip time is not only determined by the hyperfine interaction, but also by the fast cotunnelling process, resetting the spin evolution by swapping the electron between the quantum dot and the Fermi sea, which is highly dependent on the applied voltage (see Fig. 5.5). Furthermore, we have also observed deviations of this optimal voltage as a function of time, indicating slow fluctuations of the device behavior on a timescale of a few minutes.

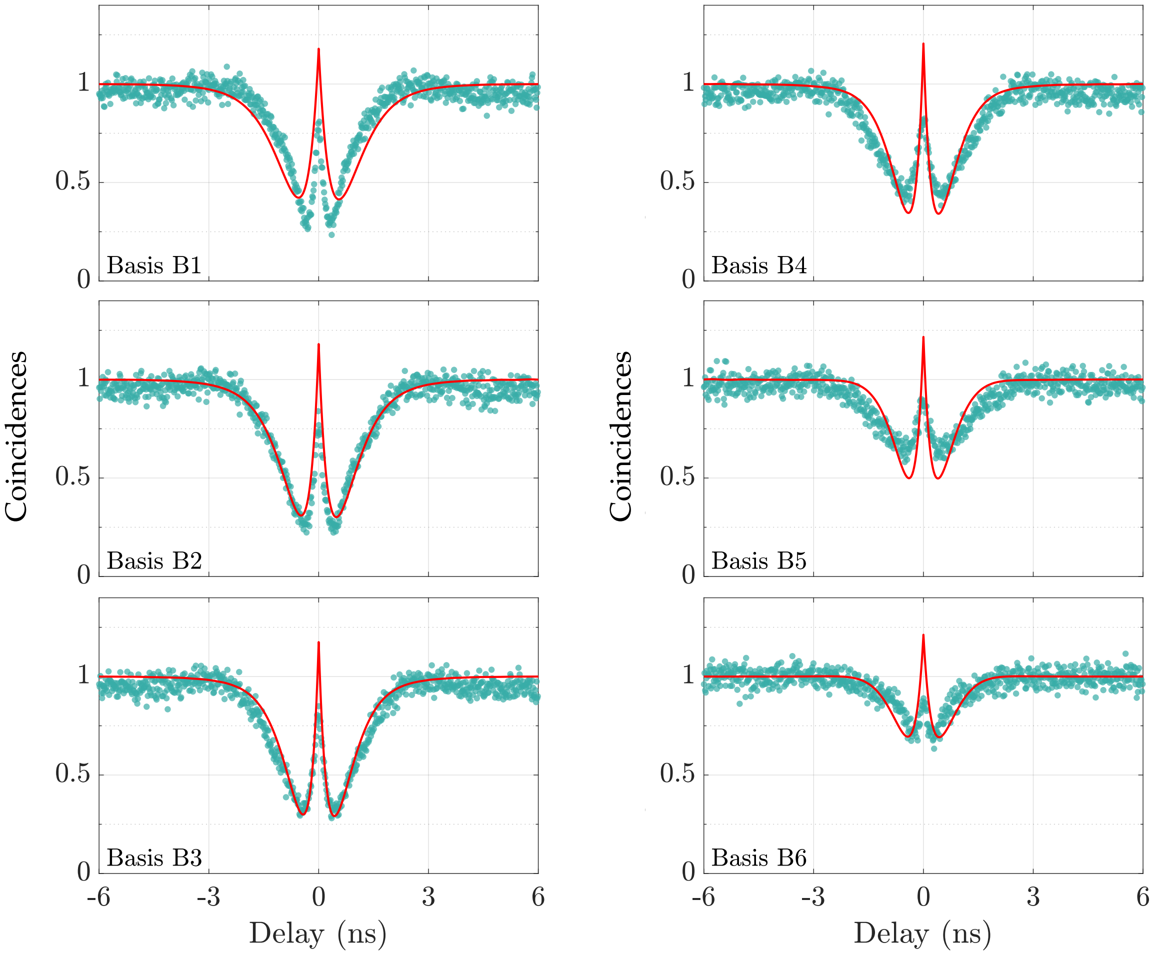

FIGURE 5.12: Cross-correlations in bases B1 to B6, with simulations accounting for the change in the measurement basis, with all other parameters unchanged.

As for the detuning dependence presented in Fig. 5.13, we now fix the simulated measurement basis B2 and change the simulated laser-quantum dot detuning. The decreased contrast of the anti-correlation dip when $\omega - \omega_d$ strays from its previous value of 1 µeV roughly reflects in the simulation, but the fast oscillations they include are not visible in the experiment. These oscillations, however, should necessarily appear in the presence of a non-zero detuning $\omega - \omega_d$. Indeed, they arise from the generalized damped Rabi oscillations, induced by the incoming laser, between each ground state and its corresponding excited state. Since these oscillations don't manifest experimentally, and since ω is well measured, there is a possibility that ω_d has varied in between the measurements, to keep a closer-than-expected value compared to ω. Overall, the simulation partially follows the experiment, and reproduces it very well in the optimal conditions.

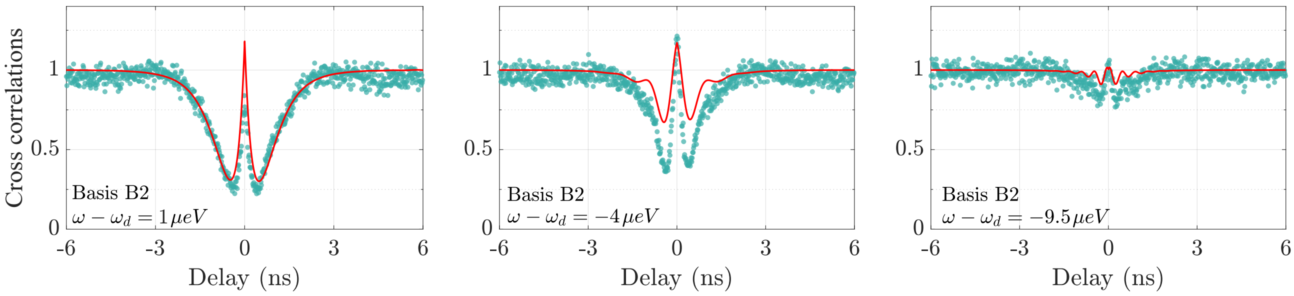

FIGURE 5.13: Dependence of the experimental cross-correlations with the detuning in basis B2, along with the simulated data.

5.2.4 Towards the ideal device

In the experiments from the current section, two factors have hindered the performance of the system as a spin-photon interface: first, the difficulty to align the measurement basis to the best theoretical one and to set the appropriate detuning, and second the short spin memory time.

We begin by simulating the difference in the measurement basis between B2 and S2 at the appropriate detuning, all the other parameters left unchanged. In Fig. 5.14, we plot on the left the experimental cross-correlations in B2 along with the simulation in B2 and S2. In comparison, the anti-correlation dip is only slightly deeper in S2 than B2. On the right side of the figure is the simulated conditional spin polarization $\widetilde{s_z}$ after a detected photon, which quantifies the efficiency of the spin projection:

$$\widetilde{s_z} = \frac{\widetilde{P(\downarrow)} - \widetilde{P(\uparrow)}}{\widetilde{P(\downarrow)} - \widetilde{P(\uparrow)}} \tag{5.4}$$

Ideally, $\widetilde{s_z}$ would reach unity. Here, the spin projection is higher in S2 with $\widetilde{s_{z,max}}(\mathrm{B2}) = 0.75$ and $\widetilde{s_{z,max}}(\mathrm{S2}) = 0.90$, respectively corresponding to values of the conditional occupation of the $|\uparrow\rangle$ state, $\widetilde{P(\uparrow)}$, of 0.88 and 0.95. The spin projection is very close to ideal in S2, and the remaining imperfection is probably due to the interplay between the fast spin flips and the short radiative transitory regime. The spin polarization is maintained for a few hundred picoseconds, which is very fast and could be significantly extended using a hole spin.

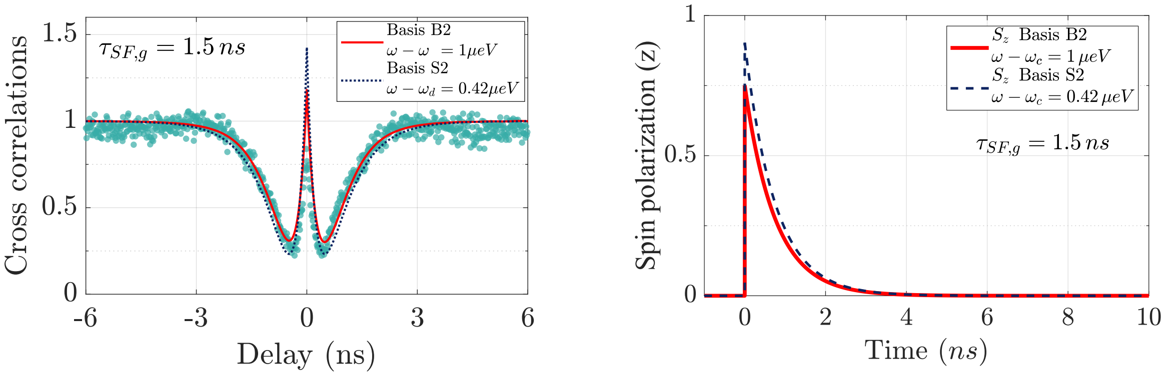

(a) (b)

FIGURE 5.14: Comparison between measurement bases B2 (experimental) and S2 (best theoretical). **(Left)** Cross-correlations (experiment and theory) at the appropriate detunings for the optimal operation as a spin-photon interface. **(Right)** Conditional spin polarization $\widetilde{s_z}$ (theory only). The maximum values of the spin polarization are $\widetilde{s_{z,max}}(\text{B2}) = 0.75$ and $\widetilde{s_{z,max}}(\text{S2}) = 0.90$.

Finally, we extend the simulations to a hypothetical increased spin-flip timescale of $\tau_{SF,g} = 1.5\,\mu\text{s}$ and show the result in Fig. 5.15. As mentioned above, such a long timescale would be accessible by a hole spin qubit, but technological improvements are needed to produce such a device with as little noise as the *negatively charged device*. The graphs show a very contrasted anti-correlation and spin polarization in basis B2, with $\widetilde{s_{z,max}}(B2) = 0.80$, which become perfect in the case of S2.

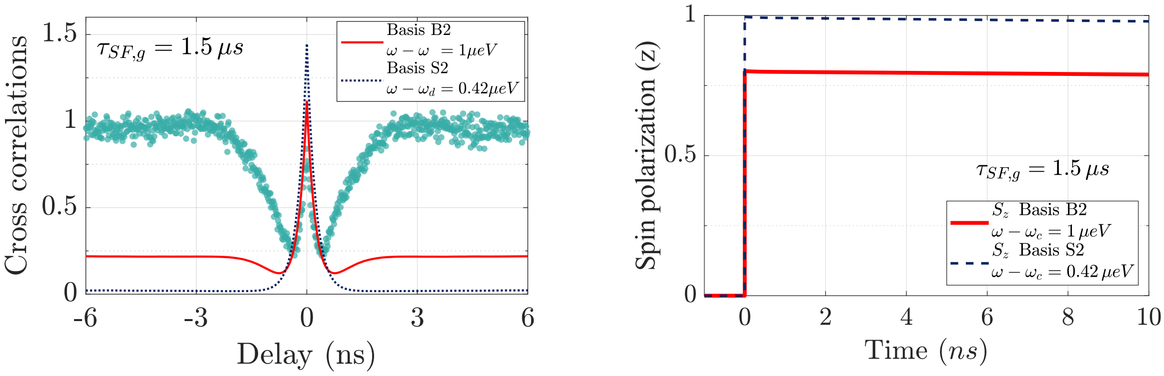

(a) (b)

FIGURE 5.15: Comparison between measurement bases B2 (experimental) and S2 (best theoretical) with a hypothetical $\tau_{SF,g} = 1.5\,\mu\text{s}$. **(Left)** Cross-correlations (experiment and theory). **(Right)** Spin polarization s_z (theory only). The maximum values of the spin polarization are $\widetilde{s_{z,max}}(\text{B2}) = 0.80$ and $\widetilde{s_{z,max}}(\text{S2}) = 1.0$.

The scope of the predicted spin polarization conditioned by photon detection must still be nuanced. Indeed, the interplay between the short radiative regime and the very fast decay of the anti-correlation dip becomes complex when both their timescales are similar (in the ns range): the correspondence between the presence of the anti-correlation dip and the measurement-induced spin projection might not be as straightforward as when the two timescales are clearly separated, as was the case in subsection 3.3.3. In addition, our numerical simulations do not directly take into account the change of orientation of the Overhauser field experienced by the electron spin, nor the cotunnelling (escape and capture) processes, since we used $P_c = 1$ for simplicity. The estimated value of $\widetilde{P(\uparrow)} = 0.88$ is thus both model- and parameter-dependent, requiring further analysis to estimate its probably large uncertainty.

5.3 Conclusion

Throughout the chapter, the *negatively charged device* was progressively characterized as a spin-photon interface and a first theoretical model was built to fit the whole dataset. We started with reflectivity and tomography measurements in the steady state to assess the spin-induced Faraday rotation: the device demonstrated values of s_{HV} far below zero, making it theoretically suitable to operate as an ideal spin-photon interface. We followed with cross-correlation measurements to probe the system dynamics: as suggested by the simulation, we explored the measurement bases in the (DRAL) plane to isolate the spin effect and observed highly contrasted anti-correlation dips. The experimental shortcomings were accounted for in the simulation, and despite imperfect measurement basis and excitation energy, we estimated that the spin initialization could be as high as 88 % in the $|\uparrow\rangle$ state, induced by the measurement of a reflected photon, and maintained for a timescale of 1.5 ns (limited by the memory time of the electron spin in the ground state). We finally extrapolated the device behavior through the simulation to predict that it could demonstrate a detection-induced spin initialization of 95 % provided that the appropriate measurement basis and excitation energy are used, though the short electron dynamics make the interpretation hazardous. Indeed, the estimated performance suffers from significant uncertainties that would only be mitigated by more precise experiments.

Such a cavity QED system could operate as a nearly ideal spin-photon interface if a hole spin qubit was used, i.e., if a positively charged device could be implemented with negligible noise and long charge escape time, to take advantage of the long hole spin memory time.

Conclusion and perspectives

The experimental studies and theoretical modeling reported in this manuscript demonstrate the potential of quantum dot-micropillar devices for spin-photon interfaces. The spin-dependent polarization rotation is brought to the macroscopic scale by cavity enhancement, to the point where a photon at the right energy and input polarization could extract the whole information about the quantum dot spin state. The performance of real devices was quantified by first examining the complete polarization state of the reflected photons in the steady state, assessing if the polarization rotation is high enough for an ideal spin-photon interface. Then, observing photon-photon cross-correlations in different polarization bases revealed the dynamics of the system as well as the noise sources and imperfections it suffers. We concluded that the device based on a hole spin presented a polarization rotation which, despite macroscopic, was not stable enough to achieve an ideal spin-photon interface. However, its dynamics proved the main limitation to reside in slow charge noise, and simulations predicted a significant improvement if charge noise was overcome (for example using a feedback scheme applied to the sample bias [180, 181]). On the other hand, we showed that the device based on an electron spin, though presenting a polarization rotation larger than what is required for ideality, suffered from the hyperfine interaction with the neighboring nuclei. As a consequence, the short spin lifetime is tainted by the effect of radiative population rebalancing, blurring out the potentially ideal operation as a spin-photon interface.

The immediate perspectives opened by this manuscript consist, in the short term, in the elaboration of more robust polarization control and detection accuracy to avoid the experimental flaws encountered in chapter 5. Pursuing this goal, the C2N team showed in results to be published that the *negatively charged device* could reflect single photons in arbitrary polarization states by properly setting the detuning and longitudinal magnetic field degrees of freedom [182]. Refining the numerical models is also an interesting prospect, for instance by rigorously accounting for the hyperfine interaction through a simulated fluctuating magnetic field. Indeed, we only included in this manuscript an empirical contribution of incoherent spin flips (see subsection 3.1.4), which does not encompass the entire physical phenomenon. Such a complete model should thoroughly reproduce the dependence of cross-correlations with a longitudinal magnetic field from chapter 4 (see Fig. 4.16), where the hyperfine interaction is progressively screened. An explanation to the mismatch with the detuned cross-correlations in chapter 5 is pursued as well (see Fig. 5.13), which could bring insights on (and ultimately separate) the contributions of radiative transitory regime and actual spin flips of the electron.

Other perspectives are investigated by the extended C2N group led by P. Senellart. On the sample design and fabrication side, an intermediate heterostructure is sought, benefiting from the stability of electrical charge injection (and thus of resonant excitation) combined with the long spin lifetime of holes. Structures analogous to those developed by *Najer et al. (2019)* [113] in the group of R. Warburton are currently pursued. On the single-photon sources side, a complementary approach currently investigated uses longitudinal acoustic (LA) phonon excitation to address trion transitions (see subsection 1.1.5): this peculiar spin-preserving quasi-resonant excitation exhibits the same optical selection rules as resonant excitation, but with a detuned laser that can conveniently be spectrally filtered out in the collection. Such a scheme is very promising, both for single-photon sources and for spin-photon interfaces [69, 183].

The medium to long-term projects pertaining to the spin-photon interface are presented below, starting with applications of the potentially ideal Faraday rotation of future devices, which would offer the ability to fundamentally study quantum measurements and to generate cluster states. Next, the Raman spin-flip phenomenon is presented as an alternative to Faraday rotation to achieve two-qubit gates with spins and photons.

Exploring the quantum measurement regimes

A spin-photon interface offers a platform of choice to study the back action induced on the spin when measuring photons reflected from the device. Photonic cross-correlation measurements with single photon detectors in fact directly monitor this effect [179]. Let the spin state be initialized in $|\Uparrow\rangle_z$ at $t = 0$ and evolve in the presence of a transverse magnetic field: the spin precession between the $|\Uparrow\rangle_z$ and $|\Downarrow\rangle_z$ states translates in an oscillation between the corresponding photon polarizations $|\Psi_\Uparrow\rangle$ and $|\Psi_\Downarrow\rangle$. From this point, the projective measurement of photons might manifest in different ways:

- The strength of the measurement could be tuned by adapting the overlap between the measured polarizations and the ($|\Psi_\Uparrow\rangle$,$|\Psi_\Downarrow\rangle$) basis. The weak measurement [84] of a photon in a polarization far from these would extract little information on the spin, and the inefficient projection would leave its coherent evolution mostly undisturbed. On the opposite, measuring photons exactly along $|\Psi_\Uparrow\rangle$ and $|\Psi_\Downarrow\rangle$ would perform a perfectly projective measurement, resetting the spin evolution. In the extreme case of high-rate projective measurements, the spin state would in turn be frozen. This corresponds to the *quantum Zeno effect* [32, 83].
- The amount of information lost in the environment through unread measurements could be varied by changing the excitation power and/or the optical losses in the setup. Since an unread photon applies a random back-action on the spin, high excitation power would in turn lead to measurement-induced decoherence.

The spin-photon interface provides a textbook illustration to precisely control the measurement and monitor its back action, testing the fundamental principles of quantum mechanics.

Generating cluster states with a spin-photon interface

The long-term prospect of a perfect spin-photon interface based on Faraday rotation opens the way to the successive entanglement of multiple photons with a single spin in what is referred to as a *cluster state* [29]. The ideal spin-photon interface has the fundamental property of mapping the spin states ($|\Uparrow\rangle_z$, $|\Downarrow\rangle_z$) on two complementary polarization states when an H-polarized photon impinges on the device. The associated polarization basis was written $(|\Psi_\Uparrow\rangle, |\Psi_\Downarrow\rangle)$ in previous chapters and we identify it to $(|D\rangle, |A\rangle)$ here for convenience. This property allows to entangle the spin state with an *incoming* photon, which is notably different from the spin-photon entanglement with emitted photons summed up in subsection 3.1.4.

Cluster states are multipartite entangled states: they involve multiple particles recursively entangled together such that the loss of a particle preserves the entanglement of the remaining state. Proposals for universal quantum computing with photonic cluster states make them very sought after [184–187]. Pioneering work by the group of D. Gershoni showed the generation of a five-photon cluster state by successively entangling photons to the confined spin, not of an electron or hole, but of a *dark exciton* [188]. The current record based on an atomic qubit involves 12 photons entangled to a single atom [189]. In the C2N team, recent progress demonstrated the high-rate generation of a spin-photon-photon cluster state [190].

The cluster state generation with a hole-based spin-photon interface would unfold as the steps described in the figure below. Let the spin coherently evolve in a transverse magnetic field with the Larmor frequency Ω_B after it was prepared in $|D\rangle$ (Step 0). Dropping the z indices for the spin eigenstates, its coherent evolution is given by:

$$|\Psi_s\rangle = \cos\frac{\Omega_B t}{2}|\Uparrow\rangle + \sin\frac{\Omega_B t}{2}|\Downarrow\rangle$$

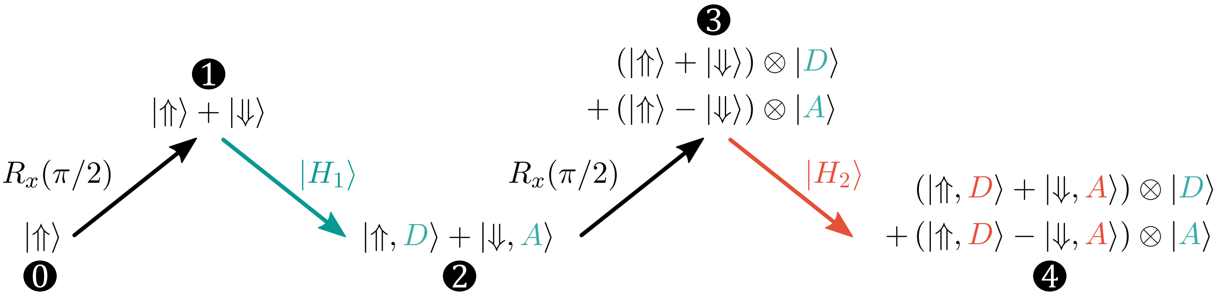

Sequential generation of a linear cluster state using a spin-photon interface.

- Step 1: after a delay, $t = \pi/(2\Omega_B)$, the magnetic field has rotated the spin by $\pi/2$ about the x-axis, bringing it to a coherent superposition.
- Step 2: a first H-polarized photon then interacts with the spin to generate the spin-photon entangled state.

- Step 3: after a second $\pi/2$ rotation, each spin state has again evolved to a coherent superposition.
- Step 4: when the second H photon interacts with the spin, it is entangled with the spin and the first photon.

Let us apply a final $\pi/2$ rotation to the spin to get the spin-photon-photon cluster state:

$$\begin{aligned}&|\Uparrow, D, D\rangle + |\Downarrow, D, D\rangle + |\Uparrow, A, D\rangle - |\Downarrow, A, D\rangle\\ +&|\Uparrow, D, A\rangle + |\Downarrow, D, A\rangle - |\Uparrow, A, A\rangle + |\Downarrow, A, A\rangle\end{aligned}$$

Such a recursive entanglement can be generalized to an arbitrary long string of photons, provided the spin coherence is maintained.

Cluster states are robust against loss in the sense that projecting one of the qubits doesn't destroy the remaining entanglement. Let us imagine that the spin is projected in $|\Uparrow\rangle$. The resulting state is written below as a maximally entangled state involving polarizations H and V, which explains in a simple manner their great interest for quantum computation schemes.

$$\begin{aligned}&|D, D\rangle + |A, D\rangle + |D, A\rangle - |A, A\rangle\\ =&|D, D + A\rangle + |A, D - A\rangle\\ =&|D, H\rangle + |A, V\rangle\end{aligned}$$

Harnessing Raman spin-flip transitions

The single-photon Raman interaction (or SPRINT) is a novel approach to achieve spin-photon and photon-photon gates [33, 191]. Contrary to the Faraday rotation approach, based on the optical selection rules (see Fig. 1.9a), the SPRINT relies on quantum pathway interference between the input photons and those scattered from the spin. Let us review its principle and possible applications to quantum dot-micropillar cavity devices.

Principle

Let us follow the extended analysis by *Rosenblum et al. (2017)* [192], which starts with the simple case of a 1D-atom coupled to a waveguide (left panel below): the input mode of amplitude 1 propagates forwards and impinges on the atom, which scatters a portion x of the field forwards and the same portion backwards. We emphasize that, in this thought experiment, the forward- and backward-propagating modes don't interfere. The total transmitted field then results from the interference of the two forward-propagating fields, of amplitude $1 + x$, whereas the reflected field only contains the x portion scattered backwards. The transmission and reflection coefficients read $t = 1 + x$ and $r = x$. Since the energy conservation imposes that $|t|^2 + |r|^2 = 1$, the only non-trivial solution is $x = -1$. A 1D-atom therefore fully reflects the input field. A condition must yet be fulfilled for the interference to manifest: the temporal shape of the input photons must be longer than the lifetime of the excited level.

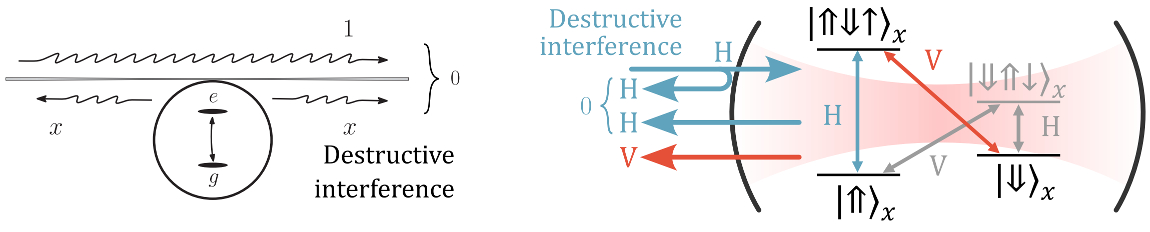

(a)

(b)

(a) A two-level system coupled to a waveguide as a 1D-atom. The probe field amplitude is fixed at 1, and x quantifies the portion scattered by the atom in both directions. Figure from [192]. **(b)** The positive trion 4-level system under a transverse magnetic field. A Λ-system is isolated when addressing only the two colored transition and ignoring the (far-detuned) grayed-out ones.

To translate this problem to a quantum dot spin coupled to a micropillar cavity, let us isolate two of its transitions of polarization H and V when a transverse magnetic field is applied to form a Λ-system (right panel above). Let the H-polarized transition correspond to the forward mode of the previous example and the V-polarized transition, to the backward mode. In this regime, an H photon couples to $|\Uparrow\rangle_x$ and the trion state is forced to de-excite through V due to the destructive interference between the H emission channel and the H-polarized field directly reflected by the top mirror. As a consequence, a V photon is emitted and the spin is flipped to $|\Downarrow\rangle_x$. This situation is analogous to the Faraday rotation on resonance, where the input $|H\rangle$ is completely converted in $|V\rangle$ upon reflection (see Fig. 3.10).

Direct applications

- Ultra-narrow single-photon source: in the Raman spin-flip regime, the emitted single photon inherits the temporal shape of the excitation [193]: using a continuous laser input could then bring about extremely narrow single photons sources that would help maintaining a good entanglement fidelity in a future quantum network, as previously investigated in the so-called *Heitler regime* [194, 195].
- Spin-photon switch: the Raman spin-flip phenomenon materializes a switch gate, where an input photon tuned to the $|\Uparrow\rangle_x \leftrightarrow |\Uparrow\Downarrow\uparrow\rangle_x$ transition and polarized along H is converted to V in the presence of the spin, but is left unchanged in its absence. A similar gate was produced with a quantum dot coupled to a photonic crystal cavity [196].
- Photon router: let the spin be initialized in $|\Uparrow\rangle_x$ and two H-polarized single photons impinge on the device. The Raman spin flip is triggered by the first photon, so the second one experiences an empty cavity as it can't address the $|\Downarrow\rangle_x$ state. This scheme can effectively *route* the two photons to different detectors, and is an important building block for photonic-based quantum computation. It was first demonstrated in the cold atom community [15] and could be translated to the solid-state with realistic devices [196].

Towards SWAP gates

A spin-photon SWAP gate would coherently *swap* any quantum superposition state between a single photon and a single spin: starting with the initial states $\alpha_1 \left|H\right\rangle + \alpha_2 \left|V\right\rangle$ and $\beta_1 \left|\Uparrow\right\rangle_x + \beta_2 \left|\Downarrow\right\rangle_x$, the system would end up in $\beta_2 \left|H\right\rangle + \beta_1 \left|V\right\rangle$ and $\alpha_2 \left|\Uparrow\right\rangle_x + \alpha_1 \left|\Downarrow\right\rangle_x$. The Raman spin-flip process allows to implement such a gate in an energy-degenerate Λ-system, and even opens the path to photon-photon swap gates using the spin as memory [191]. However, in our non-degenerate Λ-system, the additional requirement is to encode the polarization qubit on two energy-split polarizations, written $\alpha_1 \left|H, \omega_H\right\rangle + \alpha_2 \left|V, \omega_V\right\rangle$. This could be achieved by first modulating a continuous laser through an acousto-optic modulator to obtain two contributions, each tuned to one of the transitions of the Λ-system, before setting their amplitude in the quantum state through a set of spectral filters and waveplates [95, 106, 197].

These various prospects make quantum-dot micropillar devices platforms of choice for the future of large-scale quantum information.

Appendix A

Fourier-limited width of a quantum dot transition

The lifetime of the photons emitted by a single charge trapped in a quantum dot inside a micropillar cavity is linked with the physical parameters of the system. The Purcell-enhanced emission rate in the fundamental mode of the cavity is given by $\Gamma_0 = \frac{4g^2}{\kappa}$ when the cavity is in resonance with the quantum dot and by $\Gamma_0 = \frac{4g^2}{\kappa}\frac{1}{1+\Delta^2}$ when the quantum dot is detuned from the cavity by a fraction of the cavity linewidth $\Delta = 2\frac{\omega_{QD}-\omega_{cav}}{\kappa}$. For the trion transition in the absence of an external magnetic field, the excited state decays with an equal probability in H or V. The total lifetime, including the spontaneous emission outside of the cavity mode is therefore:

$$\Gamma = \frac{2g^2/\kappa_H}{1+\left(2\cdot\frac{\omega_{QD}-\omega_H}{\kappa_H}\right)^2} + \frac{2g^2/\kappa_V}{1+\left(2\cdot\frac{\omega_{QD}-\omega_V}{\kappa_V}\right)^2} + \gamma_{sp,H} + \gamma_{sp,V} \tag{A.1}$$

Appendix B

Semi-analytical cross-correlations with slow electrical fluctuations

The idea of the semi-analytical calculation of the cross-correlations at intermediate time developed in subsection 3.3.5 can be extended to model any variation slower than τ_{int} yet faster than the measurement apparatus, and which does not induce spin flips. An electric noise or a longitudinal magnetic noise meet these conditions. Let us examine the case of slow electric fluctuations: it is computed by running the steady state simulation for different values of the quantum dot energy ω_d around the average $\overline{\omega_d}$, shifted by the quantity $\delta\omega_d$, that is: $\omega_d = \overline{\omega_d} + \delta\omega_d$. The simulated parameters are still the intensities in the output polarizations when the quantum dot is initialized in $s \in [\Uparrow, \Downarrow, \varnothing]$ and the probability of these charge states, but this time as a function of the shift of ω_d: we label them $I_X(s, \delta\omega_d)$ and $P(s|\delta\omega_d)$.

We start by inserting the shift of ω_d induced by the noise in Eq. 3.59:

$$g^{(2)}_{XY} = \sum_{\substack{s\in[\Uparrow,\Downarrow,\varnothing]\\ \delta\omega_d}} \frac{P(Y|s,\delta\omega_d)P(s,\delta\omega_d|X)}{P(Y)} \tag{B.1}$$

The probability to detect a photon in X when the quantum dot is in the charge state s and its energy is $\overline{\omega_d} + \delta\omega_d$ is:

$$P(X|s,\delta\omega_d) \propto I_X(s,\delta\omega_d) \tag{B.2}$$

We can then follow the same logic in the Bayesian inference:

$$P(s,\delta\omega_d|X) = \frac{P(X|s,\delta\omega_d)P(s,\delta\omega_d)}{P(X)} \tag{B.3}$$

where this time $P(s, \delta\omega_d)$ is the probability that the quantum dot is in the charge state s and that ω_d is shifted by $\delta\omega_d$. We can then introduce the Gaussian distribution of spectral shifts:

$$P(s,\delta\omega_d) = P(s|\delta\omega_d)P(\delta\omega_d) \tag{B.4}$$

$$P(\delta\omega_d) = \frac{1}{\sqrt{2\pi}\sigma_{sw}} e^{-\left(\frac{\delta\omega_d}{2\sigma_{sw}}\right)^2} \tag{B.5}$$

We define a distribution of shifts over which to compute the intensities and occupation probabilities : $\delta\omega_d \in [-N, N] \times \mathrm{d}\omega$, where N and $\mathrm{d}\omega$ set the range and the step of the distribution of samples to average. For instance, the unconditioned probability to detect an X-polarized photon reads:

$$\begin{aligned} P(X) &= \sum_{\substack{s\in[\Uparrow,\Downarrow,\varnothing] \\ j\in[-N,N]}} P(X|s, j\mathrm{d}\omega)P(s, j\mathrm{d}\omega) \times \mathrm{d}\omega \\ &= \sum_{\substack{s\in[\Uparrow,\Downarrow,\varnothing] \\ j\in[-N,N]}} P(X|s, j\mathrm{d}\omega)P(s|j\mathrm{d}\omega)P(j\mathrm{d}\omega) \times \mathrm{d}\omega \\ &\propto \sum_{\substack{s\in[\Uparrow,\Downarrow,\varnothing] \\ j\in[-N,N]}} I_X(s, j\mathrm{d}\omega)P(s|j\mathrm{d}\omega)P(j\mathrm{d}\omega) \times \mathrm{d}\omega \end{aligned} \tag{B.6}$$

where we successively injected Eq. B.4 and B.2 to find an expression containing only the simulated data and the probability distribution of the spectral shifts. The final expression of the cross-correlations is the following:

$$\begin{aligned} g^{(2)}_{XY} &= \frac{\sum_{s,\delta\omega_d} I_Y(s, \delta\omega_d)I_X(s, \delta\omega_d)P(s, \delta\omega_d)}{\sum_{s,\delta\omega_d} I_Y(s, \delta\omega_d)P(s, \delta\omega_d) \times \sum_{s,\delta\omega_d} I_X(s, \delta\omega_d)P(s, \delta\omega_d)} \\ &= \frac{\sum_{s,\delta\omega_d} I_Y(s, \delta\omega_d)I_X(s, \delta\omega_d)P(s, \delta\omega_d)}{I_X I_Y} \end{aligned} \tag{B.7}$$

where the $P(s, \delta\omega_d)$ terms are summed over the sampling range as in Eq. B.6, and the denominator terms were regrouped in the total intensities I_X and I_Y. This formula was used to calculate the cross-correlations in the pure electric noise case, it also works for a purely longitudinal magnetic noise. However, a transverse magnetic noise induces spin flips and therefore differs from this semi-analytical model.

Appendix C

Correction of the tomography experimental data

Here we explain why the polarization basis of the collection is not aligned with that at the quantum dot position and how to compensate for this effect by applying rotations of the experimental points in the Poincaré sphere.

The natural orientation of the Poincaré sphere is the one defined by $[HVDARL]_{cav}$ in which H_{cav} and V_{cav} coincide with the eigenaxes of the cavity and R_{cav} and L_{cav} correspond to right- and left-handed circular polarizations in the micropillar, quantified along the growth axis z. If we want to describe the measurement basis defined by QWP2, HWP2 and the Wollaston in this Poincaré sphere of reference (see Fig. 2.5 for the optical setup), we need to take into account the unitary transformation that light undergoes from the micropillar to QWP2. This unitary transformation is due primarily to the ellipticity induced by the optics that we try to minimize by using dielectric mirrors with a s polarized input; however, the main source of ellipticity is the reflection on the beam splitter, on the way to the collection path.

It is important to note that the polarization analysis on the collection path was calibrated for a set of polarizations $[HVDARL]_{coll}$ that define an orthonormal basis, but this collection basis does not need to be the same as the reference basis of the microcavity as a rotation can be applied to the experimental data to correct them by any unitary transformation induced by the unwanted ellipticity. In Fig. C.1, we show the Stokes parameters and Poincaré representation of the raw experimental quantum dot tomography corresponding to the corrected data from Fig. 4.3 at $B = 0\,\mathrm{mT}$. The correction consists in assuming that the out-of-resonance points are unaffected by the quantum dot and should be brought back to H by a rotation. The same rotation is applied for the tomographies at different Faraday magnetic fields.

Another correction that was not applied in this manuscript is to make sure that the circular polarizations of the collection basis are aligned with that of the cavity basis. This proved to be difficult to assess experimentally as the preparation of a circular polarization on the location of the sample is quite challenging. Nevertheless, another factor validates the chosen orientation of the sphere: the fact that the measured trajectories of the polarization states at different longitudinal magnetic fields are all contained in the $(H, \theta_o, V, \overline{\theta_o})$ circle, as shown in the corrected data of Fig. 4.3. Indeed, this feature arises from the energy-splitting of the cavity modes as predicted by the simulation (see Fig. 3.12).

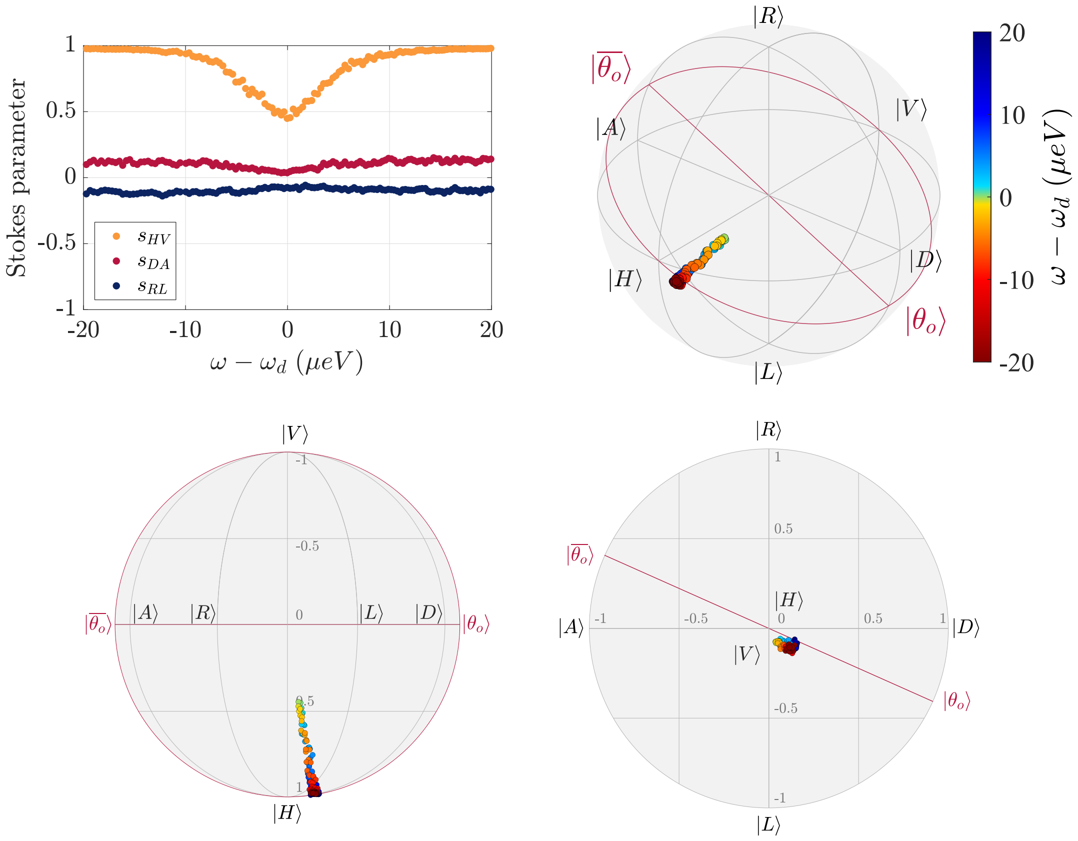

FIGURE C.1: Raw experimental polarization tomography of the reflected photons. Excitation laser polarized along H_{cav} with a power of 8 pW coupled to a 2 µW 901 nm quasi-resonant laser. The out-of-resonance points are assumed to be unaffected by the quantum dot and are therefore corrected to be along H_{cav} as shown on the corrected data in Fig. 4.3.

List of publications

Generation of non-classical light in a photon-number superposition
J. C. Loredo, C. Antón, B. Reznychenko, P. Hilaire, A. Harouri, C. Millet, H. Ollivier, N. Somaschi, L. De Santis, A. Lemaître, I. Sagnes, L. Lanco, A. Auffèves, O. Krebs, and P. Senellart.
Nature Photonics **13** (2019), pp. 803–808. DOI: 10.1038/s41566-019-0506-3.

Deterministic assembly of a charged quantum-dot–micropillar cavity device
P. Hilaire, C. Millet, J. C. Loredo, C. Antón, A. Harouri, A. Lemaître, I. Sagnes, N. Somaschi, O. Krebs, P. Senellart, and L. Lanco.
Physical Review B **102** (2020), pp. 1–9. DOI: 10.1103/PhysRevB.102.195402.

Sequential generation of linear cluster states from a single photon emitter
D. Istrati, Y. Pilnyak, J. C. Loredo, C. Antón, N. Somaschi, P. Hilaire, H. Ollivier, M. Esmann, L. Cohen, L. Vidro, C. Millet, A. Lemaître, I. Sagnes, A. Harouri, L. Lanco, P. Senellart, and H. S. Eisenberg.
Nature Communications **11** (2020), pp. 1–8. DOI: 10.1038/s41467-020-19341-4.

Reproducibility of High-Performance Quantum Dot Single-Photon Sources
H. Ollivier, I. Maillette de Buy Wenniger, S. Thomas, S. C. Wein, A. Harouri, G. Coppola, P. Hilaire, C. Millet, A. Lemaître, I. Sagnes, O. Krebs, L. Lanco, J. C. Loredo, C. Antón, N. Somaschi, and P. Senellart.
ACS Photonics **7** (2020), pp. 1050–1059. DOI: 10.1021/acsphotonics.9b01805.

Probing the dynamics and coherence of a semiconductor hole spin via acoustic phonon-assisted excitation
N. Coste, M. Gundin, D. Fioretto, S. E. Thomas, C. Millet, E. Medhi, M. Gundin, N. Somaschi, M. Morassi, M. Pont, A. Lemaître, N. Belabas, O. Krebs, L. Lanco, and P. Senellart.
arXiv (2022), pp. 1–6. URL: http://arxiv.org/abs/2207.05981.

Controlling photon polarisation with a single quantum dot spin
E. Mehdi, M. Gundín-Martínez, C. Millet, N. Somaschi, A. Lemaître, I. Sagnes, L. Le Gratiet, D. Fioretto, N. Belabas, O. Krebs, P. Senellart, and L. Lanco.
arXiv (2022), pp. 29-32. URL: https://arxiv.org/abs/2212.03767.

Measuring single spin noise with single detected photons
P. Hilaire, C. Millet, M. Gundín Martínez, E. Mehdi, C. Antón, A. Harouri, A. Lemaître, I. Sagnes, N. Somaschi, O. Krebs, P. Senellart, and L. Lanco.
In preparation

Bibliography

[1] I. M. Georgescu, S. Ashhab, and F. Nori. “Quantum simulation”. In: *Reviews of Modern Physics* **86** (2014), pp. 153–185. DOI: 10.1103/RevModPhys.86.153.

[2] C. L. Degen, F. Reinhard, and P. Cappellaro. “Quantum sensing”. In: *Reviews of Modern Physics* **89** (2017), pp. 1–39. DOI: 10.1103/RevModPhys.89.035002.

[3] H. J. Kimble. “The quantum internet”. In: *Nature* **453** (2008), pp. 1023–1030. DOI: 10.1038/nature07127.

[4] E. Diamanti, H.-K. Lo, B. Qi, and Z. Yuan. “Practical challenges in quantum key distribution”. In: *npj Quantum Information* **2** (2016), p. 16025. DOI: 10.1038/npjqi.2016.25.

[5] D. P. DiVincenzo. “The Physical Implementation of Quantum Computation”. In: *Fortschritte der Physik* **48** (2000), pp. 771–783. DOI: 10.1002/1521-3978(200009)48:9/11<771::AID-PROP771>3.0.CO;2-E.

[6] M. A. Nielsen and I. L. Chuang. *Quantum Computation and Quantum Information*. Cambridge University Press, 2010. DOI: 10.1017/CBO9780511976667.

[7] Q. A. Turchette, C. S. Wood, B. E. King, C. J. Myatt, D. Leibfried, W. M. Itano, C. Monroe, and D. J. Wineland. “Deterministic entanglement of two trapped ions”. In: *Physical Review Letters* **81** (1998), pp. 3631–3634. DOI: 10.1103/PhysRevLett.81.3631.

[8] F. Arute et al. “Quantum supremacy using a programmable superconducting processor”. In: *Nature* **574** (2019), pp. 505–510. DOI: 10.1038/s41586-019-1666-5.

[9] M. Atatüre, D. Englund, N. Vamivakas, S. Y. Lee, and J. Wrachtrup. “Material platforms for spin-based photonic quantum technologies”. In: *Nature Reviews Materials* **3** (2018), pp. 38–51. DOI: 10.1038/s41578-018-0008-9.

[10] E. Knill, R. Laflamme, and G. J. Milburn. “A scheme for efficient quantum computation with linear optics”. In: *Nature* **409** (2001), pp. 46–52. DOI: 10.1038/35051009.

[11] J. Borregaard, H. Pichler, T. Schröder, M. D. Lukin, P. Lodahl, and A. S. Sørensen. “One-Way Quantum Repeater Based on Near-Deterministic Photon-Emitter Interfaces”. In: *Physical Review X* **10** (2020), p. 21071. DOI: 10.1103/PHYSREVX.10.021071.

[12] H. Pichler, S. Choi, P. Zoller, and M. D. Lukin. “Universal photonic quantum computation via time-delayed feedback”. In: *Proceedings of the National Academy of Sciences of the United States of America* **114** (2017), pp. 11362–11367. DOI: 10.1073/pnas.1711003114.

[13] R. J. Thompson, G. Rempe, and H. J. Kimble. “Observation of normal-mode splitting for an atom in an optical cavity”. In: *Physical Review Letters* **68** (1992), pp. 1132–1135. DOI: 10.1103/PhysRevLett.68.1132.

[14] T. Wilk, S. C. Webster, A. Kuhn, and G. Rempe. “Single-atom single-photon quantum interface”. In: *Science* **317** (2007), pp. 488–490. DOI: 10.1126/science.1143835.

[15] I. Shomroni, S. Rosenblum, Y. Lovsky, O. Bechler, G. Guendelman, and B. Dayan. “All-optical routing of single photons by a one-atom switch controlled by a single photon”. In: *Science* **345** (2014), pp. 903–906. DOI: 10.1126/science.1254699.

[16] S. Daiß, S. Langenfeld, S. Welte, E. Distante, P. Thomas, L. Hartung, O. Morin, and G. Rempe. “A quantum-logic gate between distant quantum-network modules”. In: *Science* **371** (2021), pp. 614–617. DOI: 10.1126/science.abe3150.

[17] R. C. Ashoori. “Electrons in artificial atoms”. In: *Nature* **379** (1996), pp. 413–419. DOI: 10.1038/379413a0.

[18] K. J. Vahala. “Optical microcavities”. In: *Nature* **424** (2003), pp. 839–846. DOI: 10.1038/nature01939.

[19] E. Moreau, I. Robert, J. M. Gérard, I. Abram, L. Manin, and V. Thierry-Mieg. “Single-mode solid-state single photon source based on isolated quantum dots in pillar microcavities”. In: *Applied Physics Letters* **79** (2001), pp. 2865–2867. DOI: 10.1063/1.1415346.

[20] B. D. Gerardot, D. Brunner, P. A. Dalgarno, P. Öhberg, S. Seidl, M. Kroner, K. Karrai, N. G. Stoltz, P. M. Petroff, and R. J. Warburton. “Optical pumping of a single hole spin in a quantum dot”. In: *Nature* **451** (2008), pp. 441–444. DOI: 10.1038/nature06472.

[21] D. Press, T. D. Ladd, B. Zhang, and Y. Yamamoto. “Complete quantum control of a single quantum dot spin using ultrafast optical pulses”. In: *Nature* **456** (2008), pp. 218–221. DOI: 10.1038/nature07530.

[22] W. B. Gao, P. Fallahi, E. Togan, J. Miguel-Sanchez, and A. Imamoglu. “Observation of entanglement between a quantum dot spin and a single photon”. In: *Nature* **491** (2012), pp. 426–430. DOI: 10.1038/nature11573.

[23] A. Dousse, L. Lanco, J. Suffczyński, E. Semenova, A. Miard, A. Lemaître, I. Sagnes, C. Roblin, J. Bloch, and P. Senellart. “Controlled light-matter coupling for a single quantum dot embedded in a pillar microcavity using far-field optical lithography”. In: *Physical Review Letters* **101** (2008), pp. 30–33. DOI: 10.1103/PhysRevLett.101.267404.

[24] N. Somaschi et al. “Near-optimal single-photon sources in the solid state”. In: *Nature Photonics* **10** (2016), pp. 340–345. DOI: 10.1038/nphoton.2016.23.

[25] V. Giesz, N. Somaschi, G. Hornecker, T. Grange, B. Reznychenko, L. De Santis, J. Demory, C. Gomez, I. Sagnes, A. Lemaître, O. Krebs, N. D. Lanzillotti-Kimura, L. Lanco, A. Auffeves, and P. Senellart. "Coherent manipulation of a solid-state artificial atom with few photons". In: *Nature Communications* **7** (2016). DOI: 10.1038/ncomms11986.

[26] L. De Santis, C. Antón, B. Reznychenko, N. Somaschi, G. Coppola, J. Senellart, C. Gómez, A. Lemaître, I. Sagnes, A. G. White, L. Lanco, A. Auffèves, and P. Senellart. "A solid-state single-photon filter". In: *Nature Nanotechnology* **12** (2017), pp. 663–667. DOI: 10.1038/nnano.2017.85.

[27] C. Arnold, J. Demory, V. Loo, A. Lemaître, I. Sagnes, M. Glazov, O. Krebs, P. Voisin, P. Senellart, and L. Lanco. "Macroscopic rotation of photon polarization induced by a single spin". In: *Nature Communications* **6** (2015), pp. 1–6. DOI: 10.1038/ncomms7236.

[28] P. Androvitsaneas, A. B. Young, J. M. Lennon, C. Schneider, S. Maier, J. J. Hinchliff, G. S. Atkinson, E. Harbord, M. Kamp, S. Höfling, J. G. Rarity, and R. Oulton. "Efficient Quantum Photonic Phase Shift in a Low Q-Factor Regime". In: *ACS Photonics* **6** (2019), pp. 429–435. DOI: 10.1021/acsphotonics.8b01380.

[29] C. Y. Hu, W. J. Munro, and J. G. Rarity. "Deterministic photon entangler using a charged quantum dot inside a microcavity". In: *Physical Review B* **78** (2008), p. 125318. DOI: 10.1103/PhysRevB.78.125318.

[30] N. H. Lindner and T. Rudolph. "Proposal for Pulsed On-Demand Sources of Photonic Cluster State Strings". In: *Physical Review Letters* **103** (2009), p. 113602. DOI: 10.1103/PhysRevLett.103.113602.

[31] P. Grangier, J. A. Levenson, and J.-P. Poizat. "Quantum non-demolition measurements in optics". In: *Nature* **396** (1998), pp. 537–542. DOI: 10.1038/25059.

[32] N. V. Leppenen, L. Lanco, and D. S. Smirnov. "Quantum Zeno effect and quantum non-demolition spin measurement in a quantum dot-micropillar cavity in the strong coupling regime". In: *Physical Review B* **103** (2021), pp. 1–15. DOI: 10.1103/PhysRevB.103.045413.

[33] O. Bechler, A. Borne, S. Rosenblum, G. Guendelman, O. E. Mor, M. Netser, T. Ohana, Z. Aqua, N. Drucker, R. Finkelstein, Y. Lovsky, R. Bruch, D. Gurovich, E. Shafir, and B. Dayan. "A passive photon–atom qubit swap operation". In: *Nature Physics* **14** (2018), pp. 996–1000. DOI: 10.1038/s41567-018-0241-6.

[34] L. Goldstein, F. Glas, J. Y. Marzin, M. N. Charasse, and G. Le Roux. "Growth by molecular beam epitaxy and characterization of InAs/GaAs strained-layer superlattices". In: *Applied Physics Letters* **47** (1985), pp. 1099–1101. DOI: 10.1063/1.96342.

[35] D. Leonard, M. Krishnamurthy, C. M. Reaves, S. P. Denbaars, and P. M. Petroff. "Direct formation of quantum-sized dots from uniform coherent islands of InGaAs on GaAs surfaces". In: *Applied Physics Letters* **63** (1993), pp. 3203–3205. DOI: 10.1063/1.110199.

[36] S. Figge, C. Tessarek, T. Aschenbrenner, and D. Hommel. “InGaN quantum dot growth in the limits of Stranski-Krastanov and spinodal decomposition”. In: *physica status solidi (b)* **248** (2011), pp. 1765–1776. DOI: 10.1002/pssb.201147165.

[37] P. Senellart, V. Giesz, and L. Lanco. “Ultrabright single-photon sources”. In: *Photoniques* (2017), pp. 23–26. DOI: 10.1051/photon/2017S223.

[38] M. Y. Petrov, I. V. Ignatiev, S. V. Poltavtsev, A. Greilich, A. Bauschulte, D. R. Yakovlev, and M. Bayer. “Effect of thermal annealing on the hyperfine interaction in InAs/GaAs quantum dots”. In: *Physical Review B* **78** (2008), p. 045315. DOI: 10.1103/PhysRevB.78.045315.

[39] M. Gurioli, Z. Wang, A. Rastelli, T. Kuroda, and S. Sanguinetti. “Droplet epitaxy of semiconductor nanostructures for quantum photonic devices”. In: *Nature Materials* **18** (2019), pp. 799–810. DOI: 10.1038/s41563-019-0355-y.

[40] C. Schneider, T. Heindel, A. Huggenberger, T. A. Niederstrasser, S. Reitzenstein, A. Forchel, S. Höfling, and M. Kamp. “Microcavity enhanced single photon emission from an electrically driven site-controlled quantum dot”. In: *Applied Physics Letters* **100** (2012). DOI: 10.1063/1.3689782.

[41] G. Juska, V. Dimastrodonato, L. O. Mereni, A. Gocalinska, and E. Pelucchi. “Towards quantum-dot arrays of entangled photon emitters”. In: *Nature Photonics* **7** (2013), pp. 527–531. DOI: 10.1038/nphoton.2013.128.

[42] M. Gong, K. Duan, C.-F. Li, R. Magri, G. A. Narvaez, and L. He. “Electronic structure of self-assembled InAs/InP quantum dots: Comparison with self-assembled InAs/GaAs quantum dots”. In: *Physical Review B* **77** (2008), p. 045326. DOI: 10.1103/PhysRevB.77.045326.

[43] M. Ediger, G. Bester, A. Badolato, P. M. Petroff, K. Karrai, A. Zunger, and R. J. Warburton. “Peculiar many-body effects revealed in the spectroscopy of highly charged quantum dots”. In: *Nature Physics* **3** (2007), pp. 774–779. DOI: 10.1038/nphys748.

[44] C. Kittel. *Introduction to Solid State Physics*. 8th ed. Wiley, 2004.

[45] O. Gazzano. “Sources brillantes de photons uniques indiscernables et démonstration d’une porte logique quantique”. PhD thesis. 2013. URL: https://tel.archives-ouvertes.fr/tel-01006555.

[46] P.-L. Ardelt, T. Simmet, K. Müller, C. Dory, K. A. Fischer, A. Bechtold, A. Kleinkauf, H. Riedl, and J. J. Finley. “Controlled tunneling-induced dephasing of Rabi rotations for high-fidelity hole spin initialization”. In: *Physical Review B* **92** (2015), p. 115306. DOI: 10.1103/PhysRevB.92.115306.

[47] J. H. Prechtel, A. V. Kuhlmann, J. Houel, A. Ludwig, S. R. Valentin, A. D. Wieck, and R. J. Warburton. “Decoupling a hole spin qubit from the nuclear spins”. In: *Nature Materials* **15** (2016), pp. 981–986. DOI: 10.1038/nmat4704.

[48] G. Burkard. "Positively spin coherent". In: *Nature Materials* **7** (2008), pp. 100–101. DOI: 10.1038/nmat2107.

[49] R. J. Warburton. "Single spins in self-assembled quantum dots". In: *Nature Materials* **12** (2013), pp. 483–493. DOI: 10.1038/nmat3585.

[50] B. Urbaszek, X. Marie, T. Amand, O. Krebs, P. Voisin, P. Maletinsky, A. Högele, and A. Imamoglu. "Nuclear spin physics in quantum dots: An optical investigation". In: *Reviews of Modern Physics* **85** (2013), pp. 79–133. DOI: 10.1103/RevModPhys.85.79.

[51] B. J. Witek, R. W. Heeres, U. Perinetti, E. P. A. M. Bakkers, L. P. Kouwenhoven, and V. Zwiller. "Measurement of the g-factor tensor in a quantum dot and disentanglement of exciton spins". In: *Physical Review B* **84** (2011), p. 195305. DOI: 10.1103/PhysRevB.84.195305.

[52] R. M. Stevenson, R. J. Young, P. See, D. G. Gevaux, K. Cooper, P. Atkinson, I. Farrer, D. A. Ritchie, and A. J. Shields. "Magnetic-field-induced reduction of the exciton polarization splitting in InAs quantum dots". In: *Physical Review B* **73** (2006), p. 033306. DOI: 10.1103/PhysRevB.73.033306.

[53] M. Bayer, G. Ortner, O. Stern, A. Kuther, A. A. Gorbunov, A. Forchel, P. Hawrylak, S. Fafard, K. Hinzer, T. L. Reinecke, S. N. Walck, J. P. Reithmaier, F. Klopf, and F. Schäfer. "Fine structure of neutral and charged excitons in self-assembled In(Ga)As/(Al)GaAs quantum dots". In: *Physical Review B* **65** (2002), p. 195315. DOI: 10.1103/PhysRevB.65.195315.

[54] B. Eble, C. Testelin, P. Desfonds, F. Bernardot, A. Balocchi, T. Amand, A. Miard, A. Lemaître, X. Marie, and M. Chamarro. "Hole-nuclear spin interaction in quantum dots". In: *Physical Review Letters* **102** (2009), pp. 1–4. DOI: 10.1103/PhysRevLett.102.146601.

[55] P. F. Braun, X. Marie, L. Lombez, B. Urbaszek, T. Amand, P. Renucci, V. K. Kalevich, K. V. Kavokin, O. Krebs, P. Voisin, and Y. Masumoto. "Direct observation of the electron spin relaxation induced by nuclei in quantum dots". In: *Physical Review Letters* **94** (2005), pp. 1–4. DOI: 10.1103/PhysRevLett.94.116601.

[56] X. Xu, Y. Wu, B. Sun, Q. Huang, J. Cheng, D. G. Steel, A. S. Bracker, D. Gammon, C. Emary, and L. J. Sham. "Fast spin state initialization in a singly charged InAs-GaAs quantum dot by optical cooling". In: *Physical Review Letters* **99** (2007), pp. 1–4. DOI: 10.1103/PhysRevLett.99.097401.

[57] M. Atatüre, J. Dreiser, A. Badolato, and A. Imamoglu. "Observation of Faraday rotation from a single confined spin". In: *Nature Physics* **3** (2007), pp. 101–106. DOI: 10.1038/nphys521.

[58] K. Takemoto, Y. Nambu, T. Miyazawa, Y. Sakuma, T. Yamamoto, S. Yorozu, and Y. Arakawa. "Quantum key distribution over 120km using ultrahigh purity single-photon source and superconducting single-photon detectors". In: *Scientific Reports* **5** (2015), pp. 4–6. DOI: 10.1038/srep14383.

[59] J. Tang, L. Tang, H. Wu, Y. Wu, H. Sun, H. Zhang, T. Li, Y. Lu, M. Xiao, and K. Xia. "Towards On-Demand Heralded Single-Photon Sources via Photon Blockade". In: *Physical Review Applied* **15** (2021), p. 1. DOI: 10.1103/PhysRevApplied.15.064020.

[60] D. B. Higginbottom, L. Slodička, G. Araneda, L. Lachman, R. Filip, M. Hennrich, and R. Blatt. "Pure single photons from a trapped atom source". In: *New Journal of Physics* **18** (2016). DOI: 10.1088/1367-2630/18/9/093038.

[61] T. M. Babinec, B. J. Hausmann, M. Khan, Y. Zhang, J. R. Maze, P. R. Hemmer, and M. Lončar. "A diamond nanowire single-photon source". In: *Nature Nanotechnology* **5** (2010), pp. 195–199. DOI: 10.1038/nnano.2010.6.

[62] M. Reindl, J. H. Weber, D. Huber, C. Schimpf, S. F. Covre Da Silva, S. L. Portalupi, R. Trotta, P. Michler, and A. Rastelli. "Highly indistinguishable single photons from incoherently excited quantum dots". In: *Physical Review B* **100** (2019), p. 155420. DOI: 10.1103/PhysRevB.100.155420.

[63] X. Ding, Y. He, Z.-C. Duan, N. Gregersen, M.-C. Chen, S. Unsleber, S. Maier, C. Schneider, M. Kamp, S. Höfling, C.-Y. Lu, and J.-W. Pan. "On-Demand Single Photons with High Extraction Efficiency and Near-Unity Indistinguishability from a Resonantly Driven Quantum Dot in a Micropillar". In: *Physical Review Letters* **116** (2016), p. 020401. DOI: 10.1103/PhysRevLett.116.020401.

[64] S. Ates, S. M. Ulrich, S. Reitzenstein, A. Löffler, A. Forchel, and P. Michler. "Post-Selected Indistinguishable Photons from the Resonance Fluorescence of a Single Quantum Dot in a Microcavity". In: *Physical Review Letters* **103** (2009), pp. 1–4. DOI: 10.1103/PhysRevLett.103.167402.

[65] M. Glässl, A. M. Barth, and V. M. Axt. "Proposed robust and high-fidelity preparation of excitons and biexcitons in semiconductor quantum dots making active use of phonons". In: *Physical Review Letters* **110** (2013), pp. 1–5. DOI: 10.1103/PhysRevLett.110.147401.

[66] A. M. Barth, S. Lüker, A. Vagov, D. E. Reiter, T. Kuhn, and V. M. Axt. "Fast and selective phonon-assisted state preparation of a quantum dot by adiabatic undressing". In: *Physical Review B* **94** (2016), pp. 1–10. DOI: 10.1103/PhysRevB.94.045306.

[67] M. Cosacchi, F. Ungar, M. Cygorek, A. Vagov, and V. M. Axt. "Emission-Frequency Separated High Quality Single-Photon Sources Enabled by Phonons". In: *Physical Review Letters* **123** (2019), p. 17403. DOI: 10.1103/PhysRevLett.123.017403.

[68] C. Gustin and S. Hughes. “Efficient Pulse-Excitation Techniques for Single Photon Sources from Quantum Dots in Optical Cavities”. In: *Advanced Quantum Technologies* **3** (2020), p. 1900073. DOI: 10.1002/qute.201900073.

[69] S. E. Thomas, M. Billard, N. Coste, S. C. Wein, Priya, H. Ollivier, O. Krebs, L. Tazaïrt, A. Harouri, A. Lemaitre, I. Sagnes, C. Anton, L. Lanco, N. Somaschi, J. C. Loredo, and P. Senellart. “Bright Polarized Single-Photon Source Based on a Linear Dipole”. In: *Physical Review Letters* **126** (2021), p. 233601. DOI: 10.1103/PhysRevLett.126.233601.

[70] M. Billard. “Practical and efficient solid-state sources of single and indistinguishable photons for quantum applications”. PhD thesis. 2021. URL: https://www.theses.fr/2021UPASP015.

[71] P.-L. L. Ardelt, L. Hanschke, K. A. Fischer, K. Müller, A. Kleinkauf, M. Koller, A. Bechtold, T. Simmet, J. Wierzbowski, H. Riedl, G. Abstreiter, and J. J. Finley. “Dissipative preparation of the exciton and biexciton in self-assembled quantum dots on picosecond time scales”. In: *Physical Review B* **90** (2014), p. 241404. DOI: 10.1103/PhysRevB.90.241404.

[72] J. H. Quilter, A. J. Brash, F. Liu, M. Glässl, A. M. Barth, V. M. Axt, A. J. Ramsay, M. S. Skolnick, and A. M. Fox. “Phonon-Assisted Population Inversion of a Single InGaAs/GaAs Quantum Dot by Pulsed Laser Excitation”. In: *Physical Review Letters* **114** (2015), pp. 1–5. DOI: 10.1103/PhysRevLett.114.137401.

[73] O. Gazzano, S. Michaelis De Vasconcellos, C. Arnold, A. Nowak, E. Galopin, I. Sagnes, L. Lanco, A. Lemaître, and P. Senellart. “Bright solid-state sources of indistinguishable single photons”. In: *Nature Communications* **4** (2013). DOI: 10.1038/ncomms2434.

[74] L. Hanschke, K. A. Fischer, S. Appel, D. Lukin, J. Wierzbowski, S. Sun, R. Trivedi, J. Vučković, J. J. Finley, and K. Müller. “Quantum dot single-photon sources with ultralow multi-photon probability”. In: *npj Quantum Information* **4** (2018), p. 43. DOI: 10.1038/s41534-018-0092-0.

[75] S. E. Economou, L. J. Sham, Y. Wu, and D. G. Steel. “Proposal for optical U(1) rotations of electron spin trapped in a quantum dot”. In: *Physical Review B* **74** (2006), p. 205415. DOI: 10.1103/PhysRevB.74.205415.

[76] K. De Greve, P. L. McMahon, D. Press, T. D. Ladd, D. Bisping, C. Schneider, M. Kamp, L. Worschech, S. Höfling, A. Forchel, and Y. Yamamoto. “Ultrafast coherent control and suppressed nuclear feedback of a single quantum dot hole qubit”. In: *Nature Physics* **7** (2011), pp. 872–878. DOI: 10.1038/nphys2078.

[77] A. Greilich, S. G. Carter, D. Kim, A. S. Bracker, and D. Gammon. “Optical control of one and two hole spins in interacting quantum dots”. In: *Nature Photonics* **5** (2011), pp. 702–708. DOI: 10.1038/nphoton.2011.237.

[78] T. M. Godden, J. H. Quilter, A. J. Ramsay, Y. Wu, P. Brereton, S. J. Boyle, I. J. Luxmoore, J. Puebla-Nunez, A. M. Fox, and M. S. Skolnick. "Coherent optical control of the spin of a single hole in an InAs/GaAs quantum dot". In: *Physical Review Letters* **108** (2012), pp. 1–5. DOI: 10.1103/PhysRevLett.108.017402.

[79] D. Ding, M. H. Appel, A. Javadi, X. Zhou, M. C. Löbl, I. Söllner, R. Schott, C. Papon, T. Pregnolato, L. Midolo, A. D. Wieck, A. Ludwig, R. J. Warburton, T. Schröder, and P. Lodahl. "Coherent Optical Control of a Quantum-Dot Spin-Qubit in a Waveguide-Based Spin-Photon Interface". In: *Physical Review Applied* **11** (2019), p. 031002. DOI: 10.1103/PhysRevApplied.11.031002.

[80] K. De Greve, P. L. McMahon, L. Yu, J. S. Pelc, C. Jones, C. M. Natarajan, N. Y. Kim, E. Abe, S. Maier, C. Schneider, M. Kamp, S. Höfling, R. H. Hadfield, A. Forchel, M. M. Fejer, and Y. Yamamoto. "Complete tomography of a high-fidelity solid-state entangled spin-photon qubit pair". In: *Nature Communications* **4** (2013), pp. 1–7. DOI: 10.1038/ncomms3228.

[81] H. M. Wiseman and G. J. Milburn. *Quantum Measurement and Control*. Cambridge University Press, 2009. DOI: 10.1017/CBO9780511813948.

[82] J. Berezovsky, M. H. Mikkelsen, O. Gywat, W. G. Stoltz, L. A. Coldren, and D. D. Awschalom. "Nondestructive optical measurements of a single electron spin in a quantum dot". In: *Science* **314** (2006), pp. 1916–1920. DOI: 10.1126/science.1133862.

[83] W. M. Itano, D. J. Heinzen, J. J. Bollinger, and D. J. Wineland. "Quantum Zero effect". In: *Physical Review A* **41** (1990), pp. 2295–2300. DOI: 10.1103/PhysRevA.41.2295.

[84] A. Palacios-Laloy, F. Mallet, F. Nguyen, P. Bertet, D. Vion, D. Esteve, and A. N. Korotkov. "Experimental violation of a Bells inequality in time with weak measurement". In: *Nature Physics* **6** (2010), pp. 442–447. DOI: 10.1038/nphys1641.

[85] D. S. Smirnov, E. A. Zhukov, D. R. Yakovlev, E. Kirstein, M. Bayer, and A. Greilich. "Spin polarization recovery and Hanle effect for charge carriers interacting with nuclear spins in semiconductors". In: *Physical Review B* **102** (2020), p. 235413. DOI: 10.1103/PhysRevB.102.235413.

[86] I. A. Merkulov, A. L. Efros, and M. Rosen. "Electron spin relaxation by nuclei in semiconductor quantum dots". In: *Physical Review B* **65** (2002), p. 205309. DOI: 10.1103/PhysRevB.65.205309.

[87] D. Brunner, B. D. Gerardot, P. A. Dalgarno, G. Wüst, K. Karrai, N. G. Stoltz, P. M. Petroff, and R. J. Warburton. "A coherent single-hole spin in a semiconductor". In: *Science* **325** (2009), pp. 70–72. DOI: 10.1126/science.1173684.

[88] D. Press, K. De Greve, P. L. McMahon, T. D. Ladd, B. Friess, C. Schneider, M. Kamp, S. Höfling, A. Forchel, and Y. Yamamoto. "Ultrafast optical spin echo in a single quantum dot". In: *Nature Photonics* **4** (2010), pp. 367–370. DOI: 10.1038/nphoton.2010.83.

[89] A. Bechtold, D. Rauch, F. Li, T. Simmet, P. L. Ardelt, A. Regler, K. Müller, N. A. Sinitsyn, and J. J. Finley. "Three-stage decoherence dynamics of an electron spin qubit in an optically active quantum dot". In: *Nature Physics* **11** (2015), pp. 1005–1008. DOI: 10.1038/nphys3470.

[90] X. J. Wang, S. Chesi, and W. A. Coish. "Spin-echo dynamics of a heavy hole in a quantum dot". In: *Physical Review Letters* **109** (2012), pp. 1–5. DOI: 10.1103/PhysRevLett.109.237601.

[91] E. A. Chekhovich, M. N. Makhonin, A. I. Tartakovskii, A. Yacoby, H. Bluhm, K. C. Nowack, and L. M. Vandersypen. "Nuclear spin effects in semiconductor quantum dots". In: *Nature Materials* **12** (2013), pp. 494–504. DOI: 10.1038/nmat3652.

[92] P.-F. Braun, B. Urbaszek, T. Amand, X. Marie, O. Krebs, B. Eble, A. Lemaitre, and P. Voisin. "Bistability of the nuclear polarization created through optical pumping in $\mathrm{In}_{1-x}\mathrm{Ga}_x\mathrm{As}$ quantum dots". In: *Physical Review B* **74** (2006), p. 245306. DOI: 10.1103/PhysRevB.74.245306.

[93] E. A. Chekhovich, M. N. Makhonin, K. V. Kavokin, A. B. Krysa, M. S. Skolnick, and A. I. Tartakovskii. "Pumping of nuclear spins by optical excitation of spin-forbidden transitions in a quantum dot". In: *Physical Review Letters* **104** (2010), pp. 1–4. DOI: 10.1103/PhysRevLett.104.066804.

[94] G. Éthier-Majcher, D. Gangloff, R. Stockill, E. Clarke, M. Hugues, C. Le Gall, and M. Atatüre. "Improving a Solid-State Qubit through an Engineered Mesoscopic Environment". In: *Physical Review Letters* **119** (2017), pp. 1–6. DOI: 10.1103/PhysRevLett.119.130503.

[95] D. A. Gangloff, G. Éthier-Majcher, C. Lang, E. V. Denning, J. H. Bodey, D. M. Jackson, E. Clarke, M. Hugues, C. Le Gall, and M. Atatüre. "Quantum interface of an electron and a nuclear ensemble". In: *Science* **364** (2019), pp. 62–66. DOI: 10.1126/science.aaw2906.

[96] G. M. Müller, M. Oestreich, M. Römer, and J. Hübner. "Semiconductor spin noise spectroscopy: Fundamentals, accomplishments, and challenges". In: *Physica E: Low-Dimensional Systems and Nanostructures* **43** (2010), pp. 569–587. DOI: 10.1016/j.physe.2010.08.010.

[97] V. S. Zapasskii. "Spin-noise spectroscopy: from proof of principle to applications". In: *Advances in Optics and Photonics* **5** (2013), p. 131. DOI: 10.1364/aop.5.000131.

[98] N. A. Sinitsyn and Y. V. Pershin. "The theory of spin noise spectroscopy: A review". In: *Reports on Progress in Physics* **79** (2016), p. 106501. DOI: 10.1088/0034-4885/79/10/106501.

[99] M. Oestreich, M. Römer, R. J. Haug, and D. Hägele. "Spin noise spectroscopy in GaAs". In: *Physical Review Letters* **95** (2005), pp. 1–4. DOI: 10.1103/PhysRevLett.95.216603.

[100] S. A. Crooker, J. Brandt, C. Sandfort, A. Greilich, D. R. Yakovlev, D. Reuter, A. D. Wieck, and M. Bayer. “Spin Noise of Electrons and Holes in Self-Assembled Quantum Dots”. In: *Physical Review Letters* **104** (2010), pp. 1–4. DOI: 10.1103/PhysRevLett.104.036601.

[101] R. Dahbashi, J. Hübner, F. Berski, K. Pierz, and M. Oestreich. “Optical spin noise of a single hole spin localized in an (InGa)as quantum dot”. In: *Physical Review Letters* **112** (2014), pp. 1–5. DOI: 10.1103/PhysRevLett.112.156601.

[102] V. B. Braginsky, Y. I. Vorontsov, and K. S. Thorne. “Quantum Nondemolition Measurements”. In: *Science* **209** (1980), pp. 547–557. DOI: 10.1126/science.209.4456.547.

[103] K. De Greve, L. Yu, P. L. McMahon, J. S. Pelc, C. M. Natarajan, N. Y. Kim, E. Abe, S. Maier, C. Schneider, M. Kamp, S. Höfling, R. H. Hadfield, A. Forchel, M. M. Fejer, and Y. Yamamoto. “Quantum-dot spin-photon entanglement via frequency downconversion to telecom wavelength”. In: *Nature* **491** (2012), pp. 421–425. DOI: 10.1038/nature11577.

[104] J. R. Schaibley, A. P. Burgers, G. A. McCracken, L. M. Duan, P. R. Berman, D. G. Steel, A. S. Bracker, D. Gammon, and L. J. Sham. “Demonstration of quantum entanglement between a single electron spin confined to an InAs quantum dot and a photon”. In: *Physical Review Letters* **110** (2013), pp. 1–5. DOI: 10.1103/PhysRevLett.110.167401.

[105] A. Delteil, Z. Sun, W. B. Gao, E. Togan, S. Faelt, and A. Imamoglu. “Generation of heralded entanglement between distant hole spins”. In: *Nature Physics* **12** (2016), pp. 218–223. DOI: 10.1038/nphys3605.

[106] R. Stockill, M. J. Stanley, L. Huthmacher, E. Clarke, M. Hugues, A. J. Miller, C. Matthiesen, C. Le Gall, and M. Atatüre. “Phase-Tuned Entangled State Generation between Distant Spin Qubits”. In: *Physical Review Letters* **119** (2017), pp. 1–6. DOI: 10.1103/PhysRevLett.119.010503.

[107] M. H. Appel, A. Tiranov, S. Pabst, M. L. Chan, C. Starup, Y. Wang, L. Midolo, K. Tiurev, S. Scholz, A. D. Wieck, A. Ludwig, A. S. Sørensen, and P. Lodahl. “Entangling a Hole Spin with a Time-Bin Photon: A Waveguide Approach for Quantum Dot Sources of Multiphoton Entanglement”. In: *Physical Review Letters* **128** (2022), p. 233602. DOI: 10.1103/PhysRevLett.128.233602.

[108] E. Jaynes and F. Cummings. “Comparison of quantum and semiclassical radiation theories with application to the beam maser”. In: *Proceedings of the IEEE* **51** (1963), pp. 89–109. DOI: 10.1109/PROC.1963.1664.

[109] A. Frisk Kockum, A. Miranowicz, S. De Liberato, S. Savasta, and F. Nori. “Ultrastrong coupling between light and matter”. In: *Nature Reviews Physics* **1** (2019), pp. 19–40. DOI: 10.1038/s42254-018-0006-2.

[110] L. C. Andreani, G. Panzarini, and J.-M. Gérard. “Strong-coupling regime for quantum boxes in pillar microcavities: Theory”. In: *Physical Review B* **60** (1999), pp. 13276–13279. DOI: 10.1103/PhysRevB.60.13276.

[111] E. M. Purcell. “Spontaneous Emission Probabilities at Radio Frequencies”. In: *Confined Electrons and Photons: New Physics and Applications*. Springer US, 1995, p. 839. DOI: 10.1007/978-1-4615-1963-8_40.

[112] A. Auffèves-Garnier, C. Simon, J.-M. M. Gérard, and J.-P. P. Poizat. “Giant optical nonlinearity induced by a single two-level system interacting with a cavity in the Purcell regime”. In: *Physical Review A* **75** (2007), p. 053823. DOI: 10.1103/PhysRevA.75.053823.

[113] D. Najer, I. Söllner, P. Sekatski, V. Dolique, M. C. Löbl, D. Riedel, R. Schott, S. Starosielec, S. R. Valentin, A. D. Wieck, N. Sangouard, A. Ludwig, and R. J. Warburton. “A gated quantum dot strongly coupled to an optical microcavity”. In: *Nature* **575** (2019), pp. 622–627. DOI: 10.1038/s41586-019-1709-y.

[114] O. Painter, R. K. Lee, A. Scherer, A. Yariv, J. D. O’Brien, P. D. Dapkus, and I. Kim. “Two-dimensional photonic band-gap defect mode laser”. In: *Science* **284** (1999), pp. 1819–1821. DOI: 10.1126/science.284.5421.1819.

[115] Y. Akahane, T. Asano, B. S. Song, and S. Noda. “High-Q photonic nanocavity in a two-dimensional photonic crystal”. In: *Nature* **425** (2003), pp. 944–947. DOI: 10.1038/nature02063.

[116] T. Yoshie, A. Scherer, J. Hendrickson, G. Khitrova, H. M. Gibbs, G. Rupper, C. Ell, O. B. Shchekin, and D. G. Deppe. “Vacuum Rabi splitting with a single quantum dot in a photonic crystal nanocavity”. In: *Nature* **432** (2004), pp. 200–203. DOI: 10.1038/nature03119.

[117] D. Englund, D. Fattal, E. Waks, G. Solomon, B. Zhang, T. Nakaoka, Y. Arakawa, Y. Yamamoto, and J. Vučković. “Controlling the spontaneous emission rate of single quantum dots in a two-dimensional photonic crystal”. In: *Physical Review Letters* **95** (2005), pp. 2–5. DOI: 10.1103/PhysRevLett.95.013904.

[118] S. Combrié, A. De Rossi, Q. V. Tran, and H. Benisty. “GaAs photonic crystal cavity with ultrahigh Q: microwatt nonlinearity at 1.55 μm”. In: *Optics Letters* **33** (2008), p. 1908. DOI: 10.1364/OL.33.001908.

[119] S. Sun, H. Kim, G. S. Solomon, and E. Waks. “A quantum phase switch between a single solid-state spin and a photon”. In: *Nature Nanotechnology* **11** (2016), pp. 539–544. DOI: 10.1038/nnano.2015.334.

[120] S. L. McCall, A. F. Levi, R. E. Slusher, S. J. Pearton, and R. A. Logan. “Whispering-gallery mode microdisk lasers”. In: *Applied Physics Letters* **60** (1992), pp. 289–291. DOI: 10.1063/1.106688.

[121] B. Gayral, J. M. Gérard, A. Lemaître, C. Dupuis, L. Manin, and J. L. Pelouard. "High-Q wet-etched GaAs microdisks containing InAs quantum boxes". In: *Applied Physics Letters* **75** (1999), pp. 1908–1910. DOI: 10.1063/1.124894.

[122] B. Gayral, J. M. Gérard, B. Sermage, A. Lemaître, and C. Dupuis. "Time-resolved probing of the Purcell effect for InAs quantum boxes in GaAs microdisks". In: *Applied Physics Letters* **78** (2001), pp. 2828–2830. DOI: 10.1063/1.1370123.

[123] P. Michler, A. Kiraz, C. Becher, W. V. Schoenfeld, P. M. Petroff, L. Zhang, E. Hu, and A. Imamoglu. "A Quantum Dot Single-Photon Turnstile Device". In: *Science* **290** (2000), pp. 2282–2285. DOI: 10.1126/science.290.5500.2282.

[124] E. Peter, P. Senellart, D. Martrou, A. Lemaître, J. Hours, J. M. Gérard, and J. Bloch. "Exciton-photon strong-coupling regime for a single quantum dot embedded in a microcavity". In: *Physical Review Letters* **95** (2005), pp. 1–4. DOI: 10.1103/PhysRevLett.95.067401.

[125] K. Srinivasan, M. Borselli, T. J. Johnson, P. E. Barclay, O. Painter, A. Stintz, and S. Krishna. "Optical loss and lasing characteristics of high-quality-factor AlGaAs microdisk resonators with embedded quantum dots". In: *Applied Physics Letters* **86** (2005), pp. 1–3. DOI: 10.1063/1.1901810.

[126] M. Davanço, M. T. Rakher, D. Schuh, A. Badolato, and K. Srinivasan. "A circular dielectric grating for vertical extraction of single quantum dot emission". In: *Applied Physics Letters* **99** (2011), pp. 1–4. DOI: 10.1063/1.3615051.

[127] H. Wang et al. "Towards optimal single-photon sources from polarized microcavities". In: *Nature Photonics* **13** (2019), pp. 770–775. DOI: 10.1038/s41566-019-0494-3.

[128] O. Iff, Q. Buchinger, M. Moczała-Dusanowska, M. Kamp, S. Betzold, M. Davanco, K. Srinivasan, S. Tongay, C. Antón-Solanas, S. Höfling, and C. Schneider. "Purcell-Enhanced Single Photon Source Based on a Deterministically Placed WSe2 Monolayer Quantum Dot in a Circular Bragg Grating Cavity". In: *Nano Letters* **21** (2021), pp. 4715–4720. DOI: 10.1021/acs.nanolett.1c00978.

[129] J. M. Gérard, B. Sermage, B. Gayral, B. Legrand, E. Costard, and V. Thierry-Mieg. "Enhanced spontaneous emission by quantum boxes in a monolithic optical microcavity". In: *Physical Review Letters* **81** (1998), pp. 1110–1113. DOI: 10.1103/PhysRevLett.81.1110.

[130] M. Pelton, C. Santori, J. Vučković, B. Zhang, G. S. Solomon, J. Plant, and Y. Yamamoto. "Efficient Source of Single Photons: A Single Quantum Dot in a Micropost Microcavity". In: *Physical Review Letters* **89** (2002), pp. 1–4. DOI: 10.1103/PhysRevLett.89.233602.

[131] J. P. Reithmaier, G. Sęk, A. Löffler, C. Hofmann, S. Kuhn, S. Reitzenstein, L. V. Keldysh, V. D. Kulakovskii, T. L. Reinecke, and A. Forchel. "Strong coupling in a single quantum dot-semiconductor microcavity system". In: *Nature* **432** (2004), pp. 197–200. DOI: 10.1038/nature02969.

[132] C. Arnold, V. Loo, A. Lematre, I. Sagnes, O. Krebs, P. Voisin, P. Senellart, and L. Lanco. "Optical bistability in a quantum dots/micropillar device with a quality factor exceeding 200 000". In: *Applied Physics Letters* **100** (2012), pp. 0–3. DOI: 10.1063/1.3694026.

[133] P. Hilaire, C. Antón, C. Kessler, A. Lemaître, I. Sagnes, N. Somaschi, P. Senellart, and L. Lanco. "Accurate measurement of a 96% input coupling into a cavity using polarization tomography". In: *Applied Physics Letters* **112** (2018), p. 201101. DOI: 10.1063/1.5026799.

[134] M. Munsch, N. S. Malik, E. Dupuy, A. Delga, J. Bleuse, J. M. Gérard, J. Claudon, N. Gregersen, and J. Mørk. "Dielectric GaAs antenna ensuring an efficient broadband coupling between an InAs quantum dot and a gaussian optical beam". In: *Physical Review Letters* **110** (2013), pp. 1–5. DOI: 10.1103/PhysRevLett.110.177402.

[135] J. Miguel-Sánchez, A. Reinhard, E. Togan, T. Volz, A. Imamoglu, B. Besga, J. Reichel, and J. Estève. "Cavity quantum electrodynamics with charge-controlled quantum dots coupled to a fiber Fabry-Perot cavity". In: *New Journal of Physics* **15** (2013). DOI: 10.1088/1367-2630/15/4/045002.

[136] A. Dousse. "Deterministic cavity-quantum dot coupling and fabrication of an ultrabright source of entangled photon pairs". PhD thesis. 2010. URL: http://www.theses.fr/2010PA077134.

[137] A. Dousse et al. "Scalable implementation of strongly coupled cavity-quantum dot devices". In: *Applied Physics Letters* **94** (2009), p. 121102. DOI: 10.1063/1.3100781.

[138] B. Gayral, J. M. Gérard, B. Legrand, E. Costard, and V. Thierry-Mieg. "Optical study of GaAs/AlAs pillar microcavities with elliptical cross section". In: *Applied Physics Letters* **72** (1998), pp. 1421–1423. DOI: 10.1063/1.120582.

[139] N. Tomm, A. Javadi, N. O. Antoniadis, D. Najer, M. C. Löbl, A. R. Korsch, R. Schott, S. R. Valentin, A. D. Wieck, A. Ludwig, and R. J. Warburton. "A bright and fast source of coherent single photons". In: *Nature Nanotechnology* **16** (2021). DOI: 10.1038/s41565-020-00831-x.

[140] A. K. Nowak, S. L. Portalupi, V. Giesz, O. Gazzano, C. Dal Savio, P. F. Braun, K. Karrai, C. Arnold, L. Lanco, I. Sagnes, A. Lemaître, and P. Senellart. "Deterministic and electrically tunable bright single-photon source". In: *Nature Communications* **5** (2014), pp. 1–7. DOI: 10.1038/ncomms4240.

[141] J. C. Loredo, C. Antón, B. Reznychenko, P. Hilaire, A. Harouri, C. Millet, H. Ollivier, N. Somaschi, L. De Santis, A. Lemaître, I. Sagnes, L. Lanco, A. Auffèves, O. Krebs, and P. Senellart. "Generation of non-classical light in a photon-number superposition". In: *Nature Photonics* **13** (2019), pp. 803–808. DOI: 10.1038/s41566-019-0506-3.

[142] D. Istrati, Y. Pilnyak, J. C. Loredo, C. Antón, N. Somaschi, P. Hilaire, H. Ollivier, M. Esmann, L. Cohen, L. Vidro, C. Millet, A. Lemaître, I. Sagnes, A. Harouri, L. Lanco, P. Senellart, and H. S. Eisenberg. "Sequential generation of linear cluster states from a single photon emitter". In: *Nature Communications* **11** (2020), pp. 1–8. DOI: 10.1038/s41467-020-19341-4.

[143] C. Y. Hu, A. Young, J. L. O'Brien, W. J. Munro, and J. G. Rarity. "Giant optical Faraday rotation induced by a single-electron spin in a quantum dot: Applications to entangling remote spins via a single photon". In: *Physical Review B* **78** (2008), p. 085307. DOI: 10.1103/PhysRevB.78.085307.

[144] V. Loo, L. Lanco, A. Lemaître, I. Sagnes, O. Krebs, P. Voisin, and P. Senellart. "Quantum dot-cavity strong-coupling regime measured through coherent reflection spectroscopy in a very high-Q micropillar". In: *Applied Physics Letters* **97** (2010), pp. 10–13. DOI: 10.1063/1.3527930.

[145] M. T. Rakher, N. G. Stoltz, L. A. Coldren, P. M. Petroff, and D. Bouwmeester. "Externally mode-matched cavity quantum electrodynamics with charge-tunable quantum dots". In: *Physical Review Letters* **102** (2009), pp. 6–9. DOI: 10.1103/PhysRevLett.102.097403.

[146] A. J. Bennett, J. P. Lee, D. J. Ellis, I. Farrer, D. A. Ritchie, and A. J. Shields. "A semiconductor photon-sorter". In: *Nature Nanotechnology* **11** (2016), pp. 857–860. DOI: 10.1038/nnano.2016.113.

[147] C. Antón, P. Hilaire, C. A. Kessler, J. Demory, C. Gómez, A. Lemaître, I. Sagnes, N. D. Lanzillotti-Kimura, O. Krebs, N. Somaschi, P. Senellart, and L. Lanco. "Tomography of the optical polarization rotation induced by a single quantum dot in a cavity". In: *Optica* **4** (2017), p. 1326. DOI: 10.1364/OPTICA.4.001326.

[148] P. Hilaire, C. Millet, J. C. Loredo, C. Antón, A. Harouri, A. Lemaître, I. Sagnes, N. Somaschi, O. Krebs, P. Senellart, and L. Lanco. "Deterministic assembly of a charged-quantum-dot–micropillar cavity device". In: *Physical Review B* **102** (2020), pp. 1–9. DOI: 10.1103/PhysRevB.102.195402.

[149] H. C. Casey, D. D. Sell, and K. W. Wecht. "Concentration dependence of the absorption coefficient for n- and p- type GaAs between 1.3 and 1.6 eV". In: *Journal of Applied Physics* **46** (1975), pp. 250–257. DOI: 10.1063/1.321330.

[150] K. Kowalik, O. Krebs, A. Lemaître, S. Laurent, P. Senellart, P. Voisin, and J. A. Gaj. "Influence of an in-plane electric field on exciton fine structure in InAs-GaAs self-assembled quantum dots". In: *Applied Physics Letters* **86** (2005), p. 041907. DOI: 10.1063/1.1855409.

[151] A. Schwan, B. M. Meiners, A. Greilich, D. R. Yakovlev, M. Bayer, A. D. Maia, A. A. Quivy, and A. B. Henriques. "Anisotropy of electron and hole g-factors in (In,Ga)As quantum dots". In: *Applied Physics Letters* **99** (2011), pp. 2009–2012. DOI: 10.1063/1.3665634.

[152] A. V. Trifonov, I. A. Akimov, L. E. Golub, E. L. Ivchenko, I. A. Yugova, A. N. Kosarev, S. E. Scholz, C. Sgroi, A. Ludwig, A. D. Wieck, D. R. Yakovlev, and M. Bayer. "Strong enhancement of heavy-hole Landé factor in InGaAs symmetric quantum dots revealed by coherent optical spectroscopy". In: *arXiv* (2021), pp. 1–17. URL: http://arxiv.org/abs/2103.13653.

[153] T. Braun, S. Betzold, N. Lundt, M. Kamp, S. Höfling, and C. Schneider. "Impact of ex situ rapid thermal annealing on magneto-optical properties and oscillator strength of In(Ga)As quantum dots". In: *Physical Review B* **93** (2016), pp. 1–7. DOI: 10.1103/PhysRevB.93.155307.

[154] H. Ollivier, I. Maillette de Buy Wenniger, S. Thomas, S. C. Wein, A. Harouri, G. Coppola, P. Hilaire, C. Millet, A. Lemaître, I. Sagnes, O. Krebs, L. Lanco, J. C. Loredo, C. Antón, N. Somaschi, and P. Senellart. "Reproducibility of High-Performance Quantum Dot Single-Photon Sources". In: *ACS Photonics* **7** (2020), pp. 1050–1059. DOI: 10.1021/acsphotonics.9b01805.

[155] P. Hilaire. "A cavity-based spin-photon interface". PhD thesis. 2019. URL: https://www.theses.fr/2019USPCC108.

[156] M. E. Ware, E. A. Stinaff, D. Gammon, M. F. Doty, A. S. Bracker, D. Gershoni, V. L. Korenev, S. C. Badescu, Y. Lyanda-Geller, and T. L. Reinecke. "Polarized Fine Structure in the Photoluminescence Excitation Spectrum of a Negatively Charged Quantum Dot". In: *Physical Review Letters* **95** (2005), p. 177403. DOI: 10.1103/PhysRevLett.95.177403.

[157] P. Podemski, A. Maryński, P. Wyborski, A. Bercha, W. Trzeciakowski, and G. Sęk. "Single dot photoluminescence excitation spectroscopy in the telecommunication spectral range". In: *Journal of Luminescence* **212** (2019), pp. 300–305. DOI: 10.1016/j.jlumin.2019.04.058.

[158] R. J. Glauber. "The quantum theory of optical coherence". In: *Physical Review* **130** (1963), pp. 2529–2539. DOI: 10.1103/PhysRev.130.2529.

[159] M. Fox. *Quantum optics: an introduction*. Oxford Univ. Press, 2006. URL: https://global.oup.com/ukhe/product/quantum-optics-9780198566731.

[160] R. Hanbury Brown and R. Q. Twiss. "Correlation between Photons in two Coherent Beams of Light". In: *Nature* **177** (1956), pp. 27–29. DOI: 10.1038/177027a0.

[161] C. K. Hong, Z. Y. Ou, and L. Mandel. "Measurement of subpicosecond time intervals between two photons by interference". In: *Physical Review Letters* **59** (1987), pp. 2044–2046. DOI: 10.1103/PhysRevLett.59.2044.

[162] H. Ollivier et al. "Hong-Ou-Mandel Interference with Imperfect Single Photon Sources". In: *Physical Review Letters* **126** (2021), p. 063602. DOI: 10.1103/PhysRevLett.126.063602.

[163] J. C. Loredo, N. A. Zakaria, N. Somaschi, C. Anton, L. de Santis, V. Giesz, T. Grange, M. A. Broome, O. Gazzano, G. Coppola, I. Sagnes, A. Lemaitre, A. Auffeves, P. Senellart, M. P. Almeida, and A. G. White. "Scalable performance in solid-state single-photon sources". In: *Optica* **3** (2016), p. 433. DOI: 10.1364/OPTICA.3.000433.

[164] B. Piętka, J. Suffczyński, M. Goryca, T. Kazimierczuk, A. Golnik, P. Kossacki, A. Wysmolek, J. A. Gaj, R. Stępniewski, and M. Potemski. "Photon correlation studies of charge variation in a single GaAlAs quantum dot". In: *Physical Review B* **87** (2013), p. 035310. DOI: 10.1103/PhysRevB.87.035310.

[165] A. Kiraz, S. Fälth, C. Becher, B. Gayral, W. V. Schoenfeld, P. M. Petroff, L. Zhang, E. Hu, and A. Imamoğlu. "Photon correlation spectroscopy of a single quantum dot". In: *Physical Review B* **65** (2002), p. 161303. DOI: 10.1103/PhysRevB.65.161303.

[166] M. C. Löbl, C. Spinnler, A. Javadi, L. Zhai, G. N. Nguyen, J. Ritzmann, L. Midolo, P. Lodahl, A. D. Wieck, A. Ludwig, and R. J. Warburton. "Radiative Auger process in the single-photon limit". In: *Nature Nanotechnology* **15** (2020), pp. 558–562. DOI: 10.1038/s41565-020-0697-2.

[167] G. Sallen, A. Tribu, T. Aichele, R. André, L. Besombes, C. Bougerol, M. Richard, S. Tatarenko, K. Kheng, and J. P. Poizat. "Subnanosecond spectral diffusion measurement using photon correlation". In: *Nature Photonics* **4** (2010), pp. 696–699. DOI: 10.1038/nphoton.2010.174.

[168] A. V. Kuhlmann, J. Houel, A. Ludwig, L. Greuter, D. Reuter, A. D. Wieck, M. Poggio, and R. J. Warburton. "Charge noise and spin noise in a semiconductor quantum device". In: *Nature Physics* **9** (2013), pp. 570–575. DOI: 10.1038/nphys2688.

[169] H. J. Carmichael. *Statistical Methods in Quantum Optics 1*. Springer Berlin Heidelberg, 1999. DOI: 10.1007/978-3-662-03875-8.

[170] C. Cohen-Tannoudji, J. Dupont-Roc, and G. Grynberg. *Atom-Photon Interactions*. Wiley, 1998. DOI: 10.1002/9783527617197.

[171] C. W. Gardiner and M. J. Collett. "Input and output in damped quantum systems: Quantum stochastic differential equations and the master equation". In: *Physical Review A* **31** (1985), pp. 3761–3774. DOI: 10.1103/PhysRevA.31.3761.

[172] B. Y. Wang, T. Häyrynen, L. Vannucci, M. A. Jacobsen, C. Y. Lu, and N. Gregersen. "Suppression of background emission for efficient single-photon generation in micropillar cavities". In: *Applied Physics Letters* **118** (2021). DOI: 10.1063/5.0044018.

[173] A. V. Khaetskii and Y. V. Nazarov. "Spin-flip transitions between Zeeman sublevels in semiconductor quantum dots". In: *Physical Review B* **64** (2001), p. 125316. DOI: 10.1103/PhysRevB.64.125316.

[174] V. I. Fal'ko, B. L. Altshuler, and O. Tsyplyatyev. "Anisotropy of spin splitting and spin relaxation in lateral quantum dots". In: *Physical Review Letters* **95** (2005), pp. 1–4. DOI: 10.1103/PhysRevLett.95.076603.

[175] N. A. Sinitsyn, Y. Li, S. A. Crooker, A. Saxena, and D. L. Smith. "Role of nuclear quadrupole coupling on decoherence and relaxation of central spins in quantum dots". In: *Physical Review Letters* **109** (2012), pp. 1–5. DOI: 10.1103/PhysRevLett.109.166605.

[176] S. M. Tan. "Computational toolbox for quantum and atomic optics". In: *Journal of Optics B: Quantum and Semiclassical Optics* **1** (1999), pp. 424–432. DOI: 10.1088/1464-4266/1/4/312.

[177] J. R. Johansson, P. D. Nation, and F. Nori. "QuTiP: An open-source Python framework for the dynamics of open quantum systems". In: *Computer Physics Communications* **183** (2012), pp. 1760–1772. DOI: 10.1016/j.cpc.2012.02.021.

[178] J. R. Johansson, P. D. Nation, and F. Nori. "QuTiP 2: A Python framework for the dynamics of open quantum systems". In: *Computer Physics Communications* **184** (2013), pp. 1234–1240. DOI: 10.1016/j.cpc.2012.11.019.

[179] D. S. Smirnov, B. Reznychenko, A. Auffèves, and L. Lanco. "Measurement back action and spin noise spectroscopy in a charged cavity QED device in the strong coupling regime". In: *Physical Review B* **96** (2017), p. 165308. DOI: 10.1103/PhysRevB.96.165308.

[180] J. Hansom, C. H. Schulte, C. Matthiesen, M. J. Stanley, and M. Atature. "Frequency stabilization of the zero-phonon line of a quantum dot via phonon-assisted active feedback". In: *Applied Physics Letters* **105** (2014). DOI: 10.1063/1.4901045.

[181] J. H. Prechtel, A. V. Kuhlmann, J. Houel, L. Greuter, A. Ludwig, D. Reuter, A. D. Wieck, and R. J. Warburton. "Frequency-Stabilized Source of Single Photons from a Solid-State Qubit". In: *Physical Review X* **3** (2013), pp. 1–7. DOI: 10.1103/PhysRevX.3.041006.

[182] E. Mehdi, M. Gundin-Martinez, C. Millet, N. Somaschi, A. Lemaître, I. Sagnes, L. L. Gratiet, D. Fioretto, N. Belabas, O. Krebs, P. Senellart, and L. Lanco. "Controlling photon polarisation with a single quantum dot spin". In: *arXiv* (2022), pp. 29–32. URL: http://arxiv.org/abs/2212.03767.

[183] N. Coste, M. Gundin, D. Fioretto, S. E. Thomas, C. Millet, E. Medhi, M. Gundin, N. Somaschi, M. Morassi, M. Pont, A. Lemaitre, N. Belabas, O. Krebs, L. Lanco, and P. Senellart. "Probing the dynamics and coherence of a semiconductor hole spin via acoustic phonon-assisted excitation". In: *arXiv* (2022), pp. 1–6. URL: http://arxiv.org/abs/2207.05981.

[184] R. Raussendorf and H. J. Briegel. "A one-way quantum computer". In: *Physical Review Letters* **86** (2001), pp. 5188–5191. DOI: 10.1103/PhysRevLett.86.5188.

[185] R. Raussendorf, D. E. Browne, and H. J. Briegel. “Measurement-based quantum computation on cluster states”. In: *Physical Review A* **68** (2003), p. 022312. DOI: 10.1103/PhysRevA.68.022312.

[186] H. J. Briegel, D. E. Browne, W. Dür, R. Raussendorf, and M. Van Den Nest. “Measurement-based quantum computation”. In: *Nature Physics* **5** (2009), pp. 19–36. DOI: 10.1038/nphys1157.

[187] P. Hilaire, E. Barnes, and S. E. Economou. “Resource requirements for efficient quantum communication using all-photonic graph states generated from a few matter qubits”. In: *Quantum* **5** (2021). DOI: 10.22331/Q-2021-02-15-397.

[188] I. Schwartz, D. Cogan, E. R. Schmidgall, Y. Don, L. Gantz, O. Kenneth, N. H. Lindner, and D. Gershoni. “Deterministic generation of a cluster state of entangled photons”. In: *Science* **354** (2016), pp. 434–437. DOI: 10.1126/science.aah4758.

[189] P. Thomas, L. Ruscio, O. Morin, and G. Rempe. “Efficient generation of entangled multiphoton graph states from a single atom”. In: *Nature* **608** (2022), pp. 677–681. DOI: 10.1038/s41586-022-04987-5.

[190] N. Coste, D. Fioretto, N. Belabas, S. C. Wein, P. Hilaire, R. Frantzeskakis, M. Gundin, B. Goes, N. Somaschi, M. Morassi, A. Lemaître, I. Sagnes, A. Harouri, S. E. Economou, A. Auffeves, O. Krebs, L. Lanco, and P. Senellart. “High-rate entanglement between a semiconductor spin and indistinguishable photons”. In: *arXiv* (2022), pp. 1–17. URL: http://arxiv.org/abs/2207.09881.

[191] K. Koshino, S. Ishizaka, and Y. Nakamura. “Deterministic photon-photon $\sqrt{\text{SWAP}}$ gate using a Λ system”. In: *Physical Review A* **82** (2010), p. 010301. DOI: 10.1103/PhysRevA.82.010301.

[192] S. Rosenblum, A. Borne, and B. Dayan. “Analysis of deterministic swapping of photonic and atomic states through single-photon Raman interaction”. In: *Physical Review A* **95** (2017), pp. 1–11. DOI: 10.1103/PhysRevA.95.033814.

[193] L. Béguin, J. P. Jahn, J. Wolters, M. Reindl, Y. Huo, R. Trotta, A. Rastelli, F. Ding, O. G. Schmidt, P. Treutlein, and R. J. Warburton. “On-demand semiconductor source of 780-nm single photons with controlled temporal wave packets”. In: *Physical Review B* **97** (2018), pp. 1–8. DOI: 10.1103/PhysRevB.97.205304.

[194] C. Matthiesen, A. N. Vamivakas, and M. Atatüre. “Subnatural linewidth single photons from a quantum dot”. In: *Physical Review Letters* **108** (2012), pp. 1–4. DOI: 10.1103/PhysRevLett.108.093602.

[195] H. S. Nguyen, G. Sallen, C. Voisin, P. Roussignol, C. Diederichs, and G. Cassabois. “Ultra-coherent single photon source”. In: *Applied Physics Letters* **99** (2011), pp. 97–100. DOI: 10.1063/1.3672034.

[196] S. Sun, H. Kim, Z. Luo, G. S. Solomon, and E. Waks. "A single-photon switch and transistor enabled by a solid-state quantum memory". In: *Science* **361** (2018), pp. 57–60. DOI: 10.1126/science.aat3581.

[197] J. Hansom, C. H. Schulte, C. Le Gall, C. Matthiesen, E. Clarke, M. Hugues, J. M. Taylor, and M. Atatüre. "Environment-assisted quantum control of a solid-state spin via coherent dark states". In: *Nature Physics* **10** (2014), pp. 725–730. DOI: 10.1038/nphys3077.